Cranfield University

Vivien Beyer

A study of Laser-Induced Incandescence under high vacuum conditions

School of Engineering

PhD Thesis

Cranfield University School of Engineering
Automotive Department

A study of Laser-Induced Incandescence under high vacuum conditions

PhD Thesis

Vivien Beyer

Academic year 2005/2006

July 2006

Supervisor: Professor D.A. Greenhalgh

This thesis is submitted in fulfilment of the requirements for the degree of doctor of philosophy

Abstract

Laser-Induced Incandescence (LII) occurs when a high-energy pulsed laser beam encounters graphitic particulate matter particles like soot or carbon black. The particles absorb laser energy from the beam and see an increase in their internal energy, resulting in an increase of temperature. At the same time, the particles loose energy through heat transfer mechanisms. If the energy absorption rate is sufficiently high, particle temperature will rise to levels where significant incandescence (blackbody emission) can occur .Typically, Laser-Induced Incandescence produces 50ns to 1μs long light pulses at atmospheric pressure.

So far, LII measurements had been restrained to conduction-dominated conditions, whereby signals are short-lived (less than one microsecond) and require sensitive nanosecond resolution instrumentation. This thesis introduces a novel LII – based measurement method performed under high vacuum conditions. The novelty of LII under vacuum resided in the fact that heat conduction away from the soot particle becomes negligible below 10^{-2} mbar and this constituted a step away from the typical situation, whereby laser absorption is followed by heat conduction from the particles to the surrounding medium. Instead, sublimation and radiative heat transfer would follow laser absorption. The consequence was the obtention of long-lived LII signals (up to 100 microseconds) and a large gain of photons (ranging between 50 to 300) emitted per primary soot particle during LII temperature decays. Furthermore, the refractive index function E(m) value could be determined directly from measured radiative temperature decays, with potentially an uncertainty of circa 7%, which outperformed current soot extinction measurements. In addition, for laser fluences below 0.06 J/cm^2, a regime where only laser energy absorption and radiative heat transfer apply would be reached and LII signals became independent of particle size.

Throughout this project, Laser-Induced Incandescence under vacuum was applied to a sample of carbon powder (agglomerated soot particles) sealed in a glass vessel and held below 10^{-3} mbar. Initial spectral measurements performed at a laser fluence of 0.3 J/cm^2 confirmed the obtention of long-lived (60 microseconds long) blackbody spectra, which confirmed the feasibility of the technique and yielded an E(m) measurement of between 0.35 and 0.45. A second study was performed with a dual-wavelength pyrometric system specifically designed for recording live LII temperatures and signal intensities coupled to an absolute light intensity calibrated intensified imaging system. Experimental results unveiled the thermo-physical behaviours of agglomerates enduring LII. The most remarkable outcomes of the results concerning carbon nanoparticles agglomerates were that: clusterous particulate matter absorbs and radiates light in a very similarly to single isolated carbon nanoparticles and therefore obey largely the Rayleigh limit; soot agglomerates also dissociate during LII in an explosive mode and ejecta were measured to reach up to 400 m/s following chain dissociations; complete agglomerate dissociations can be obtained and measurements performed on individual aggregates of primary soot nanoparticles. In parallel, LII measurements revealed that optical shielding is largely present within agglomerates, and therefore clusters dissociations exposed large quantities of particulate matter and increased greatly LII signal levels. Overall, radiative heat transfer measurements yielded E(m) = 0.4 to 0.6 and time-integrated ICCD measurements resolved signal levels as low as groups of 6 carbon

nanoparticles. This sensitivity clearly was the highest recorded to date for Laser Induced Incandescence and the sensitivity boundary of the technique was increased to nearly resolving single nanoparticles.

Further measurements were performed in collaboration with the National Research Council (NRC) of Ottawa, Canada, at the Combustion Research Group facility. The results obtained validated the obtention of repeatable temperature profiles for Laser-Induced Incandescence under vacuum. In addition, comparison between results obtained on a controlled source of agglomerates at atmospheric pressure established that the increase for LII signals with laser fluence for both atmospheric and vacuum conditions could be directly associated with agglomerates dissociations. Indeed, net diminutions in optical shielding were measured in both conditions and could be coupled with diminutions in thermal shielding at atmospheric pressures. High-resolution temperature measurements established that laser absorption, annealing, sublimation and radiative heat transfer rates could be unprecedently and directly measured by laser-induced incandescence under vacuum. Annealing and sublimation of soot primary particles could also reasonably be assumed to be the phenomena at the heart of agglomerate dissociations. It was also established that agglomerate dissociation was dependent not only on laser fluence but also on the instantaneous laser power absorbed by the carbon agglomerates: indeed measurements performed at NRC were effected with a instantaneous laser powers four times lower than previously and radiative heat transfer measurements attested incomplete agglomerate dissociations with E(m) values measured between 0.8 and 1.

Overall, the present work introduces LII under vacuum as a high sensitivity measurement method for particulate matter. The sensitivities obtained approached nanoparticles resolution and constitutes one of the most sensitive particulate matter measurement technique to date with real-time measurements capability. Because of the sample studied, agglomerate dynamics during LII were unveiled for the first time and explained the increase of LII signals with laser fluence as a diminution of both thermal and optical shielding. The LII under vacuum technique also proved its ability to resolve and isolate some of the key phenomena occurring during LII: laser absorption, annealing, sublimation and heat radiation.

Acknowledgements

In am indebted to my supervisor, Douglas A. Greenhalgh, for his participation , encouragements, personal involvement, interest and enthusiasm throughout this work.
I would also like to gratefully acknowledge the technical support and advice from the late Bob Wilson.
I am also grateful to the National Research Council (NRC), Ottawa, Canada, and in particular the Combustion Research Team from ICPET for their great encouragements and advices in my research, including Gregory J. Smallwood, Dave Snelling, Kyle Daun, Kevin Thomson, Fengshan Liu, Dan Clavel, Daniel Gareau, Regent Smith, Fazil Baksh, and in particular Bob Sawchuck for his great commitment at performing experimental work with me while at NRC. I would like to thank my friends at Cranfield, in particular Cristina Bertoni, Marie-Pierre Chappuis, Michel Fouinneteau and Ennio Capria for their constant support and help. I would also like to thank my Colleagues at Cranfield, in particular Marko Tirović for his support and Dr. Glenn Sherwood for his expertise.

My fondest thanks to my girlfriend Nadia for her support, encouragement, revolutionary scientific innovations and initiatives throughout my PhD as well as my mum and dad, who have always done more than necessary to ease the process of completing this degree.

To Thérèse, Barbe and Alphonse …

Foreword

Soot, also called particulate matter, is a by-product of both human and natural activity. When originating from human activity, soot is formed in processes involving fuel-rich combustion conditions. It constitutes a carrier for carcerinogenic and toxic compounds, such as polyaromatic hydrocarbons, sulphur and metallic ashes into the human lung epithelium. As well, it is the second contributor to climatic changes after carbon dioxide and had a large contribution as an solar radiation absorber within the atmosphere.

Soot production is largely associated with vehicular emissions and industrial activities. Even though recent regulations led to strict reductions in terms of mass of particulate matter emissions, these same regulations have led to a situation where the vast majority of particulate matter emissions are now in the $PM_{2.5}$ (particulate matter below 2.5 microns) size range. The consequence of this is that, in terms of vehicular emissions, the total particulate mass emitted has been drastically reduced. However, this mass reduction has since translated into a larger number of smaller emitted particles having a greater penetration depth and active surface area in human lungs epithelium and therefore a greater toxicity potential.
In terms of particulate matter measurements, this translates into the progressive obsolescence of the current measurement standard, the gravimetric procedure, whereby part of an exhaust stream is passed through a high efficiency particle filter held at 52°C and the particulate mass loading of the filter measured.

Therefore the need for a new particulate matter measurement legal standard has been recognized in the recent years and the focus is on particulate matter measurement methods that can prove highly sensitive, repeatable, resolve sharp transients and particle sizes. Laser-Induced Incandescence fulfils these criteria: its current sensitivity in the order of a few parts per trillion and the technique is highly repeatable, partly because the measurement is performed on the “solid” part of the particle and volatile and metallic compounds are vaporized by the laser beam. In parallel, the time resolution is dependent of the laser repetition rate and can be chosen by the end user between 10 and 100 measurements per second with measurements taken within a microsecond, making LII highly suited for transient measurements. The last point is the particle size measurement: LII is not sensitive to the overall particulate matter size but to its primary constituents size, which are called primary soot particles. These particles are broadly spherical in shape and are present in the atmosphere as aggregated chains that eventually agglomerate into large entities. LII provides a direct measure of the soot primary particle size and research is currently focussing on associating laser-induced incandescence with elastic light scattering measurements in order to provide both overall and primary particle sizes. This would eventually lead to the capability of measuring particulate matter particles concentrations and active surface area and therefore toxicity potential in terms of lung penetration and active carrying surface area.

At the beginning of this project, the Laser-Induced Incandescence (LII) technique had recently transitioned from requiring an external calibration with a source of particles having a known concentration and size to a novel calibration technique based on an absolute light intensity calibration. Indeed, prior to LII migrating to being an independent measurement technique, measurements were taken utilizing in general

the whole incandescence emission spectrum in the visible and deriving soot particle sizes and concentrations from an hypothetical peak temperature and reference measurements performed on particulate matter sources more or less well characterized. The invention of the independent calibration technique by Smallwood, Snelling et al. in 2001 led to the following measurement capability during LII: time-resolved LII measurements would yield particle temperatures and light intensity measurements and provide a direct link between theoretical modelling and practical situations. The overall enhancement was based on using 2-color pyrometry to measure particle temperature and calibrating the pyrometric system in terms of absolute light intensity provided direct measurements of particle concentrations. However, the pyrometric technique imposed limitations in terms of measurement volumes configurations and sizes and the technique evolved into extractive sampling from exhaust streams and performing measurements within well-controlled sampling cells. In parallel, the spectral emission measured represented only a fraction of the visible incandescence spectrum emitted during LII as two bandpass filters were used simultaneously to resolve instantaneous particle matter temperatures. Because of these new constrains imposed by this measurement method, LII measurements became limited to resolving only a few parts per billion in terms of particulate matter concentration.

Therefore an increase in sensitivity was clearly the focus and early in the project two directions became evident: either a technical solution was achieved, with the use of faster optics, larger probe volumes and increased collection and transmission efficiencies; or a physical solution could be reached, with a larger number of photons emitted per unit primary soot particle. With these two choices in mind, Professor Greenhalgh and I started a fruitful collaboration with the Combustion Research Group at the National Research Council (NRC, Ottawa, Canada). Our common objective was to achieve each between 100 and 1000 times greater sensitivities for LII and resolve parts per trillion particle matter concentrations. The approach I favoured at Cranfield was to obtain physically more signal per unit primary soot particle, whereas Greg Smallwood and Dave Snelling focussed on revising optical designs and increasing collection and transmission efficiencies, bearing in mind that our combined efforts would eventually lead LII into sub-parts per trillion sensitivities…

From the start of this project, two methods for increasing the emission of photons per primary soot nanoparticles were identified: either higher nanoparticles temperatures or longer signal durations could have been used. Clearly, higher temperatures were attractive, has they would have been associated with larger instantaneous incandescence signals. However, bringing carbon nanoparticle temperatures above 4000 K during LII also implies large sublimative losses and therefore overall decreases in signal. However, this could have been compensated by performing measurements in conditions were sublimation would lead to large concentrations of thermally excited C_2 vapours being released from the particle carbonaceous structure and produce large emission signal levels. Unfortunately, This route was not chosen as it would not constitute laser-induced incandescence, require extremely high laser fluences and prevent any particle morphology measurement to be performed because of the large volumic losses required to achieve large sublimative rates.

Instead, a more subtle approach was to lengthen LII signals. Typically, LII is associated with sharp light pulses lasting less than a microsecond. Short signal durations are due to the rapid heat conduction from the laser-irradiated soot particle to its surrounding gas. Therefore a decrease conductive heat loss rates was necessary in order to lengthen LII signals. Hence the principle of LII under vacuum was defined: by performing LII under vacuum, light signals could be modelled to last up to 100 microseconds and the associated gain in number of photons emitted per primary soot particle was predicted to be in the order range of 50 to 300 (depending on primary soot particle size). In parallel, because heat conduction away from the unit soot particle is reduced to negligible, the sublimative and the radiative properties of soot nanoparticles could be measured by the technique.

Therefore this thesis is based on an analysis of Laser-Induced Incandescence under vacuum conditions and a thorough study of the signals obtained for a large laser excitation range using the dual-wavelength pyrometric technique applied to time-resolved LII combined with imaging and spectral analysis.

Contents

List of figures

Figure 104: Measurements obtained and fit with theoretical temperature decays. The pyrometric ratios obtained at fluences of 0.18, 0.24 and 0.28 J/cm^2 were processed using two different methods: particulate temperatures were first calculated assuming that particles emit in the Rayleigh regime and subsequent fit to data for E(m)=0.4 and 0.6 were performed. The second (Mie) approach was also put into practice and is labelled "bulk", but both corresponding temperature decays and fit for an emissivity value were not consistent.

Figure 105: First 2μs LII signals. (a) ICCD measurement of the incandescent particulates for a gate duration of 2μs and a delay of 500 ns after laser irradiation. The scale is in ICCD counts whereas laser beam propagation is from the left to the right; (b) Initial signals presented characteristic 170 ns long emission peak for low carbon concentrations (circa 1 ppt). LII signal level is more reliably measured by the red channel (PMT_2) whereas the blue channel (PMT_1) presents the emission peak.

Figure 106: C_2 Swan bands spectral investigation. (a) 500 nm filter used in front of PMT_1 transmissivity versus wavelength and location of the main Swan bands. (b) Spectrum measured in conditions similar to the present experiment for a laser fluence of 0.3 J/cm^2 with a 100ns gate duration and just after laser irradiation.

Figure 107: Typical broadband LII under vacuum signals. Single LII signals 1 and 2 are filtered with a time constant of 50ns for clarity and the average LII signal was obtained by averaging 500 LII pulses.

Figure 108: Example of the anomalous behavior of the incandescence signal for a fluence of 0.28 J/cm^2 for a single shot LII signal after noise filtering, left. The average measured temperatures are given on the left.

Figure 109: Average ratios and standard deviations of initial and peak soot volume fraction measured for the three laser fluences we measured.

Figure 110: Time-integrated (from the start of the laser pulse for a gate duration of 50μs) ICCD measurement taken at 0.24 J/cm^2 laser fluence and revealing miniature "starbursts".

Figure 111: Average Feret diameter (see text) as a function of time for an agglomerate explosion. Each point represents an average of approximately 300 measurements.

Figure 112: Images of incandescence from particles irradiated with a fluence of 0.18J/cm^2 (left) and a fluence of 0.24J/cm^2 (right) with the intensifier gate timing open and shut at: (a) 0-5 μsec after laser pulse, (b) 5-10 μsec after laser pulse, (c) 20-25 μsec after laser pulse, (d) 25-30 μsec after laser pulse. All color scales in ICCD counts.

Figure 113: An example of a single frame, double exposure PIV image. Laser propagates left to right and the first exposure is at 2 μsec and second at 14 μsec both with a gate width of 1μs. The very bright spot is the initial particle from the first exposure and the scattered ejecta are from the second.

Figure 160: Temperature (a) and soot volume fraction (b) signal analysis comparison between Cranfield and NRC.

Figure 161: Cold carbon aerosol generator working schematic – inside view.

Figure 162 : Cabot Carbon Cab-O-Jet 200 ® ionic configuration schematic – the pigment represented here is indeed a carbon aggregate.(Cabot Carbon, 2006)

Figure 163: Illustration of soot generator aerosol particle (agglomerate) formation from heated ink droplet. Each dot represents a carbon aggregate (Wainner, 1999).

Figure 164: Virtual impactor stage evacuation testing. The blue line is a moving average and the green circles are measurements. The nebuliser was actuated by an inlet pressure of 69 KPa. After 55s the vacuum pump valve was closed and the impactor compressed air inlets blocked.

Figure 165: Artium LII200® Soot Volume Fraction (SVF) measurement (a) and primary particle determination (b) for a blocked virtual impactor and atomiser inlet pressure at 69 KPa. The blue line is a moving average whereas green circles represent pointwise measurements. SVF and primary particle measurements are performed on the same dataset (i.e. are simultaneous).

Figure 166 Top view of the virtual impactor in the radial blowing configuration. Since all the flows inside the apparatus are monitored in terms of upstream pressure for each pressure inlet, applying the same positive pressure on both pressure inlets of the virtual impactor has an immediate effect of creating a zone of counterflow at the nozzle location, thus increasing the air flow out to the drier . Since the pressure on the atomiser side has always been maintained above 68 KPa, the air flow direction was maintained from the bottom – atomizer - to the top – drier output.

Figure 166: Soot volume fraction (a) and primary particle size (b) recorded by the LII 200® instrument during test 21. The blue line is a moving average whereas green circles represent pointwise measurements. SVF and primary particle measurements are performed on the same dataset (i.e. are simultaneous).

Figure 167 : Typical cold carbon generator agglomerate imaging using the SEM method. The white surfaces are carbon nanoparticles agglomerates produced by the device. Clearly SEM micrographs are suited uniquely to measure agglomerate overall parameters, but do not provide any form of insight on the agglomerate primary particle composition.

Figure 168: example of high resolution TEM imaging results obtained at NRC. (a) & (b) are 6300:1 magnified images, while (c) has a magnification factor of 24 000:1 and (d) is 33 000:1 magnified. Note that the carbon film substrate in the background presents a smooth uniform negligibly absorbing surface and is hardly discernable.

Nomenclature

A_{AP}	aperture area
A_{strip}	Area of the strip filament lamp used for calibration
a	primary soot particle radius
$B_\lambda(T)$	intensity radiated by a blackbody as a function of wavelength and temperature
C_{abs}	primary soot particle cross-sectio
C_{Em}	constant used for radiative transfer modelling (eq. 66 and 67)
C_{G1}	calibration factor 1
C_{G2}	calibration factor 2
C_p	molar heat capacity of the surrounding gas
C_s	primary soot particle heat capacity
C_1	first radiation constant
C_2	second radiation constant
c	velocity of light
c_s	soot specific heat capacity
D	primary soot particle diameter
D_f	mass fractal dimension
d_p	primary particle diameter
d_{mp}	geometric mean particle diameter
E(m)	refractive index function
F	laser fluence
f	Eucken correction factor
f_v	soot volume fraction
G	geometry-dependent heat transfer factor
G_1	Gain 1
G_2	Gain 2
h	Planck's constant
I_c	calibration lamp current
$I(\lambda_1,T)$	light intensity measured on channel 1 of the pyrometer
$I(\lambda_2,T)$	light intensity measured on channel 2 of the pyrometer
I_m	measured photocurrent
K_a	thermal conductivity of the surrounding gas
K_n	Knudsen number
k	imaginary part of the soot refractive index
k	Boltzmann's constant
k_f	fractal prefactor

M	mass of the primary soot particle
M_v	molecular vapour mass of carbon
m	complex soot refractive index
N	number of soot primary particles per aggregate / within the measurement volume
N_a	Avogadro's number
N_v	molecular flux of sublimated carbon clusters
N_c	molecular flux of evaporated carbon clusters in the continuum regime
N_k	molecular flux of evaporated carbon clusters in the Knudsen regime
n	real part of the soot refractive index
n_v	molecule number density of soot vapour
P_0	surrounding gas pressure
P_{CAL}	filament radiant power
P_v	vaporization pressure of carbon/ soot vapour pressure
R_1	Resistor 1
R_2	Resistor 2
$R_s(\lambda)$	spectral radiance of the calibration lamp
R_Z	photodetector internal impedance
T_B	calibration lamp filament brightness temperature
T_s	true calibration lamp filament temperature
Q_{int}	rate of change of internal energy of the primary soot particle
Q_{abs}	rate of laser energy absorption by the primary soot particle
Q_{rad}	rate of energy losses through radiation by the primary soot particle
Q_{cond}	rate of energy losses through heat conduction to the surrounding gas by the primary soot particle
Q_{sub}	rate of energy losses through sublimation by the primary soot particle
q_{exp}	experimentally measured laser temporal profile
q_{max}	peak laser intensity
R	molar gas constant
R_g	radius of gyration of an aggregate
S_{agg}	light intensity emitted per aggregate
S_{gate}	light intensity measured during an intensifier gating
T	primary soot particle temperature
T_b	calibration lamp brightness temperature
T_0	surrounding gas temperature
t	time
V	measurement volume
V_{CAL}	photodetector output signal during calibration

V_{DAQ} voltage supplied by the data acquisition system
V_G gain control voltage
V_m measured voltage
W_a molecular weight of the surrounding gas
w_{temp} half width at half maximum of the laser temporal profile
Z_{surf} collision rate of ambient air molecules with the primary soot particle surface

Greek letters

α_T thermal accommodation of the surrounding gas
β fractal scaling factor
ΔH_v carbon heat of vaporization
ξ fractal dispersion exponent
Σ_λ detector spectral response
ε_λ wavelength dependent emissivity of soot
$\varepsilon(\lambda,T_S)$ emissivity of tungsten as a function of wavelength and temperature
γ heat capacity ratio of the surrounding gas
λ wavelength of light
λ_{laser} laser excitation wavelength
λ_{mfp} mean free path
μ uncertainty
η calibration factor
σ_p geometric standard deviation
ρ_s density of soot
Φ total energy flux radiated by a blackbody
σ_a mean molecular cross section of air
Γ intermolecular diffusion coefficient of C_3
τ conduction temperature decay time constant
$\tau(\lambda)$ filter spectral transmittance
Ω solid angle of detection

Chapter I: Soot

Although Laser-Induced Incandescence (LII) can potentially be applied to any nanoparticles capable of sustaining temperatures above 1000K, historically soot has been the main target particle for LII. As well the focus was set on soot nanoparticles as their large presence in the atmosphere, originating either from natural fires or human activities, is one of the major causes of global warming beside the rising carbon dioxide concentration. Also, the regulative interest for soot nanoparticles naturally lead to the focus remaining on soot, with ageing measurement techniques becoming obsolete and LII instruments having the potential for becoming the next generation of standard measurement technique for soot.
Therefore, as Laser-Induced Incandescence of soot nanoparticles has been extensively studied and thorough models (Michelsen, 2003; Snelling et al 2000-1 and 2004; Smallwood et al.; Smallwood et al. 2001-1) are available together with thermophysical properties of graphitic carbon up to high temperatures (Leider et al, 1973), soot will remain the nanoparticle of interest for this study.
This chapter presents soot in its different aspects of relevance to the present thesis, which is laser-induced incandescence of soot under high vacuum conditions. The general conditions of LII are first set, and then the pollution, health and regulation issues associated with soot are explained. The remainder of the chapter will then depict the chemical reactions leading soot formation during combustion, its typical composition and its physical properties involved during LII in details.

I.1. Laser-Induced Incandescence (LII) of soot.

Laser-Induced Incandescence (LII) of soot occurs when a high-energy pulsed laser beam encounters graphitic particulate matter particles like soot or carbon black (AIAA,2003). The particle absorbs energy from the laser beam and sees an increase in its internal energy, resulting in an increase of temperature. In parallel, the particulate looses energy through heat transfer mechanisms. If the energy absorption rate is sufficiently high, the temperature will rise to levels where significant incandescence (blackbody emission) can be measured as illustrated by figure 1 (AIAA, 2003). Typically, Laser-Induced Incandescence produces 50ns to 1µs long light pulses at atmospheric pressure. The phenomenon has been first outlined by Eckbreth (1977) as a source of interference during Raman Scattering experiments. Later on, Melton (1984) proposed a first model and measurements of Laser-Induced Incandescence, which have then been developed by other researchers**.**

The Laser-Induced Incandescence has then been developed as a soot volume fraction measurement technique by Vander Wal et al. (1995, 1996-1&2, 1998, 1999-1) and Snelling et al. (1997,2000), yielding good correlation with the standard technique used in this domain, the gravimetric procedure. The gravimetric technique consists of collecting particulate matter on a filter kept at 52ºC and then determining the change of weight for the sample as a relation to the flux of gas crossing the filter (Vander Wal, 1996-2).

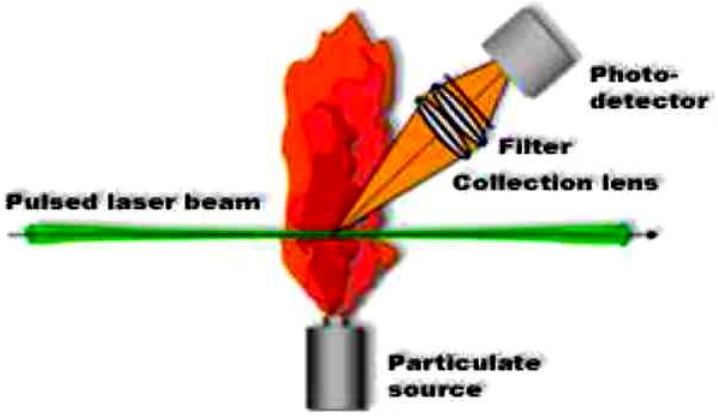

Figure 1: description of LII- an aerosol containing particulate matter is irradiated with a high power pulsed laser beam, resulting in measurable soot incandescence light signal(Particulate Matter Collaboratory , 2006-1).

A later improvement proposed in the determination of the particulate matter size as an analysis for conduction of heat from the heated particulate to its surrounding gas was proposed by McCoy and Cha (1974) and implemented successfully by Will et al (1998), Schraml et al (2000), Snelling et al. (1997) and Mewes & Seitzmann (1997).

A further step would the determination of the primary particles size distribution, proposed by Roth & Filippov et al. (1996, 1999) but is still limited by the difficulty of dealing with soot primary particle aggregation and complex conduction heat transfer modelling (Liu et al, 2006).

The dynamic range of measurement (from a few ppt to highly loaded aerosol) and the fact that measurement are quasi instantaneous (<1μs) make of LII an ideal technique for particulate matter measurements in most practical combustion systems, engine and gas turbine exhausts. The typical concentration measurement ranges are illustrated in figure 2. Even the possibility of inferring the soot volume fraction in urban areas has been outlined by Vander Wal & Ticich (1999-2).

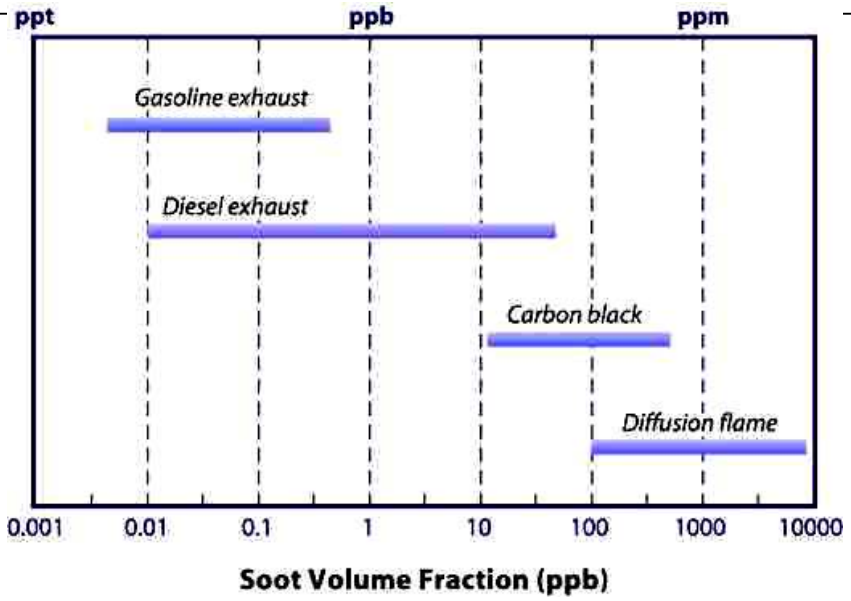

Figure 2: Representation of the soot volume fractions range in practical systems (Particulate Matter Collaboratory, 2003).

The application of laser-induced incandescence to measure soot particles in most of the conditions that can be found, other than solely for scientific interest, is mainly driven by a need arising from the health concerns raised by soot pollution that tighter and tighter regulations are progressively addressing.

I.2. Pollution, Health, and regulation concerns

Soot can be the result of natural fires. However, theses natural causes are far beyond human production. As a result, urban areas are more and more concerned by pollution from vehicles and health concerns, such as premature death of individuals and increase in occurrences of lung cancers due in part to soot production. On a larger scale, the increased soot presence in the atmosphere can be considered as the main source of climatic change after carbon dioxide and losses of the ozone layer (Seinfeld and Pandis, 1998). Quantities of airborne particles in industrialized regions of the Northern Hemisphere have increased markedly since the Industrial Revolution. The classical figure is the realization in the 1950's that motor vehicle emissions could lead to urban smog.

The main effect of soot is not due to its graphitic carbon portion, which has been shown to cause no biological effect, as demonstrated by Murphy et al.(1998), but its loading in hydrocarbons and sulphur, and eventually metallic ash, act as vector of carcinogenic substances into human lungs and causes for asthmas and respiratory track irritations. The principle feature of this effect is that the smaller the soot particulates , the deeper they penetrate into the lung epithelium and can have adverse consequences upon human health.

The first on-highway diesel emissions legislation in Europe in the early 1970's addressed visible exhaust in an arbitrary manner, through smoke opacity monitoring. The test was clearly lacking accuracy. It was not until the 1990's that legislators in

Europe and North America added a quantitative limit for particulate matter to those established a few years earlier for pollutant gaseous emissions and related them to the power of the engine for vehicular emissions. Permitted particulate levels have since been progressively reduced on both sides of the Atlantic and further tightening of emission laws in this decade will impose yet lower particulate emissions limits (Riccardo Quaterly review, 2002).

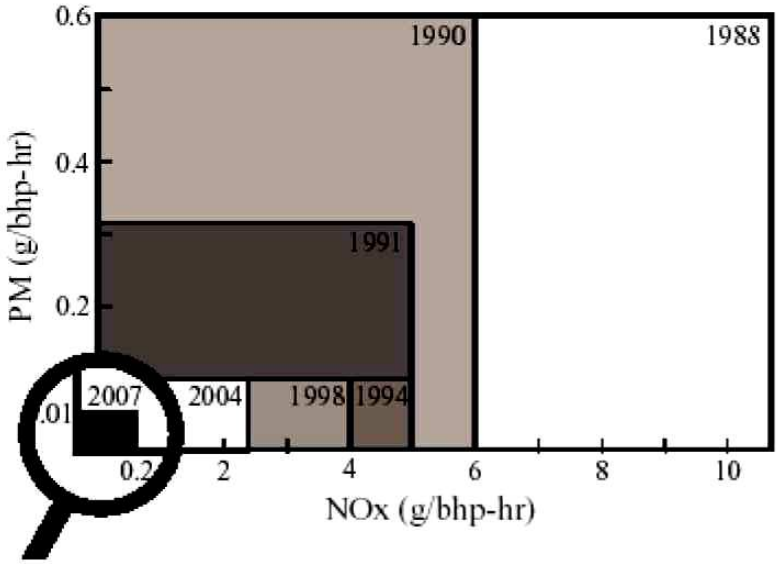

Figure 3: Evolution of US heavy-duty engine emission regulation (Witze, 2001).

However, this improvement in regulation is limited by the measurement standard used so far to comply with regulations, which is the standard gravimetric procedure and does not fill the ability of measuring the particulate matter size and cannot deal with the future low concentrations and transient measurements. The limits of the gravimetric method are mainly due to the very nature of the measurement method as measurement are taken over a long sampling time (between minutes and hours). As well, size measurements cannot be performed on the collected samples as particles agglomerate on the sampling filter therefore rendering any sizing and structural determination impossible. It can be believed that better instrumentation and the possibility of inferring the carcerinogenic capabilities of soot's (with the carcerinogic potential of soot nanoparticles being a function of active surface area and size) will lead to more precise regulations, resulting in health improvements in urban areas. Clearly, LII, in particular when combined with elastic light scattering to correct for soot structural effects arising with aggregation and agglomeration, has the potential to fulfil future regulative requirements for soot active surface area as well as real-time concentration measurements. Whereas the issues arising with the presence of soot particles in the atmosphere and the need for regulating human emissions have been described above, the origins of soot have yet to be explained.

I.3. Soot formation

A significant portion of atmospheric particulate matter arises from combustion of fuels in various engines and fires (Snelling et al., 1999). In urban areas, mobile sources are major contributors to ambient particulate matter (PM) concentrations. The main constituent of the particulates generated by combustion is carbon. These carbonaceous particles are called soot. Soot particles are structural entities of small roughly spherical elementary carbonaceous particles. While the size and morphology of the aggregates vary widely, the small spherical elementary particles are remarkably consistent from one another. These elementary particles vary in size and cluster with each other, forming straight or branched aggregates. These chains agglomerate and form visible soot particles that have sizes up to a few micrometers (Seinfeld & Pandis, 1998).

The following analysis has been proposed by Seinfeld & Pandis:
The formation of soot depends critically on the carbon/oxygen ratio in the hydrocarbon - air mixture. Assuming that the mixture has insufficient oxygen to form CO_2 and that CO is the combustion product of the fuel C_mH_n. Then the combustion stoichiometry is:

$$C_m H_n + a \cdot O_2 \rightarrow 2\,a \cdot CO + 0.5\,n \cdot H_2 + (m - 2\,a) \cdot C_s \quad \textbf{(1)}$$

Where C_s is the soot formed and the ratio of carbon to oxygen, C/O is also equal to *m/2a*:

- if C/O = 1, there is sufficient oxygen to tie up all the available carbon as CO and no soot is formed.
- if there is even more oxygen, i.e. C/O < 1 , the extra oxygen will be used to produce CO and CO_2
- if there is less oxygen, i.e. C/O > 1, soot will start forming

As a summary, a fuel-gas mixture being too rich (C/O >1) during combustion will produce extra available carbon atoms and therefore will increase the possibility of amorphous graphite (i.e. a form of bulk solid carbon) being produced as the end result of a combustion process.
In more details, soot forms in a flame as the result of chain reactions, starting with the oxidation and pyrolysis of the fuel into small molecules. Acetylene, C_2H_2, and Polycyclic Aromatic Hydrocarbons (PAH's) are considered the main molecular intermediates for soot formation and growth. The growth of soot particles involves first the formation of soot nuclei and then their rapid growth through surface reactions. The soot nuclei themselves represent only a small fraction of the overall soot mass produced. However, the final soot mass depends critically on the number of nuclei formed and does not show strong dependency upon the fuel composition. The formation of the nuclei involves a series of gas-phase polymerization reactions producing large polycyclic aromatic hydrocarbons and eventually soot particles (see figure 4).
Since acetylene is the most abundant hydrocarbon in rich flames, especially in the soot nucleation zone, it is believed that this specie is the one responsible for mass addition to the soot particle and models are proposing that the acetylene molecules fuse to form an aromatic ring and then continue to react with the aromatic compound leading to PAH formation. Reactive collisions between the large PAH molecules

accelerate their growth. The soot nuclei grow through these chemical reactions, reaching diameters larger than 10 nm, at which point they begin coagulating to form chain aggregates (see figure 5) by picking up molecules from the gas phase. The final size of the soot particles results from coagulation of primary particles into larger aggregates. As a summary, soot particles are mixture of amalgamated and coagulated particles. As well, their turbostratic structure (amorphously superposed graphitic layers) and their relatively large surface area suggest that these particles are inherently capable of adsorbing and condensing unburnt hydrocarbons and sulphurs from the combustion process as well as incorporating solid residues from the combustion environment.

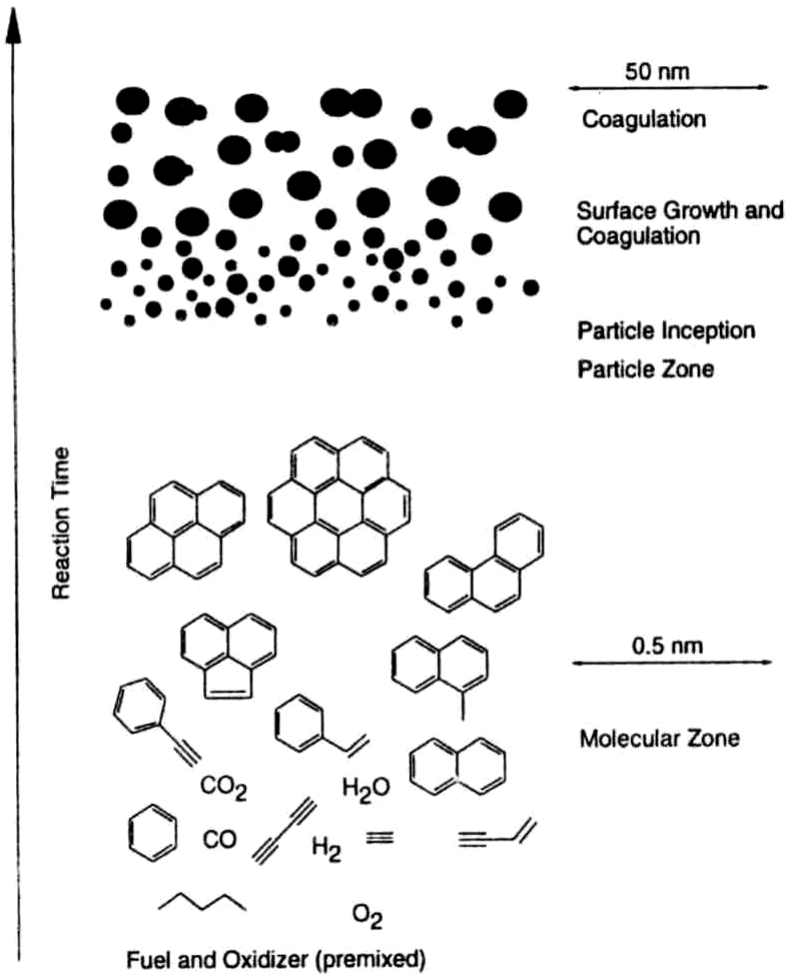

Figure 4: Schematic representation of soot nucleation in combustion (Seinfeld & Pandis, 1998).

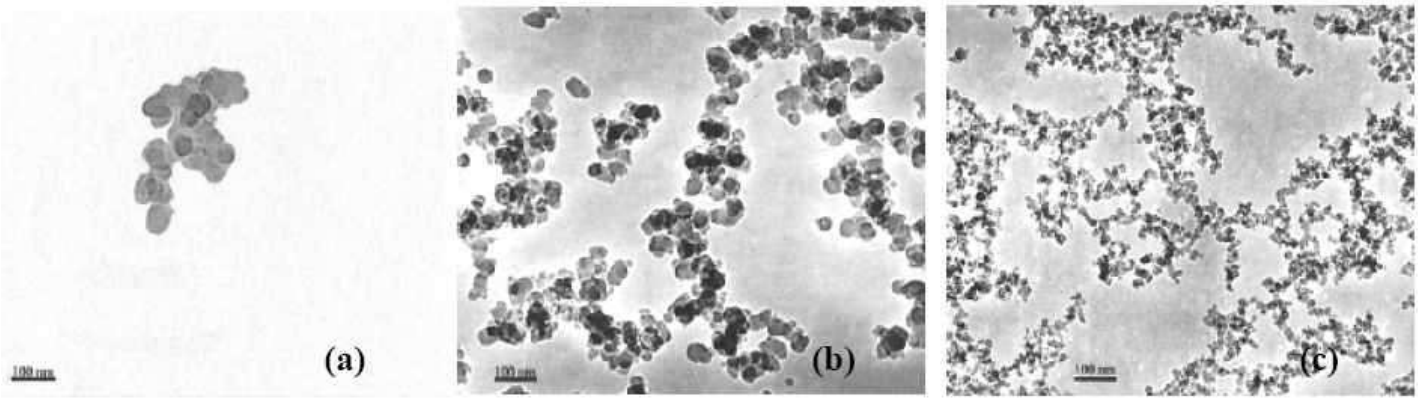

Figure 5: Evolution of soot in an acetylene flame (Xu, 2003)
(a) Soot nucleation
(b) Soot maximum concentration condition
(End of coagulation phase)
(c) End of soot surface oxidation

I.4. Soot composition

Soot formed in combustion processes is not a unique substance. It consists mainly of carbon atoms in the form of amorphous graphitic layers, but also contains hydrogen and other elements. Furthermore, soot particles absorb organic vapours when the combustion products cool down, frequently accumulating significant quantities of organic compounds (Seinfelf & Pandis, 1998).
For example in figure 6 the particle emissions from diesel engines are in the form of complex aerosols consisting primarily of soot and volatile organics:

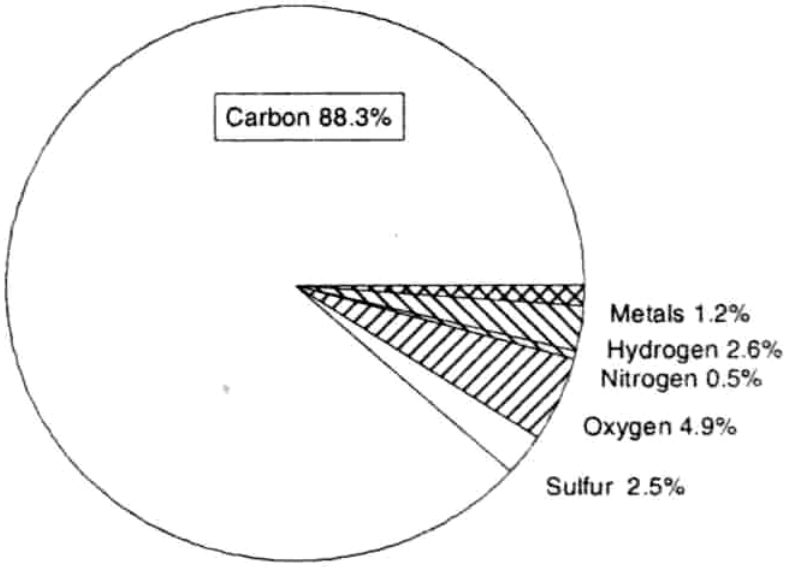

Figure 6: Typical elemental composition of the typical diesel particulate mater by mass (Snelling et al., 1999).

Even though soot particles are know to act as adsorbents and condensers for combustion residual products, laser-induced incandescence measurements are not affected by the post-combustion composition changes. Effectively no other material than Carbon remains in a solid state when reaching LII peak temperatures far superior to 2000K and therefore no measurable effect is expected from materials other

than carbon during LII except for minor structural voids and modified particle surface due to the evaporation of secondary constituents. Overall, laser-induced incandescence of soot presents a far greater sensitivity to soot structural properties than composition. Therefore an insight into the structural properties and physical characteristics of soot is presented in the following section.

I.5. Soot physical and optical properties involved during LII.

In order to provide an overview of the main properties of soot that will be later involved in modelling and performing LII, the following sections will focus on structural properties of soot, with their resultant optical properties and additional physical properties involved. Particulate matter presents three structural levels: (i) agglomerates, which are clusters of loosely bound soot aggregates bound together by weak Van der Waals forces(ii)aggregates, which are chain-like structures containing a number of primary particles fused together; (iii) primary particulates, which are the basic structural unit. As agglomeration effects have so far been neglected during LII theoretical investigations, the following section is centred on soot primary particle size distributions and aggregation.

I.5.1. Primary particle size distribution

Soot primary particles are the primary structural entities of soot. Although they aggregate after inception, soot primary particles possess lognormal primary particle size distributions as demonstrated by Koylu and Faeth measurements (see figure 7) in pool fires (Koylu, 1992). The probability density function for a primary soot particle of diameter d_p,, PDF (d_p), is given by the relationship:

$$PDF\left(d_p\right) = exp\left[\frac{-\left(\frac{ln\left(\frac{d_p}{d_{mp}}\right)}{ln\left(\sigma_p\right)}\right)^2}{\sqrt{2\pi}\cdot d_p \cdot ln\left(\sigma_p\right)}\right] \qquad \textbf{(2)}$$

Where d_{mp} is the geometric mean particulate diameter:

$$ln\left(d_{mp}\right) = \frac{\sum_{i=1}^{n_t}\left(n_i \cdot ln\left(d_{p_i}\right)\right)}{n_t} \qquad \textbf{(3)}$$

And n_i is the number of particles having a value of d_{pi} while n_t is the total number of samples. σ_p is the geometric standard deviation, as defined by equation 4.

$$ln(\sigma_p) = \sqrt{\sum_{i=1}^{n_t} \frac{ln\left(\frac{d_{p_i}}{d_{mp}}\right)^2}{n_t - 1}} \qquad \textbf{(4)}$$

Given the statistical distribution of the primary particle size, one can now consider the aggregate structures which are obtained during coagulation of ensembles of primary particles.

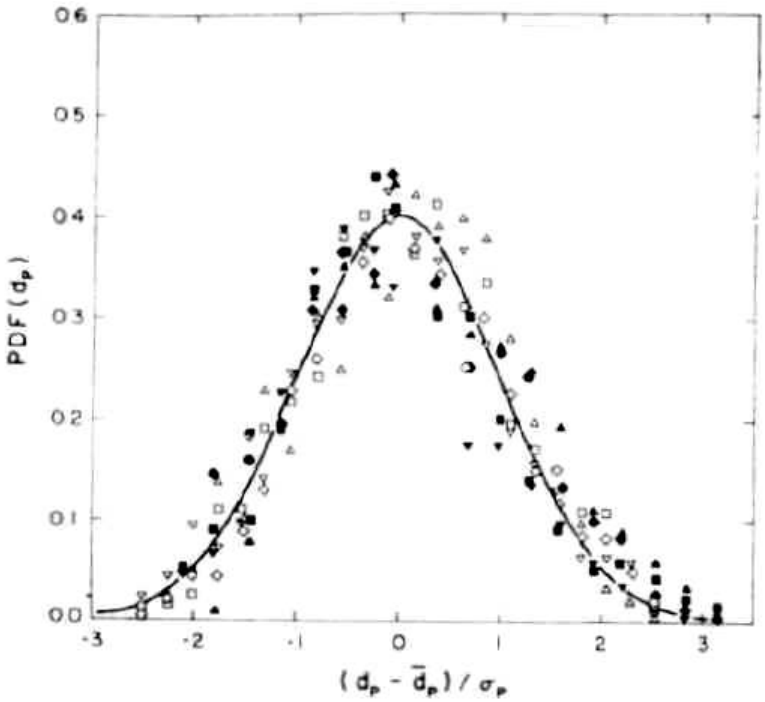

Figure 7: probability density functions of primary particle diameters for acetylene and ethylene soot (Koylu, 1992).

I.5.2. Aggregation

Soot consist of primary spherical particles, with a diameter comprised between 5 and 100 nm. For a population of soot nanoparticles, the overall diameter distribution is considered as log-normal. As described in section I.3 and figures 4 and 5, soot particles coagulate into aggregate during combustion, resulting in fused open structured aggregates with broad distributions in terms of number of particles per aggregate (Koylu et al, 1995). Typically, large chained aggregates originate from cluster – cluster coagulation of single particles and pairs joining a common aggregate. Hence the aggregates obtained after the oxidation stage can therefore be considered as formed of just-touching primary soot particulates, and this is illustrated in figure 8. Complex aggregates structures with various shapes and sizes can be conveniently characterized using the mass fractal concept, which implies the following statistical relationship for N, the number of primary particles in an aggregate:

$$N = k_f \left(\frac{2R_g}{d_p} \right)^{D_f} \qquad \textbf{(5)}$$

Where D_f *[ ]* is the mass fractal dimension, k_f [ ] the fractal prefactor, R_g *[cm]* the radius of gyration of an aggregate, d_p *[cm]*, the primary particle diameter. This fractal approach was successfully validated by Koylu et al.(1992, 1995,1996, 1997 1&2) in their studies on soot aggregation in flames.

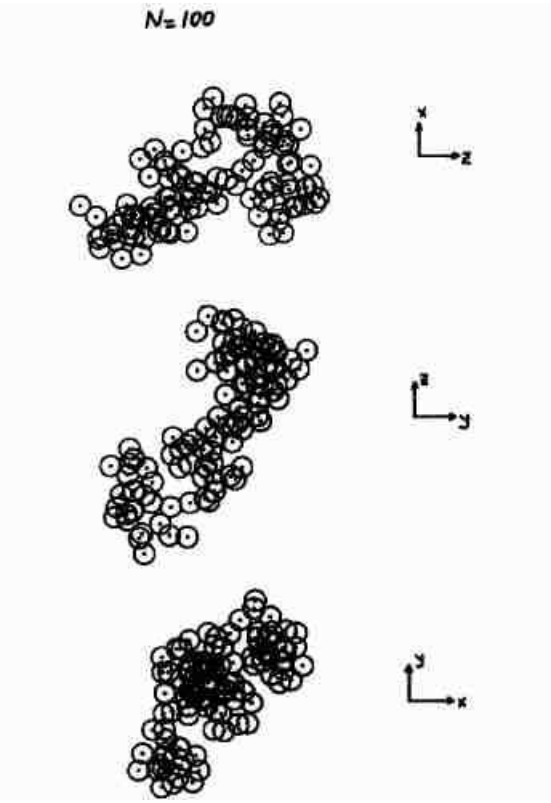

Figure 8: Schematic views of a modelled soot aggregate containing 100 monodisperse particles of 50 nm diameter each (Koylu et al, 1995). Three views of each Cartesian plan (from top to bottom :yz,zy and yx) are shown here to obtain an overall view of the complex aggregation geometry.

At the beginning of this chapter, soot is described as presenting three structural levels: spherical primary particles (the basic structural units) fuse themselves into larger chains of aggregates which in turn agglomerate loosely between each others (Van der Waals forces) . However, providing a general description for agglomerates would be difficult (if not impossible) as the size, shape and structure of agglomerates changes with time, particle concentration and eventually measurement conditions. Therefore the reader has to be reminded that agglomeration occurs outside of the combustion process and is a function of time residence, environmental conditions and aerosol electrostatic state.

Once the initial structural entity of soot is defined both in terms of the primary particle size distribution and structural arrangement, one has to consider the physical changes occurring during laser irradiation. Indeed laser-induced incandescence is considered as a non-intrusive measurement method as the number of particles irradiated by the laser beam is negligible when compared to the total number of particles within an exhaust flow or a flame, for example. As well, the particle number is not affected when LII measurements. However, as often LII induces carbon sublimation and removal of volatile organic matter and eventually metallic ashes due to the very high peak temperature achieved (above 2500K), particle size and inner primary particle structural changes are to be expected during laser irradiation.

I.5.3. Primary particle structural changes during laser irradiation

Soot primary particles are approximated as spherical entities. They present a turbostratic structure: parallel layers of graphite are present inside the sphere formed by the particle on the orders of a few nanometres but these crystallites show disorder over larger scales (Palotas et al,1996), see figure 9 below . The interspaces between graphite crystallites are filled with amorphous carbon and volatile components (Polycyclic Aromatic Hydrocarbons, metal from the normal wear of an engine, oil…). And the degree of order of such structures is strongly dependent on the thermal treatment the material is been subjected to.

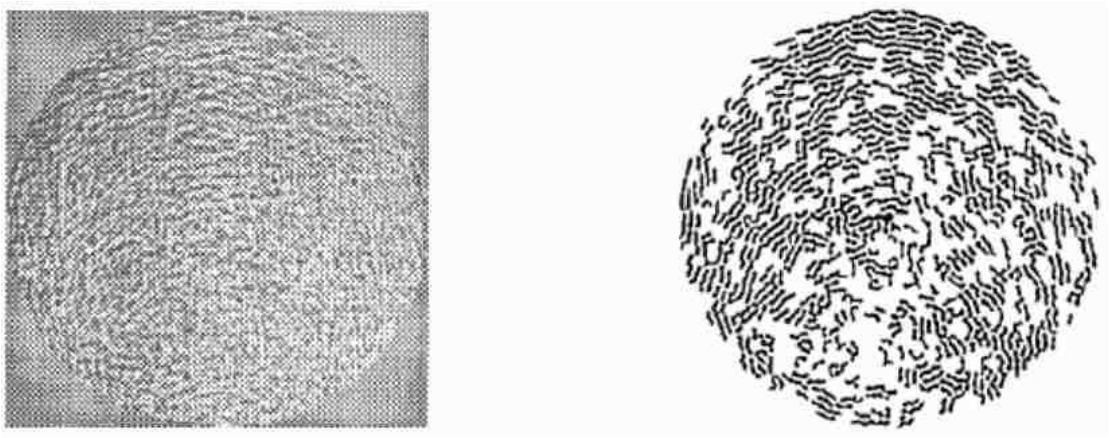

(a) **(b)**

Figure 9: Primary Soot Particle Overall Structure (Palotas et al, 1996)
(a) High Resolution Transmission Electron Microscope Image of a primary soot particle including both amorphous and graphitic carbon
(b) Extracted structure through Inverse Fourier Transform filtering (Extraction of crystallites -picture excluding amorphous carbon).

The graphitic crystallites inside the soot primary particle have been shown to typically present three layers of carbon planes (figure 10), which dimensions have been measured by Vander Wal and Choi (1999), through measurement of the Bragg diffraction pattern of soot produced by an ethylene - air flame:

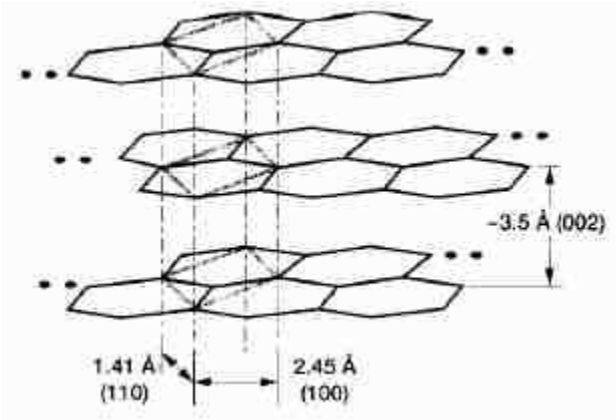

Figure 10: Graphitic crystallite structure and spacing. Each line cross correspond to an atom of carbon (Vander Wal and Choi ,1999).

A graphitization process of soot has been reported to occur upon laser irradiation, and this for temperatures ranging between 1000 to 3000K: the crystallites of graphite inside the soot primary particle increase in size and their ordering dimension increases. As figure 11 illustrates it, for temperatures above 2500 K hollow graphitic shells are created (Vander Wal and Choi ,1999; Vander Wal et al, 1998). The soot primary particles structural had been observed to change from a near- spherical agglomerate of small graphite crystallites and amorphous carbon to a hollow graphitic shell formed by curved layers of graphite above 2500 K.
This can be explained by the fact that during laser irradiation, energetic barriers can be overcome. The elevated temperature allows crystallite layer planes growth through reorientation, realignment and through addition of amorphous carbon, consuming the initial amorphous carbon present before irradiation to form spherical layers of graphite. Also, carbon vaporization from the interior of the soot particle is assumed to take place (Vander Wal et al., 1999). Then, because defects are eliminated, an energetically more stable configuration is achieved and kept during cooling of the soot particle (Vander Wal and Choi, 1999). Therefore the particle, after cooling, presents a fullerenic structure: carbon curved layers forming an onion shaped closed structure (Van der Wal and Choi., 1999).

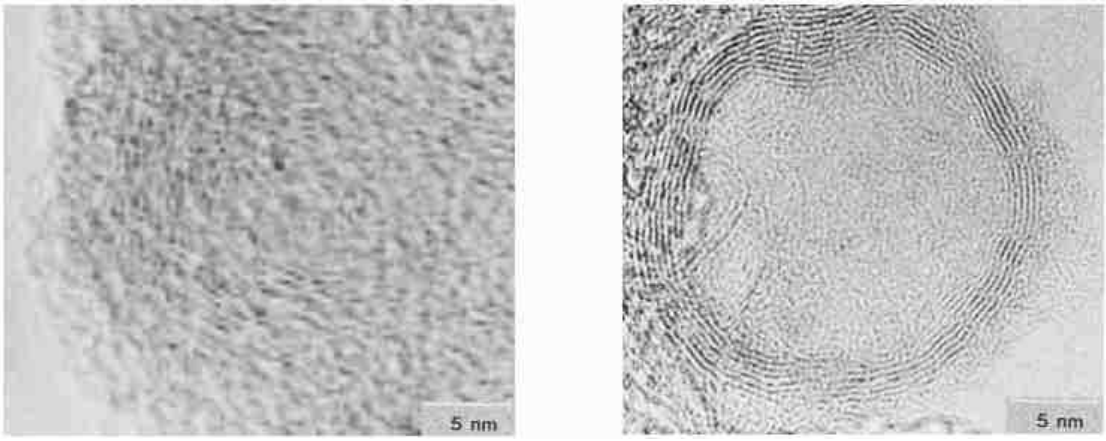

(a) **(b)**

Figure 11: Structural changes of the soot primary particle during LII
(a) High Resolution Transmission Electron Microscope picture of a non laser - heated soot primary particle showing a turbostratic structure comprising small graphite crystallites surrounded by amorphous carbon(Van der Wal and Choi., 1999)
(b) High Resolution Transmission Electron Microscope picture of a laser - heated soot primary particle showing a fullerenic structure: hollow particle formed of curved graphitic structure and surrounded by amorphous carbon, probably carbon vapour deposition while cooling (Van der Wal and Choi., 1999).

The density of primary particles has been predicted to decrease with annealing: the thermal annealing mechanism aligns the atoms of carbon to form an annealed structure of a smaller diameter and comprising a void in the middle(Michelsen, 2003).
The aggregated structure of soot has been shown not to be modified by the laser - heating process invoked in Laser - Induced Incandescence(Van der Wal, 1995), eventhough disaggregation was predicted by Filippov. Et al.(Roth and Filippov,

1995; Filippov et al. , 1999). Annealing is predicted to influence LII temporal profiles significantly at all fluences: as the primary particle anneals, its emissivity decreases and is predicted to be 2 - 9 times smaller than that of soot, as reviewed by Hope Michelsen (2003) and Vander Wal et al. (1995). As a result of laser irradiation, annealing can be predicted to be most significant effect during laser-induced incandescence: because LII measurement are a direct measure of the blackbody radiation and light intensities are proportional to the volume of the emitting particle (provided the Rayleigh approximation holds for emission wavelengths much larger than the emitting primary particle itself), any change in primary particle emissivity will affect the soot volume fraction measured during LII. Indeed Planck's law states that for a blackbody the amount of light emitted is directly proportional to the emissivity of the entity itself.

A qualitative study of the structure of carbonaceous and its effects on optical properties has been proposed by Michel et al.(1999). This study was made for astronomical purposes, but shows the optical variation due to the variation of structure for a carbonaceous particle, reflecting qualitatively the change of structure for soot enduring laser irradiation. The following figures 12 to 16 are from Michel et al. (1999) and depict structural carbon nanoparticles structures possibilities:

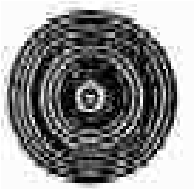

Figure 12: Graphitic onion (annealed particle without central void).

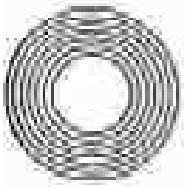

Figure 13: graphitic onion with a central void (annealed particle with central void).

Figure 14: randomly aligned BSUs (Basic Standard Units, graphite crystallites).

Figure 15: Monocrytalline graphite.

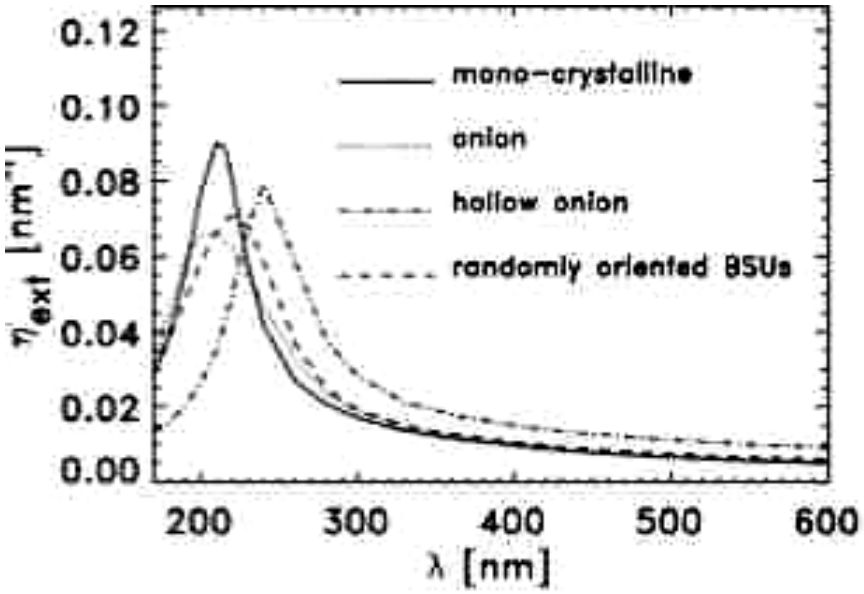

Figure 16: Variation of the extinction cross - section per volume, n_{ext} for graphite particle with various internal structures in the UV/Visible wavelengths.

Figure 16 shows the variation for the extinction cross-sections for the different types of carbon we are expected to face while using the LII technique. According to the Mie scattering theory (Hottel and Sarofim, 1967), the absorptivity and emissivity of soot can be expected to vary the same way during laser heating and cooling afterwards. The randomly oriented BSUs (Basic Standard Units) emissivity curve plotted against wavelength in figure 16 reflects the turbostratic structure optical variations with wavelengths, whereas the hollow onion and onion structure appear to show discrepancies when compared to the turbostratic soot. Therefore these variations for the optical properties of soot need to be accounted for if one wants to produce an accurate model for LII. This section highlighted the primary particle structural properties and their modifications as well as consequences. A now more detailed description of the main physical property of soot primary particles involved during LII - the soot particles capacity to absorb and emit light - follows.

I.54. Optical absorption, emissivity and absorptivity of soot nanoparticles during LII.

The physical property of soot that attracted so far the most interest is its emissivity and therefore its absorptivity, as stated by Kirchhoff's law. This interest relies on the fact that soot is the dominant medium of heat transfer through radiation between the flame and the surrounding medium in most practical combustion systems (boilers, turbines,etc..). As a summary, the radiative heat transfer within a combustion system is a function of both soot concentration and emissivity. However, soot emissivity measurements have proved so far unaccurate (typically >10% uncertainty) and fuel-dependent. As well, for LII, soot absorptivity defines the achievable peak temperature for the laser-irradiated nanoparticles. Another consequence is that, because LII in itself is a measure of the blackbody radiation emitted by the said particles, both particle concentration and temperature measurement are directly

dependent on the emissivity of the particles. Particle temperature measurement is made using multiple wavelengths pyrometry: by measuring the blackbody radiation emitted by the particles and computing the ratio of light emitted between multiple wavelengths, time-dependent temperature measurements are obtained. Therefore multiple wavelengths optical pyrometry and temperature determination has a strong dependency on soot emissivity variations with wavelengths. Concerning particles concentration measurements, the amount of light measured at the photodetector site is directly proportional to the emissivity value of soot for the wavelength at which the measurement is taken. Soot optical absorption varies with the source and fuel of the soot (flame, exhaust…), soot temperature (in the case of morphological changes) and the wavelength considered. The source of the soot determines its structure: the aggregate properties of soot vary only with the fuel and aggregation of soot is responsible for the discrepancies concerning the measurement of the soot complex refractive index m, defined below in equation 6:

$$m = n - i \cdot k \qquad \textbf{(6)}$$

Where n represents the real part of m , k the imaginary one and $i^2 = -1$. For example, the absorption cross - section of light from a non-aggregated soot particle can be 2 times lower than the one for an aggregated particle(Koylu and Faeth, 1992).In **(6)** general, the emissivity of soot calculated using a refractive index measured not accounting for aggregation is 20 % lower than those calculated considering aggregation. In the case of LII, the laser-heating process anneals and changes the optical properties of the primary soot particle over 2500 K, and some structural changes of the graphitic planes are expected for the particle (Vander Wal, 1999) with oxidation (reduction of the interlayer spacing of graphite), altering the soot emissivity during signal collection. Wu, Krishnan and Faeth (1979) reviewed and measured different refractive indexes corresponding to the different soot which have been measured so far at different wavelengths, as illustrated by figure 17. The uncertainties on these values and the calculated emissivities is within 10 to 20% and accounts for most of the uncertainty in LII. A review of refractive indexes for soot found in the literature and evaluation of particles emissivities are proposed in Appendix A. Kirchoff's law states the equality of the absorptivity and emissivity of soot ε_λ(Wu, Krishnan and Faeth, 1979):

$$\text{emissivity of soot} = \text{absorptivity of soot} = \varepsilon_\lambda \qquad \textbf{(7)}$$

In a practical situation, the relevant dimension for absorption is the soot primary particle radius *a*. As typically soot primary nanoparticles are small compared to the excitation laser wavelength as well as the emission wavelength, the optical behaviour of soot obeys the Rayleigh scattering theory ($\pi.D/\lambda << 1$, D being the particle diameter and λ the light wavelength). This allows us to express and derive the absorption cross section of soot, C_{abs} $[cm^2]$, in equations 8 and 9:

$$C_{abs} = \pi \cdot a^2 \cdot \varepsilon_\lambda \qquad \textbf{(8)}$$

$$C_{abs} = \frac{8 \cdot \pi^2 \cdot a^3 \cdot E(m)}{\lambda_{laser}} \qquad \textbf{(9)}$$

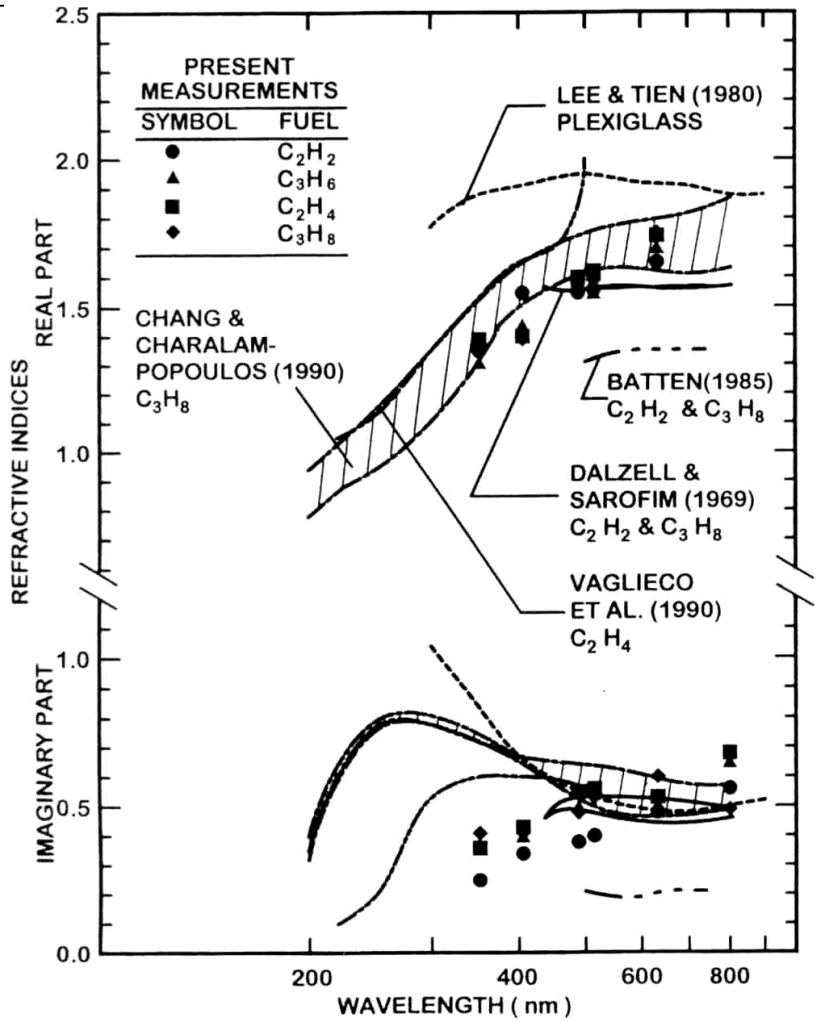

Figure 17: The imaginary and real part of the complex refractive index of soot, as found in the literature (Wu, Krishnan and Faeth, 1979).

The wavelength of the laser irradiation is typically 1064nm (first harmonic of a Nd:YAG laser), whereas emission wavelengths are comprised between 400 and 800 nm , whereas *a [cm]* is the particle radius and *E(m) [ ]* the dimensionless complex refractive index function. In turn , the complex refractive index function is defined in equation 10 and developed into equation 11:

$$E(m) = -\mathrm{Im}\left(\frac{m^2-1}{m^2+2}\right) \qquad \textbf{(10)}$$

$$E(m) = \frac{6 \cdot n \cdot k}{\left(n^2 - k^2 + 2\right)^2 + 4 \cdot n^2 \cdot k^2} \qquad \textbf{(11)}$$

Although the emissivity of soot and the emission as well as absorption by soot nanoparticles during LII is typically derived using equations 8 to 11, the Rayleigh - Debye - Gans scattering theory is more appropriate for accounting soot particles aggregation Therefore emissivity expressing the emissivity of soot ε_λ can be expressed as in equation 12 (Hope Michelsen, 2003):

$$\varepsilon_\lambda = \frac{4 \cdot \beta \cdot a}{3 \cdot \lambda^\xi} \qquad \textbf{(12)}$$

Where β [ ] is the fractal scaling factor and ξ [ ] the fractal dispersion exponent. Value for these two factors were determined for reasonably aggregated soot particles, heavily aggregated soot particles, annealed soot particles and liquid graphite by Hope Michelsen (2003), through fits to the data provided by Koylu et al.(1995, 1997). Koylu and Faeth (1992,1996) and Koylu (1997):

Soot physical state	**B**	**ξ**
Aggregated soot particles	28.72	0.83
Heavily aggregated soot particles	0.101	1.39
Annealed soot particles1	1.364	0.626
Liquid graphite	$1.115 \cdot 10^5$	0

Table 1: Emissity fractal scaling factors and fractal dispersion exponents values derived by Hope Michelsen (2003).

Equation 12 allows for a better accounting for aggregation, increasing the absorptivity of soot by 15 %, which is coherent with experimental observations. The link between Rayleigh scattering theory and the more complex Rayleigh - Debye - Gans theory can be done by expressing the refractive index function, *E (m)*, as derived from the absorption cross-section, $C_{abs,}$ and therefore going through equations 9, 8 and 12 leads to equation 13:

$$\text{If } C_{abs} = \frac{8 \cdot \pi^2 \cdot a^3 \cdot E(m)}{\lambda} \qquad \textbf{(9)}$$

$$\text{And } C_{abs} = \pi \cdot a^2 \cdot \varepsilon_\lambda = \pi \cdot a^2 \cdot \frac{4 \cdot \beta \cdot a}{3 \cdot \lambda^\xi} \qquad \textbf{(8 \&12)}$$

$$\text{Then } E(m) = \frac{\lambda^{1-\xi} \cdot \beta}{6 \cdot \pi} \qquad \textbf{(13)}$$

Hope Michelsen (2003) proposed values that are the most accurate found in the literature up to now. However, their uncertainty is not mentioned and can be expected to keep the 10 to 20% uncertainty values since they are based on results obtained by extinction measurements in flames and do not represent a precise account of atmospheric soot produced by complex systems such as diesel engines, gasoline engines and gas turbines, all with various atmospheric residence time and agglomeration states. Now that the main physical phenomenon occurring during LII can be described with accuracy using actual values for both emissivity and absorptivity of soot, one can set about drawing a context for the second most

important phenomena occurring after absorbing of laser energy and blackbody emission: conduction heat transfer through gas molecules – soot nanoparticles collisions and sublimation. Therefore both thermophysical properties of soot and the target gas (air) have to be described.

I.5.5. Thermo-physical properties of soot and air

For LII, because soot is laser-heated to temperatures above 2000 K, soot thermophysical properties are approximated as the ones for carbon. Effectively, conduction becomes the dominant cooling mechanism for LII after absorption of laser energy and reaching of the peak LII temperature. Therefore the properties of graphite are believed to drive the thermo-physical processes during Laser - Induced Incandescence. Leider et al. propose refined thermodynamic data on carbon (Leider, Krikorian and Young, 1973) from room temperature to the high temperature domain, from which fits to data permitted Smallwood et al.(2001) to compute the following expressions for the vaporization pressure of carbon P_V (equation 14), the molecular vapour mass of carbon M_v (equation 15), carbon heat of vaporization ΔH_v (equation 16) and carbon specific heat capacity c_s (equation 17):

$$P_v = \exp(-122.96 + 0.090558 \cdot T - 2.7637 \cdot 10^{-5} \cdot T^2 + 4.1754 \cdot 10^{-9} \cdot T^3 - 2.4875 \cdot 10^{-13} \cdot T^4) \quad \textbf{(14)}$$

$$M_v = 17.179 + 6.8654 \cdot 10^{-4} \cdot T + 2.9962 \cdot 10^{-6} \cdot T^2 - 8.5954 \cdot 10^{-10} \cdot T^3 + 1.0486 \cdot 10^{-13} \cdot T^4 \quad \textbf{(15)}$$

$$\Delta H_v = 205398 + 736.60 \cdot T - 0.40713 \cdot T^2 + 1.992 \cdot 10^{-4} \cdot T^3 - 1.7946 \cdot 10^{-8} \cdot T^4 + 1.0717 \cdot 10^{-12} \cdot T^5 \quad \textbf{(16)}$$

$$c_s = \left(\frac{R}{12.01}\right) \cdot \left\{ \begin{array}{l} 1.115 \cdot \left(\frac{597}{T}\right)^2 \cdot \exp\left(\frac{597}{T}\right) \cdot \left[\exp\left(\frac{597}{T}\right) - 1\right]^{-2} \\ +1.789 \cdot \left(\frac{1739}{T}\right)^2 \cdot \exp\left(\frac{1739}{T}\right) \cdot \left[\exp\left(\frac{1739}{T}\right) - 1\right]^{-2} \\ +1.16 \cdot 10^{-4} \cdot T \end{array} \right\} \quad \textbf{(17)}$$

The intermolecular diffusion of C_3, Γ *[cm^2.s^{-1}]*, the main carbon cluster evaporated during pulsed laser evaporation of carbon(accounting for 59% of the mass loss during vaporization of carbon using a high power laser beam - Douglas J. Krajnovich, 1995), has been communicated by Smallwood (2003):

$$\Gamma = \frac{706}{760} \cdot \left(\frac{T_0}{1000}\right)^{1.65} \quad \textbf{(18)}$$

Where T_0 *[K]* represents the surrounding gas temperature. Soot density, ρ_s *[g.cm^{-3}]*, has been reviewed by Hope Michelsen (2003) and expressed as dependant of the

temperature of soot, accounting for evaporation from the inside of the particle, during laser heating:

$$\rho_s = 2.3031 - 7.3106 \cdot 10^{-5} \cdot T \quad \textbf{(19)}$$

The thermo-physical properties of air are approximated as the ones of nitrogen as its dominant constituent. Nitrogen properties are described in equations 20 to 24:

$$C_p = R \cdot \left\{ \begin{array}{l} 3.498 \cdot \left(\frac{1}{T}\right)^2 \cdot \exp\left(\frac{1}{T}\right) \cdot \left[\exp\left(\frac{1}{T}\right) - 1\right]^{-2} \\ + 0.98378 \cdot \left(\frac{3353.5}{T}\right) \cdot \exp\left(\frac{3353.5}{T}\right) \cdot \left[\exp\left(\frac{3353.5}{T}\right) - 1\right]^{-2} \\ + 2.5766 \cdot 10^{-5} \cdot T \end{array} \right\} \quad \textbf{(20)}$$

$$K_a = 1.0811 \cdot 10^{-4} + 5.1519 \cdot 10^{-7} \cdot T_0 \quad \textbf{(21)}$$

$$\gamma = C_p / C_v \quad \textbf{(22)}$$

$$\alpha_T = 0.8 \quad \textbf{(23)}$$

$$W_a = 28.74 \quad \textbf{(24)}$$

Where γ [ ], C_p [$J.mol^{-1}.K^{-1}$], K_a [$W.cm^{-1}.K^{-1}$], α_T [ ],and W_a [$g.mol^{-1}$] are respectively the heat capacity ratio for the gas surrounding the particles, the molar heat capacity of N_2, the thermal conductivity of N_2, the thermal accommodation coefficient of air at 300K, and the average molecular weight of air. γ is said to vary from 1.4 for air at 300 K to 1.3 for air at 1500 K (Hope Michelsen, 2003). The molar heat capacity is quoted from the study of Fried and Howard (2000), whereas K_a is quoted from Hope Michelsen (2003).

I.6. Chapter I conclusion

Throughout this chapter, Laser-Induced Incandescence of soot has been given a general presentation and outlined resulting from the laser irradiation of soot nanoparticles contained within an aerosol. Various measurement conditions are addressed by LII, such as: vehicular exhaust, flames, carbon black, atmospheric pollution, etc… Although soot was initially considered as source of interference and then a soot volume fraction measurement method, it is also being developed into a particulate sizing technique, even though aggregation and eventually agglomeration of nanoparticles are the actual concerns for the technique and future refinements of the LII technique can be believed to include both primary particle and aggregate sizing. Even though particle sizing remains an issue, LII has a distinct advantage over the other particle measurement methods as the technique allows measurements to be performed for a large range of soot concentrations, from undiluted heavily loaded exhaust streams and carbon black production measurements to atmospheric and sub-ppb pollutant monitoring. Furthermore, because the actual phenomenon lasts less than one microsecond, instantaneous volume fractions are obtained and the time

resolutions obtained with LII are source of concerns for concurrent particulate matter monitoring techniques.

Soot is a by-product of human activity and raises health concerns. Indeed, even though the graphitic and amorphous carbonaceous content of soot is proved to be non-toxic by itself, soot is known for condensing and adsorbing toxic compounds such as carcerinogenic polyaromatic hydrocarbons, metallic ashes, etc… Overall, soot acts as a carrier substrates that, because of it submicron size, delivers harmful substances into the lung epithelium and as such represents a health concern. Therefore increasingly stricter emission regulations are being implemented.

In more details, soot itself is primarily a by-product of combustion. Soot formation results from excess carbon (rich) combustion conditions. Soot nucleation is associated with acetylene molecules and polyaromatic hydrocarbons coagulation. This eventually leads to the coagulation of gas-phase aromatic compounds into nearly spherical particles which in turn agglomerate between each others and result into fused aggregates after a later oxidation stage. Therefore soot is mainly composed of amorphous and graphitic carbon, but also polyaromatic hydrocarbons and adsorbed combustion byproducts. This explains that soot present in the atmosphere or within vehicle exhaust gases contain a vast majority of carbon, followed by portions of metallic ashes, Sulfur, oxygen, hydrogen and nitrogen.

When related to laser-induced incandescence, the main particularities of soot that are of interest are: the soot primary particle size distribution, aggregation characteristics and primary particle structural properties changes during LII. Laser-Induced Incandescence yields a measurement of the soot volume fraction but also an estimate of the primary particle size. The primary particle measurement reveals complex because influenced by primary particle size distribution, aggregation, primary particle structural changes and eventually agglomeration of aggregates. Primary particles are known to follow the lognormal size distribution whereas aggregate size distributions are better described by a fractal expression. Primary particle structural changes are highlighted after findings that annealing and consequently fullerene formation occur. These have direct implications on the optical emission and absorption from soot, which are also described. Even though agglomeration would prove difficult to characterize in general terms, the phenomenon is known to be time-dependent but also dependent on local gas and particulate matter properties.

Optical properties of soot are then discussed in terms of emissivity and absorptivity. A substantial research effort has been made in the past forty years to measure the complex refractive index (m) of soot. However, even though values for the refractive index for common fuel types have been measured more or less reliably using extinction method measurements, the refractive index of soot can hardly be considered as accurate to less than 10%, with reported uncertainty values ranging from 10 to 20%. On hand, the direct consequence of the difficulty associated with measuring soot refractive index is that because radiative heat transfer from soot is the major contributor to heat transfer within many combustion systems, the said combustion systems become difficult to model and predict. On the other hand, because the soot volume fraction measurement obtained with LII is directly proportional to emissivity, any uncertainty on emissivity is directly reported into soot volume fraction uncertainty. Section 1.5.5 then illustrates the thermo-physical

properties of soot and air, given the fact that LII measurements are typically performed on airborne particulate matter.

Overall, chapter I is dedicated to providing a description of soot both in general terms and in more physical terms relevant to laser-induced incandescence. Following the description of soot, chapter II present Laser-induced incandescence, both in terms of a validated general model and the measurement method used throughout this thesis.

Chapter II: LII model and measurement method

An obvious need when dealing with laser-induced incandescence is to understand and predict the underlying physics. This second chapter first details the general model for LII that has been adopted throughout the course of this thesis. The said model is validated against currently available data in the literature and limits itself to the characterized phenomena that occur during LII rather than hypothetical considerations of annealing rates, melting and oxidation (Hope Michelsen, 2003).The self-calibrated time –resolved LII method is an extension of the LII model itself. Indeed, the method consists of measuring directly soot temperatures, match the temperature decays and light intensities with the modelled temperature decays and intensity to produce both an estimate of the soot primary particle diameter and volume fraction.

The LII model has been assembled using the basis of Melton's work(1984) and other researchers findings, such as Weeks and Duley (1974), Bryce (1996), Tait (1994), Santoro and Shaddix (2000), Michelsen (2003),Snelling et al. (1997-1&2, 2000), Von Allmen (1987), Grigorian (2001), Will et al. (1998), Schraml et al. (2000), Vander Wal et al. (1995, 1996, 1999), Mewes and Seitzman (1997). The heat transfers occurring during LII are best illustrated in figure 18:

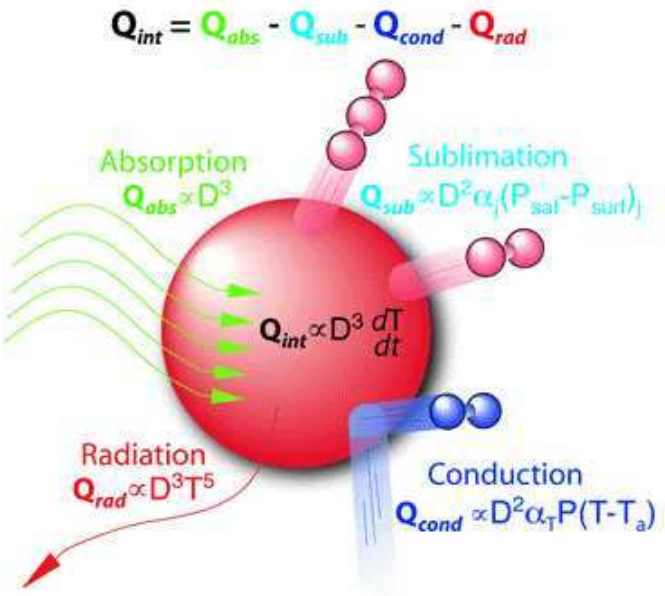

Figure 18: Microphysical description of LII (2006).

Laser-induced incandescence occurs when a laser beam encounters particulate matter like soot. The internal rate of energy change of the particle is represented by Q_{int} on figure 18, followed by energy absorption rate from the laser beam Q_{abs}, the sublimation heat loss rate Q_{sub}, the radiation heat loss rate Q_{rad} and the conduction heat loss Q_{cond}. Since the wavelength of the laser obeys the Rayleigh condition (i.e. $\pi.D/\lambda < 1/3$, D being the particle diameter and λ the laser wavelength), laser energy absorption is volumic and therefore the laser energy absorption rate Q_{abs} is proportional to D^3 . Sublimation is surfacic (and therefore scales with D^2) and depends on the pressure difference between gas saturation pressure P_{sat} and the pressure at the surface of the particle P_{surf}, overall weighted by each gas release rate α_j. Radiation energy loss rate Q_{rad} obeys Planck's law applied to a sphere and as such

is proportional to D^3T^5. As well, conduction results from the particle – gas molecules collisions on the surface of a spherical particle; therefore the conduction cooling rate Q_{cond} is proportional to $D^2\alpha_T$ $(T-T_a)$, with $(T-T_a)$ the temperature difference between the particle and air and α_T accommodation coefficient of air.

The model applies to a single primary particle and assumes the primary particle does not interact with any other surrounding soot primary particles. Therefore the general rate equation that describes the energy rates balance equation for LII can be expressed using equation :

$$Q_{int} = Q_{abs} - Q_{rad} - Q_{cond} - Q_{sub} \qquad \textbf{(25)}$$

Where Q_{int} $[J.s^{-1}]$ represents the rate of change of internal energy for the particle , Q_{abs} $[J.s^{-1}]$ accounts for the rate of energy change incurred during laser irradiation, Q_{rad} $[J.s^{-1}]$ describes the rate of radiative energy transfer through blackbody radiation, Q_{cond} $[J.s^{-1}]$ represents the rate of energy dissipation by conduction and Q_{sub} $[J.s^{-1}]$ is the rate of energy loss by evaporation of carbon clusters (mainly C_3). The rate of internal energy change is the energy lost or gained as a result of respectively either temperature increase of loss, $\frac{dT}{dt}$. Therefore, Q_{int} can be expressed as:

$$Q_{int} = C_s \cdot \frac{dT}{dt} = m_s \cdot c_s \cdot \frac{dT}{dt} = \frac{4}{3} \cdot \pi \cdot a^3 \cdot \rho_s \cdot c_s \cdot \frac{dT}{dt} \qquad \textbf{(26)}$$

Where C_s $[J.K^{-1}]$ is the particle heat capacity, c_s is the soot specific heat capacity approximated as the specific heat capacity of graphite and m_s the particle mass. The first factor to take into account into LII is the initiation of the phenomenon, that is the absorption of laser light energy by the particle, which initiates a temperature increase.

II.1. Absorption of laser light energy

The amount of heat gained by a particle can be expressed as:

$$Q_{abs} = C_{abs} \cdot \frac{F \cdot q_{exp}(t)}{\int_0^{60ns} q_{exp}(t) \cdot dt} \qquad \textbf{(27)}$$

Where F $[J.cm^2]$ is the laser fluence (also called irradiance) and q_{exp} (t) $[\ ]$ is the temporal laser beam profile normalized to its area over the heating pulse length (60 ns is just an indication).The temporal profile of the laser beam can be expressed as a Gaussian function as most of the pulsed Q-switched laser beams temporal profiles obey a Gaussian energy deposition over time (see figure 19):

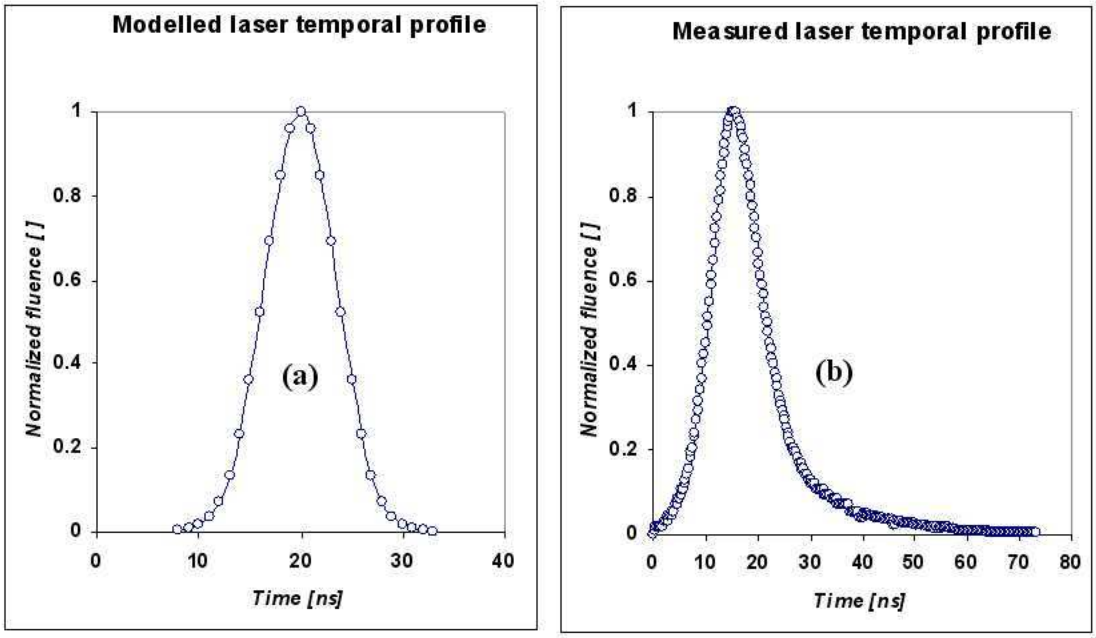

Figure 19: (a)Laser temporal profile, q_{exp} (t), as used in the model, corresponding to a 7 ns full width at half maximum gaussian
(b)Laser temporal profile as measured by Smallwood (2003). The additional tailing observed is indeed typical of Si relaxation following intense photon bombardments and therefore is an artefact of the laser pulse measurement mean.

The mathematical expression for a Gaussian temporal profile is:

$$q_{\exp}(t) = \frac{q_{\max}}{\sqrt{2 \cdot \pi \cdot w_{temporal}{}^2}} \cdot \exp\left(- \frac{t^2}{2 \cdot w_{temporal}{}^2} \right) \qquad \textbf{(28)}$$

Where q_{max} *[W.cm^{-2}]* is the peak fluence encountered by the soot particle, $w_{temporal}$ *[s]* is the half width at half maximum whereas *t [s]* stands for the time. As well as absorbing light, soot particles incandesce and radiate light and the radiative heat transfer is best explained in the following section.

II.2 Radiative heat losses

The radiative energy transfer is the source of the LII signal itself: soot become incandescent upon laser heating, emitting a measurable amount of light. Eckbreth discovered the phenomenon (1977). The Planck law expresses the intensity B_λ *[W.m^{-3}.ster^{-1}]* (or brightness) radiated by a blackbody as a function of wavelength and temperature of the blackbody (Eric Wienstein, 2003 – 1&2):

$$B_\lambda(T) = \frac{2 \cdot c^2 \cdot h}{\lambda^5 \cdot \left(e^{\frac{h \cdot c}{\lambda \cdot k \cdot T}} - 1 \right)} \qquad \textbf{(29)}$$

The Planck law is integrated to obtain Stefan-Boltzmann law, which expresses the total energy flux Φ *[w.m^{-2}]*, emitted from a blackbody as:

$$\Phi = \pi \int_0^{\infty} B_\lambda d\lambda = 2\pi \cdot c^2 \cdot h \cdot \int_0^{\infty} \frac{1}{\lambda^5 \cdot \left(e^{\frac{h \cdot c}{\lambda \cdot k \cdot T}} - 1 \right)} d\lambda \qquad \textbf{(30)}$$

Note that the extra factor π converts from brightness per solid angle to total brightness. Then the total energy flux Φ emitted from a blackbody and defined by Stefan – Boltzmann law can be converted to an emitted power through multiplying by the surface area of the particle. Moreover, the emissivity takes in account that the particle does not emit quite like a perfect blackbody radiator. Then the rate of cooling for a spherical soot particle can be expressed as:

$$Q_{rad} = 4 \cdot \pi \cdot a^2 \cdot \varepsilon_\lambda \cdot \Phi \qquad \textbf{(31)}$$

The radiative cooling rate has been neglected by most authors since heat loss is insignificant compared to the other mechanism of heat loss. It has been considered as negligible unless under very high temperatures for soot (above 10 000 K) and very high temperature wall inside a combustion system (Santoro & Shaddix, 2000).
In this case the radiative heat loss is not neglected and the integration of Planck's law performed by Hope Michelsen (2003), in the case of the Rayleigh scattering theory:

$$Q_{rad} = \frac{199 \cdot \pi^3 \cdot \left(8 \cdot a^3 \right) \cdot (k \cdot T)^5 \cdot E(m)}{h \cdot (h \cdot c)^3} \qquad \textbf{(32)}$$

The following section addresses the gas molecule-particle collisions that are the vector for heat conduction to the surrounding gas.

II.3 Heat conduction to the surrounding gas

The soot particles, once heated above the surrounding gas temperature, exchange heat through conduction (collision of gas particles against their surface). The expression used for conduction is the one used by Michelsen (2003), Snelling et al. (1997, 1999, 2000-1,2&3), Smallwood et al.(2001-1,2,3,4), and McManus (1997,1998). The model presented here for conduction is quoted from the detailed development provided by Hope Michelsen (2003) and has been first introduced by Nigel Tait (1994).The conduction of heat from the particle to hits surrounding gas is dependent upon the mean free path of the gas molecules surrounding the particle and the particle diameter. Two cases can be distinguished: if the particle size is much larger than the mean free path of the surrounding gas molecules (continuum regime, figure 20-a), the gas behaves as a continuous fluid. At the other extreme, if the particle is much smaller than the mean free path of the surrounding fluid (free molecule or kinetic regime, figure 20-b), an outsider of the system sees a small particle and gas molecule moving discretely around it. The particle is small enough that it looks like another gas molecule. Also, a transition regime (figure 10-c) exists when the particle diameter equates the gas mean free path.

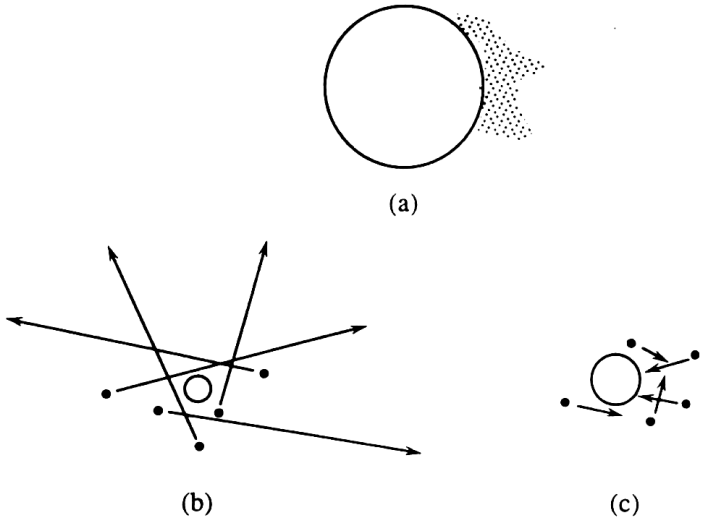

Figure 20: Schematic of the three regimes of suspending fluid-particle interactions (Seinfeld & Pandis, 1998):
(a) Continuum regime ($K_n \rightarrow 0$)
(b) Free molecule (kinetic) regime ($K_n \rightarrow \infty$)
(c) Transition regime ($K_n \sim 1$).

Since the conduction phenomena are due to the choc of gas particles (N_2 approximated as air in our case), it is convenient to express first the gas molecules mean free path λ_{mfp} *[cm]* in air as a function of its temperature T_0 *[K]* and pressure P_0 *[atm]*:

$$\lambda_{mfp} = \frac{k_p \cdot T_0}{\sqrt{2} \cdot \sigma_a \cdot P_0} \qquad \textbf{(33)}$$

Where σ_a *[cm^2]* is the mean molecular cross section of air.

To be able to define our conduction regime, it is also convenient to express the Knudsen number, K_n *[ ]* as:

$$K_n = \frac{\lambda_{mfp}}{2 \cdot a} \qquad \textbf{(34)}$$

When the mean free path greatly exceeds the particle radius, i.e. $K_n > 5\sqrt{\frac{\gamma \cdot \pi}{2}}$, heat and mass transfer are in the Knudsen (molecular) regime that can be described in the context of the kinetic theory of gases (Michelsen, 2003):

$$Q_{cond} = \frac{4 \cdot \pi \cdot a^2 \cdot \alpha_T \cdot Z_{surf}}{N_a} \cdot \left(C_p - \frac{R}{2}\right)(T - T_0) \qquad \textbf{(35)}$$

Z_{surf} *[$s^{-1}.cm^{-2}$]* is the collision rate of ambient air molecules with the particle surface:

$$Z_{surf} = \frac{P_0}{k_p \cdot T_0} \cdot \sqrt{\frac{R_m \cdot T_0}{2 \cdot \pi \cdot W_a}} \qquad \textbf{(36)}$$

Where W_a *[$g.mol^{-1}$]* is the average molecular weight of air. If the pressure is greater

and/or we face a larger particle size, i.e. $K_n < 5\sqrt{\frac{\gamma \cdot \pi}{2}}$, we face a transition between the Knudsen (molecular) and the continuum conduction flow of heat:

$$Q_{cond} = \frac{8 \cdot K_a \cdot \pi \cdot a^2}{\left(2 \cdot a + G \cdot \lambda_{mfp}\right)} \cdot \left(T - T_0\right) \qquad \textbf{(37)}$$

The geometry-dependent heat transfer factor *G [ ]* can be expressed as:

$$G = \frac{8 \cdot f}{\alpha_T \cdot (\gamma + 1)} \qquad \textbf{(38)}$$

Where *f [ ]* is the Eucken correction factor to the thermal conductivity of a polyatomic gas ($f = 5/2$ for a monoatomic gas):

$$f = \frac{9 \cdot \gamma - 5}{4} \qquad \textbf{(39)}$$

As a summary for this heat conduction section, one could adopt the following expression:

$$Q_{cond} = \begin{array}{l} \frac{4 \cdot \pi \cdot a^2 \cdot \alpha_T \cdot Z_{surf}}{N_a} \cdot \left(C_p - \frac{R}{2}\right)\left(T - T_0\right) \text{ if } K_n > 5\sqrt{\frac{\gamma \cdot \pi}{2}} \\ \frac{8 \cdot K_a \cdot \pi \cdot a^2}{\left(2 \cdot a + G \cdot \lambda_{mfp}\right)} \cdot \left(T - T_0\right) \text{ if } K_n < 5\sqrt{\frac{\gamma \cdot \pi}{2}} \end{array} \qquad \textbf{(40)}$$

Other authors such as Weeks and Duley (1974), Tait (1994), Grigorian (2001), Will et al. (1998), Schraml et al. (2000, 2002), take into account that the heat loss through conduction is controlled by the heat transfer across the Langmuir layer, which is not studied in this case and make the statement that the particles are small compared to the mean free path, which is equivalent to the Knudsen (molecular) flow model. The last term of the "classical" LII model is the sublimation, as melting of carbon nanoparticles has not been given any evidence so far, although melting was confused for LII with the presence of a so-called "plateau" region circa 3800-4000K peak temperature was believed to be achieved. This later proved erratic when pyrometric techniques were employed to measure the real-time soot temperature and proved that the so-called "plateau" region was an artefact of Gaussian laser energy distribution.

II.4. Rate of heat losses through sublimation of carbon clusters

During soot sublimation by the laser beam, different species of carbon coexist in the produced vapour with C_3 as the dominant specie (Smallwood et al., 2001-1; Dreyfus et al, 1987), correlating to 59% of the mass loss during laser heating. The behaviour of soot can be approximated as the one of pyrolytic graphite enduring laser heating (Krajnovich, 1995). The sublimation of pyrolytic graphite can actually be assimilated with a serie of releases of carbon clusters due to the break-up of single and double bonds within the graphitic structure, and this is illustrated in figure 21. The breaking of bonds within the structure originates from the high level of molecular agitation associated with high temperatures: sublimation of graphite is typically initiated as from 1800 K and upwards, but is considered as a major contributor for laser-induced incandescent soot as from 2500-2600K.

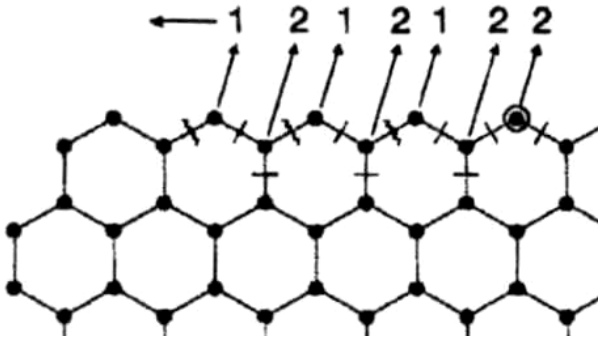

Figure 21:Schematic of the graphite sublimation process. Starting at the carbon atom circled vaporization proceeds around the edges of the graphitic plane by alternating sequence of single-bond and double - bond rupture (Krajnovich, 1995).

The rate of energy loss through sublimation is the cause of many errors in the literature. These errors have been outlined by Smallwood et al.(2001-1), who clarified the situation. The expression for heat loss through evaporation of the soot particle which was chosen and checked for errors is the one developed by Snelling et al.(2001-1):

$$Q_{sub} = -\frac{\Delta H_v}{M_v}\cdot\frac{dM}{dt} \qquad \textbf{(41)}$$

Where M is the mass of the particle. The mass conservation equation is developed as:

$$\frac{dM}{dt} = 2\cdot\rho_s\cdot\pi\cdot a^2\cdot\frac{dD}{dt} = -4\cdot\pi\cdot a^2\cdot N_v\cdot\frac{M_v}{N_a} \qquad \textbf{(42)}$$

Where *D [cm]* is the diameter of the particle and N_v *[molecules.cm^{-2}.s^{-1}]* the molecular flux of sublimated carbon clusters (Hofeld, 1993):

$$\frac{1}{N_v} = \frac{1}{N_c} + \frac{1}{N_k} \qquad \textbf{(43)}$$

N_c *[molecules.cm^{-2}.s^{-1}]* is the molecular flux of evaporated carbon in the continuum regime and N_v *[molecules.cm^{-2}.s^{-1}]* is the molecular flux of dissociated carbon clusters in the Knudsen (molecular) regime:

$$N_k = \beta\cdot n_v\cdot\sqrt{\frac{R\cdot T}{2\cdot\pi\cdot M_v}} \qquad \textbf{(44)}$$

Where n_v is the molecule number density of soot vapour, calculated using the ideal gas equation:

$$n_v = \frac{P_v\cdot N_a}{R\cdot T} \qquad \textbf{(45)}$$

In the continuum regime, the soot vapour molecular flux N_c can be calculated as(McCoy and Cha, 1974):

$$N_c = n_v\cdot\frac{\Gamma}{a} \qquad \textbf{(46)}$$

The global sublimation heat loss rate is therefore expressed as:

$$Q_{sub} = -4 \cdot \pi \cdot \Delta H_v \cdot a^2 \cdot \frac{\frac{P_v}{R \cdot T}}{\frac{1}{\beta} \cdot \sqrt{\frac{2 \cdot \pi \cdot M_v}{R \cdot T}} + \frac{a}{\Gamma}} \qquad \textbf{(47)}$$

Now that Sublimation, conduction, radiation and absorption as well as internal energy have been detailed, the energy balance equation 25 ($Q_{int} = Q_{abs} - Q_{rad} - Q_{cond} - Q_{sub}$) needs solving, which is the subject of the following section.

II.5. Integration and solving of the mathematical system for Laser-Induced Incandescence.

The aim of this section is to highlight the solving method for the LII energy balance equation. Out of the set of equations available, two variables are of interest: the variation of the particle temperature with time as well as the particle size. Substituting equation 26 ($Q_{int} = C_s \cdot \frac{dT}{dt}$) into equation 25 ($Q_{int} = Q_{abs} - Q_{rad} - Q_{cond} - Q_{sub}$) yields:

$$\frac{dT}{dt} = \frac{1}{C_s} \cdot \left[Q_{abs} - Q_{rad} - Q_{cond} - Q_{sub} \right] \qquad \textbf{(48)}$$

And the mass conservation equation yields:

$$\frac{da}{dt} = -\frac{M_v}{\rho_s} \cdot \frac{\frac{P_v}{R \cdot T}}{\frac{1}{\beta} \cdot \sqrt{\frac{2 \cdot \pi \cdot M_v}{R \cdot T}} + \frac{a}{\Gamma}} \qquad \textbf{(49)}$$

These two differential equations are coupled and solving this system of differential equations by using an adaptive step-size Runge-Kutta integration routine yields the particle radius as a function of time and the temperature of the particle, from which we can predict the LII signal S_{LII} [ ] as measured by a photomultiplier (Hope Michelsen, 2003):

$$S_{LII} = \Omega \pi D^2 \cdot \int_{\lambda} \varepsilon_{\lambda} \cdot \frac{2\pi \cdot h \cdot c^2}{\lambda^5 \cdot \left[\exp\left(h \cdot c \,/\, \lambda \cdot k \cdot T \right) - 1 \right]} \cdot \Sigma_{\lambda}(\lambda) \cdot d\lambda \qquad \textbf{(50)}$$

Where Ω [ ] is the calculated signal normalization factor and accounts for the gain and field of view of the detector, and Σ_{λ} [ ] its spectral sensitivity response. Initially, the LII model was implemented with National Research Council, Canada, providing a "standard" LII model in form of MathCAD® calculation spreadsheets . This model was first adapted to include the chosen parameters and approaches described in sections II-1 to II-5. However, a more sophisticated approach was developed in the form of a finite difference solver with variable successive integration time steps using LabView®.

Overall, the laser-induced incandescence model in its implementation allows for: determination of the particle temperature and size history during and after laser irradiation; a determination of the energy heat loss and gain rates; and also the direct convolution of the expected laser-induced incandescence signal in terms of absolute

light intensity per primary soot nanoparticles. Therefore adequate light signals and corresponding temperature profile and physical contributions can be obtained for any measurement condition.

II.6. Comparison of the model with literature values and use for particle size and soot volume fraction measurements.

Once the model and its implementation was completed, a few checks were necessary to confirm the physical reality of the results obtained. The most thorough and developed model published to date was by Hope Michelsen (2003). Her results stand therefore as a reference to check the validity of any newly-written piece of calculation. Also, the "classical" myth of the LII "plateau" region can be investigated. The "plateau" region is a feature of tradition obtained when measured LII signals: circa 0.3 J/cm^2, LII signals appear constant even if the laser fluence is increased. At this stage, the onset of vaporization (3800-4000 peak soot temperature) is supposed to be reached and therefore explains the measured feature. In addition, Will et al.(1998) published measured particle signal decays as a function of particle temperature that can be compared with the present model.

II.6.1. Energy loss rates comparison

The Knudsen theory has been proved to follow accurately the heat conduction phenomena involved during LII (Schraml et al., 2002).The vaporization point of carbon is evaluated to stand between 3800 and 4000 K (Fried and Howard, 2000; Leider et al., 1973), corresponding to a calculated vaporization threshold of LII at a fluence of 0.3 J/cm^2, above which heat and mass transfer largely dominant as a heat loss during LII. A comparison with Hope Michelsen's model (2003) for the energetic rate losses, which is the thorough available to date, can be performed, as illustrated in figure 22. The figure shows a good agreement for conduction and radiation, but clearly under predicts the sublimation rate by a large factor when compared to Michelsen's results, which is mainly due to Michelsen considering not only sublimation from C_{2-3} but rather C_{1-10} (Wu et al., 1998; Gingerich et al., 1974; Krajnovich, 1994). And the present model incorporates uniquely C_3 sublimation at the major contributor, with a predominance estimated to 59% .

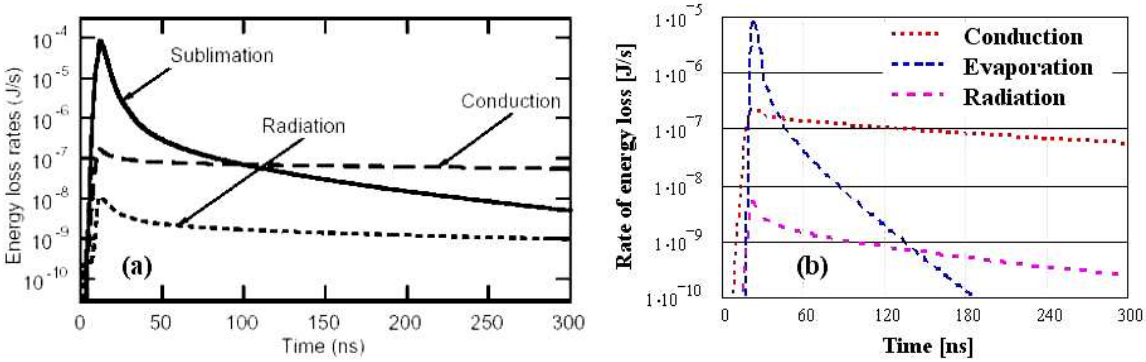

Figure 22: Energy losses rates calculated by Hope Michelsen for a fluence of 0.436 J/cm^2 acting upon a 20 nm diameter particle for a surrounding gas temperature of 1900 K
(a) Hope Michelsen (2003)
(b) Cranfield.

However, successive efforts were performed in conjunction with NRC (Liu, 2005) to implement Michelsen model in terms of sublimation for $C_{1\text{-}10}$ but success was not met. It is not know at the present date if this is due to data misinterpretation or an erroneous calculation of the sublimation terms, enven though a finite difference approach was privileged by Michelsen (Michelsen, 2003; Ozisik, 1993) over a more classical Runge-Kutta integration method. In her work, Michelsen (2003) provides a model for surface melting, thermal annealing, photodesorption and oxidation. Even though these prove tedious to implement and some of them have been reported to be non measurable (in particular photodesorption and surface melting), future LII modelling and studies could be aimed at specific isolated studies of these phenomena provided they can be physically quantified and measured. As a conclusion to this subsection, energy loss rates obtained with the current model seem reliable and comparable with published scientific data. A second point of comparison is the conduction decay of LII signals.

II.6.2. Conduction decay of LII signals.

The conduction model has been reported to provide good agreement with experimental data (Will et al., 1998).The Laser-Induced Incandescence can be shown to be composed of two exponential decay curves: the first one, when vaporization is the dominant heat loss mechanism, occurs during the first 50ns, whereas the second one lasts typically from 50 ns to the end of the light detection and is dominated by conduction heat losses to the surrounding gas. These conduction heat losses are strongly dependent on the particle temperature and therefore show a strong dependency with the particle size and its heat capacity (the larger the particle, the larger its heat capacity and the slower the cooling, and the smaller the particle, the faster the cooling through conduction). A comparison lead between the results obtained by Will et al. (1998) and the Cranfield model showed a consistent agreement, as illustrated in figure 23. Therefore, as the signal shapes and typical measured signal infers, the current model is successful at reproducing realistic laser-induced incandescence light pulses. As the LII model has now been checked against Hope Michelsen's reference work and typical measurements found in the literature, and insight into the specifity of LII signals will be the later subject. In particular, the following subsection addresses the plateau region and the characteristic fluence curve (or excitation curve) of LII.

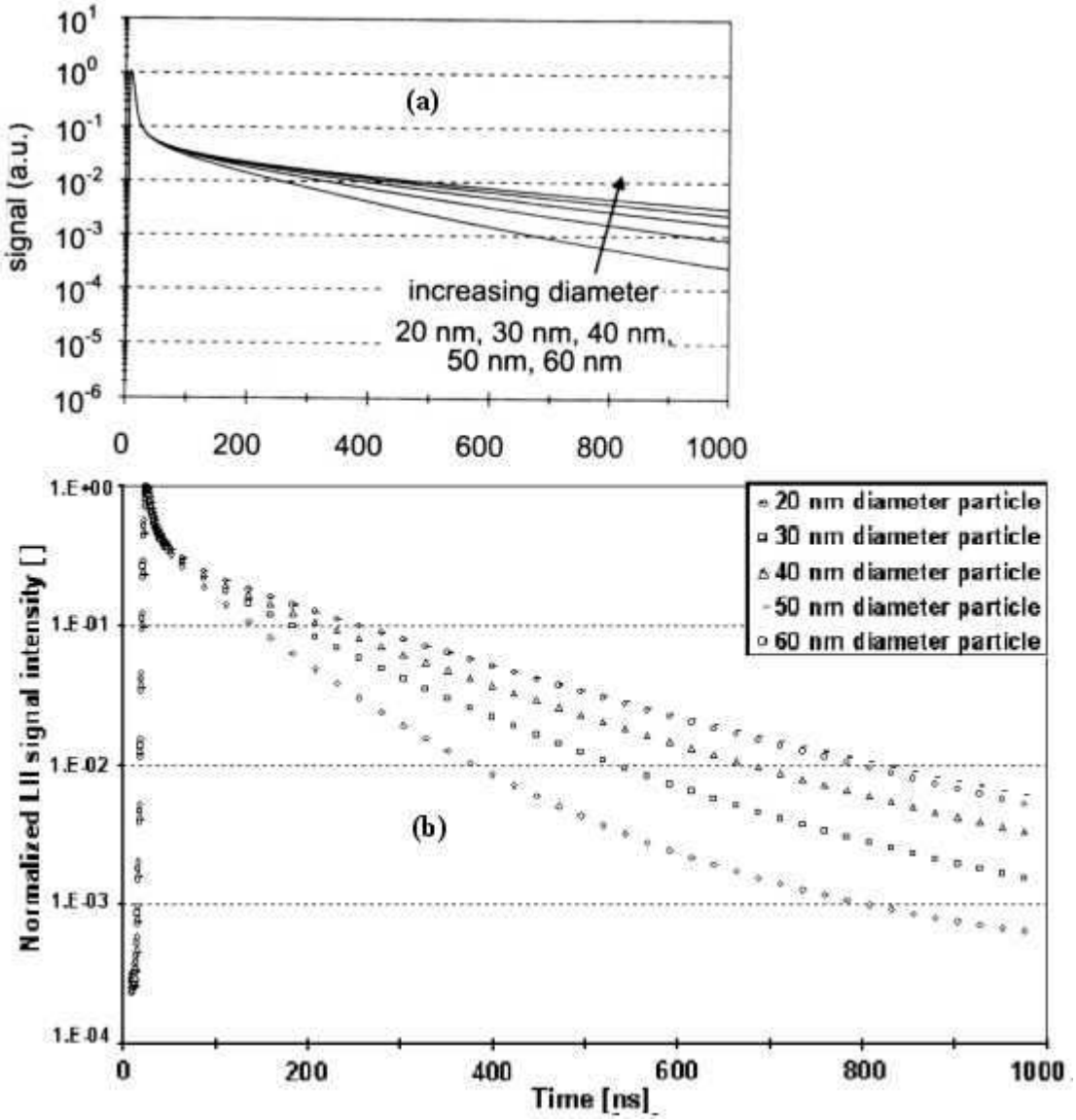

Figure 23: LII conduction decay rate dependence with particle size
(a) Data from Will et al.(1998) for an ethene flame at 1900 K
(b) Modelled results for and ethene flame at 1900 K.

II.6.3. Fluence variation of LII - excitation curve.

The variation of the Laser-Induced Incandescence signal intensity with laser fluence is referred to as the excitation curve or fluence curve. Two radically different excitation curves are available in the literature. These are best described in figure 23 (a) and (b). Although the two excitation curves are completely different in terms of shape, they are the results of measurements effected on similar soot nanoparticles. On one hand, figure 24 (a) is nearly an expression of the "plateau" region, but actually translates into a relatively low rate of increase of LII signal with laser fluence. On the other hand, figure 24 (b) shows a net increase in LII signal until a maximum is reached near 0.25 J/cm^2 followed by an abrupt diminution in LII signal with fluence thereafter. The explanation for this difference between the two figures lies on the laser spatial beam profile. The results obtained by Witze et al. in 2001 (figure 24-b) are obtained with a uniform laser energy profile: higher LII signal are obtained as higher peak temperatures are reached with increasing fluence. However, higher temperatures

also imply larger sublimation rates and therefore volumic losses, resulting in a net diminution of the effective emissive cross-section of the incandescent particles. Therefore a peak in LII signal is quickly reached circa 0.2-0.25 J/cm^2 with increasing peak temperature, but volumic losses counterbalance eventual peak temperature gains beyond these fluences and lead to a net reduction in LII signals. The same interpretation applies to the results displayed in figure 24 (a). Because the results obtained by Shaddix et al. in 1996 where obtained with a Gaussian laser spatial energy distribution, the centre of the said Gaussian profile represents a small fraction of the overall laser beam surface. As a consequence, as the overall fluence level of the Gaussian beam is increased, a sharp increase in LII signal is first obtained and this is dictated by the sharp increase of the peak temperature at the centre of the laser beam. However, further increase in fluence will actually decrease the portion of LII signal emitted by the centre of the Gaussian profile as this region benefits from higher fluence levels and therefore consequent volumic losses. In parallel, the wings of the laser beam gradually increase in fluence, until they emit larger amounts of signals than the centre of the laser, which in turns explains the overall increase of LII signal with laser fluence. As for many "classical" figures, similar results to figure 24 (a) were obtained, with typically either a "plateau" feature or a slow rate of increase of signal with fluence . A few other publications attest the observation of the said "plateau" region (Bryce, 1996;Grigorian, 2001; Snelling et al., 1997). These lead to the misinterpretation that reaching the 3800-4000K region would trigger melting of the nanoparticles and therefore limit the peak LII temperature to the actual effective fusion temperature of graphite. This interpretation was later proved wrong as on one hand melting has never been practically proven for soot nanoparticles and on the other hand introduction of multiple wavelength pyrometry allowed for the measurement of carbon nanoparticles temperatures above 4300K.

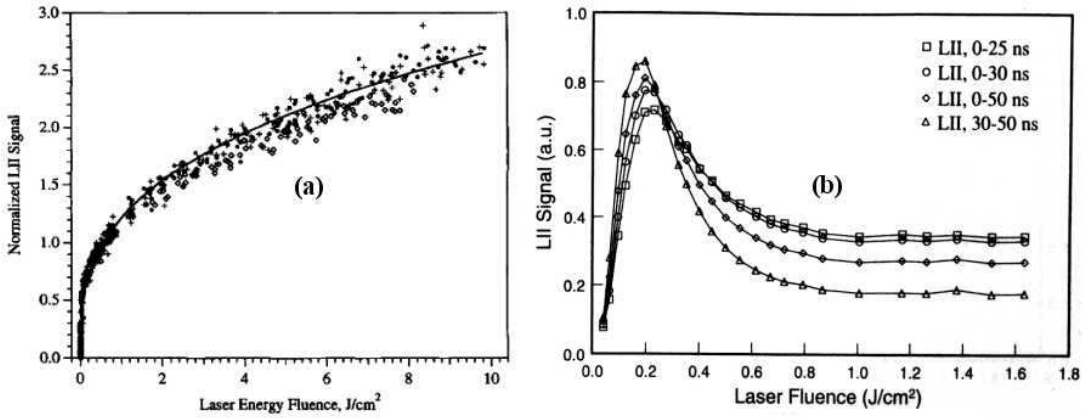

Figure 24: Excitation curves of LII for a gaussian and a top hat laser fluence profile

(a)LII signal variation with Fluence (integration over 0 -19 ns) for a Gaussian laser beam profile and normalized to 1 for 0.6 J/cm^2 (Shaddix et al., 1996)

(b)Time averaged LII signals for a top - hat spatial profile (Witze et al., 2001-2).

The spatial distribution of the laser light intensity (or fluence) has a significant effect upon the quality of the Laser-Induced Incandescence signal measured, causing either non - uniform temperatures within the test volume (for a two dimensional fluence profile, which is the classical feature of an Nd: YAG pulsed laser beam) and spatial

discrepancies in LII signal within the test volume, or a near-perfect uniform temperature distribution in the case of the top-hat spatial profile. Conventional LII is typically operated in this "plateau region", where the LII signal is somewhat independent of the laser fluence. The behaviour at fluence beyond the plateau region is dramatically different from the "top-hat" profile in comparison to the Gaussian profile. This is due to the sublimation of the carbon causing a mass (and volume) loss at the centre of the laser light beam where the decrease in the LII signal due to mass loss at the centre of the laser beam where the peak fluence is located is offset by the increasing contribution from the "wing" of the spatial profile.

In terms of applicability of the LII technique, the "classical" LII technique has proven inapt to any kind of independent calibration. As a consequence, non-uniform laser beam profiles are associated with calibration by another particulate matter measurement technique. Therefore the uniform laser energy spatial profile is preferred, as LII signals present a direct dependence on particle temperature (actually T^5) as near- uniform temperature distributions are obtained at the site of the laser-irradiation. This clearly has an advantage as temperatures are nearly uniform, and therefore become measurable. As well, if one can measure the particles temperature and the light intensity emitted by these during LII, particle concentrations become measurable by applying an absolute light intensity calibration to the measuring photodetector. A more detailed insight into such a possibility is given in the next subsection.

II.6.4. Laser-Induced Incandescence measurements using dual wavelength time-resolved optical pyrometry.

A practical way to measure incandescence temperature decay with time is the multiple wavelength pyrometry technique. Even though spectral measurements can be used to measure point-wise blackbody spectra and therefore temperatures using either an Intensified CCD (ICCD) or a back-thinned CCD camera after spectral separation by an optical grating, multiple wavelength pyrometry has the advantage of using multiple high speed photodectectors (such as photomultiplier tubes and avalanche photodiodes) each set at a fixed wavelength using individual bandpass filters. Overall, the pyrometric technique is a simplification of spectral measurements using typically two set wavelengths. The use of the technique therefore permits the measurement of time-resolved temperature decays and light intensities. Eventually the principle of this technique relies on the particle temperature dependency of a intensity ratio of light emitted at two different wavelengths, as illustrated in figure 25.

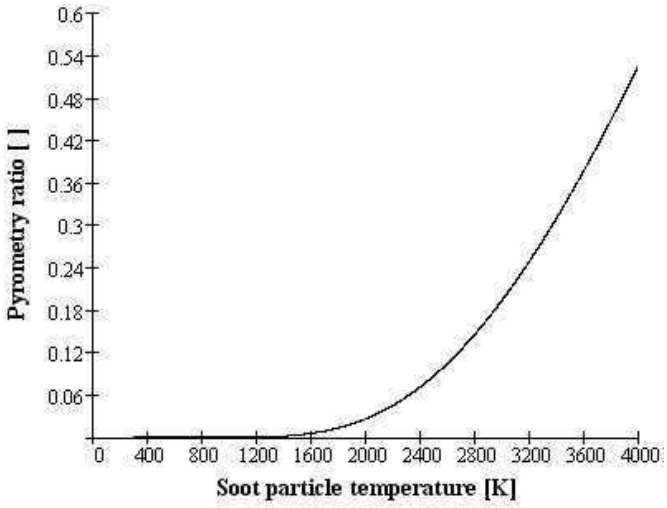

Figure 25:Modelled ratios of emitted light at 400nm and 600nm, LII_{400nm}/LII_{600nm}, for a 20 nm soot primary particle in the temperature range 0 to 4000 K, assuming equal emissivity at both wavelengths.

Therefore, by simultaneously measuring the LII signals at two different wavelengths using two calibrated photodetectors, one can obtain a direct measure of the soot instantaneous incandescent temperature during LII. A determination of primary particle size relying upon the Knudsen modelling of heat conduction to the surrounding gas can be proposed. Assuming monodisperse primary particle size, the temperature difference between the particle at a temperature T and the surrounding gas at a temperature T_0 can be expressed using an exponential temperature decay expression:

$$T - T_0 = A \cdot e^{-t/\tau} \qquad \textbf{(51)}$$

This equation can therefore be fit to the temperature decay of the soot temperature during the conduction-dominated phase of Laser -Induced Incandescence and the primary particle diameter retrieved (Schraml et al., 2000; Will et al., 1998, Snelling, 2000-2) using the equation:

$$d_p = \frac{12 \cdot K_a \cdot \alpha_T}{G \cdot \lambda_{mfp} \cdot c_s \cdot \rho_s \cdot \tau} \qquad \textbf{(52)}$$

The main source of uncertainties are: the thermal accommodation of air α_T, the morphological changes of soot, its changes of emissivity with wavelength and the surrounding gas temperature. Overall, all these parameters have potential to be measured directly. Another source of error in this method is the assumption that the soot primary particle size is monodisperse, which is an approximation. Indeed, primary particle are essentially aggregated, and this results into thermal shielding between primary soot particles. An attempt to retrieve this lognormal size distribution has been made by Filippov and Roth (1996, 1999), assuming a good fit of the experimental data to the model and therefore retrieving the particle size distribution using the iterative algorithm proposed by Twomey (1975) and Markowski (1987) . Application of soot primary particle size distribution and correction for aggregation are still the subject of intense research (Liu et al., 2006), and a combination of elastic light scattering with LII has potential to yield corrections for aggregation.

The two-colour Pyrometry method also infers the possibility to calculate directly the soot volume fraction f_v: having measured the primary particle diameter, the radiation rate for one particle can be calculated, and therefore the detected light signal intensity, can be divided by the modelled signal for one primary particle, to yield the number of detected particles, N inside the measurement volume V:

$$f_v = \frac{\pi \cdot d_p^3}{6} \cdot \frac{N}{V} \qquad \textbf{(53)}$$

However, this requires an absolute light intensity calibration for the light detectors, which can be operated with a calibrated tungsten filament lamp of known radiance, which is described in the next section.

II.6.5. Absolute light intensity calibration of LII

Many ways of calibrating Laser-Induced incandescence have been proposed so far. On one hand, for flame measurements, LII can be calibrated using tomographic inversion routine from extinction measurements or line- of sight extinction measurements (Choi and Jensen, 1998;Shaddix and Smith, 1996; McManus et al., 1997). On the other hand, soot emitted from current engines are currently measured using the gravimetric sampling methods, during which soot is collected onto a filter held at 52ºC (for condensation purposes) and the amount of soot collected therefore weighted. Others techniques such as SMPS (Scanning Mobility Particle Sizer), the Tapered Element Oscillating Microbalance (TEOM), opacity meter and ELPI (electrical low pressure impactor) have the ability to measure volume fraction of soot and eventually the size of the particulates (Witze, 2001). However, an independent calibration procedure is preferable and has been proposed by Snelling et al.(2001), relying upon the two colour Pyrometry technique explained in the section. This measurement technique is called Time- Resolved LII (TIRE-LII). Current comparisons and experiments are led by the NRC (National Research Council, Canada) and their Particulate Matter Collaboratory to infer Time-Resolved LII and Elastic Scattering of Light so as to validate TIRE-LII as a measurement technique capable of determining the primary particle size and soot volume fraction whereas the elastic scattering measurement would yield the aggregation information and the active surface area of the soot aggregate, which is the main factor affecting human health (Snelling et al., 1997;Smallwood et al, 2001-1-2-3; Witze, 2001; Axelsson & Witze, 2001; Dalzell and Sarofim, 1969, Green & Witze, 2000). The LII calibration against the gravimetric sampling technique has proven successful (Vander Wal, 1996, Choi et al., 1995). However, the self-calibrated TIRE - LII technique has been proven to be more sensitive than the calibration procedures studied so far as it was proven by Snelling et al (2001) against the standard gravimetric procedure, as depicted by figure 26. Another feature outlined is the specificity of LII to measure exclusively the carbon content of soot (since any other present organic compound is volatilized during the high energy laser heat up), provoking discrepancies with the standard gravimetric procedure (Snelling et al, 2000) and proving that TIRE - LII is a technique better suited for carbonaceous particulate matter measurements than the gravimetric procedure. More insight into the details of the technique are presented in the following section.

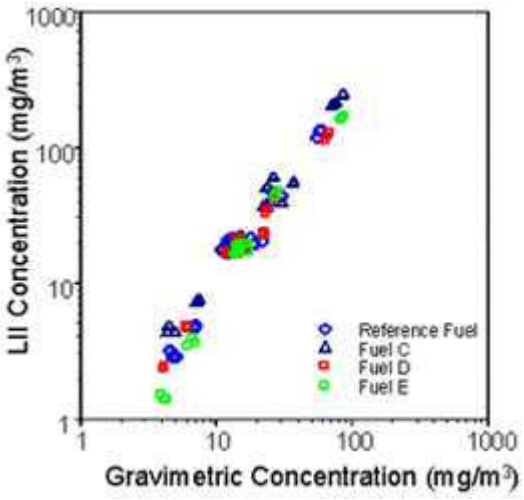

Figure 26:Comparison of LII and gravimetric measurements performed on the exhaust of a diesel engine (Sandia, 2006).

II.6.6. The Self - calibrated LII method

The self-calibrated LII technique relies on the light intensity calibration of the light detectors imaging the TIRE-LII signals and has been proposed and patented by Snelling et al.(2001, 2001-2, 2000-5). A calibrated strip filament is placed so that its filament is coincident with the LII signal generation position, which is also called the measurement volume. The lamp has a known brightness temperature (at 654 nm) as a function of lamp current. The filament is imaged with a lens onto an aperture in front of the light detector, as described by figure 27. Typical aperture dimensions are 1.0 mm diameter, and a typical lens would be 190 mm focal length and 54 mm diameter.

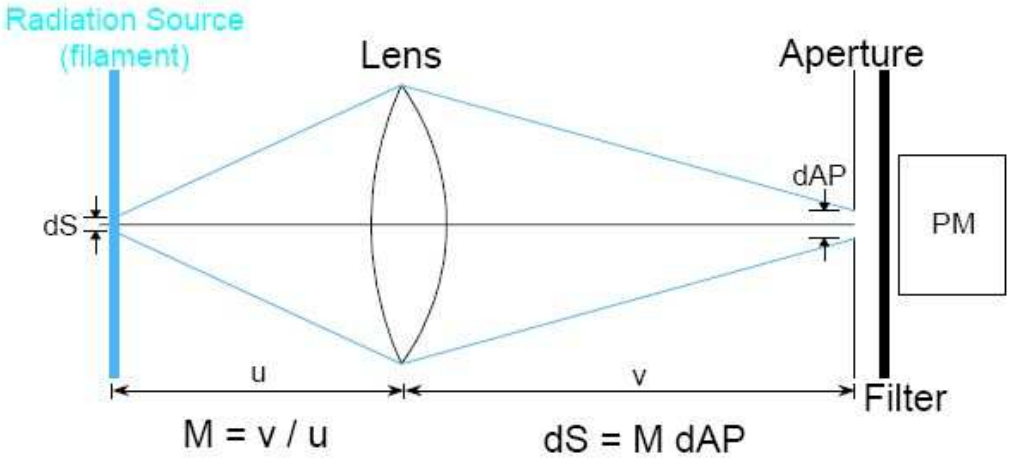

Figure 27: Optical setup for absolute intensity calibration(Snelling et al., 2001).

The spectral radiance of the lamp, R_s (the power emitted per unit area, per unit solid angle, and per unit wavelength), is given by Planck's law:

$$R_s(\lambda) = 2\pi \cdot c^2 \cdot h \cdot \frac{\varepsilon(\lambda,T)}{\lambda^5 \cdot \left(e^{\frac{h \cdot c}{\lambda \cdot k \cdot T}} - 1 \right)} \qquad \textbf{(54)}$$

Where $\varepsilon(\lambda,T)$ [ ] is the emissivity of the filament as function of its temperature T and the wavelength λ. The calibrated lamp has a known brightness temperature T_B (temperature at which a perfect black body would emit the same amount of radiation) at 654 nm from which the true filament temperature (T_s) can be obtained from:

$$T_s = \left(\frac{1}{T_B} + \frac{\lambda}{h \cdot c / k} \cdot \ln\left(\varepsilon(\lambda, T_B)\right) \right) \qquad \textbf{(55)}$$

With the known emissivity of tungsten as a function of temperature and wavelength the filament radiance can be obtained at any desired wavelength the filament from Planck's equation. Therefore the filament radiant power incident (P_{CAL})on the detector is given by:

$$P_{CAL} = M^2 \cdot A_{AP} \cdot \frac{A_L}{u^2} \cdot \int_{\lambda} R_s(\lambda) \cdot \tau(\lambda) \cdot d\lambda \qquad \textbf{(56)}$$

The distance ratio M and the distance u are specified on figure 27. A_{AP} is the area of the aperture, and $\tau(\lambda)$ is the filter transmission as function of wavelength. The signal obtained at the output of the light detector, V_{CAL}, from the calibration lamp then provides a detection system calibration factor, η:

$$\eta = \frac{P_{CAL}}{V_{CAL}} \qquad \textbf{(57)}$$

Using this calibration and the two colours Pyrometry technique, one can relate the photomultiplier voltage signal to the particle size and therefore infer the number of soot primary particles detected in the measurement volume. However, correction is needed for the filter and light detector spectral sensitivity, since one cannot effectively measure the emission of soot through a "perfect top hat" neutral density filter centred on one wavelength. Typical filters shapes are given in figure 28.

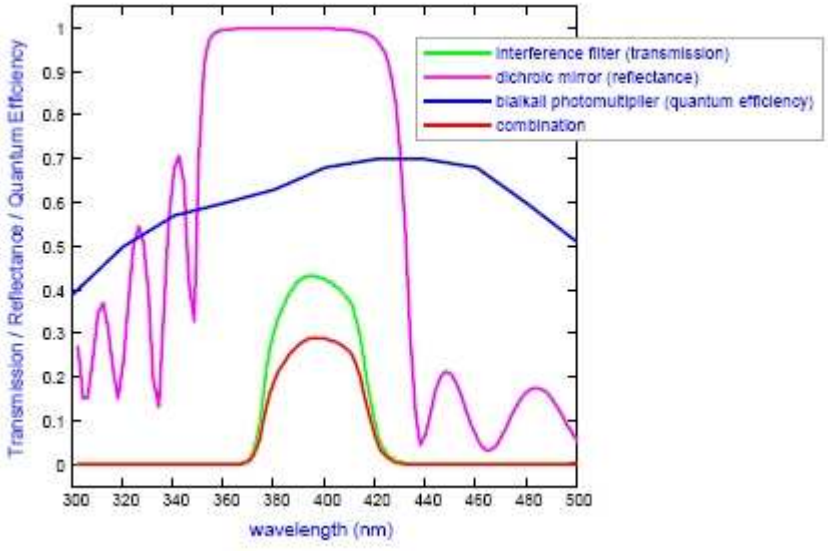

Figure 28:Example of filter and photomultiplier spectral transmission combination effect onto the overall spectral sensitivity of the measuring system (Snelling et al., 2001).

II.7. Conclusions to chapter II.

A general model for LII has been provided. The focus of the present thesis is a study of LII under vacuum rather than a reinterpretation of part of the Laser-Induced Incandescence theoretical grounds. Therefore all physical interpretations that remain in a hypothetical state or unknown were excluded. This includes: oxidation energy rates, annealing rates, multiple cluster sublimation, melting of carbon, etc… The consequence is a "classical" LII model based on the energy balance equation, expressed in equation 25. The model itself includes: laser energy absorption (Q_{abs}), radiative heat transfer (Q_{rad}), conduction heat transfer between the particle and air (Q_{cond}) and C_3 sublimation (Q_{sub}). Physical descriptions and corresponding mathematical embodiments of each of the cited above are provided in section II.1 to II.4. Overall, modelling LII resumes as solving the following system constituted by the two differential equations 48 (energy balance equation) and 49 (mass balance equation):

$$\frac{dT}{dt}=\frac{1}{C_s}\left[Q_{abs}-Q_{rad}-Q_{cond}-Q_{sub}\right] \qquad \textbf{(48)}$$

$$\frac{da}{dt}=-\frac{M_v}{\rho_s}\cdot\frac{\frac{P_v}{R\cdot T}}{\frac{1}{\beta}\cdot\sqrt{\frac{2\cdot\pi\cdot M_v}{R\cdot T}}+\frac{a}{\Gamma}} \qquad \textbf{(49)}$$

Solving of the system described above yields both particle size history and temperature history. Using the solutions obtained, the LII signal S_{LII} can be predicted as a function of particle size and temperature using Planck's law as adapted to the practical ,measurement system by Hope Michelsen (2003) in equation 50:

$$S_{LII}=\Omega\pi D^2\cdot\int_{\lambda}\varepsilon_{\lambda}\cdot\frac{2\pi\cdot h\cdot c^2}{\lambda^5\cdot\left[\exp\left(h\cdot c/\lambda\cdot k\cdot T\right)-1\right]}\cdot\Sigma_{\lambda}(\lambda)\cdot d\lambda \qquad \textbf{(50)}$$

The equation system is solved using either using a standard Runge-Kutta 4th order solving method or a finite difference approach. When compared to Hope Michelsen's (2003) published results, the model produced similar energy loss rates (Q_{rad}, Q_{cond} and Q_{sub}) levels, except for a comparatively different sublimation levels, with the present model possibly underestimating carbon sublimation during LII. However, sublimation rates during LII have not been directly measured to date and discriminating between Hope Michelsen results and those obtained during this study is not possible. Temperature conduction decay rates have also been compared with measurements taken by Will et al. (1998) for an ethene flame and showed agreement. The excitation curve of LII, defined as the signal intensity versus laser energy function, is also discussed. Until recently, Laser-Induced Incandescence was performed using a Gaussian or non-uniform laser spatial energy profile. This resulted into an excitation curve showing either a "plateau" region past circa 0.3 J/cm^2 or a reduced rate of change of signal with fluence. Common belief was that the "plateau" region resulted from the fact that soot particles eventually reached the graphite melting point (between 3800 and 4000K) and therefore melting limited soot particle temperatures from reaching any higher temperatures, hence the absence of increase of LII signal with fluence observed. However later studies confirmed that the "plateau" region was actually an artefact of the laser spatial energy profile. Measurements

performed with uniform laser energy profiles showed that an increase in fluence past the melting point of graphite would not result in a higher temperature limit being reached but high sublimation rates being achieved. Sublimation therefore would reduce greatly the emitting volume of particles to actually reduce signal levels past approximately 0.3 J/cm^2. Hence measuring LII using a non-uniform laser profile would result in large "wing" contributions for Gaussian spatial energy distributions past the threshold of 3800K, whereas the centre of the laser beam would simply diminish its overall signal contribution with increasing fluence levels past the melting point of graphite.
More interestingly, a direct consequence of the LII model is that if soot instantaneous temperature can be measured during LII simultaneously with the signal absolute intensity, it becomes possible to: measure the conductive temperature decays and therefore deduct the soot primary particle size; calculate the soot volume fraction. Snelling et al. (2000-2) introduced successfully, after Mewes and Seitzmann's (1997) suggestion, the use of two-colour pyrometry to measure soot particle temperature during LII. Dual wavelength pyrometry is a simplification of the spectral measurement technique and relies on the principle of measuring the ratio of emission from soot at two different wavelengths using two photodetectors. Eventually this ratio follows Planck's Law for a blackbody and is therefore temperature dependent. Using the two-colour LII, the self-calibrated technique was introduced by Snelling et al.(2000-2). The technique, called Time Resolved LII (TIRE-LII) simply relies on the absolute light intensity calibration of two high-speed photodetectors set behind optical bandpass filters. Therefore intensity ratios can be measured, instantaneous particle temperature measured, soot primary particle size calculated and the soot volume fraction deducted from the measurement. As well, agreement between TIRE-LII and the gravimetric sampling technique has been found, proving that the technique and calibration method is giving reliable results.

Overall, a general realistic and verified model has been established throughout chapter II. Secondary physical phenomena such as carbon melting, annealing or oxidation were not taken into account have they have not been either verified or quantified. The time-resolved laser-induced incandescence technique permits a direct measurement of the instantaneous soot temperature by dual wavelength pyrometry. This allows for direct comparisons with the physical model: primary particle sizing can be performed by comparing the measured temperature decay with the conduction model and soot volume fraction measurements are based on the association between the measured temperatures and absolute light intensities.
The model behind laser-induced incandescence under vacuum is a transposition of the classical model and measurement method presented throughout chapter II into vacuum conditions. The consequences of this transposition are predicted, modelled and described in chapter III.

Chapter III – Laser-Induced Incandescence Under Vacuum: Principles

The laser induced incandescence (LII) method has evolved over three decades from being initially a limitation in laser spectroscopy of flames (Eckbreth, 1977) to being recognised as a useful phenomena by Melton (1984) and subsequently through some fifteen years of development it has today become recognised as an important tool in the study of nanoparticles, especially soot and black carbon. Many studies of LII have been performed so far: for the study of sooting flames, at high pressure, vehicle exhausts, urban pollution monitoring, etc… However, so far laser-induced incandescence had not yet been defined for vacuum conditions. Eventually laser-sputtered graphite incandescence signals were accidentally measured by Rolhfing (1988) within the throat of a molecular beam expansion. The observed signals were reported to last longer than 40µs and a attempt to apply Melton's model was performed to conclude that the incandescent nanoscopic graphitic debris sputtered from the graphitic target were cooling from approximately 3900 to 2700 K over circa 42 microseconds. However, Rolhfing's principal interest was not LII but laser-sputtering of graphite and the laser-induced incandescence technique was still in its infancy following the then recent publication of Melton's model (1984). The consequence of this experiment lead Rohlfing's work to being limited to a spectral measurement and incandescent temperature determination together with a Mie scattering approach aimed at resolving the graphitic ejecta size.

In all the conditions studied so far, laser-induced incandescence has been involving conductive heat transfer as the dominant heat transfer mechanism during the temperature decay. And because conductive heat transfer cooling occurs on the region of less than a microsecond, this particle- medium interaction actually represents an actual limitation to incandescence signals. Practically, the energy balance equation 25 ($Q_{int}=Q_{abs}-Q_{rad}-Q_{cond}-Q_{sub}$) takes into account the changes in internal energy of a soot nanoparticle caused by the absorption of laser energy by the particle and followed by: radiation of heat through incandescence, conduction of heat to the surrounding medium and carbon sublimation. In terms of timescale, absorption is dictated by the laser beam temporal profile and leads to a peak LII temperature within less than 50 ns. Sublimation is temperature dependent. For peak LII temperatures above 2800 K at atmospheric pressure, sublimation becomes the main contributor before being overruled by the conductive heat transfer below 2800 K. This situation is clearly illustrated in figure 22 (chapter II). In standard conditions, both conduction and sublimation render the radiative heat transfer from the particle completely negligible simply because radiative heat transfer represents an energy loss rate generally 100 times lower than conduction and sublimation. However, because blackbody radiation is what is actually measured during LII and is dependent on the refractive index of soot, it is desirable to measure solely the radiative heat transfer. If radiative temperature decays are to be measured, the sole mean to reduce to negligible the other contributors, which are conduction and sublimation, is to perform laser-induced incandescence under vacuum conditions. Because the particle conductive heat transfer toward its surrounding would become negligible due to the lowered gas density and large mean free path associated with vacuum conditions, sublimation would limit itself to temperatures above 2800 K and therefore leave the radiative term as the

dominant heat transfer from 2800K to the lower measurement limit, typically 1800-2000K for soot.

The focus of this chapter is to define laser-induced incandescence under vacuum conditions as an extension of LII itself. LII under vacuum relies on the same energy balance equation as LII itself. However, the physical relationships are not the same. On one hand, Laser-Induced Incandescence under standard conditions reduces the actual energy balance equation 48 into the following simplification during the temperature decay of LII:

$$\frac{dT}{dt} = \frac{1}{C_s} \cdot [-Q_{cond} - Q_{sub}] \qquad \textbf{(58)}$$

Where Cs is the heat capacity of a particle of temperature T at the time t. On the other hand, Laser-Incandescence under vacuum simplifies into the preponderance of the radiative heat transfer over conduction during the temperature decay of LII:

$$\frac{dT}{dt} = \frac{1}{C_s} \cdot [-Q_{rad} - Q_{sub}] \qquad \textbf{(59)}$$

Because the rate of energy loss through conduction (Q_{cond}) is typically hundreds of time greater than the rate of energy loss due to the radiative heat transfer (Q_{rad}), the first noticeable difference between standard LII and LII under vacuum will be their respective time scale. Standard LII lasts approximately less than one microsecond. Estimates of LII under vacuum are signals lasting between 60 and 100 microseconds. The direct consequence of lengthened signals arising from nanoparticles is a dramatic increase in time-integrated signal levels and potentially an increase in sensitivity provided the LII measurement is performed with a photon integrating system (for example a Charge Coupled Device). Therefore the detection of isolated small aggregates comprising only a few nanoparticles would ultimately become foreseeable. Also, lengthening the LII signals from less than one microsecond to eventually 100 microseconds changes completely the nature of the measurement when applying the time resolved LII (TIRE-LII) method: LII under vacuum allows for the use of photodetectors presenting slower time response and higher noise rejection. The same applies to eventual preamplifiers and signal acquisition systems. Overall, LII under vacuum brings LII from the status of a high speed and high noise level pulse requiring nanosecond resolution instrumentation to a more reasonable signal that can be accessible to standard 2-20 MHz instrumentation.

Another ambition would also arise from the principle of LII under vacuum: because a radiative-only temperature decay can be measured using time –resolved LII, the shape of the cooling curve measured for soot nanoparticles would be dominated by the optical properties of the said nanoparticles. Thus emerges the possibility to re-evaluate the emissivity or complex refractive index function E(m) defined in equations 10 and 11. Provided the measured nanoparticles obey the Rayleigh criterion for blackbody radiation (that is, the wavelength of the light emitted is inferior to 1.5 times the circumference of each primary particle), laser-induced incandescence would become a novel method for measuring nanoparticles emissivity.
In addition, since conduction is not the dominant mechanism, this is an opportunity to investigate soot nanoparticles sublimation and other supposed phenomena (such as annealing, photodesorption, melting, etc) currently under scrutiny in the domain as suggested by Michelsen (2003).

Therefore LII under vacuum has potential to:

- be acquired with less sophisticated equipment than the currently GHz rated signal acquisition systems, conditioning and processing electronics required for standard LII.
- provide much larger signals than "standard" LII in terms of time-integrated photons emission. Therefore LII under vacuum should primarily be interesting on a detection point of view and extend the lowest detectivity limit for the measurements of nanoparticles through LII.
- become a method for determining the refractive index function E(m) defined in equation 10 and 11 and from E(m) the actual emissivity of soot.
- offer the appeal to study laser energy absorption, sublimation, radiation and other eventual phenomena usually quenched by conduction.
- unveil phenomena that have been undetectable until now for particle incandescence times longer than one microsecond.

Overall, this chapter is aimed at defining the basis of laser-induced incandescence under vacuum. The first step is therefore to define the adequate conditions for LII under vacuum to occur, that is the surrounding gas pressure required to operate in a regime where the conduction becomes negligible when compared to radiation.

III.1. Laser-Induced Incandescence and pressure: what are the conditions required for LII under vacuum?

In the following pages, Laser-Induced Incandescence temperature and energy loss rates contributions have been modelled as a function of pressure. Laser- induced incandescence under vacuum can be defined as a form of LII where heat conduction is reduced to negligible by reducing the soot particles surrounding gas pressure and lengthening the associated gas molecules mean free path. Therefore modelling is required to identify the pressure at which "standard" LII, defined in equation 58 ($\frac{dT}{dt} \approx \frac{1}{C_s} \cdot [-Q_{cond} - Q_{sub}]$), is best described by equation 59 ($\frac{dT}{dt} \approx \frac{1}{C_s} \cdot [-Q_{rad} - Q_{sub}]$). A physical translation is a reduction of contribution to the total energy loss rate by conduction. Conduction would eventually become negligible when compared to the contribution of radiation and sublimation when the surrounding gas pressure is lowered. Also, because both sublimation and radiation are not dependent on pressure, the soot temporal temperature profile would remain unchanged even if pressure were lowered further below the maximal acceptable pressure needed to achieve LII under vacuum. In order to represent a wide range of soot particle sizes, three primary particles diameters were modelled: 5, 20 and 100nm. Five nanometres is considered in the LII domain as most certainly the smallest primary particle size than can be defined. Twenty nanometres is a more common primary particle size whereas 100 nm is considered as exceptionally large.

On more technical grounds, the pulsed laser temporal energy profile was modelled as a Gaussian with a full-width at half maximum of 7.5 ns and an excitation wavelength of 532 nm. The expected range of temperature that is considered is from 2000 up to 4000 Kelvin, corresponding to a calculated peak emission wavelength between respectively 1200 and 600 nm. The refractive index function E(m) is approximated as constant (0.4) over this wavelength range and particles were assumed spherical in shape and obeying the Rayleigh criterion. The value 0.4 for E(m) is adopted here

since recent findings by Snelling et al. (2004) measured values of 0.395 and 0.42 in flames during laser absorption at 1064nm. Also, measurements performed on carbon black agglomerates at 532nm concluded to E(m) = 0.415. The surrounding gas temperature was set at 300 K and the surrounding gas pressure was successively lowered, from 10^3 mbar to 10^{-4} mbar. The energy loss rates contributions are illustrated in figure 29 for the more common 20 nm diameter primary soot particle. The laser excitation fluence used to trigger LII was 0.1 J/cm^2. The choice of a medium fluence here is made in order to raise the soot peak temperature toward 4000K and initiate significant sublimation at the beginning of LII. Figure 29 shows clearly two regimes separated by a transition zone:

- from 10^3 to 10^0 mbar, sublimation is the initial dominant heat transfer followed by conduction
- from 10^0 to 10^{-1} mbar, sublimation remains the initial dominant heat transfer; however the dominance of the conductive heat transfer that follows the sublimation cooling is taken over by the radiative heat transfer contribution.
- from 10^{-1} mbar and below, conduction is negligible and a one microsecond sublimation phase is followed by a radiative-only phase lasting more than 100 microseconds.

One could also note that for a 20 nm particle below 10^{-1}mbar, the surrounding gas pressure does not influence the heat loss rate equilibrium. Therefore lowering the surrounding gas pressure below 10^{-1}mbar would not affect the LII physics at these pressures. Figure 30 details the temperature histories versus pressure associated with the heat loss rate relationships depicted in figure 29. Three primary particle diameters are modelled: 5, 20 and 100 nm. Overall, a similar situation can be observed: LII temperature decays gradually lengthen with decreasing pressures from 10^3 mbar to between 10^1 and 10^{-1} mbar. A transition zone is also remarkable for all particles. However, LII temperature decays become independent of the surrounding gas pressures and remain unchanged below the following pressures: 10^{-2} mbar for the 5 nm diameter particle, 10^{-1} mbar for the 20 nm particle and 3.10^{-1} mbar for the 100 nm diameter. Because 5 nm diameter soot primary particles are the smallest particles that can be encountered for LII and presents the lowest pressure for the onset of LII under vacuum, LII under vacuum can be estimated to occur at or below 10^{-2} mbar.

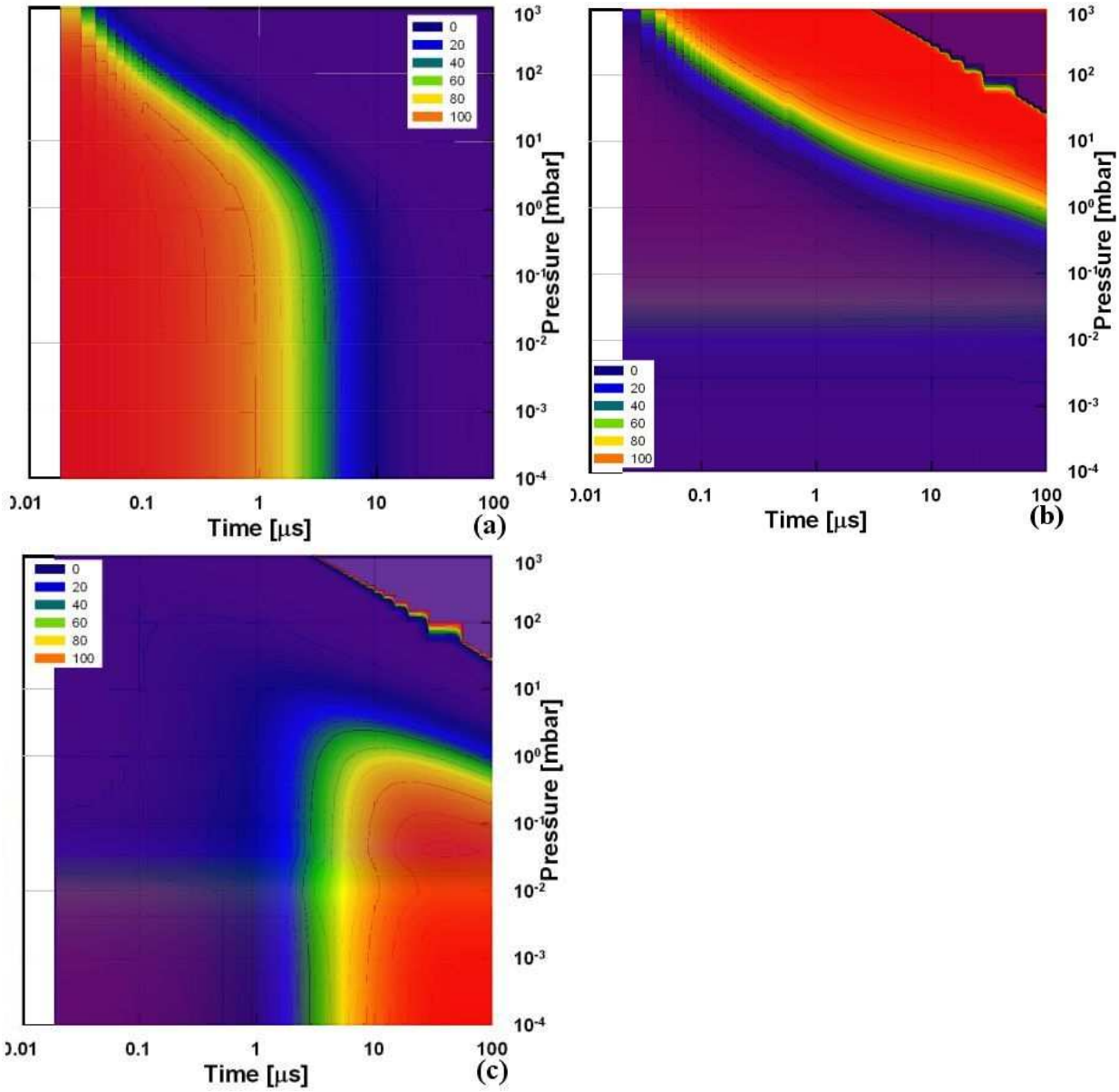

Figure 29: heat loss rates contributions in % for a 20nm diameter primary soot particle during laser-induced incandescence for an excitation laser fluence of 0.1 J/cm^2 according to time and surrounding gas pressure:
(a) Sublimation heat loss rate contribution
(b) Conduction heat loss rate contribution
(c) Radiation heat loss rate contribution
The corresponding LII temperature profiles can be found in figure 30(b). One could note that irregularities are generated during computations when particles reach gas temperature (300K) and are not to be considered. Indeed conduction stops and radiative heat transfer become predominant at the gas temperature;

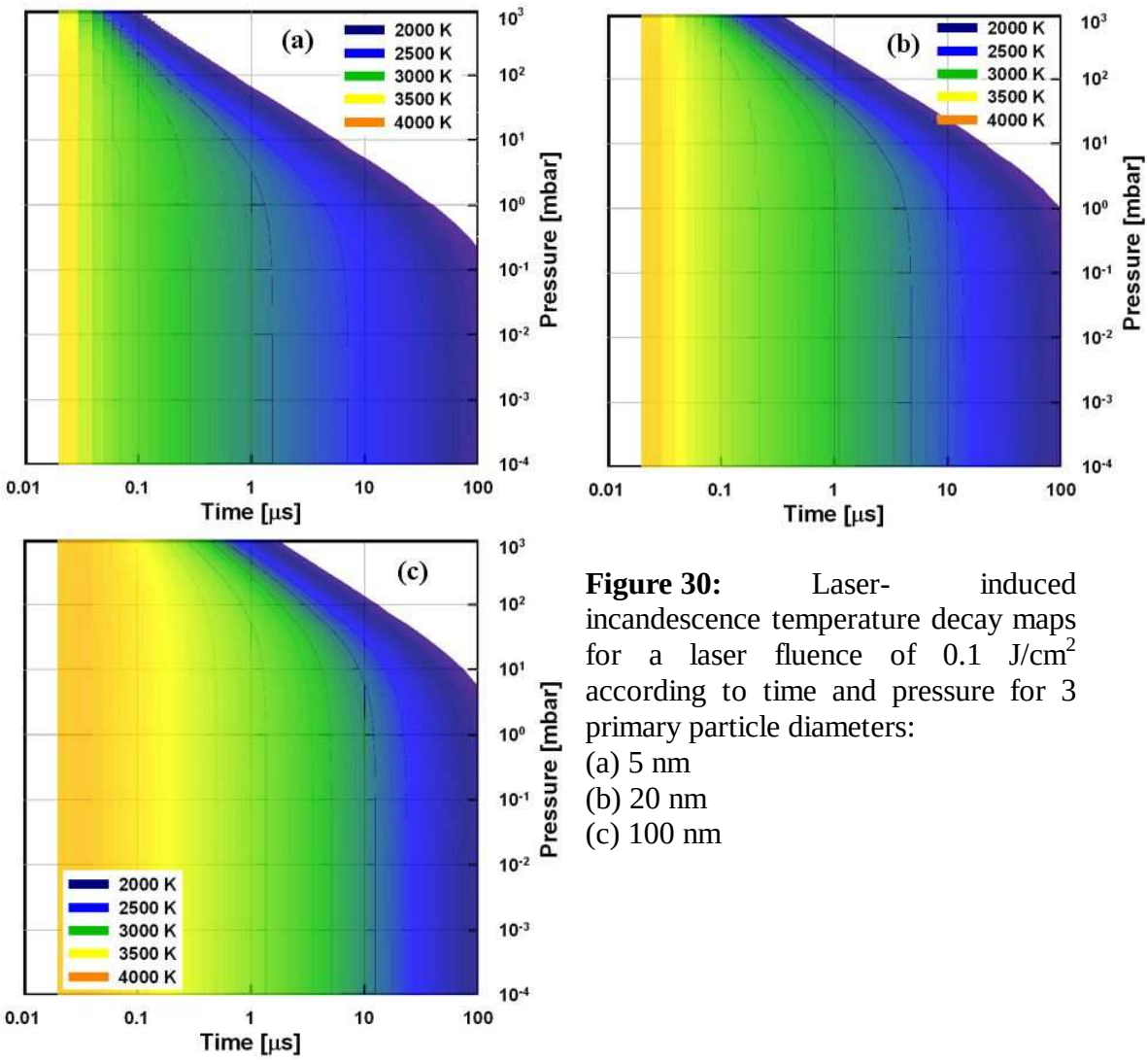

Figure 30: Laser- induced incandescence temperature decay maps for a laser fluence of 0.1 J/cm^2 according to time and pressure for 3 primary particle diameters:
(a) 5 nm
(b) 20 nm
(c) 100 nm

As a summary, the conductive heat transfer becomes negligible between 0.3 and 10^{-2} mbar, and this limit depends only on the soot primary particle: the smaller the primary particle, the lower the pressure at which conduction becomes. Overall, a pressure of 10^{-2}mbar can be used to define the onset of laser-induced incandescence. The classical model for LII includes a temperature decay analysis based on conduction, from which the primary particle size can be estimated. Also, a few subtleties occur for LII under vacuum and these are developed in the following subsection.

III. 2. Modelling Laser-Induced Incandescence Under Vacuum.

The model for LII under vacuum presented in this section is based on the general LII model described in chapter II, with some interesting simplifications applied to it. In addition, assumptions are made. On one hand, the primary assumption in the following section is that soot particles are considered to be spherical in shape, whether they are primary soot particles, aggregates (hard fused primary particles) or agglomerates (loosely bound aggregates) (Seinfeld and Pandis, 1998). Even though the assumption of spherical particles is crude and for many aggregates a fractal model (Filippov et al., 2000; Balthasar and Frenklach, 2005) would be better but is beyond the scope of this thesis. On the other hand, heat conduction losses are considered in the Knudsen (or continuum) regime, where the gas mean free path is of equivalent

dimension or greater than the diameter of a spherical particle. This is a logical consequence of extended mean free paths associated with low pressures and vacuum conditions. Now that the main two assumptions on which the model relies are precised, a more detailed insight into radiative temperature decays follows.

III.2.1.Radiative temperature decay and determination of E(m).

During heat-up by the laser beam, carbon nanoparticles reach temperatures above 2500K, which is the onset for sublimation. Therefore the first temperature decay is expected to be dominated by sublimative heat losses, followed by a radiative-only temperature cooling decay. From section II.2, the radiative heat loss rate Q_{abs} can be expressed as:

$$Q_{rad}=\frac{199\pi^3 d_p^3\cdot(kT)^5\cdot E(m)}{h\cdot(hc)^3} \qquad \textbf{(60)}$$

for a particle satisfying the Rayleigh criterion. This expression results from the integration of the Planck function for a particle emitting with a constant E(m) (Michelsen, 2003).

In the eventuality of a radiative-only temperature decay, the energy balance equation becomes:

$$Q_{internal}\approx Q_{radiation} \qquad \textbf{(61)}$$

this develops into, using equation 60:

$$\frac{4}{3}\cdot\pi a^3\cdot\rho_s\cdot c_s\cdot\frac{dT}{dt}=\frac{199\pi^3\cdot\left(8a^3\right)\cdot(k\cdot T)^5\cdot E(m)}{h\cdot(h\cdot c)^3} \qquad \textbf{(62)}$$

$$\frac{dT}{dt}=\frac{199\cdot\pi^3\cdot\left(8a^3\right)\cdot(k\cdot T)^5\cdot E(m)}{h\cdot(h\cdot c)^3}\cdot\frac{1}{\frac{4}{3}\cdot\pi a^3\cdot\rho_s\cdot c_s} \qquad \textbf{(63)}$$

$$\frac{dT}{dt}=\frac{1194\cdot\pi^2\cdot k^5\cdot T^5}{h^4\cdot c^3\cdot\rho_s\cdot c_s}\cdot E(m) \qquad \textbf{(64)}$$

Hence we now have a situation were the soot primary particle temperature gradient is independent of particle size. Temperature losses occur on a much longer time scale than is normal for an atmospheric bath gas (typically 200ns to 1 µsec) and will likely lie in the range of 50 µsec or longer. Indeed rearranging equation 64 suggests that it should be possible to estimate E(m) directly:

$$E(m)\approx\frac{h^4\cdot c^3}{1194\cdot\pi^2\cdot k^5}\cdot\frac{\rho_s(T)\cdot c_s(T)}{T^5}\cdot\frac{dT}{dt} \qquad \textbf{(65)}$$

Thus by measuring the particles temperature T decay with time t we can determine dT/dt while approximating the density and specific heat capacity of soot ρ_s and c_s to the graphite ones. This is expected to yield an uncertainty lying within the 5-10% range (Fried & Howard, 2000). Hence a direct determination of E(m) becomes

foreseeable. Also, the density and specific heat capacity of graphite in the temperature range of interest – that is, 2000 to circa 2600-2800K - are slowly varying functions of the particle temperature T. However equations 64 and 65 need solving for a further analysis. The constant part can be simplified using an equivalent constant C_{Em}:

$$C_{Em}=\frac{h^4 \cdot c^3}{1194 \cdot \pi^2 \cdot k^5} \quad \textbf{(66)}$$

For simplification, both density and specific heat capacity are assumed constant over the temperature range 2000-2800 K. Equation 65 then develops into:

$$E(m)=C_{Em} \cdot \frac{\rho_s \cdot c_s}{T^5} \cdot \frac{dT}{dt} = C_{Em} \cdot \rho_s \cdot c_s \cdot \frac{1}{T^5} \cdot \frac{dT}{dt} \quad \textbf{(67)}$$

We are now simply left with a first order ordinary equation. The separation of variables results into:

$$dt=\frac{C_{Em} \cdot \rho_s \cdot c_s}{E(m)} \cdot \frac{dT}{T^5} \quad \textbf{(68)}$$

Integration of each side of the equality leads to:

$$\int_0^t dt = \frac{C_{Em} \cdot \rho_s \cdot c_s}{E(m)} \cdot \int_{T_0}^{T} \frac{dT}{T^5} \quad \textbf{(69)}$$

which solves as:

$$t=-\frac{C_{Em} \cdot \rho_s \cdot c_s}{4 \cdot E(m)} \cdot \left(T_0^{-4} - T^{-4} \right) \quad \textbf{(70)}$$

with t = 0 the time at the start of the radiative decay, that is the chosen time were a radiative-only temperature decay starts at a corresponding temperature T_0. The expression can be rearranged to express the temperature history as a function of the starting temperature T_0 and time t:

$$T=\left[T_0^{-4} + \frac{4 \cdot E(m)}{C_{Em} \cdot \rho_s \cdot c_s} \cdot t \right]^{-1/4} \quad \textbf{(71)}$$

and the actual E(m) value can be obtained during measurements from a fit to the equation:

$$E(m)=-\frac{C_{Em} \cdot \rho_s \cdot c_s}{4 \cdot t} \cdot \left(T_0^{-4} - T^{-4} \right) \quad \textbf{(72)}$$

Therefore we have an expression where E(m) depends on: the density and specific heat capacity of graphite, and the initial and actual temperature measured. One would note that equations 71 and 72 do not include any mention of particle size (diameter). This is because the particle radius a cancels out in equation 63. The direct consequence of this is that the radiative temperature decay of particles suspended in vacuum is not size dependent and depends only on the measurement of the soot

temperatures T and T_0, the density and specific heat capacity of soot and the refractive index function of soot, E(m). The uncertainty $\mu_{E(m)}$ on an E(m) determination can be expressed as (NIST, 2004) :

$$\mu_{E(m)}=\sqrt{\left(\frac{dE(m)}{d\rho_s}\right)^2\cdot\mu\rho_s^{\,2}+\left(\frac{dE(m)}{dc_s}\right)^2\cdot\mu c_s^{\,2}+\left(\frac{dE(m)}{dt}\right)^2\cdot\mu t^2+\left(\frac{dE(m)}{dT_0}\right)^2\cdot\mu T_0^{\,2}+\left(\frac{dE(m)}{dT}\right)^2\cdot\mu T^2} \quad \textbf{(73)}$$

The time resolution and subpicosecond jitter of the oscilloscope used to take the temperature measurements are usually of the order of tenths of nanoseconds for a measurement taken over longer than 50 microseconds. Therefore the error on the time measurement will be neglected here. The uncertainty expression then develops into:

$$\mu E(m)=\sqrt{\left[-\frac{C_{Em}\cdot c_s}{4\cdot t}\cdot\left(T_0^{-4}-T^{-4}\right)\right]^2\cdot\mu\rho_s^{\,2}+\left[-\frac{C_{Em}\cdot\rho_s}{4\cdot t}\cdot\left(T_0^{-4}-T^{-4}\right)\right]^2\cdot\mu c_s^{\,2}+\left[\frac{C_{Em}\cdot\rho_s\cdot c_s}{t}\cdot T_0^{-5}\right]^2\cdot\mu T_0^{\,2}+\left[-\frac{C_{Em}\cdot\rho_s\cdot c_s}{t}\cdot T^{-5}\right]^2\cdot\mu T^2} \quad \textbf{(74)}$$

Taking into account that the relative uncertainty value of 5% (Fried & Howard, 2000) is accepted for the expression of density and heat capacity of soot and assuming a constant temperature uncertainty μ_T over the temperature measurement range. The two limits generally accepted in the domain for E(m), which are 0.4 and 0.2 are being studied and the corresponding uncertainty for E(m) determination calculated. Results are displayed on figure 31. A first observation is that the uncertainty on density and heat capacity sum up to less than 4 to 5% of the total uncertainty on E(m) when dealing with high temperature measurements, whether these are resolved at 50 K or an ideal 10 K. Overall, a difference of a factor 2 for the value of E(m) represents a difference of 208 K over 60 µs for a start temperature of 2800K, with final temperatures of 2231 and 2439 K for E(m) = 0.4 and 0.2 respectively.

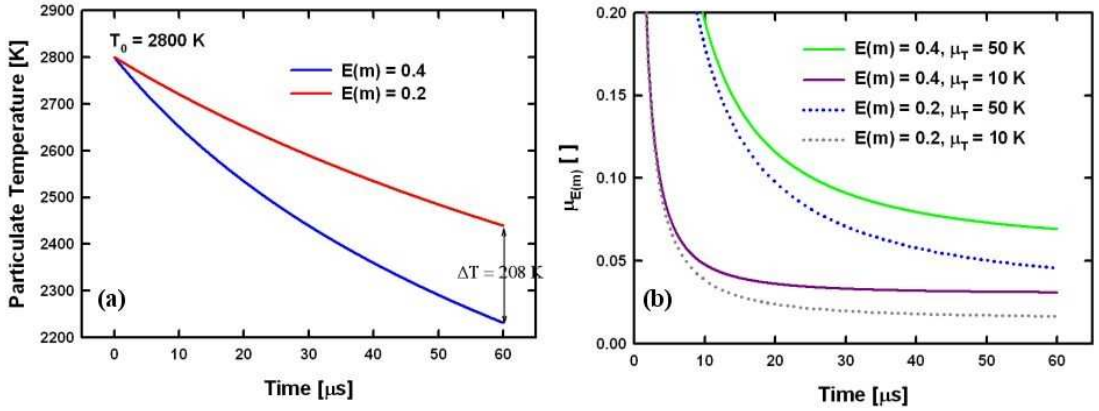

Figure 31: Radiative temperature decays (a) for an initial temperature of 2800K and corresponding uncertainties when attempting to measure E(m) with temperature uncertainties of 50K and 10K (b).

As figure 31 b illustrates, the estimated lowest errors on the E(m) measurement scale between 7 and 10% for a temperature measurement uncertainty of 10K. E(m) uncertainties are much larger for a temperature measurement uncertainty of 50K and can reach up to 17% for E(m) = 0.4 and a temperature curve measured over 60 microseconds.

As a summary, the requested conditions for performing an E(m) measurement when using Laser-Induced Incandescence under vacuum are:

- performing the measurement with the lowest temperature uncertainty possible
- using the longest recording possible of LII signals under vacuum.

Typically, 10 Kelvin is probably the lowest resolution achievable for the dual wavelength pyrometry. Effectively, for a range of temperatures varying from 2000 to 4000 Kelvin, 10K represents a resolution of $1/200^{th}$, and this is technically extremely difficult to achieve for the typical dual wavelength pyrometric system used for LII. A more realistic estimate of temperature accuracy would typically be between 10 and 50 Kelvin. The other consequence of being in the situation where $Q_{internal} \approx Q_{radiation}$ (equation 61) is that the soot radiative temperature decay is size independent. However, another implementation of laser-induced incandescence does provide with temperature depending provisionally only on the emissivity of soot. Indeed, if the sublimation temperature is not reached during laser absorption, the first nanoseconds of laser absorption and the peak temperature of the laser-induced incandescence achieved will depend uniquely on the soot complex refractive index function E(m). This principle is used in low fluence laser-induced incandescence, where negligible sublimation (associated with mass loss) is achieved.

III.2.2. Low fluence LII under vacuum

Snelling et al.(2004) suggest that for low laser fluence at atmospheric pressure (i.e. < 0.09 J/cm^2 for 300K surrounding gas temperature) the peak soot temperature for LII should be nearly independent of the soot primary particulate size d_p; it is argued that the peak soot temperature occurs at a time τ_{max} near the end of the of the laser pulse since only then can the heat loss rate (primarily conduction but also in part sublimation) start to dominate over the laser energy absorption rate. For $t < \tau_{max}$, the rate of temperature change for a primary soot particle may be written as:

$$\frac{dT}{dt} \approx \frac{6\pi \cdot E(m) \cdot F_0 \cdot q(t)}{\lambda \cdot \rho_s \cdot c_s} \qquad \textbf{(75)}$$

and integration over time of equation 75 above leads to the following expression for the peak soot temperature T_{max}:

$$T_{max} \approx T_g + \frac{6\pi E(m) F_0}{\lambda \rho_s c_s} \int_0^{\tau_{max}} q(t) dt \qquad \textbf{(76)}$$

For vacuum conditions, since excitation requires approximately 30 % less laser power, the upper fluence limit would be circa 0.06 J/cm^2 for an initial 300K soot temperature and a peak temperature close to 2800 K. If the peak soot temperature exceeds these limits, significant sublimation heat losses would start occurring during and shortly after the laser pulse, leading to particle size dependence. Another aspect to consider is the capability to use the peak temperature data as a measure of E(m) at the excitation laser wavelength using the interpretation of Snelling et al. (2004). Low fluence laser-induced incandescence under vacuum could be defined as a uniquely absorptive and radiative system, with a laser absorption phase followed strictly by a radiative phase. Therefore both laser heat-up and soot temperature decay would provide a measure of E(m) and temperatures would not be size dependent. Even though temperature measurements obtained using low-fluence LII under vacuum cannot be used to infer primary soot particle size, the technique itself does not suffer

from temperature non-uniformities due to particle size distributions and aggregation effects (Liu et al., 2006). Furthermore, the presence of long signals that can be integrated over dozens of microseconds make the LII under vacuum technique attractive for measuring soot volume fractions.

The low fluence LII under vacuum model has been applied to a five nanometres primary soot particle in the same conditions as described for figures 29 and 30, with a laser fluence limited to 0.06 J/cm^2. The results are illustrated in figure 32. A peak temperature of circa 2700 Kelvin is achieved and therefore sublimation is not triggered, as suggested by Snelling et al. (2004). This is followed by a solely radiative temperature decay below 10^{-2} mbar. Therefore size-independent laser-induced incandescence is possible and low fluence LII would provide the following characteristics: temperature uniformity, even when facing a distribution in size of primary particles and aggregation (Snelling et al., 2004; Beyer & Greenhalgh, 2006); absorptive and radiative measurements for E(m); and integrated high signal levels.

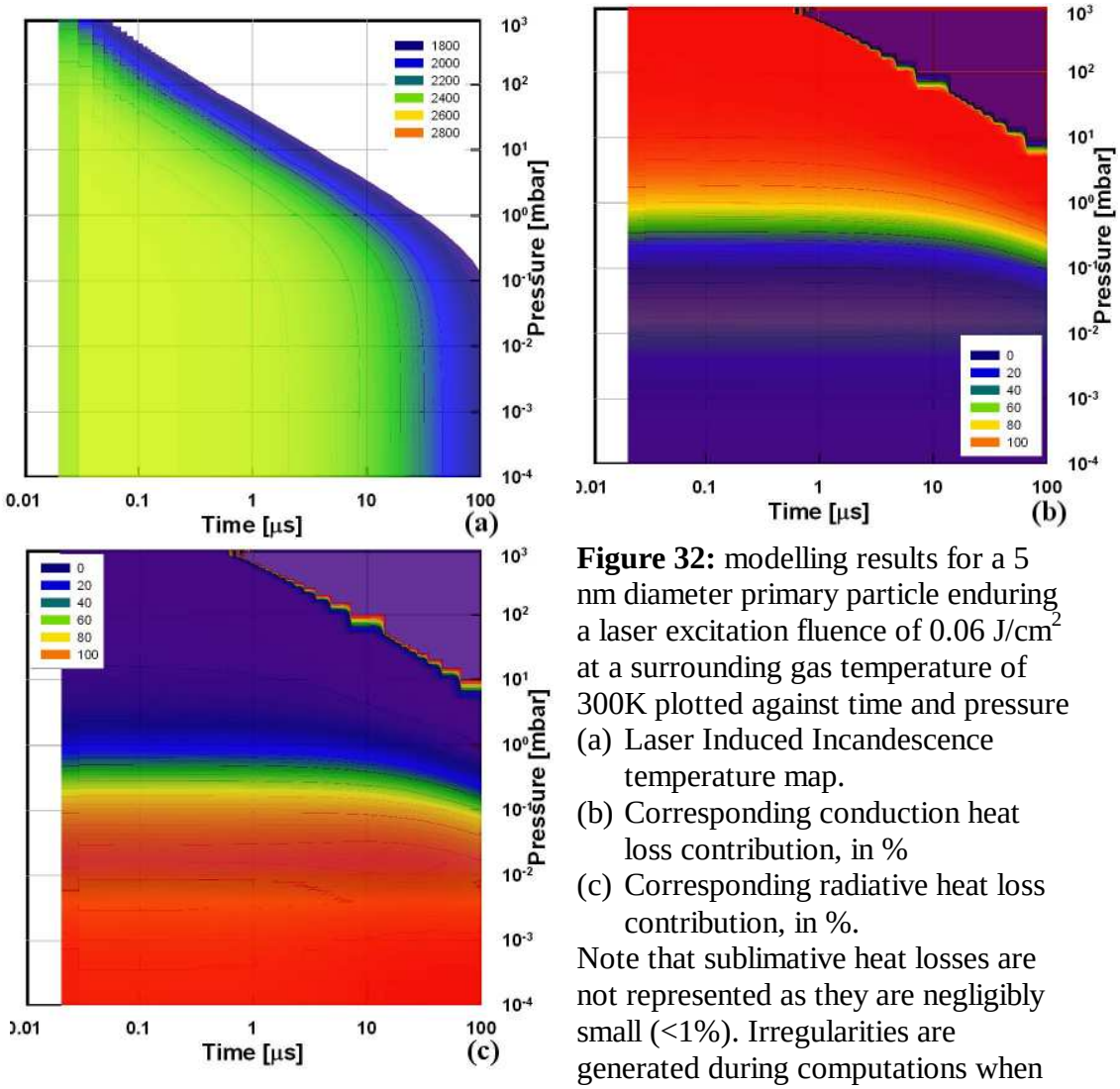

Figure 32: modelling results for a 5 nm diameter primary particle enduring a laser excitation fluence of 0.06 J/cm^2 at a surrounding gas temperature of 300K plotted against time and pressure
(a) Laser Induced Incandescence temperature map.
(b) Corresponding conduction heat loss contribution, in %
(c) Corresponding radiative heat loss contribution, in %.
Note that sublimative heat losses are not represented as they are negligibly small (<1%). Irregularities are generated during computations when the particle cools down to 300K are not to be considered.

Even though the conduction is treated as the principal size dependent heat transfer, sublimation introduces a size dependency for LII under vacuum, and this is will be the focus of the following section.

III.2.3. Sublimation Under Vacuum

For laser fluences exceeding 0.06 J/cm^2 - corresponding to peak particulate temperatures above 2800 K - sublimation should become dominant during the first microseconds for laser – induced incandescence under vacuum. For a sublimative temperature decay, the energy balance equation can be written as:

$$Q_{int} \approx Q_{evap} \qquad \textbf{(77)}$$

Developing each term of equation 77 details the mathematical relationship into equation 78:

$$\frac{\pi \cdot d_p^3 \cdot \rho_s \cdot c_s}{6} \cdot \frac{dT}{dt} \approx -\pi \cdot \Delta H_v \cdot d_p^2 \cdot \frac{\frac{P_v}{R \cdot T}}{\frac{1}{\beta} \cdot \sqrt{\frac{2\pi \cdot M_v}{R \cdot T}}} \qquad \textbf{(78)}$$

And this simplifies as:

$$\frac{dT}{dt} \approx -\frac{6 \cdot \Delta H_v}{d_p \cdot \rho_s \cdot c_s} \cdot \frac{\frac{P_v}{R \cdot T}}{\frac{1}{\beta} \cdot \sqrt{\frac{2\pi \cdot M_v}{R \cdot T}}} \qquad \textbf{(79)}$$

Where P_v represents the vapour pressure of carbon and β the sublimation rate of carbon clusters (C_3 and C_2) from the particle itself (Melton,1984). Therefore sublimation, when dominant, introduces a size dependence during the temperature decay of LII, and this will affect primarily the first microseconds of incandescence. Since the estimated high fluence limit for low fluence LII has been defined in the previous section as 0.06 J/cm^2, the effects of increasing the laser fluence on the energy balance equation is described in figure 33 for a primary particle diameter of 15 nm at a pressure of 10^{-4} mbar. Increasing the laser fluence from 0.06 to 0.07 J/cm^2 results into a non negligible sublimation energy loss rate (2 to3 times lower than the energy loss rate of the particle due to radiation), which then becomes predominant for medium (0.1J/cm^2) and high laser fluences (0.3 J/cm^2) during the first 5 to 6 microseconds of LII under vacuum.

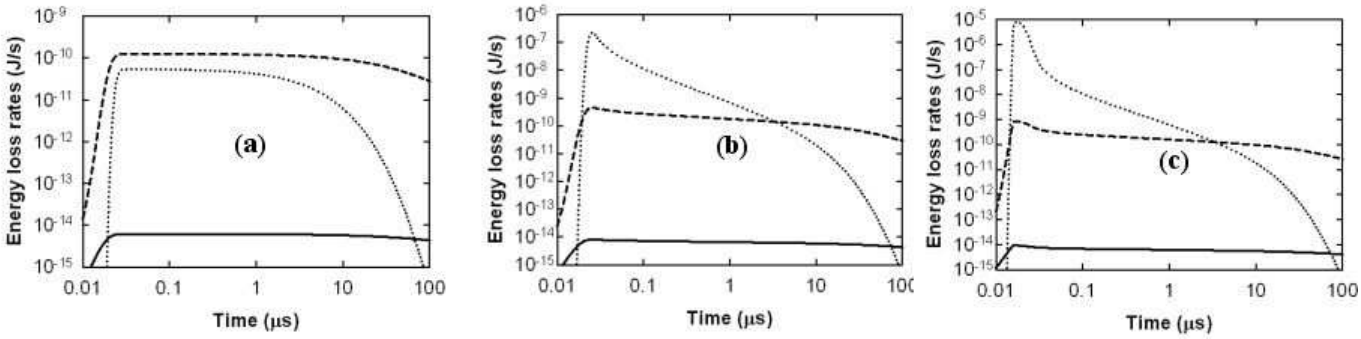

Figure 33: Plots of the energy loss rates during particle cooling, conduction - continuous line, radiation – dashed line, sublimation dotted line. Conditions are 10^{-4} mbar and laser fluences of (a) 0.07 J/cm^2, (b) 0.1 J/cm^2, (c) 0.3 J/cm^2. The particle diameter was 15 nm and the surrounding pressure 10^{-4} mbar.

The effects on sublimation on the particle temperature curve during LII are described on figure 34: expectedly the peak particle temperature increases with laser fluence. Surprisingly, temperature curves versus time become identical for both medium (0.085 J/cm^2 and 0.1 J/cm^2) and high fluences (0.3 J/cm^2) after one microsecond.

Therefore a fluence threshold exists above which the temperature at circa one microsecond remains unchanged whether the laser fluence is increased or not. Then follows a radiative temperature decay for a remaining approximately 100 microseconds. One can note that for a fluence (0.07 J/cm^2) closer to the low fluence limit of 0.06 J/cm^2, the peak LII temperature remains below 2800 K and sublimation does not dominate the cooling phase of the soot particle. However it is interesting that all temperature curves tend asymptotically to the same temperature curve after circa 30 microseconds.

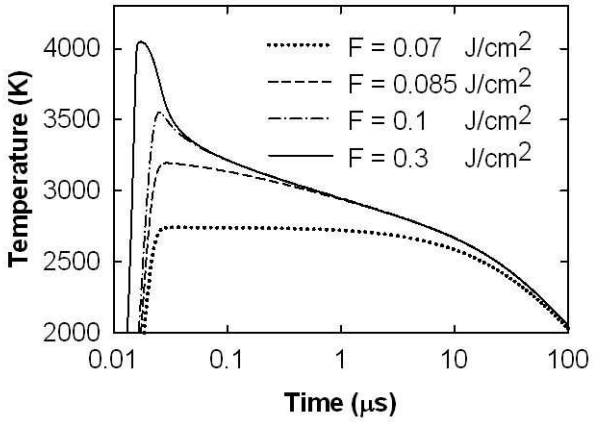

Figure 34: Variation of the temperature with laser fluence for particles of diameter 15 nm for a pressure of 10^{-4} mbar.

Whereas increasing fluence above the 0.06 J/cm^2 results into the same particle temperature history between 2 and 30 microseconds for one single primary particle diameter, increasing the laser fluence does introduce a sensitivity to particle size distribution. Even though the typical lognormal distribution of primary particle size would permit an approximation, the effective temperature curves obtained under vacuum vary accordingly to primary particle diameter. This is illustrated in figure 35:

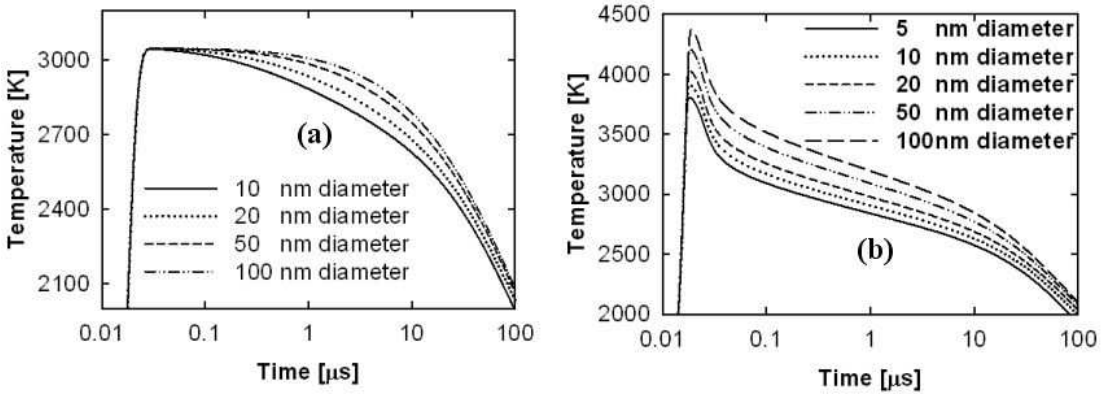

Figure 35: Variation of temperature for a selection of particle sizes for two fluences a) 0.08 J/cm^2, b) 0.2 J/cm^2.

Clearly temperature differences between primary particles of different size are expected. These compromise: the accuracy of the effective temperature measurement and, as a consequence, the eventual E(m) estimation uncertainty. Now that LII under vacuum has been reviewed under all its essential aspects, a comparison between "standard" LII and LII under vacuum can be undertaken in the next section.

III.3. Comparison between "standard" LII signals and LII under vacuum.

On one hand, the "standard" LII technique is based on the measurement of LII signals over less than one microsecond. Traditionally, laser-induced incandescence signal intensities are used to provide both the primary particle temperature and the soot volume fraction measurement. A measurement of the refractive index function E(m) is also possible at low fluence using the peak soot temperature .On the other hand, LII under vacuum provides signals that could potentially last more than 100 microseconds, provide a predictable and size-independent temperature profile at low fluences that can be associated with soot volume fraction measurements. A direct measurement of E(m) is possible both during laser absorption and radiative temperature decay and the associated uncertainty of the measurement ranges between 7 and 10%. Because the theory behind LII under standard conditions and LII under vacuum has in common mainly the laser absorption and sublimation, a theoretical comparison is not necessary. Figure 46 illustrates the difference between atmospheric LII signals and the ones expected under vacuum. Overall, because temperature decays are lengthened under vacuum, incandescence signals will become lengthened toward the 100 microseconds durations instead of less than one microsecond. Another interesting point in that atmospheric LII is particle – size dependent. This size dependency translates into short-lived signals for small particles and longer signals for large particles. This size dependency is counteracted upon during LII under vacuum as both small and large particles are expected to provide long-lived signals. The direct consequence of this is that, when LII signals are integrated in time, as they would when measured by a CCD for example, a practical gain of photon emitted per nanoparticles becomes apparent. This is illustrated in figure 46 c. Therefore smaller particles that would not be detected or hardly measurable under atmospheric conditions become measurable. Overall, this feature of LII under vacuum represents a non negligible gain in detectivity ranging between 30 and 300,for a time-integrating system. Also, a large increase in signal contributions from smaller particles when compared to LII performed at atmospheric pressure.

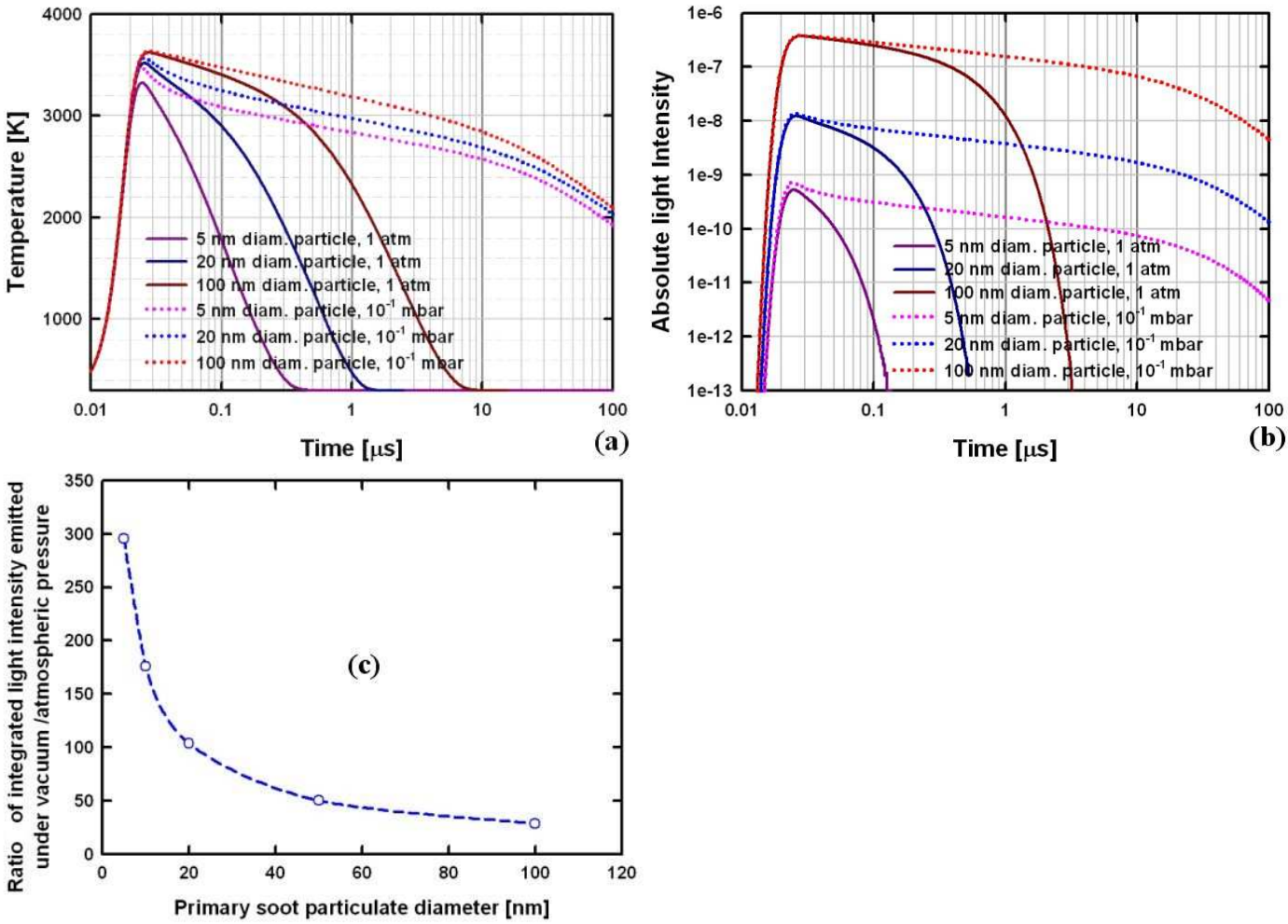

Figure 46: Comparison of laser-induced incandescence at atmospheric pressure and vacuum (10^{-1} mbar) for three particulate diameters (5, 20 and 100 nm) for a laser fluence of 0.1 J/cm^2 and a surrounding gas temperature of 300K:
(a) Temperature curves
(b) Absolute light intensity
(c) Ratio of integrated light intensity vacuum/atmospheric conditions for a few particulate diameters

III.4.Conclusions to Chapter III.

Laser Induced Incandescence under vacuum in itself is a novel LII measurement method. The radiative heat transfer under "standard" conditions was considered mainly as the source of LII signals but a rather negligible physical term compared to sublimation and conduction. Under vacuum the radiative heat transfer becomes the main contributor. Indeed, following laser absorption , the physical relationship inherent to "standard" LII is changed from $\frac{dT}{dt}=\frac{1}{C_s}\cdot\left[-Q_{cond}-Q_{sub}\right]$ (58) into $\frac{dT}{dt}=\frac{1}{C_s}\cdot\left[-Q_{rad}-Q_{sub}\right]$ (59) under vacuum. The consequences are:

(1) long-lived incandescence signals of up to 100 microseconds under vacuum instead of the traditional microsecond.
(2) because the temperature decays will have a direct relation to the radiative properties of the incandescent soot, a measurement of E(m) is possible
(3) an overall gain in signal detectivity for time-integrating photodetectors greater than 100 when compared to atmospheric LII.

Laser-induced incandescence under vacuum is defined as LII obtained at a pressure low enough for the incandescence signals to be pressure independent. A pressure of 10^{-2} mbar was found an acceptable approximation for the conduction heat transfer to become negligible.
On one hand, LII under vacuum can be used to determine the refractive index of soot function, E(m). For a measured radiative temperature decay, E(m) expresses as:

$$E(m)=-\frac{C_{Em}\cdot\rho_s\cdot c_s}{4\cdot t}\cdot\left(T_0^{-4}-T^{-4}\right) \qquad (72)$$

The density ρ_s and specific heat capacity of soot c_s are assumed to within 5% as the ones of graphite, and therefore the temperature measurement accuracy at the start (T_0) and end (T) of the radiative decay is primordial. A temperature measurement uncertainty of 10 Kelvins would result into 7% uncertainty on E(m) while 50 Kelvins would represent 10%.
On the other hand , sublimation can be avoided and low fluence LII under vacuum can be performed. This would mean that the sole physical phenomena involved would consist in laser absorption followed by radiation. Hence LII would become entirely independent of soot primary particle size. This would facilitate soot volume fraction measurements and temperature uniformities during LII.
In parallel, sublimation is triggered for peak LII temperature above 2800K. The consequences of sublimation are:

(1) an initial sublimative temperature decay lasting less than 10 microseconds
(2) size-dependent temperature decays

Overall, LII under vacuum has great potential in terms of detectivity when compared to "standard" LII. Because the primary particle size dependence is reduced to negligible when compared to "standard" LII, high gains in terms of time-integrated numbers of photons emitted are expected, in particular for primary particle diameters below 100nm, with LII under vacuum resulting in the emission of in the order range 100 to 300 times more photons per primary particle over 100 microseconds.
Overall, the conditions required to obtain LII under vacuum have been set and the overall fluence behaviour as well as the expected performances are explained, the experimental systems that were used to investigate practically the technique are described in details through chapter IV.

Chapter IV- Experimental details and methods

This chapter is focused on illustrating and providing detailed information about the measurement systems and techniques used to demonstrate and study Laser-Induced Incandescence under vacuum. The results obtained using the experimental layouts are actually described and discussed throughout chapter V. The requirements for performing LII under vacuum were the following:

(1) Provide a sample of carbon black or soot forming a suspension under vacuum below 10^{-2} mbar. Also, repeatability in terms of sample thermal, physical and morphological properties was of primordial importance in order to permit cross-comparisons between measurements systems and associated results.
(2) Once signals associated with laser-induced incandescence were obtained, a spectral investigation would be performed in order to confirm: the obtention of blackbody radiation (incandescence), signal lifetimes and temperature decays corresponding to the model.
(3) Perform simultaneous two dimensional and time-resolved LII under vacuum measurements at medium and high laser fluences. Implement a novel absolute light intensity calibrated 2D LII technique in order to confirm the sensitivity limits of LII under vacuum for time-integrated measurements.
(4) Perform high accuracy time-resolved LII measurements at both low and medium fluences using NRC instrumentation.

IV.1. Sampling carbon nanoparticles into vacuum

One of the outcomes of chapter III was that 10^{-2} mbar is a prerequisite for measuring LII under vacuum signals and obtain radiative temperature decays. The simplest solution for drawing a soot-loaded sample aerosol into a vacuum is to create a continuous sampling system made of an orifice and backed by a large capacity vacuum pump. This was initially envisaged, and details are given in appendix C. This attempt lead to the conclusion that a simple orifice system could not provide lower than 10 mbar of gas pressure and therefore two options were envisaged:

- a molecular beam sampling system
- a sealed system with a sample held under vacuum

Molecular beam sampling systems present an advantage as the aspirated sample aerosol remains airborne and particles remain physically remote from each other. The molecular beam technique is therefore the subject of the following section.

IV.1.1. Molecular beams

The molecular beam is based on the sampling, either continuous or intermittent, of a gas-loaded aerosol into vacuum, as illustrated by figure 47. Practically, particles nearly reach the speed of sound provided the orifice is small (a few hundreds of microns) and the pressure difference is large (1 to 2.5 atmospheres). This results into rectilinear particle trajectories similar to a beam of particulates:

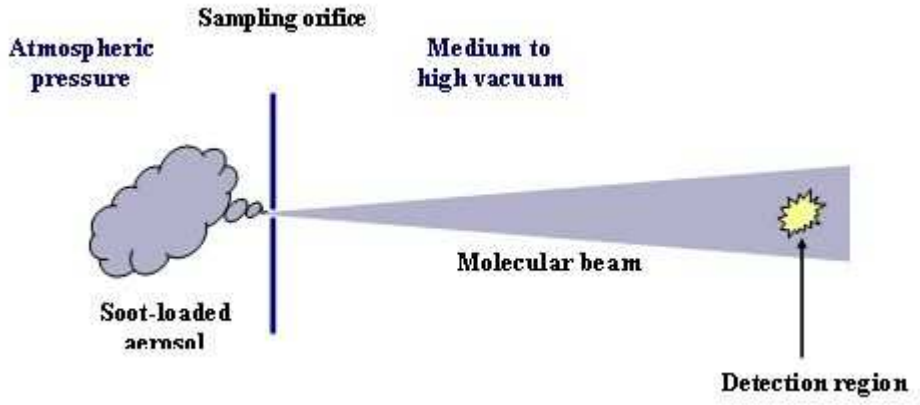

Figure 47: Sampling configuration for a molecular beam. An aerosol containing suspended soot particles is aspirated through a sampling orifice from atmospheric pressure into vacuum. The consequent gas expansion results into a molecular beam inside which measurements will be taken.

On theoretical grounds, a molecular beam is based upon the principle of a free expansion. Kennard (1938) describes the following for the phenomenon: during a free jet expansion, the gas is neither allowed to exchange with its surroundings nor to do any external work; The ideal way to perform such an expansion would be to put the gas into one compartment A of a vessel with a vacuum in an adjoining compartment B, and then suddenly to open in the partition holes so tiny that the molecules of gas could go through only one by one, as depicted in figure 48:

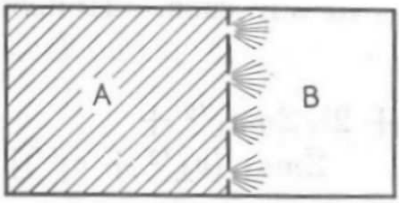

Figure 48: Principle of a free expansion (Kennard, 1938)**.**

This results into the occurrence of a "freezing" of the translational, rotational and vibrational degrees of freedom of the gas molecules (Wegener, 1974). A system free of collisions between the gas molecules in a free (or nearly free) molecular flow is therefore obtained. Hence the system is called a molecular beam. For a flow containing both molecules and particles, the particles can be considered as yielding the same collisionless behaviour as gas molecules provided the surrounding gas has a mean free path much greater than the particle diameter for a spherical particle (i.e. obeys the Knudsen conduction heat transfer regime). This is practically always verified for a nanoparticles laden gas. In more details, a molecular beam presents three zones, by decreasing gas molecule- particle collision rates: the hydrodynamic zone, the transition zone and the free jet zone, as illustrated in figure 49:

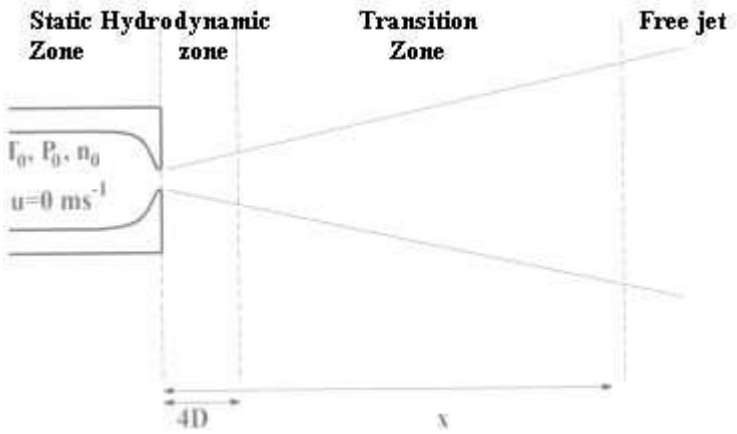

Figure 49: Flow regions in a free jet expansion. D refers to the nozzle diameter, whereas T_0, P_0, n_0 and u refer to the static (gas at rest) characteristics of the expanded gas (Doherty, 2003).

Now that the principle of the molecular beam has been laid out, a few implementations of the principle are to be considered. They differ between each other on the grounds of the pumping capacity required and the transmission efficiency (the ratio of particles passing through the inlet nozzle and of particles present within the measurement volume) desired. The description given here will be limited to only three references that depict best the problem studied, provided by Johnston (2000) and Xuefeng Zhang et al. (2002-1 and 2)**.** The determinant design component that is required to produce a focused aerosol molecular beam is the inlet nozzle(see figure 50). Three families of inlet nozzles are available to date:

- A sharp orifice or capillary left continuously open, with on one side the gas at atmospheric pressure and vacuum on the other side. However this requires high pumping speed (up to 600 litres per second), increasing highly the cost of the pumping system. Such sampling systems have been developed by Creasy et al. (1997-1&2) to avoid quenching due to local gas for laser-induced fluorescence studies of OH and HO2 in the troposphere. One would also note that a sharp orifice focuses only a single particle diameter for a given set of conditions whereas a capillary transmits a broader range of particle diameters.
- A pulsed nozzle can also be used: using a high-speed solenoid valve, the nozzle orifice is left open for a few milliseconds, with a compressed mix of the sampled gas and Helium (having a low heat capacity) held at around 4 bars and a high vacuum (10^{-6} mbar) on the other side. Therefore, the increased pressure drop between the two sides of the system and the quality of the vacuum leads to collisionless times of up to 100 ns (Rohlfing, 1988). The inconvenience here is a very unpractical system that can hardly operate synchronously to a laser (due to high repetition rates) and detection system and eventually prone to clogging when facing high particulate matter concentrations. The obvious advantage is that the pumping capacity is matched with the system's capability and therefore permits the use of lower capacity vacuum pumps.
- An aerodynamic lens system (see figure 50-C) below) focuses a wide range of particles diameters with near unit transmission efficiency while being continuously pumped. Clearly the aerodynamic lens system design is from far the most attractive as it provides additional transmission efficiency and continuity. Therefore the focus will be brought onto this method as the selected sampling technique.

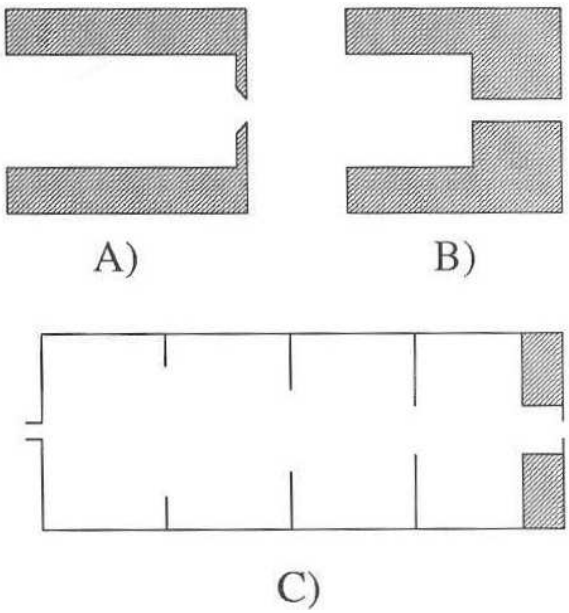

Figure 50 (Johnston, 2000): The three basic types of inlet designs available for molecular beam. (A) is a sharp orifice inlet, (B) is a capillary and (C) is an aerodynamic lens system terminated with a capillary and orifice.

Overall, an aerodynamic lens is made of a series of sharp orifices, placed in decreasing order of diameter. The decrease in diameter size between orifices is aimed at readily " focussing" the gas flow into the final capillary. Each orifice represents effectively a flat plane, as shown on figure 51 below and the particle trajectory change when flowing toward an orifice is proportional to the particle aerodynamic diameter, with a general tendency to reduce the particulate flow diameter.

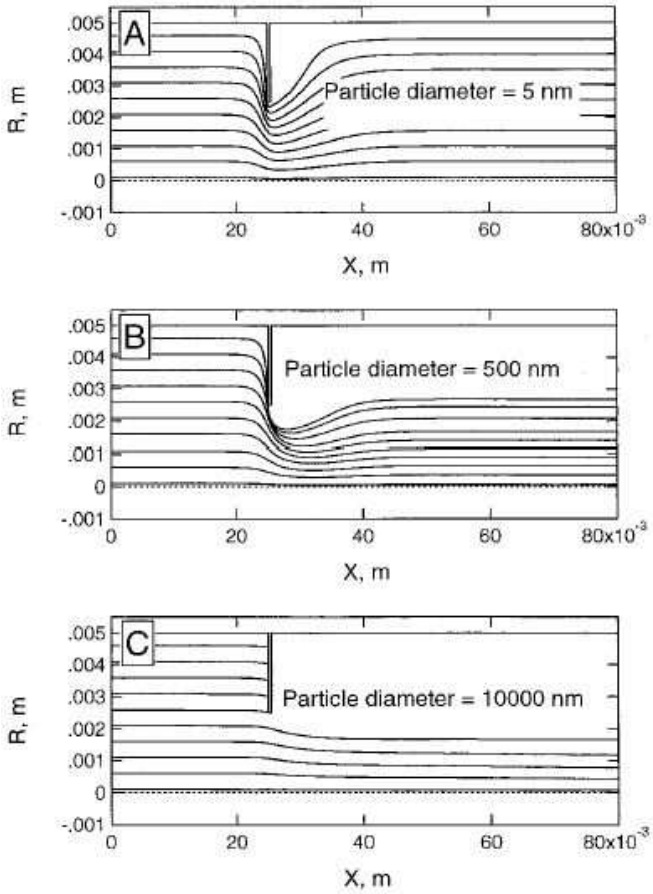

Figure 51 (Xuefeng Zhang et al., 2002-1): particle behaviour in front of one of the lenses inside the aerodynamic lens system. The notation R,m on the left hand side of the graphs is a relative distance from the centre of the cylindrical lens and X,m defines the distance from the start of the lens. Three cases are highlighted:

(A) The first one (5nm particle diameter) shows a particle having a highly divergent behaviour since its inertia is too low for the particle to remain focused by the gas stream.

(B) The second case is an averaged sized particle (500nm) that remains focused.

(C) The third one depicts the situation for a large particle (10µm): the particle inertia is too high to allow it following the gas streamlines and results into impaction of the particle onto the wall of the aerodynamic lens.

When assembled into a series of sharp orifice plates terminated by a capillary and a final orifice, the system behaves similarly to an optical lens, focussing a beam of particles of various diameters into a set measurement volume located usually between 10 and 40 cm further downstream as illustrated in figure 52. Currently aerodynamic lenses designs are available through the literature with transmission efficiencies approaching one for the particle size range 60nm to 6µm.

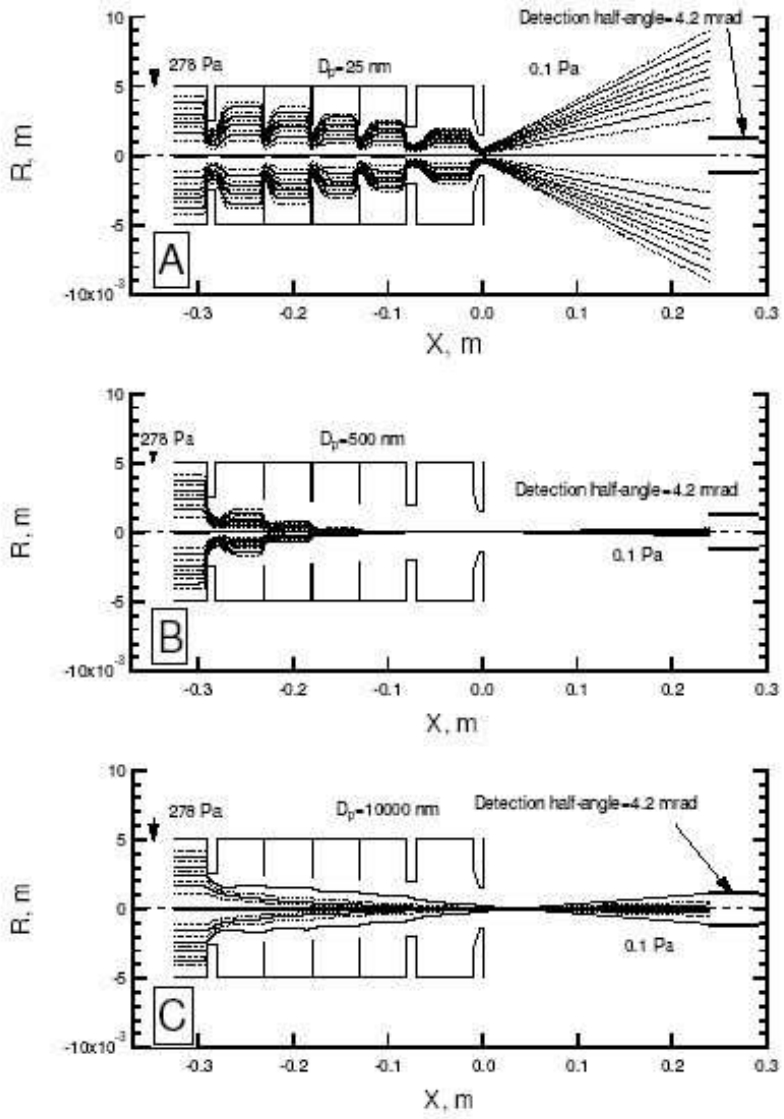

Figure 52 (Xuefeng Zhang et al., 2002-1): full aerodynamic lens apparatus modelled under working conditions for different particle sizes:
(A) 25 nm diameter particles
(B) 500 nm diameter particles
(C) 10 μm diameter particles
The notation R,m on the left hand side of the graphs is a relative distance from the centre of the cylindrical lens and X,m defines the distance from the start of the lens.

Overall, the aerodynamic lens system is a recent invention by Jimenez et al. (University of Boulder, Colorado). It is a means to literally focus a flow of particles from a sampling line into a measurement volume held under high vacuum with the highest efficiency and particle diameter acceptance available. The technology has proven its sturdiness in conditions such as measurements in altitude and urban vehicle particulate emissions characterization, and as it is being widely adopted throughout the particle analysis domain an increasing number of computations and adaptations can be found in the literature. However the engineering complexity and time required to design and assemble such a system was far beyond the subject, objectives and

budget of the present thesis. Therefore a simpler option had to be chosen. The second option that can be envisaged to obtain LII signals under vacuum is to actually seal a sample of soot inside a vessel held under vacuum. This option was ultimately chosen for its relative engineering simplicity and cost effectiveness.

IV.1.2. A sealed sample of soot under vacuum

The principle of a sealed vessel containing a sample of "dry" carbon black powder was adopted. Carbon black is obtained from the combustion of rich flames inside industrial boilers. Despite the use of carbon black as an ink for printers and a compounds, the material itself is a settled form of soot. Obviously, because an aerosol beam is not involved and LII has to be performed on suspended particles, agitation of the carbon black powder was necessary in order to obtain measurable quantities of "free falling" carbon black particles. The principle of a roller bottle on a roller system was adopted: using a 120 mm diameter cylindrical flask filled with approximately 2 g of carbon black powder disposed horizontally on a roller and rotating at a minimum of 30 turns per minute, the wall friction and rotational velocity combine to lift the carbon towards the top part of the cylindrical radius before cascading under gravity to the bottom. Therefore a controlled flow of descending carbon black particles in free space could be maintained, while side optical access through the cylindrical bottle walls can be used for detection. Both the front and bottom of the bottle were fitted with optical windows to permit laser excitation. Both elements (roller bottle and roller apparatus) are depicted in figure 53 below:

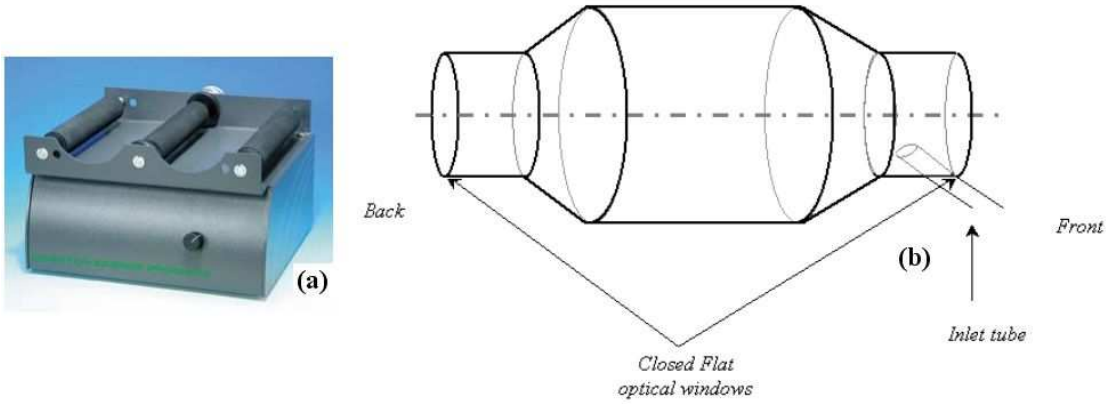

Figure 53: Evacuated roller bottle system
(a) Wheaton bench top roller bottle apparatus (Fisher,2004)
(b) Roller bottle schematic. The roller bottle is primarily a 120 mm diameter glass bottle adapted for side optical access and carbon black powder sample insertion inlet tube.

The roller bottle is a 240 mm long cylinder with a central 120mm diameter designed to accept a small sample of carbon black powder (typically 2 grams) through its inlet tube. The inlet tube comprises a reduction in its middle and a Quickfit™ 10/19 conical female joint on its extremity for attachment to the vacuum pumping system. The middle reduction is designed to be melted using either an oxy-acetylene or a forced air-propane torch when the vessel reaches adequate pressure, therefore flame-sealing the sample to be tested. Two 50 mm diameter BK7 windows were fitted on the side to accept a laser beam passing through. The roller bottle had first been modelled using IDEAS™ to make sure the inlet tube fits on the roller bottle apparatus without touching the side and then hand drawn (an electronic copy of the drawings is available

in appendix D). Five sample bottles were manufactured at Mike Caplin's Southampton University Scientific Glassblowing facility.

The principle of the vacuum system is laid on the schematic in figure 54. The pumping group is a Varian T-series turbo pumping cart, featuring a SH100 dry scroll pump backing a navigator V301 turbo pump. Its nominal pumping speed varies according to the system pressure, between 40 and 550 l/sec. The vacuum pumping system was designed to be plugged into the roller bottle quickfit adaptor and therefore the insertion of a bottle would close the system. In practice, all tubings and the roller bottle were baked circa 380K using heating tapes, and the final quickfit glass joint between the roller bottle and the quickfit glass adapter was vacuum-greased and cooled to a constant 300K using a wet cloth system, that is a piece of cloth covering the joint with its two end dipped in a glass container of cold water. Also, while evacuating the roller bottle, the system would be left running for approximately 12 to 15 hours to achieve a satisfactory pressure between 1 to 2×10^{-4} mbar. The pumping time is justified by the amount of moisture present within the black carbon powder. Once a satisfactory pressure was achieved, flame sealing was performed and three satisfactory roller bottles samples were selected for measurements. Pictures of the pumping system and of one of the sealed roller bottle are available in figure 55. The described operations lead to obtaining sample roller bottles each containing circa 2g of carbon black powder, which once dried and vacuum sealed, appeared to contain soot agglomerates, most of which were of a size visible to the naked eye but much less than a millimetre. Obviously a great number of smaller particles were also present. Therefore the practical experimental conditions achieved are similar to the irradiation of carbon black (which is a form of soot) or diesel soot from heavy duty engines under vacuum at circa 10^{-4} mbar. Both of these are composed of largely agglomerated soot particles. However, this does not change the nature of the substrate itself, as the thermophysical behaviour of ensembles of agglomerated nanoparticles can be approximated as the thermophysical behaviour of the constituent nanoparticles.

As a summary, the roller bottle method provides agglomerated soot particles that satisfy the prerequisites for LII under vacuum: a suspension of soot particles held at pressure below 10^{-2} mbar. The following step is to obtain laser-induced incandescence under vacuum signals and prove that the signals obtained: (1) are spectra continuums characteristics of blackbody radiation (2) consistent with at least a 50 microsecond long temperature decay that can be associated with an e(m) value comprised between 0.2 and 0.4. The following section is therefore centred on a spectrograph system designed and calibrated to measure LII under vacuum spectra.

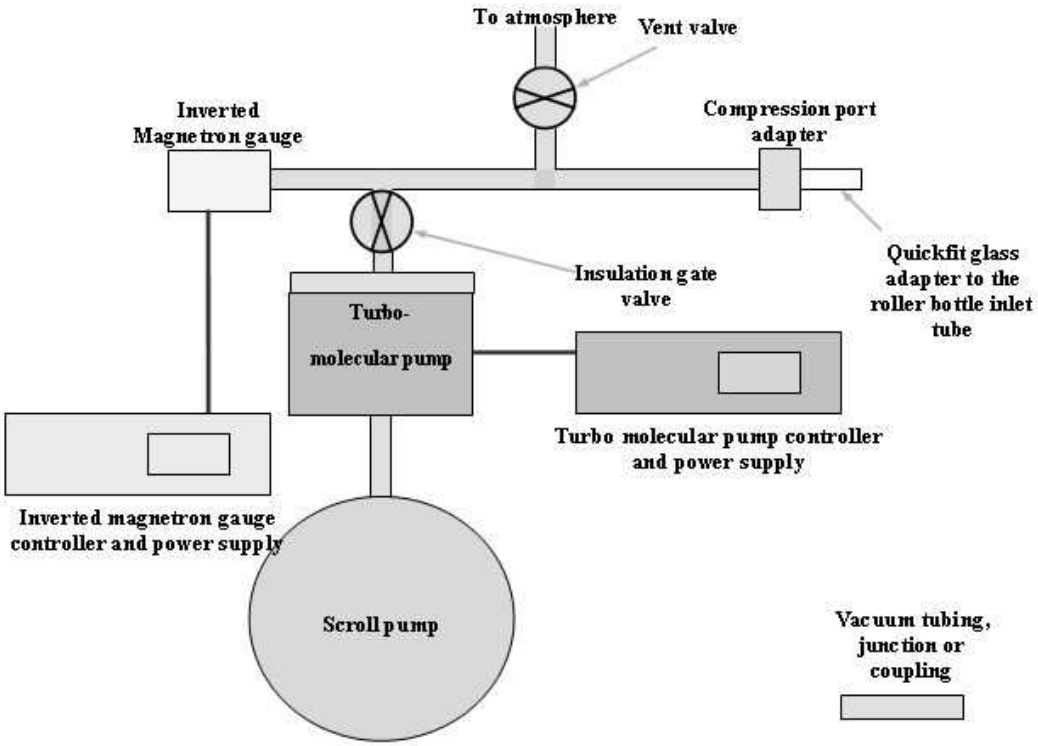

Figure 54: Initial vacuum system schematic. A large intake valve was later added between the insulation gate valve and the turbo-molecular pump to avoid damaging the pump by forming a restriction when starting to evacuate the roller bottle.

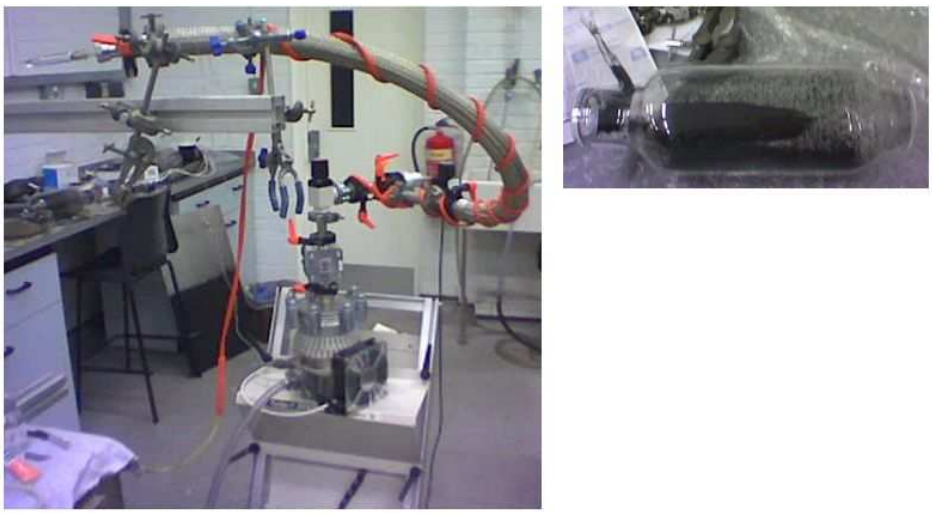

Figure 55: Vacuum pumping system picture (left) and flame-sealed roller bottle containing a sample under vacuum (above).

IV.2. Details of the spectrographic system used to validate the presence of LII under vacuum

In order to validate the feasibility of laser-induced incandescence under vacuum, the very nature of the signal had to be investigated. To attest the presence of LII under vacuum, two criteria are to be complied with : (1) blackbody spectra typical of incandescence have to be present; (2) the corresponding soot temperature recorded have to match the long-lived (50 microseconds and more) radiative temperature decay described in chapter III and yield a measurement of E(m) comprised between 0.2 and 0.4. In order to assert these two criteria, a spectrographic LII measurement system was assembled. The experimental layout is illustrated by figure 56:

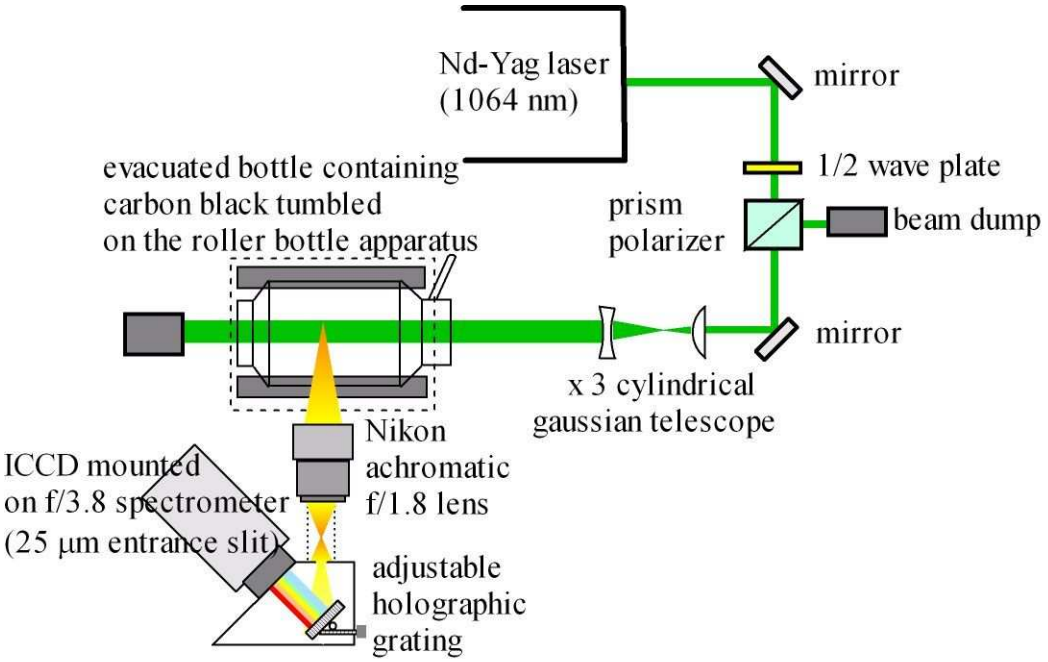

Figure 56: Spectrographic LII measurement system (excluding HeNe alignment lasers)

The laser beam is provided by a pulsed Nd-YAG Quanta Ray CGR 12 S laser emitting at 1064 nm. The laser is operated at its fundamental wavelength both in order to guarantee that the Rayleigh criterion applies here and because the frequency doubling option was not available on this particular laser. The overall laser output power was 910 mJ / pulse at 90 % of the maximal flash lamp energy setting at an optimal Q-switch delay measured of 135.8 µs. The laser fluence delivered to the measurement volume within the roller bottle is controlled by the association of a ½ wave plate and a prism polarizer: the laser beam polarization is controlled by the ½ wave plate; when the laser enters the prism polarizer, the vertical polarization is transmitted and the horizontal polarization is reflected at 45 degrees into the beam dump. This way the ½ wave plate controls the amount of vertically polarized laser light entering the prism and therefore the amount of power transmitted through the prism. This method is typically used so that the flash lamp power of the laser does not need to be varied. Eventually a greater reproducibility of the laser beam spatial profile is guaranteed this way. The cylindrical Gaussian telescope expands the laser beam by a factor 3 in the vertical direction and perpendicularly to the measurement axis of the spectrographic detector. The beam shaping optics are inserted to greatly

increase the uniformity of the laser spatial fluence profile over the measurement volume and therefore increase temperature uniformity between irradiated particles. Even though using a cylindrical Gaussian telescope does not provide as uniform spatial fluence as the relay imaging of a slit, acceptable temperature uniformities can be expected to be obtained.

The spectrographic system is made of an American Holographic f3/8 spectrometer assembled on the front of a Roper Scientific Intensified CCD (ICCD) camera. An achromatic Nikon f/1.8 camera lens is used to image a 2mm by 25 microns laser-irradiated region within the rolling bottle. The signals obtained are imaged with a magnification factor of 1:1 onto the spectrometer 25 microns entrance slit. Therefore the effective measurement section projected onto the intensifier and through the spectrometer onto the intensifier is a rectangular area of 2mm by 25 µm. The depth of field of this system is not know as it would have been difficult to measure ,but spectrometric systems do behave as very sharply focused with depths of field generally comprised around and below 1mm. The spectral resolution of the spectrographic system is roughly estimated at first as ranging between 0.3 to 0.6 nm per CCD pixel. The gating method of the Intensifier is particular to the ultra low signals levels (estimated below 3ppm, that is less than 10^{-10} W.µs.nm/m^{3}sr) associated with a small measurement volume (< 0.075 mm^3). More details of the ICCD gating is given in figure 57:

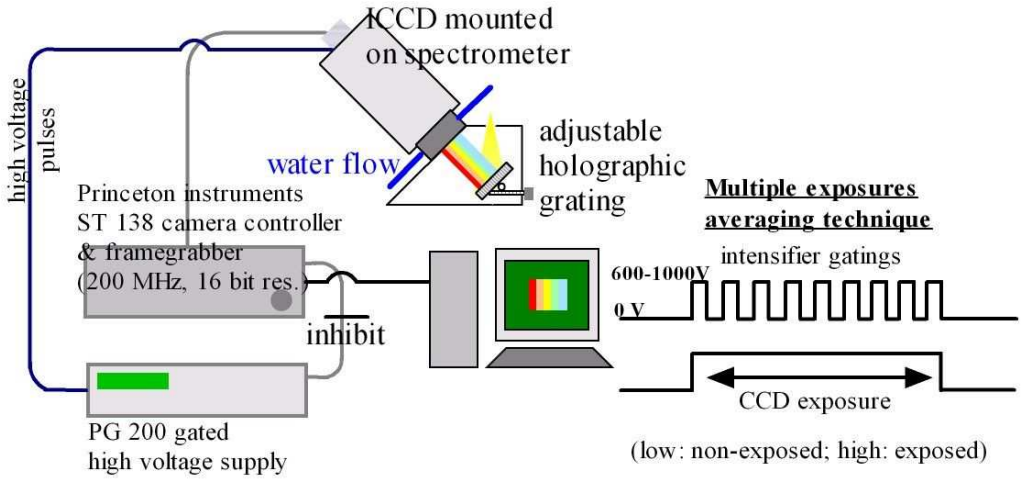

Figure 57: Details of the ICCD measurement method. The intensifier photocathode is controlled by a PG 200 gated high voltage supply while the CCD is readout through the ST138 framegrabber. Both the framegrabber and the gated high voltage supply are PC controlled and triggered synchronously with the laser pulse. On the right hand side of the figure is a schematic of the multiple exposure technique.

A multiple exposure technique was used as the CCD read-out noise was nearly the same magnitude as the signal level for each intensifier exposure. Therefore the intensifier was set to its maximum intensification level (that is, 900V) and gated a large amount of times per CCD exposure in such a way that an average 45 000 to 55 000 counts is collected on each pixel of the CCD (depending on the light intensity and the gating time use, from 1 to 50 000 exposures per CCD readout). Also, all measurements, calibrations and any use of the ICCD camera were systematically

subject to a background substraction: the background image when no signal is recorded is systematically substracted to the measurement image. Using a purpose-made software written using Labview®, each CCD pixel readout value was then divided by the number of times the intensifier had been gated and then divided again by the gating time in microsecond. This explains the use of $W.\mu s/m^3sr$ as a general measurement unit for measurements obtained with the spectrographic system.

IV.2. 1. Laser spatial profile imaging.

An attempt to control the laser spatial profile has been made in order to acquire a diffractive optical beam shaper. Therefore the laser beam spatial profile has been imaged using the attenuated reflection from an optical wedge as described in figure 58 below:

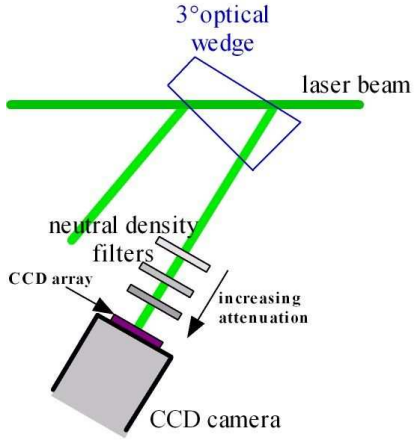

Figure 58: Laser spatial profile measurement principle. Because the laser beam itself would damage the CCD camera, the reflection (circa 1-2% of the overall laser intensity) from the facet of an optical wedge is used and attenuated. The measurement is performed by direct perpendicular illumination of the CCD array.

The wedge separates the two reflections from its surfaces using a shallow angle (3° in this case) between its front and end facet. Each reflection represents approximately 1% of the laser beam energy which is then attenuated 1 to 3 million times to accommodate the camera dynamic range while illuminating directly the CCD chip. Carefull consideration was taken so as not to cause permanent damage to the pixels array. The camera used in this configuration was an 1989 AT1® camera manufactured by Wright® Instruments, This was the solely large-array (9mm by 7 mm) CCD camera capable of measuring a laser profile section of 10 mm diameter at the wavelength of 1064 nm. Each pixel was 6,8 µm squarre. Despite many efforts and maintenance performed on the CCD camera, only profiling of the original laser beam before the horizontal cylindrical beam expander could be implemented. Beside, the original laser profile was larger than the imaging area available on the CCD chip. Therefore three different "shifted" profiles were imaged and processed in a manner to reconstruct the original plaser spatial energy distribution. Finally, althought the CCD was equipped with a Peltier-type cooler, the said cooler was out of use and the images obtained required additional spatial filtering in order to extract a realistic beam profile. The laser beam profile is displayed in figure 59. The filtering method obeys the following: using a Labview® programming platform, the laser image was passed

through a high noise rejection custom-made Bessel filter and the filtered result passed through a second smoothing filter, in order to eliminate the low intensity residual ripple noise. This resulted in a low distortion (less than 1/1000 of the CCD array) high resolution laser image (right hand side of figure 59).

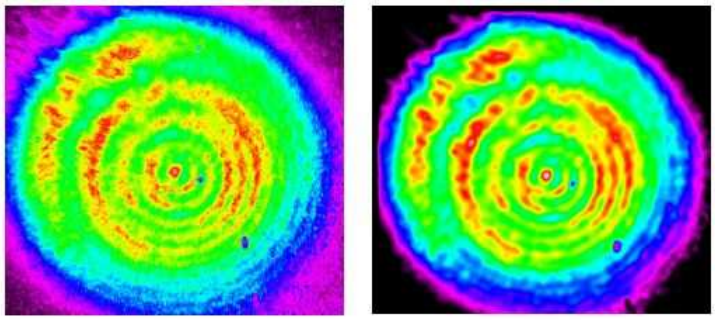

Figure 59: laser beam profiles obtained. On the left is the original measurement and on the right the filtered result.

Unfortunately, the technical limitation associated with this particular CCD camera made profiling the expanded laser beam after the Gaussian telescope (figure 56) impossible. However the laser spatial uniformity can be estimated within the range 20-50% at 100 microns resolution.
All LII measurement systems require to essential parts: a conditioned laser beam and a detection system. Now that the laser beam profiled and described in details, the detection system is to be detailled

IV.2. 1. Spectrographic system calibrations

The spectrographic measurement system sits behind the collection lens on figure 56. It is composed of a spectrometer associated with an ICCD camera. The spectrometer grating separates the wavelengths of light and images the spectrum obtained from the measurement volume onto the intensifier of the CCD camera. In practice, the CCD is illuminated along 526 pixels in the direction of the wavelength separation and 110 pixels in the vertical direction. Therefore the effective CCD area used for the spectrographic system is made of 526 wavelength bins of 110 pixels each out of an initial 576 by 386 pixels CCD array. The spectrometer was effectively illuminating near uniformly (in focus) a 110 pixels high region of interest. The measurement system has been through multiple calibrations and the first one is a spectral calibration to define the wavelengths bins themselves.

IV.2.1.1. Spectrograph spectral calibration

For a calibration standard such as a calibration pencil-style lamp was not available, a commercial Neon diode was used to reliably provide the spectral lines of Neon. The electrical system used is described in figure 60.

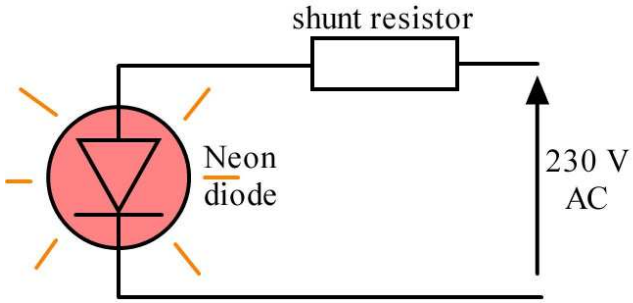

Figure 60 Electrical circuit of the Neon diode used for the spectral location calibration. A commercial power indicator Neon diode is shunted at 230V AC. The resulting illumination contains the neon spectral lines.

The spectrograph spectral calibration is best described in figure 61.Two collinear HeNe lasers (one emitting at 542 nm and the other at 633 nm) used for aligning the optical system were directed onto a piece of white paper located at the measurement point location. Using the HeNe traces on the recorded spectrum, a first rough estimate was possible. Then the very distinct Neon lines emitted by the photoluminescent diode were discerned and a third order polynomial relation established between the Intensified spectra column indices for 4 distinct grating positions used to cover the whole visible spectrum. The grating being rotated around its centre using a micrometric screw, the reading of the said micrometer was used to design the grating position. The following equation was then fitted to the wavelengths λ's assigned to the column indices of the CCD (or wavelength bin number) p's:

$$\lambda = a \cdot p^3 + b \cdot p^2 + c \cdot p + d \qquad \textbf{(80)}$$

The factors a,b,c, and d for the 4 different grating positions are included within table 2 and the final result is displayed in figure 61. As a general indication, the spectral resolution of the system ranges from 0.3 nm at 400 nm, rising linearly to 0.6 nm at 800nm. The spectral accuracy and separation is believed to be between 1 and 2nm .

Grating position (mm)	**Spectral range (nm)**	**a**	**B**	**C**	**D**
8.915	595.2 – 863.9	-6.786×10^{-8}	2.798×10^{-5}	-5.036×10^{-1}	8.890×10^{2}
9.460	500.2 - 766.6	4.265×10^{-8}	-4.653×10^{-5}	-4.927×10^{-1}	7.913×10^{2}
9.735	451.4 - 716.5	9.855×10^{-8}	-8.243×10^{-5}	-4.882×10^{-1}	7.411×10^{2}
10.010	409.8 - 668.2	1.830×10^{-7}	-1.067×10^{-4}	-4.910×10^{-1}	6.930×10^{2}

Table 2: Spectral location calibration results. The grating position indicates the micrometric adjustment screw reading.

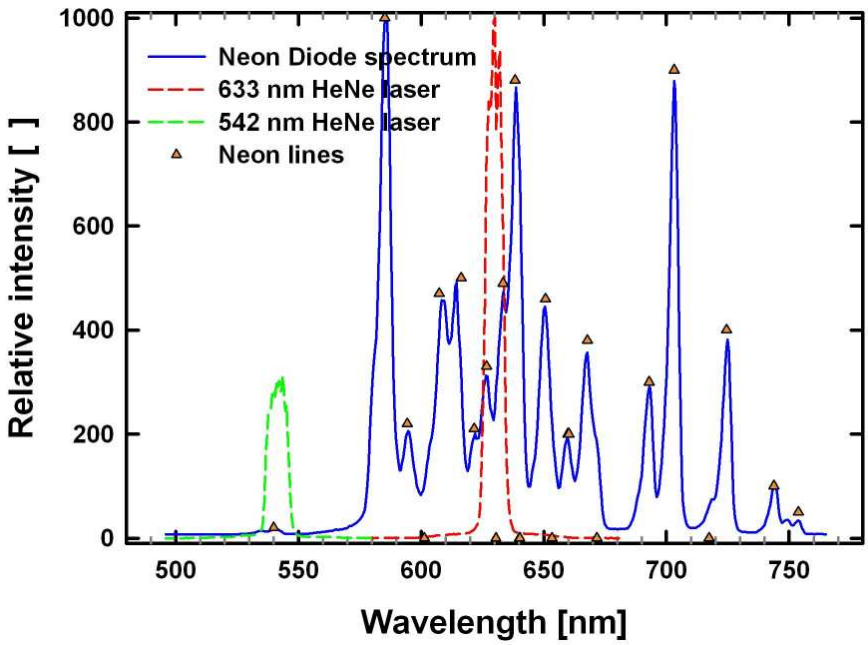

Figure 61: Calibration against a Neon diode result for a grating set at 9.460 mm. The blue line represents the Neon spectrum, with yellow triangles indicating the theoretical location of the Neon lines. The green dashed curve represents the spectrum obtained by projecting a 542nm HeNe laser beam on a piece of white paper at the focus point of the spectrograph, while the red dashed curve represents the spectrum obtained by the colinear 633nm HeNe laser beam.

In order to measure spectral light intensity profiles, a second calibration is required for this spectrographic system. Indeed, the light intensity measured by the system needs to be associated with a calibration standard. Therefore an absolute light intensity calibration was performed on the spectrograph.

IV.2.1.2. Spectrograph absolute light calibration.

To perform an absolute light intensity calibration, a tungsten strip filament lamp (see figure 62) was borrowed from the Particulate matter collaboratory group, currently lead by the Gregory John Smallwood, at the National Research Center (NRC) Ottawa (Canada). More specifically, this lamp is a General Electric Microscope Illuminator (model 18 A/T10/1-6V, Serial Number 9801), specified to produce a nearly uniform 2.2 mm diameter “hot spot” at its strip filament centre. The lamp has been calibrated against a pyrometer recording its brightness temperature at 650 nm by the Institute for National Measurement Standards which is part of the NRC (report number THY – 98 – 150, 15 July 1998).

Figure 62: The tungsten strip filament lamp used for the absolute light intensity calibration. The filament itself is a strip of tungsten presenting a flat 4mm by 6 mm polished section on its centre. It is held by 2 metallic pins within an evacuated glass cylinder.

The data for this lamp is presented in table 3 and figure 63 with the brightness temperature (which is the temperature at which a blackbody would emit the same light intensity at 650 nm) against the current (d.c.) flowing through the filament.

Brightness Temperature [°C]	Current [A]
900	6.12
1000	6.45
1100	6.84
1200	7.30
1300	7.84
1400	8.47
1500	9.18
1600	9.97
1700	10.82
1800	11.74
1900	12.71
2000	13.73
2100	14.80

Table 3 : calibration data

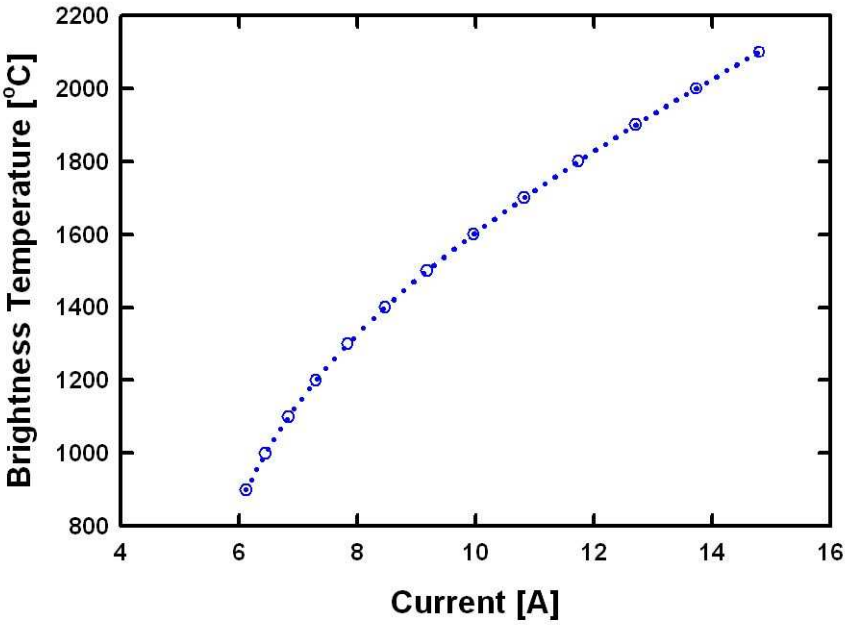

Figure 63: brightness temperature versus current for the strip filament lamp calibrator

For practical reasons, as it is extremely difficult to adjust large DC currents finely, a sixth order polynomial has been fitted to the calibration data, yielding the lamp brightness temperature T_B as a function of a coordinate substitute z_c:

$$T_B = \sum_0^6 a_i \cdot z_C^i \qquad \textbf{(81)}$$

with i the polynomial index and a the calibration coefficient given in table 4. And z_c obeying the relation:

$$z_c = \frac{I_c - 10.5}{4.3} \qquad \textbf{(82)}$$

With I_c the current flowing trough the lamp (in amperes).

I	**0**	**1**	**2**	**3**	**4**	**5**	**6**
$\mathbf{a_i}$	1663.8	499.38	-94.96	37	-21.14	51.53	-34.76

Table 4: Strip filament lamp calibration coefficients.

Using the method described above, a radiance calibration is provided with an uncertainty specified at 5 K in terms of brightness temperature provided a stable and accurate current is supplied to the lamp within more or less 0.1 mA, which is the current lamp standard requirement. Since no such equipment was capable of fulfilling these requirements, a multiple coils large capacitance 110V Japanese power supply was refurbished. The advantage of such equipement is its ability to maintain an extremely stable current, provided one can measure it and adjust the required supply.

For this purpose, a 15W 0.02Ω (±0.005%) high precision resistor was used in serie with the lamp to convert the current (6 to 15 A) to a measurable voltage (120 to 300 mV) that could be readout according to Ohm's law using a high-precision datalogger (see figure 64). This high precision current controlling system used a high precision NIST calibrated datalogger (Datascan 7220) running on a specific software architecture (through an OPC server) on a Labview® platform. In terms of performance, the data logger usually achieved a reading resolution and accuracy of 0.01 mA and the power supply showed instabilities much lower than 0.1mA. Therefore one could estimate that the lamp strip filament temperature was maintained and measured to within than 0.8° C during the spectrometric calibration.

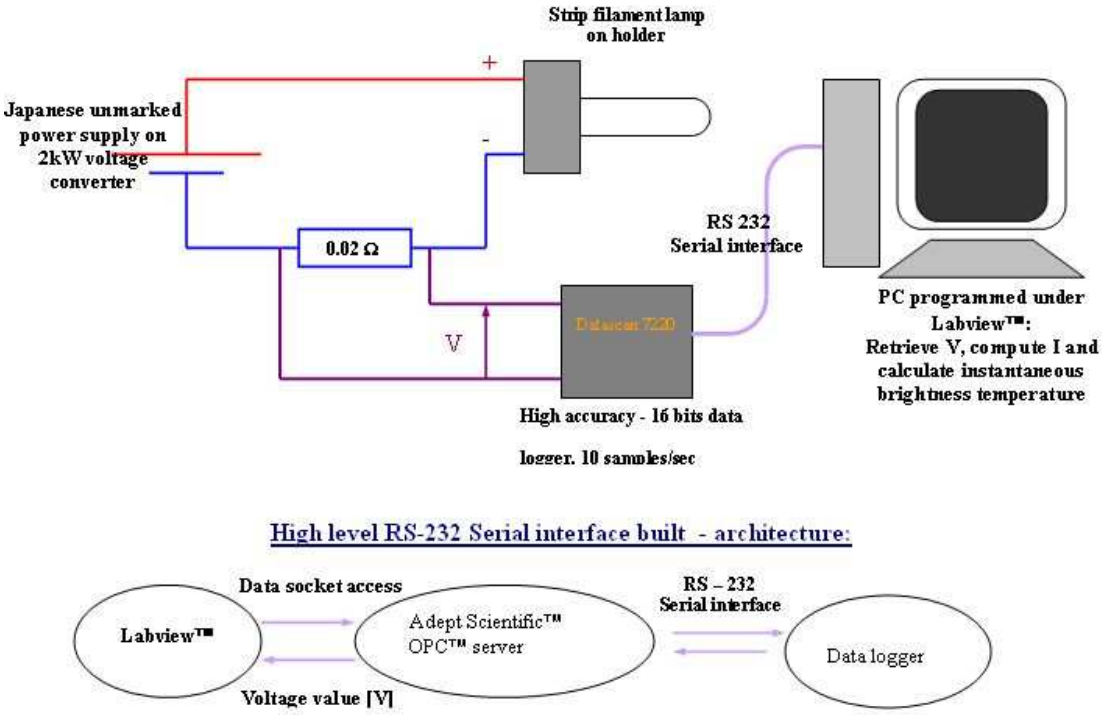

Figure 64: System used for controlling the lamp current: the top represents the hardware configuration and the bottom symbolises the specific RS 232 serial communication architecture.

Before any calibration could be applied, flat-fielding had to be performed. In this configuration, flat-fielding compensates for both sensitivity variations between pixels of the ICCD camera and non-uniform transmissivity from the grating itself. Knowing that during calibration, the spectrometric system is imaging a 2mm by 25 µm section of a 2mm diameter uniformly emitting area of the strip filament, a flat-fielding could be performed for every wavelength bin, that is 526 bins of 110 pixel each. A brightness temperature of 2205.8˚C was chosen and the sensitivity corrected was then checked using a lower 1203.1˚C brightness temperature (see figure 65). Blemishes were also listed and automatically replaced by their median wavelength bin value. Flatfield coefficients were calculated using the median value of each 110 pixels wavelength bin divided by the pixel readout value. This way a matrix of 526 by 110 pixel coefficients was built and applied to any later spectrometric measurement and calibration. Once the flatfielding performed, all 110 pixels for each wavelength bin are summed together and a 526 points spectral curve is obtained.

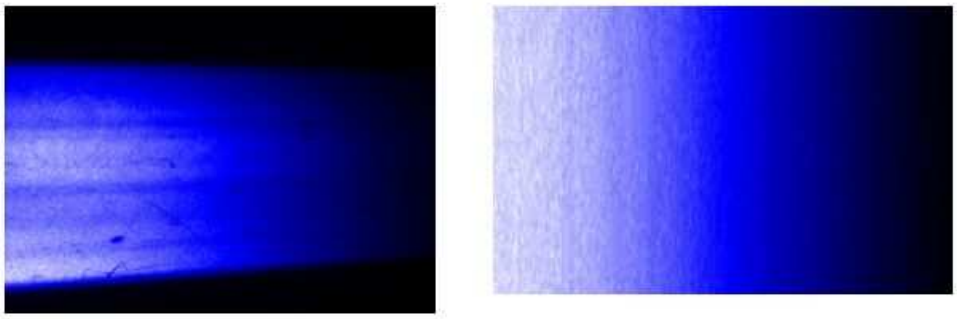

Figure 65 : Flat-fielding check at 1203.1 ˚C lamp brightness temperature. The left and right images are the filament spectra before and after flat-fielding and blemishes removal. The scale is a blue linear one with black representing the minimum and white the maximal counts value. The right hand side of the image corresponds to 500nm , while the left corresponds to 750 nm.

The calibration method is inspired from the absolute light intensity calibration for LII described by Snelling et al (2001) and will be very similar in the following text. The spectral radiance of the lamp $R_s(\lambda)$ (that is, the power emitted per unit area, per unit solid angle and per unit wavelength interval) is expressed in equation 83:

$$R_s(\lambda)=\frac{2\cdot c^2\cdot h\cdot\varepsilon(\lambda,T)}{\pi\cdot\lambda^5}\cdot\left(e^{\frac{hc}{\lambda kT}}-1\right)^{-1}=\frac{C_1\cdot\varepsilon(\lambda,T)}{\pi\cdot\lambda^5}\cdot\left(e^{\frac{C_2}{\lambda T}}-1\right)^{-1} \qquad \textbf{(83)}$$

With $C_1 = 3.74177 \times 10^{-16}$ W.m^2 and $C_2 = 0.014388$ m.K are respectively the first and second radiation constants, and $\varepsilon(\lambda,T)$ is the emissivity of Tungsten as a function of wavelength and temperature. The calibrated lamp has a known brightness temperature T_B which is the temperature at which a perfect blackbody would emit the same amount of radiation at 650 nm from which the true filament temperature T_S can be obtained considering the exponential term >>1 in equation 83 given the temperatures and wavelengths used here:

$$T_s=\left(\frac{1}{T_B}+\frac{\lambda}{C_2}\cdot\ln(\varepsilon(\lambda,T_S))\right)^{-1} \qquad \textbf{(84)}$$

With the known emissivity of Tungsten (Larrabee, 1957) as a function of temperature and wavelength, the filament radiance can be obtained at a different wavelength than the calibration one and the calibration light intensity (radiance) can be calculated using:

$$P_{CAL}=A\cdot\int_{\lambda 1}^{\lambda 2}R_s(\lambda)d\lambda \qquad \textbf{(85)}$$

Where A is the emitting area cross-section (25µm x 2mm), λ_1 and λ_2 are the start and end of the bandpass optical filter used for point-wise measurements. The system assumes that the area is emitting uniformly over 4π steradians. In the case of the spectrometric measurement system, these where the start and end of each wavelength bin. Therefore for each calibration brightness temperature the true filament temperature is deducted using equation 84; and a corresponding 526 points calibration input spectrum computed. Multiple calibrations were made at 4 different grating positions, so as to cover the whole visible spectrum. Sensitivity results are presented in figure 66. Note that depending on the focussing angle, some grating positions transmit a higher amount of light than others as a function of wavelength.

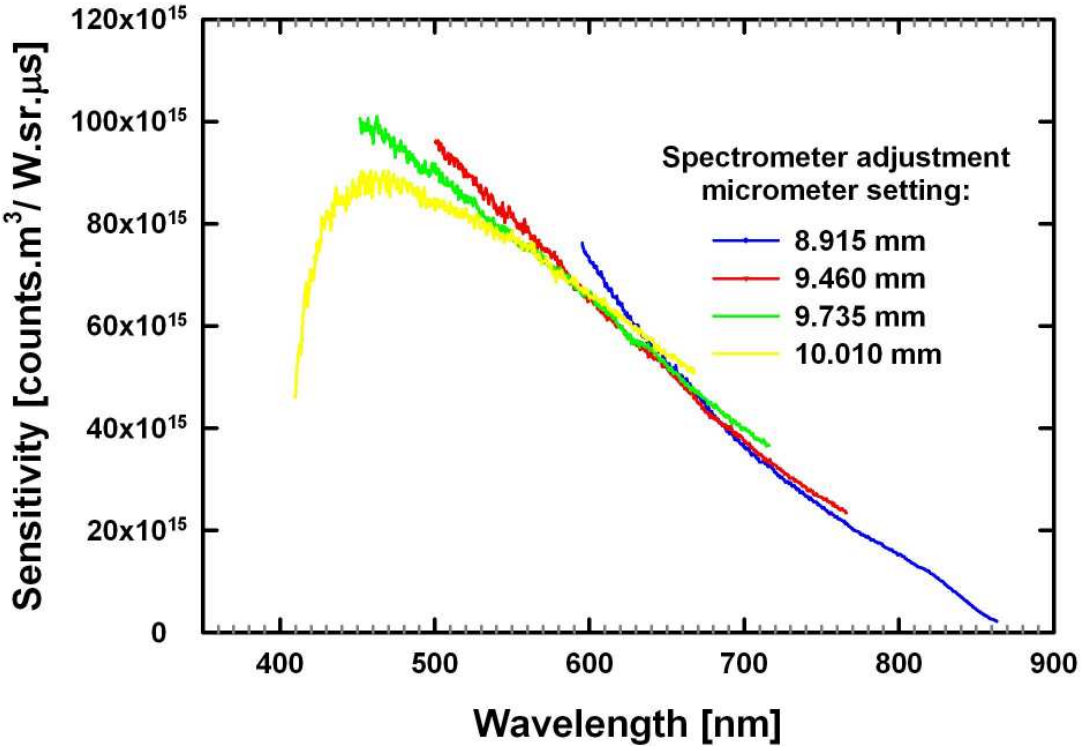

Figure 66: Spectrometric system sensitivity over the whole visible region. Results obtained with a lamp brightness temperature of 1892.5˚C maintained while the grating was scanned over the visible region.

Absolute light calibration for a spectrographic system is a complex operation, which necessitate the use of controlled calibration lamp, flat-fielding the spectra obtained and finally applying the calibration itself. However, often the calibration source is source of discrepancies and a check for the strip lamp calibrator has been performed and is the subject of the following section.

IV.2.1.3.Validation of the use of the strip filament lamp as a calibrator .

The use of a strip filament lamp as a radiance calibrator had caused some concern and showed punctual discrepancies in the order range 10-15% when compared to a more reliable irradiance calibrator. Therefore, it has been decided to investigate how reliable and repeatable a given spectrometric calibration can be. Bearing in mind that any discrepancy occurring such as shifts in sensitivity as a function of the lamp radiance (brightness) temperature would highlight the strip filament lamp calibrator as questionable. Hence the calibration method described in the preceding sub chapter has been applied to 9 different radiance temperatures ranging from 1000 to 2000 ˚C at a fixed grating position of 9.460mm. Thus the spectra obtained were centred at the 650 nm lamp calibration wavelength. The calibration input spectra are illustrated on figure 67.

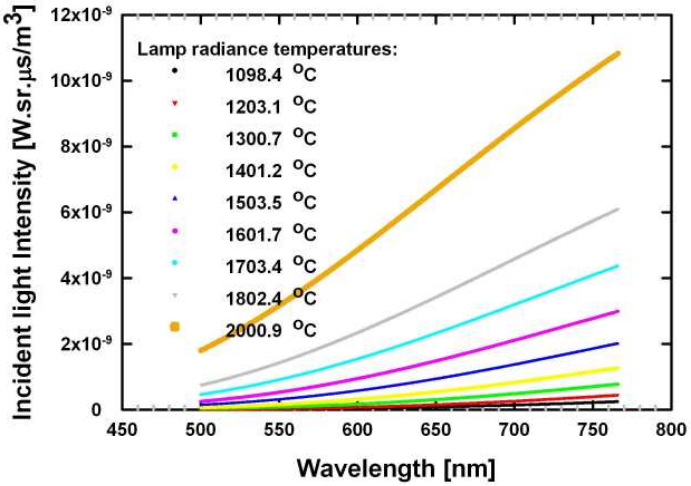

Figure 67 : Calibration input spectra centred at 650nm used during the calibration method validation.

The obtained sensitivity curves are presented on figure 68.At first, one could observe two striking features: the first one is that for a wavelength < 550nm large discrepancies are found ; the second feature is that for a wavelength > 550nm, all sensitivity curves are equal to each other within less than 2%. There can be two explanations for the discrepancies below 550nm: either the input calibration spectrum is too weak to provide measurable light intensities below 1500 C radiance temperature; or the strip filament is not uniformly emitting over the calibration surface, leading to erroneous results when considering low lamp temperatures. It has been proven in a later work that filament light emission uniformity is highly dependent on temperature and increases with higher filament temperatures. Finally, the results obtained for the lamp radiance temperatures < 1500˚C were discarded and are presented on figure 68. An estimated 2% spectral sensitivity repeatability margin can be accepted over the whole 550 – 750 nm region.

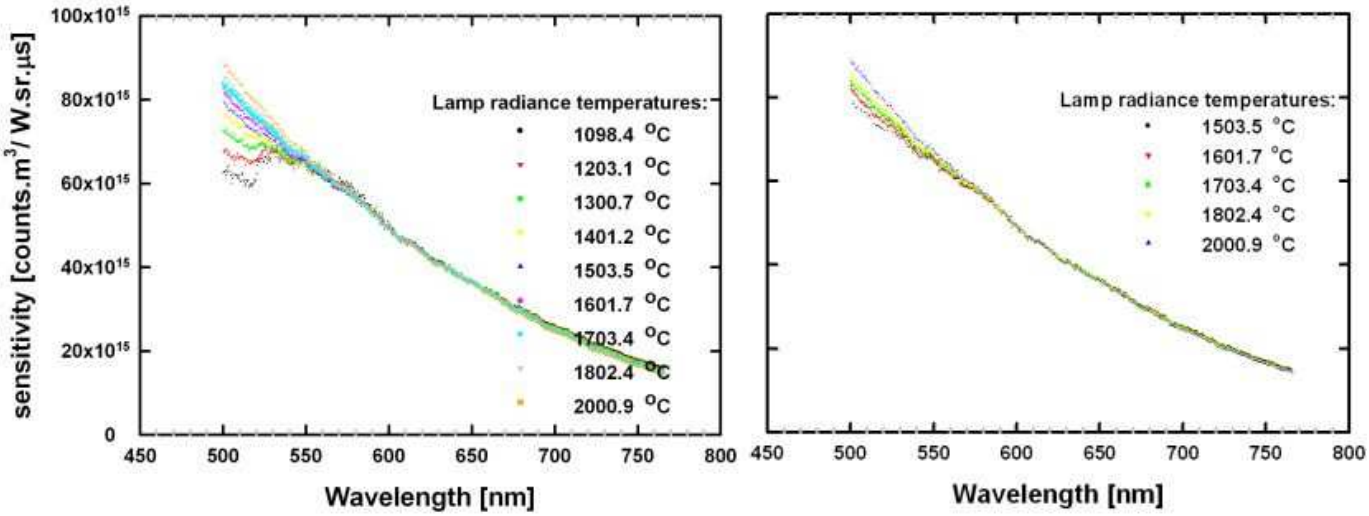

Figure 68: Calibration checks using 9 different temperatures (left) and after discarding lamp radiance temperatures < 1500 ˚C (right).

Therefore the lamp calibration method can be recognized as reliable, provided that the brightness temperature of the strip filament is maintained above 1500°C to maintain both a consistent light intensity level and illumination uniformity. Hence we now

dispose of a spectrographic system that is fully calibrated, both spectrally and in terms of absolute light intensity. However, because extremely low intensity signals are faced, a last consideration has to be taken into account, so that measurements can be taken in the best conditions possible. Indeed, the noise performance of the spectrographic system is a primordial consideration.

IV.2.1.4. Signal to –Noise ratio of the spectrographic system.

When assembling a spectrographic system, the main practical concern is the signal collection efficiency and signal levels. In this case, we are collecting light with an f/1.8 lens, corresponding to an approximate collection efficiency of 31% of the LII signal, which in turn is sent through an f/3.8 spectrometer, meaning again a collection efficiency around 7%. Both of them are placed in serie, therefore yielding a maximal combined signal collection efficiency of 2% which in turn is separated into approximately 800 wavelength bins (spread over 400nm for the visible region, with an average wavelength bin of 0.5 nm/pixel). This is the "best case" estimate and does not take into account the intensifier quantum efficiency (maximum 20% for a second generation intensifier as the one used here), grating quantum efficiency (maximum 30% for a concave reflective holographic grating) and lens optical losses. All these signal losses mean that noises such as a Q-switching laser, intensifier photocathode shot noise, CCD readout noise and background can end up being major contributors to the measurement taken.

For all the measurements performed using the spectrographic system, the CCD readout noise was reduced to negligible (<1/1000 of any CCD exposure readout) using the multiple exposure technique described precedently. Also, all measurements were taken in dark room conditions and background - substracted to reduce the background noise level to less than 50 pixels / CCD readout for a usual CCD readout of between 45 000 – 55 000 counts per pixel. Extensive checks have been performed to check for any signal corruption from laser Q-switch and it has been found no signal contribution for this source of noise.

However, when LII spectra were recorded, a large amount of noise was present and corrupted the signals. This noise was not noticed during calibration as the amount of light during calibration was merely > 1000 times the LII signal levels encountered. The strip filament lamp was used below 800 °Using the strip filament to produce a constant source of signal in the range of the LII signal itself, it has been found a large amount of variation (>30% for a single Intensifier exposure) in CCD readout, depending on how many times the intensifier had been gated before a CCD readout. This variation was recorded as a function of the number of intensifier gatings per CCD exposure as a standard variation in terms of average signal level over the whole spectral region of interest 500 – 750 nm (grating position 9.460 mm). The standard variation curve obtained was then ratioed to an ideal 55 000 counts per wavelength band (bin) readout. The curve obtained resulted into an estimate of the Signal –to-Noise Ratio (SNR) as a function of the number of intensifier exposures (gatings) per CCD readout and two typical gating durations,100 ns and 1 μs, as shown on figure 69.

The SNR is independent of the intensifier duration and tends to a value of approximately 18 after 300 gatings per exposure. Therefore the noise present after each intensifier gating has the same intensity regardless of the length of the exposure. This is typical of light intensification devices and originates from the intensifier photocathode when it is gated and therefore can be classified as a shot noise.

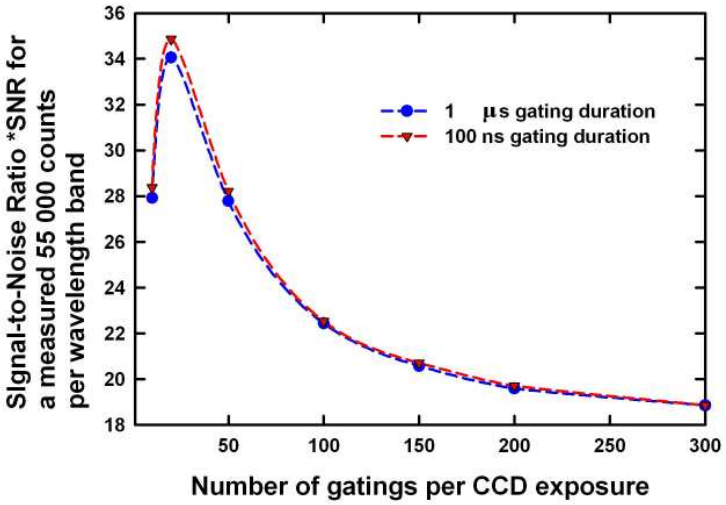

Figure 69 : Signal to Noise Ratio for a typical LII signal, as a function of signal level (proportional to the number of gatings per CCD exposure). As an example, for 3 ppb of soot presenting a temperature of ~ 4000K, 200 intensifier gatings of 100 ns duration per CCD exposure were necessary to collect ~ 50 000 counts per wavelength band. Most of all measurements were performed with a gating duration of 1 µs duration repeated 150 to 300 times per CCD exposure, yielding a standard 18 to 20 Signal to Noise ratio.

IV.2.1.5. Conclusions

Two conditions have to be fulfilled in order to validate the presence of LII under vacuum signals: (1) blackbody spectra typical of soot incandescence have to be present; and (2) the corresponding soot temperature recorded have to match the long-lived (50 microseconds and more) radiative temperature decay described in chapter III.

Therefore the spectrographic system described in figure 56 has been assembled to confirm the presence of laser-induced incandescence under vacuum inside the sample roller bottle following laser excitation. Even though difficulties were encountered when conditioning the laser beam, an appropriate laser sheet was used to induce LII. The spatial fluence distribution obtained was estimated to be uniformly distributed within 10 to 20%, with a median fluence of 0.3 J/cm^2 . Hence near-uniform temperature distributions were expected within the measurement volume located at the intersection of the laser beam and the spectrograph focal plane.

The spectrograph system is composed of: (1) and achromatic collection lens (2) an adjustable diffraction spectrometer (3) an intensified CCD camera.

The spectrograph was accurately calibrated both spectrally and in terms of absolute intensity spectral response. The effective spectral accuracy was estimated to be 1 nm for a spectral resolution of 0.5nm whereas the absolute intensity spectral calibration yielded uncertainties in the region of or below 2% for the 500-700 nm range. Because spectrographic system, when used to sense ultra-low light levels are subject to intensifier photocathode shot noise, this noise was characterized and the optimal SNR region was measured to be between ten and 50 intensifier gating per CCD exposure.

Overall, the spectrographic system is not designed to measure time-resolved LII signals but LII spectra at set gating durations and delays after the laser pulse. The purpose of the system was uniquely to prove that obtaining LII under vacuum signals was feasible and that the signals obtained could be identified as incandescence temperature decays. However, once the feasibility of LII under vacuum was established a much more complex measurement system was designed and implemented.

IV.3. The LII under vacuum investigation system: a dual wavelength pyrometer coupled to a calibrated Intensified CCD camera.

The laser-induced incandescence under vacuum investigation system was designed and implemented with the following requirements (see figure 70-a):

(1) a dual wavelength transient pyrometer is provided in order to perform time resolved LII measurements. These measurements will provide the instantaneous signal level at two distinct wavelengths, the soot instantaneous temperature and the corresponding soot volume fraction.

(2) The transient pyrometer shares its measurement volume within the roller bottle with an absolute light intensity calibrated Intensified CCD camera system of which the collection optics are spectrally.

(3) The measurement volume is formed by the intersection of the image plane of both pyrometer and ICCD with a spatially uniform laser beam.

On one hand, the use of the ICCD camera and the pyrometer rather than the pyrometer on its own is justified by the fact that Charge Coupled Devices (CCD) are time-integrating photodetectors and the increase in detectivity associated with longer LII signals under vacuum should therefore become evident on ICCD images. On the other hand, 2D imaging is also used to check the phenomena occurring during LII under vacuum. One would also note that the ICCD system coupled to the transient pyrometer is the first implementation of a two dimensional absolute light intensity calibrated LII method. This section will first start with the laser profile measurements, followed by the design of the dual wavelength pyrometer used for TIRE-LII measurements under vacuum and finally the ICCD calibration procedure, measurement method and image processing is detailed.

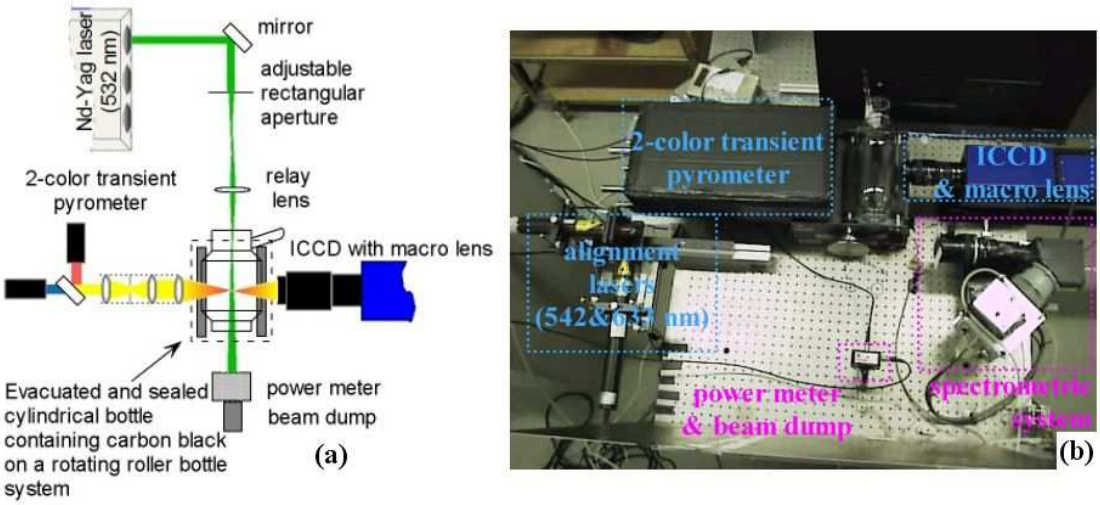

Figure 70: Schematic of the laser-induced incandescence system for high vacuum measurements (a) and corresponding picture of the optical table (b). The spectrographic system and its dedicated alignment lasers are present on the bottom part of the left hand side of the picture. The spectrographic system was used to determine the ICCD macro lens spectral efficiency.

IV.3.1. Laser spatial profile

The frequency-doubled pulsed Nd-YAG laser (Spectra physics, Quanta Ray®) emits at 532 nm for a measured pulse width at half maximum of 7,5 ns, a repetition rate of 10 Hz and 50 to 100 mJ delivered per pulse. The laser beam is first reflected by a 532 nm mirror onto an adjustable vertical rectangular aperture (see figure 70-a). The image of the laser passing through the aperture is then imaged onto the measurement volume with a magnification factor of 1:1using a spherical 25cm focal length lens. Literally, the image of the rectangular aperture is relayed onto the measurement volume. This technique was first introduced to the LII domain by Snelling et al.(2001). The relay imaging method effectively produced a 2.9mm high by 3.2mm wide near-uniform laser profile as measured using the procedure described in section IV.2.1 and figure 58 using the CCD array of the Lavision® camera used in this experiment with a pixel size of 12 x 12 µm. Diffraction patterns on the edge of the measurement volume are limited and Nd-Yag laser have limited spatial coherence. Non-uniformities can be appreciated on figure 71;taking into account sharp intensity peaks, the centre of the laser beam presented non-uniformities ranging up to 30% on a range of 20-50 µm; while using a 200 µm resolution non-uniformities averaged to less than 10% within the measurement volume.

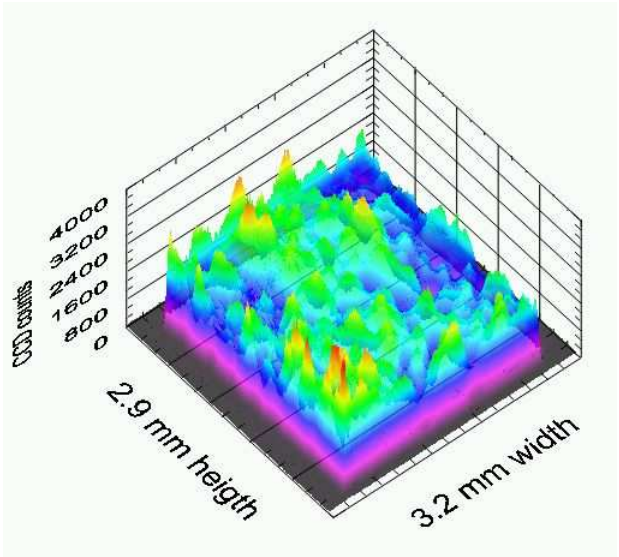

Figure 71: Laser spatial fluence profile at the measurement probe volume (units are in CCD counts)

The aperture width is adjusted to the 3.2 mm depth of field of the macro lens equipping the Intensified Charged-Coupled Device (ICCD) camera. The measurement volume is located at mid-height inside the roller bottle at the measurement point of both the 2-color transient pyrometer system and the ICCD camera. The laser beam then exits the roller bottle to end its trajectory inside a beam dump. Back-reflections from the beam dump are sensed using a Scientech® Silicone photodiode acting as a power meter. The photodiode is placed in series with a shunt resistor, a precision metal film 50Ω resistor and a battery-operated18V DC power supply. Software - automated measurements were taken at the precision resistor extremities and the current crossing the photodiode therefore deducted using Ohm's law. The photodiode itself has a 1ns time response and a quantum efficiency nearing 20% at 532nm. The photodiode was calibrated at 532 nm using a NIST traceable calorimeter with an accuracy of 4%, corresponding to an uncertainty when measuring the laser fluence of

0.02 J/cm^2. Overall, laser beam delivery at the measurement points was both conditioned and monitored to an acceptable standard for performing LII under vacuum. The central part of the system is the transient pyrometer itself as time-resolved temperature measurements are essential for the verification of LII under vacuum.

IV.3.2.The dual wavelength pyrometer

The two-color transient pyrometer had to be designed, partly build and implemented specifically for this experiment. The pyrometer is a 2-colour transient system, meaning that it aims at measuring instantaneous absolute light intensity measurement at two distinct central wavelengths. According to Planck's blackbody radiation law (Hotel and Sarofim, 1967), the peak of the blackbody spectrum shifts toward the blue when a blackbody is heated and toward the red when cooled. Therefore the ratio of two wavelengths chosen accordingly is characteristic of the temperature of the body measured. In this situation instantaneous soot particle temperatures during LII are to be measured. Temporal resolutions comprised between 6ns to 1µs were aimed at to accommodate both "standard" LII signals (50ns to 3µs long) and the duration of vacuum LII signals (>60µs). A calibration within the visible range was also desired. For this the strip filament lamp and corresponding monitoring system used for the spectrograph absolute light calibration was used to calibrate the pyrometer. As the strip filament lamp provided repeatable light intensities within 2% in the range 500 to 700nm, 500 and 700 nm were chosen as the two central wavelengths of the pyrometer, which optical design follows.

IV.3.2.1. Optical design

Laser Induced Incandescence signals are probed within a laser beam, as illustrated in figure 72. The incandescence light signal at the centre of the laser beam is probed and sent along the detection axis into the optical detection system:

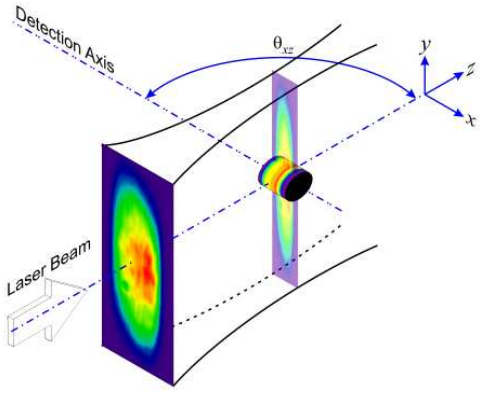

Figure 72: probing a measurement volume V_m. A probe volume is analysed out of the laser beam irradiated volume. the cylindrical shape of the measurement volume is dictated by the use of spherical optics . (Greg Smallwood, 2004)

Eventually the light signal is collected, then a blue-red separation is made using a dichroic mirror of which reflections are subsequently filtered into bandpass filters before reaching the photodetectors. Such a system is described in details in figure 73.

Figure 73: Layout of the pyrometer optical system (scale 1:2).

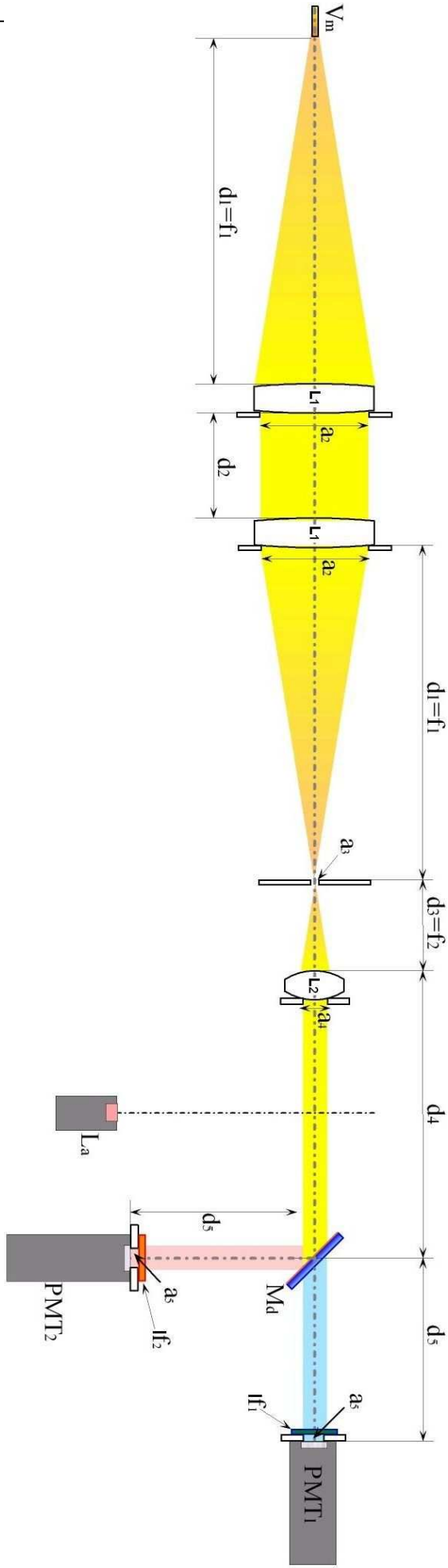

Symbol	Description
V_m	Measurement (probe) volume
d_1	Distance between V_m and the collection lens L_1, $d_1 = f_1 = 120$ mm
f_1,f_2	Focal length of the lenses L_1 and L_2
L_1	Collection lens / front lens of gaussian telescope; Melles Griot 01 LAO 138 Precision Optimized Achromat, f_1= 120 mm, diameter 40 mm
a_2	Circular aperture, diameter 38 mm
d_2	d_2 = 32mm
a_3	Cicular aperture, diameter 1mm, limits the effective size of the measurement volume V_m
d_3	$d_3 = f_2$ = 31mm
L_2	Back lens of gaussian telescope; Melles Griot 01 LAO 028 Precision Optimized Achromat, f_2 =31 mm, diameter17.5 mm
a_4	Circular aperture, diameter 8 mm
d_4	d_4 = 100 mm
La	Miniature 5mW 650nm diode alignment laser
M_d	Dichroic mirror; Edmund optics NT47-263 45^o reflective dichroic red mirror, diameter12.5 mm
d_5	d_5 = 50 mm
If1	Interference filter 1; CVI Laser F25-500.0 -4-0.50 Visible Interference filter CWL: 500 nm, FWHM: 25 nm
If2	Interference filter 2; CVI Laser F25-700.0-4-0.50 Visible Interference filter CWL: 700 nm, FWHM: 25 nm
a_5	Photomultiplier window limiting aperture, diameter 6.5 mm
PMT_1 & PMT_2	Hamamatsu H6780-20 R 7400 PMT Photomultiplier Tube (PMT) Module

The system laid out in figure 73 had been advised by Smallwood et al. as the simplest and most efficient configuration available to perform absolute-light calibrated LII. This configuration is typical of the LII detection systems currently used at NRC and enclosed in the LII Artium200®. In the configuration depicted in figure 73 and the description below, all the lenses used are 3-wavelengths corrected achromats apertured at 90% of their diameter (clear aperture surface), meaning that all wavelengths of the light signals produced within the measurement volume V_m are collected and focused at exactly the same location, with negligible geometrical distortions with wavelength (minimised longitudinal aberrations). Achromats insertion losses were negligible (spec <0.64%) and spectrally flat in the wavelength region of interest and behaved as spherical converging lenses. In this configuration, the measurement volume V_m is placed at the focal point of the collection lens L_1. Therefore rays of light originating from V_m and passing through the achromat L_1 form a parallel beam of light before entering the second achromat, which is identical to L_1. The collection efficiency achieved corresponds to an f/3.16 number, that is approximately 10% of the light intensity radiated within the measurement volume is collected and analysed by the system, assuming the measurement volume is a Lambertian source.
Parallel rays of light enter the second L_1 achromat, which forms with the achromat L_2 a Gaussian telescope that fulfils two purposes:

(1) The telescope features an $f_1/f_2 = 3.87$ reduction factor, effectively reducing the incoming parallel beam of light diameter from 38mm to 9.82 mm, then apertured to 8mm by a_4. This has primarily a function to adapt the high efficiency front collection system to a detector photocathode of only 8mm diameter.
(2) The focal point aperture a_3 of the telescope actually determines the acceptance angle of the pyrometer itself without affecting its collection efficiency. A cylindrical measurement volume of less than 2.5mm diameter was desired as no calibration source presenting a greater near-uniform emitting surface was available. Therefore extensive ray tracing modelling had to be performed to determine a suitable diameter for a_3. This will be the subject of a further section.

Light exists L_2 as a parallel beam and is further apertured by a_4 before being separated by a dichroic mirror M_d with a separation wavelength of approximately 650nm, meaning that wavelengths below 650 nm are not reflected and continue their path toward the photomultiplier tube module PMT_1 while wavelengths above 650 nm are reflected into PMT_2. Note that both detectors are equipped with identical multialkali high sensitivity red enhanced photocathode and are located at the same distance d_5 from the dichroic mirror. The first detector, PMT_1, is filtered by a bandpass interference filter If_1 centred at 500 nm with a full width at half maximum of 25 nm and then apertured to 6.5mm by a_5 to enhance photocathode spatial uniformity. The second detector, PMT_2, is also filtered by a bandpass interference filter If_2 centred at 700 nm with a full width at half maximum of 25 nm and is also apertured by an aperture a_5. A miniature battery-operated alignment diode laser (L_a) emitting at 650nm was also added for ease of alignment.

Overall, the optical system is comprised of two main parts: the first part is dedicated to collect and condition the light in order to perform the measurement itself with the second part of the system, that are the photodetectors. As photomultiplier tubes

represent an obvious choice of detectors, their characteristics of interest for this design are discussed in the following pages.

IV.3.2.1.1. Photomultiplier tubes characteristics.

Photomultiplier tubes were chosen as they represent the most affordable, sensitive and stable photodetectors available. Metal package high sensitivity photomultiplier tube modules were chosen as they presented a good thermal stability, an increased immunity to RF interferences and include an internal low voltage- fed high voltage power supply wired to the electron multiplier. Typically a photomultiplier tube (see figure 74 below) is made of a photoemissive cathode (photocathode), followed by focusing electrodes, an electron multiplier and an electron collector (anode).Light enters the photocathode, provoking the emission of photoelectrons into vacuum. These photoelectrons are then focused toward the electron multiplier, where electron multiplication processes by secondary emissions. All electrons produced are collected at the end of the device by the anode, which hence induces a measurable 0-100 μA current when shunted to ground via a typical 50Ω resistor.

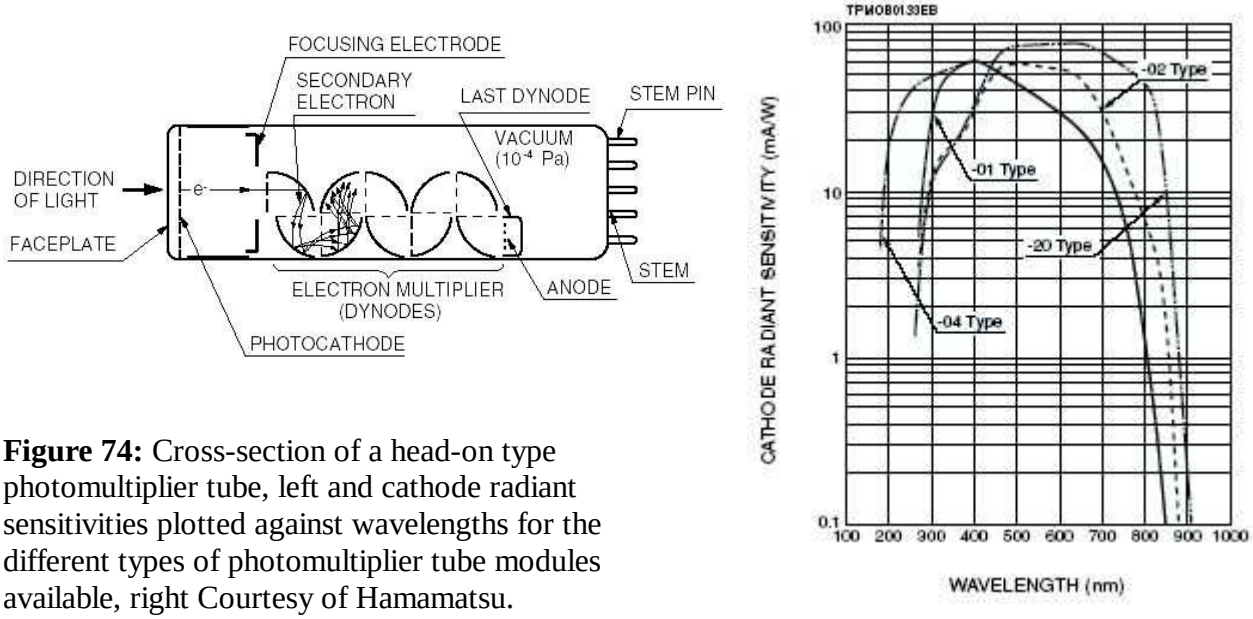

Figure 74: Cross-section of a head-on type photomultiplier tube, left and cathode radiant sensitivities plotted against wavelengths for the different types of photomultiplier tube modules available, right Courtesy of Hamamatsu.

The measurement of single-shot LII signals was anticipated. Also, because the spectral range of this study was limited from 480 to 720nm, type-20 multialkali red enhanced photomultiplier tubes were chosen as disclosing the highest sensitivity (and eventually the lowest noise) within this wavelength range.

The gain of a photomultiplier tube is defined as the obtained anode output current divided by the initial photocathode photoelectric current. Since the gain is achieved through successive electron multiplication, with one multiplication per dynode, the gain of a photomultiplier tube having n dynode stages and a secondary ratio δ per stage is δn. The secondary ratio δ is set by the high voltage fed to the dynodes, which in the case of photomultiplier tube modules is programmed via feeding a 0.25-1V DC voltage to the module. An illustration of the gain voltage programming method is given in figure 75. Another detail to note is that, although the focusing electrodes of a photomultiplier tube are designed so that electrons emitted from the photocathode or dynodes are collected efficiently by the first or following dynodes, some electrons

may deviate from their desired trajectories and therefore lower the collection efficiency. The collection efficiency varies with the position on the photocathode from which the photoelectrons are emitted and influences the spatial uniformity of a photomultiplier tube (see figure 75). The spatial uniformity is also determined by the photocathode surface uniformity itself. Therefore only 80 % of the photocathode diameter of the head-on photomultiplier tubes are used to guarantee 95% spatial sensitivity uniformity.

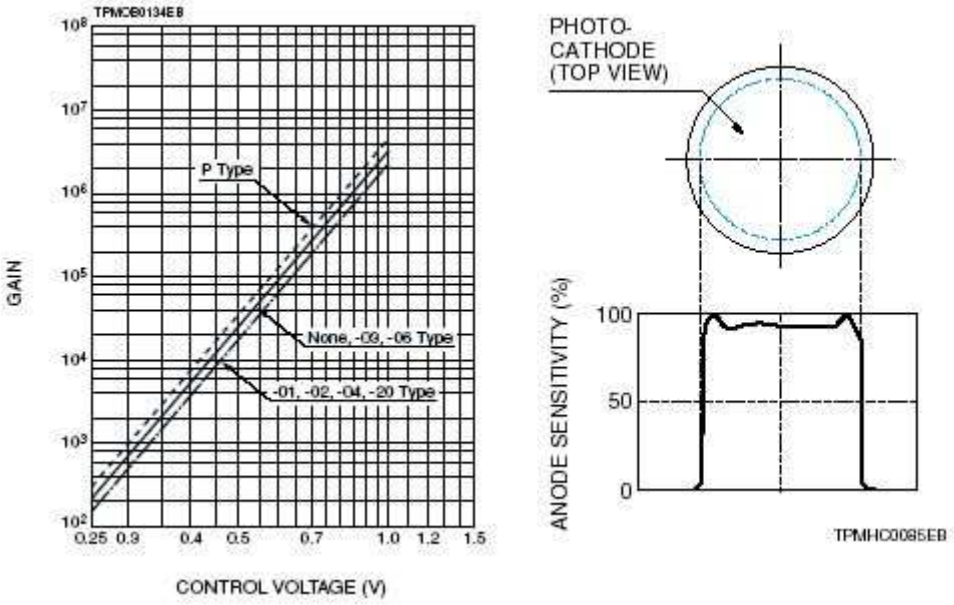

Figure 75: Gain voltage programming method illustration (left) and photomultiplier sensitivity spatial uniformity (right): the photomultiplier tube gain is plotted against the control voltage fed to the high voltage power supply. Courtesy of Hamamatsu.

IV.3.2.1.2. Collection efficiencies and choice of filters

Overall, maximum quantum efficiency was is a requirement when dealing with LII signals as the expected light intensities to be measured range around 10^{-11} W.sr.m^{-3}. Even though photomultiplier tubes are considered as some of the most sensitive detectors, they are not readily achieving quantum efficiencies higher than 20%. Also, interference filters transmissivities are close to 50% while the dichroic mirror achieves a reflectivity of circa 95 % above 650 nm and transmits 95 % of the incoming light below 650 nm. The combined efficiencies per channel have been calculated and are presented in figure 76. The total efficiency for each channel approaches 10%.

Later to the application of the present design, two years of development at NRC led to a high collection volume high efficiency system being implemented. Even though such a system presents high sensitivities in terms of particulate matter concentrations, one must take into account two parameters:

(1) the size of the measurement volume is increased to increase the signal collection. The high sensitivity LII unit comprises a cylindrical measurement volume of diameter larger than 20mm. This also means that a calibration source capable of filling such as surface is required, and this is not available at Cranfield;

(2) a large uniform laser probe volume is necessary over the measurement volume, and this represents substantial difficulties.

Filter with improved transmission efficiencies (>90% peak transmissivity) were also made available in 2005 by the firm Semrock®. Later work on the pyrometric system should include a change from the current visible interference filters to Semrock® filters as this represents an immediate improvement of a factor of two in terms of overall quantum efficiencies.

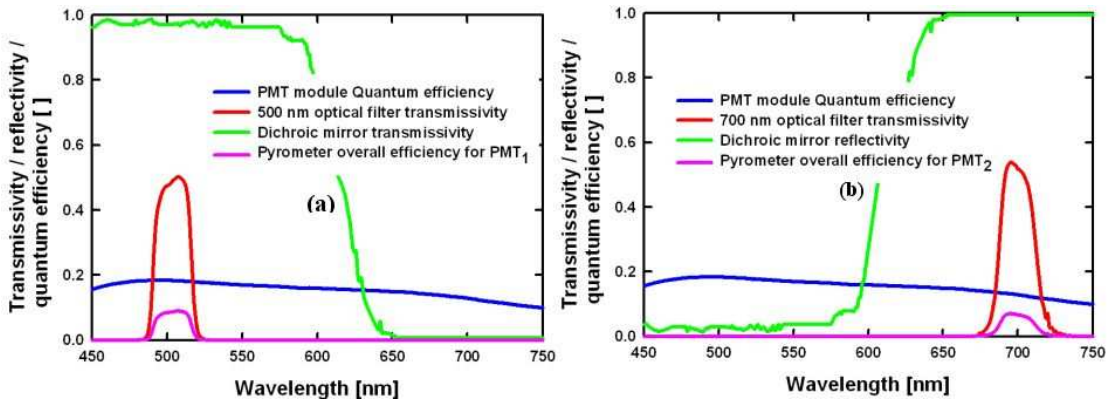

Figure 76: pyrometric system optical efficiencies for both channels :
(a) PMT_1 channel, centred at 500 nm
(b) PMT_2 channel, centred at 700 mn.

The filter bandpasses were chosen to be set at 25 nm full width at half maximum. This choice was made to keep a compromise between collection efficiency and thermal resolution. Ideally narrow bandwidths (<5nm FWHM) coupled to maximal wavelengths spacing (400 and 800 nm centre wavelengths are common) would provide high thermal resolution (~5 K). However limiting factors such as calibration uncertainties, oscilloscope resolution and uncertainties on the optical properties of soot allow us to use a wavelength spacing of 200 nm with bandwidths of 25 nm to achieve theoretical temperature resolutions circa 15 K.

The overall optical principle of the transient dual wavelength pyrometer has been explained. However, the size of the measurement volume is defined by the choice of the diameter of the aperture a_3 in figure 73. In order to match a desired 2.5mm cylindrical volume, the pyrometer had to be modelled and this is the subject of the following section.

IV.3.2.1.3. Modelling the pyrometer

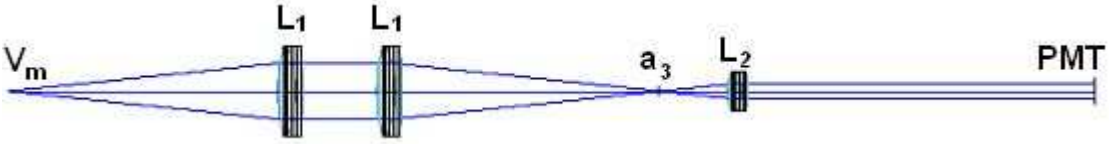

Figure 77: Side view of the pyrometer optical collection system as declared under code V. The left focal point is located within the measurement volume V_m. Note that the lens front and back apertures a_2 and a_4 are declared in the software as lens apertures and therefore solely the aperture a_3 is represented here. The PMT receiver surface on the far right is declared as the surface apertured by a_5 (6.5mm diameter).

In order to define the required diameter for the aperture a_3, Code V® was used to model the pyrometer. Since both photomultiplier tubes photocathodes have identical illumination surfaces and are set at the same distance $d_4 + d_5$ from the back lens L_2 of the Gaussian telescope, a simple flat apertured collection surface of 6.5mm diameter was used as a calculation simplification.
The aperture a_3 has to fulfil two requirements:

(1) the aperture should limits the cylindrical measurement volume diameter to less than 2.2 mm ;
(2) the detector area should to be filled with a 6.5mm parallel beam of light as the aperture not only limits the measurement volume size but also the detector illumination .

Ray tracing was performed using a large number of start points along the imaginary diameter of the measurement volume (measurement volume transverse axis). Ray tracing was also performed in the same manner on the longitudinal axis (the detection axis in figure 72) along the length of the cylinder to test for compatibility between pyrometer transmissivity and a 3.2mm wide laser beam. Transmissivity was deducted using the RMS spot size calculation method. The diameter a_3 was then determined using a "trial and error" approach, as illustrated in figure 78 below. Taking into account the circular symmetry of the system , a large number of light rays were placed along the transverse axis in place of the measurement volume by steps of 0.05 mm and the same was performed on the longitudinal axis.

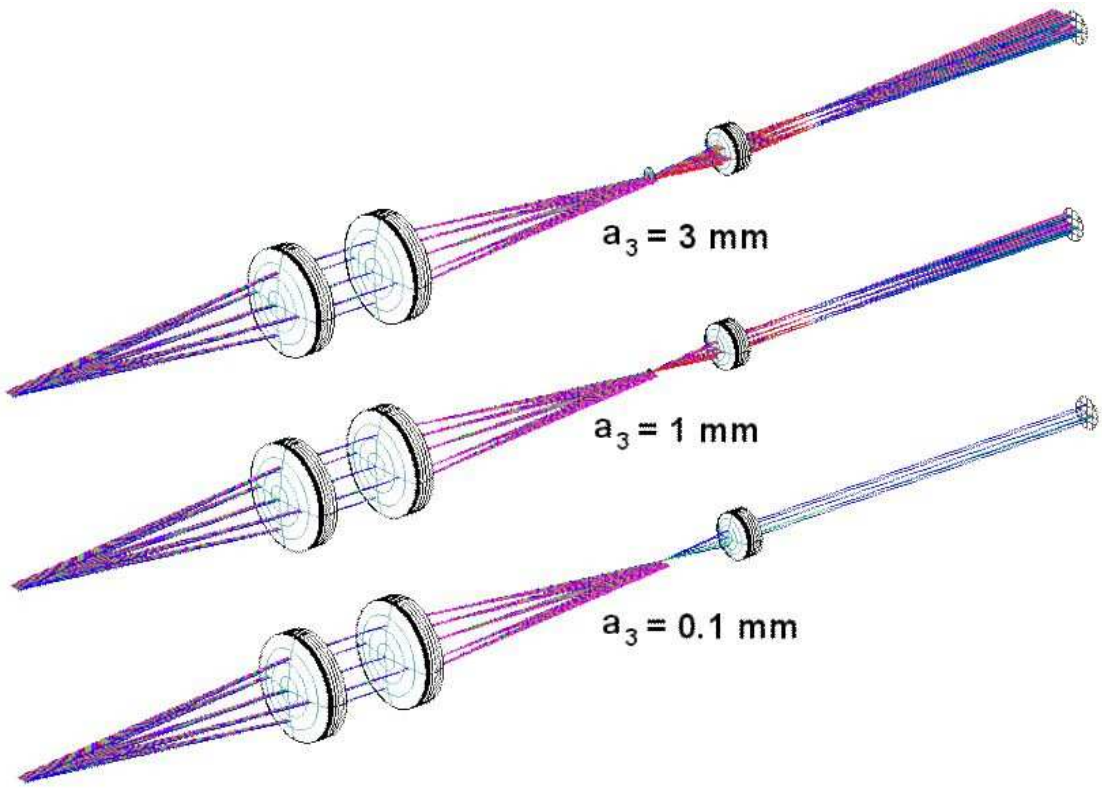

Figure 78 : The three situations faced during ray-tracing calculation. An aperture diameter of 3mm would overfill the detector surface (top), whereas a 1mm diameter matches the detector surface (middle) and a 0.1 mm diameter underfills the detector surface. Note that for illustration purposes only the ray starting along the transverse axis are illustrated.

Taking into account the rotational symmetry of the system, results are presented in figure 79. As illustrated, a diameter of 1 mm was found ideal for the aperture a_3 as it presented maximal transmissivity across 1.1mm radius (2.2 mm diameter) on the transverse axis of the measurement volume and maximal transmissivity along more than 3 mm on each side of the focal point V_m (>6mm maximal transmissivity) on the longitudinal axis of the measurement volume.
In summary, the optical design of the pyrometer includes careful consideration of:

(1) an efficient f/3.16 optical collection and light conditioning system;
(2) high gain light detectors with adequate sensitivity; quantum efficiencies, which will determine the later pyrometer efficiency and pyrometric factors;
(3) the measurement volume transmissivity and calibration requirements.

Next to be precised is the electronic system to be used in order to acquire, calibrate and perform LII measurements.

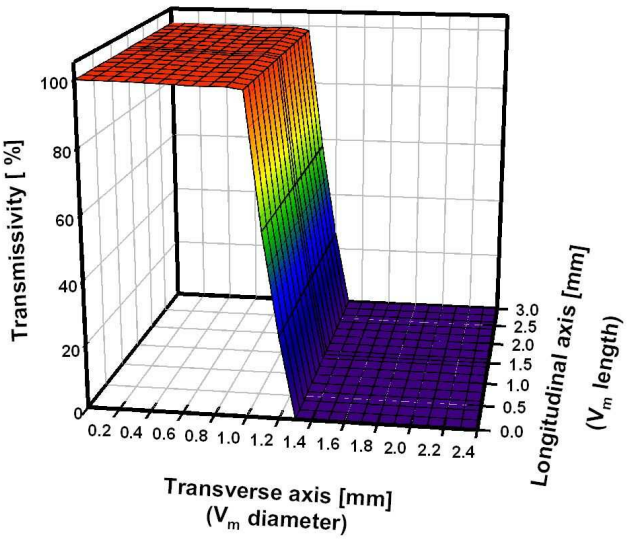

Figure 79: Transmissivity of light from the measurement volume cylindrical extremity to the detector surface . The longitudinal axis is the detection axis itself with the transverse axis perpendicular defining the diameter of the cylindrical measurement volume V_m.

IV.3.2.2. Electronic design of the pyrometer.

The requirements for the electronic system behind the pyrometer were the following:

(1) the photomultiplier modules (PMT) gains had to be programmable
(2) signals out of the PMT modules had to be acquired by means of a digital storage oscilloscope (Gould DSO 4074A, 400 MHz)
(3) the pyrometer calibration had to be traceable to NIST standards and eventually the whole instrument could become deployable as a field instrument.

The chosen electronic layout is best described in the schematic below (figure 80).

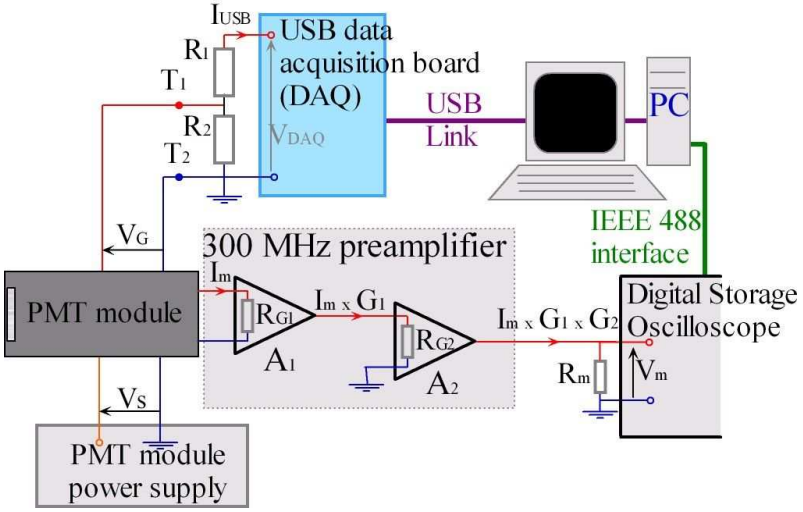

Figure 80: Pyrometer electronic system schematic used for each photomultiplier tube (PMT) module.

The photomultiplier tube being included in a module comprising a miniaturised stabilised high voltage supply requiring simply a 15 V DC feeding voltage V_s took

off the burden of supplying a high voltage directly to the electron multiplier tube divider bridge. This miniaturised high voltage supply required two electrical inputs: a stabilised 15V DC power source ; and a control voltage V_G ranging between 0.25 to 1V DC to set the high voltage level. Whereas the 15V power source was a dedicated off-the-shelf device available from Hamamatsu® (PMT power supply model C7169), the control voltage required a precise computer-programmable voltage supply. The requirements for the gain voltage V_G, as the gain is very sensitive, is to be ripple-free, stabilised and accurate, preferably set with a high resolution system, so as to achieve an accurate and stable gain. There was also a need for the PMT gains to be computer-controlled in parallel with the digital storage oscilloscope. An efficient solution was found in the used of a portable low cost USB Data Acquisition (DAQ) board (Measurement Computing PMD 1208 FS USB personal measurement device) complete with two Digital to Analogue Converters (DAC) capable of delivering a consistent 15 mA leakage current. However the DAC 's were only 12 bits resolution on a range for V_{DAQ} of 0 to 4096 V, meaning the voltage resolution available was limited to 1 mV where a resolution of 500µV and less was required to achieve a repeatable gain. It was therefore decided to use the leakage current available from the DAQ to drive a precision resistor voltage divider bridge constituted by R_1 and R_2 to match the DAQ voltage range to 0-1V. High precision (0.01%) 0.6 W resistors were used in order to get an accurate 1/3 dividing factor with R_2 = 500 Ω and R_1 = 1000 Ω. Therefore the gain voltage V_G, with the internal impedance of the PMT tube module neglected, expresses as:

$$V_G = \frac{V_{DAQ} \cdot R_2}{R_1 + R_2} \qquad \textbf{(85)}$$

corresponding to a dividing factor of $\frac{R_2}{R_1+R_2} = 1/3$. More realistically, the PMT is specified to possess and internal impedance R_Z = 100Ω. Usually, R_1 and R_2 are chosen such as $R_Z >> R_1 > R_2$ so that R_Z does not influence the system. However, R_1 and R_2 had to be chosen in order to limit the amount of current each DAC from the USB device has to provide to 3 mA. Therefore the internal impedance of the PMT module has to be taken into account and V_G becomes:

$$V_G = \frac{V_{DAQ} \cdot \frac{R_2 \cdot R_Z}{R_Z + R_2}}{R_1 + \frac{R_2 \cdot R_Z}{R_Z + R_2}} \quad \textbf{(86)} \text{ and the dividing factor } \frac{\frac{R_2 \cdot R_Z}{R_Z + R_2}}{R_1 + \frac{R_2 \cdot R_Z}{R_Z + R_2}} = 0.332226 . \textbf{(87)}$$

The main attraction for using high precision (0.01%) resistors is not to guaranty a dividing factor, but to ensure both thermal and repeatability with time so as to guarantee a fixed gain curve during the whole course of the experimental work being carried on. As the accuracy (<0.02%) of the voltage divider bridge is far better than the DAC being used, the use of a divider bridge does not add any noticeable uncertainty and will eventually divide by a 1/3 factor any systematic error characteristic of the DAC's.

The photomultiplier tube outputs a current I_m proportional to its internal gain and the light intensity shun onto its photocathode. The output current range is 0 to 100µA which are shunt to ground through a 50 Ω resistor. Therefore, without amplification *100µA x 50 Ω = 5 mV* would be generated at the input of the digital storage oscilloscope. Because the oscilloscope itself has a resolution of 1 mV and a noise level of 2mV, amplification was required. A Stanford Research 445A four channel 300 MHz current preamplifier was selected for its low noise and high linearity

characteristics. Four preamplification channels were therefore available: all four of them presented a voltage gain of five and three of them had an internal impedance R_G of 50Ω while the fourth channel had an virtual internal impedance(bootstrap) of 500Ω. This system eventually results in a current amplification factor of 5 for ordinary channels and 50 for the bootstrapped channel. The amplifier channels can also be cascaded, with a time resolution of 3 ns per channel, meaning a total of 6ns time resolution when considering a PMT output twice amplified. Predictably PMT_1 would be receiving the weakest light pulses and eventually required the most amplification. Effectively each photomultiplier tube output current was amplified twice (see figure 80 above) using two preamplifiers A_1 and A_2 of current gain respectively G_1 and G_2 and internal impedance RG_1 and RG_2. A table of the gains used is provide in table 5 below:

	PMT_1	**PMT_2**
RG_1 [Ω]	500	50
RG_2 [Ω]	50	50
G_1 [ ]	50	5
G_2 [ ]	5	5

Table 4: table of internal impedances RG and effective current gain G per current preamplifier

Finally, the amplified current I_m x G_1 x G_2 is measured on the digital storage oscilloscope across a precision metal film 50 Ω(0.01%) resistor R_m by measuring the voltage drop V_m across it. Usually digital storage oscilloscopes possess an internal programmable termination impedance but the oscilloscope used to acquire pyrometer readouts (Gould 7074A) did not include this option. Readouts were made with an automatic voltage inversion, turning negative current peaks into a positive readout, using a 10 bit equivalent resolution and sent to the computer, where the PMT output current I_m was deducted as:

$$I_m = -\frac{\frac{V_m}{R_m}}{G_1 \cdot G_2} \qquad \textbf{(88)}$$

To summarise, two parameters are computer-controlled: both pyrometer channels ($PMT_{1\&2}$) gains using two DAC's from a portable USB data acquisition board; and the PMT output measurement currents I_m, which are retrieved from the digital storage oscilloscope using a purpose-made IEEE 488 parallel interface. The digital storage oscilloscope was typically triggered from the laser Q-switch TTL output. All signals were conducted via BNC 50Ω cables to minimise noise picking.

The actual assembly and optical alignment of the pyrometer, together with the calibration of the gain electronics and a check of the Stanford Research preamplifier gains are available in great details in appendix E.
Once the dual wavelength pyrometer was assembled, aligned and checked both physically and electronically, the photomultiplier tube modules were calibrated, and this is described in the following section.

IV.3.2.3.Photomultiplier tubes calibration

The same strip filament used for calibrating the spectrographic system was used and placed of the focal plane (i.e. the measurement volume) of the pyrometer collection lens. This is best described in figure 81 below:

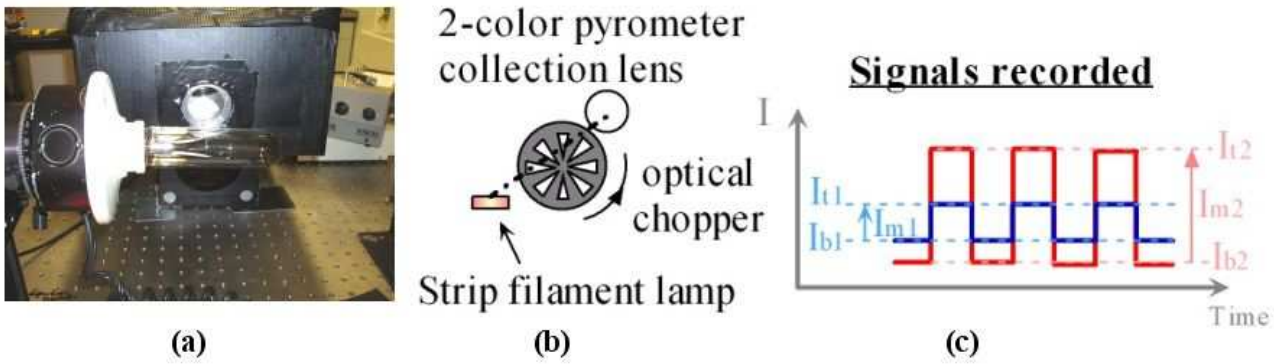

Figure 81: Calibration procedure.

(a) image of the optical table with the calibration strip filament placed at the measurement volume V_m location before insertion of the optical chopper

(b) principle of the calibration: the light emitted at the centre of the tungsten strip filament is chopped before reaching the pyrometer collection lens, effectively creating an input square wave train of light pulses of known radiance

(c) corresponding current signals with photosensors output current plotted as a function of time. The blue traces correspond to PMT_1 (500nm); red traces match PMT_2 (700 nm). I_m's are measured as pulsed currents, meaning as a signal level I_t discriminated against its base current I_b: $I_m = I_t - I_b$.

The centre of the strip filament lamp, marked by a dot , is centred on the detection axis at the focal point of the pyrometer collection lens, corresponding to the front circular surface of the collection volume V_m . The system used to monitor the filament temperature is the one described in section IV.2.1.2. for the spectrograph absolute light calibration. The light signal emitted by the filament is modulated into a square wave train using an optical chopper (chopping frequency 10 KHz) before reaching the pyrometer collection lens. The pyrometer in turn conditions the light signal into the two distinct photosensors PMT_1 and PMT_2. Measurements of the resulting current square wave trains were recorded using the digital storage oscilloscope (Gould 4074A) triggered on the leading edge of PMT_2 current output and repeatedly send to a computer data acquisition software through an IEEE 488 serial data link for recording. Photomultipliers signal outputs were multiple averaged (typically 500 averaged waveforms) to achieve high resolution and lessen noise levels. From the obtained waveforms (see figure 81-c) the signal levels I_t's were computed and a current output matched with its corresponding light intensity input. Such a pulse train configuration is used for two reasons: firstly, to relieve the photosensors electronics; secondly to provide calibration signals similar in shape to the measured signals, that are light pulses. Calibrations were performed with a constant lamp temperature while the photomultiplier gain was increased until the saturation level was reached (i.e.

>100 μA), and then a lower lamp temperature set in order to increase the gain setting until the maximum recordable gain could be calibrated.

The radiance calibration method used for the photomultiplier is the same as the one used for the spectrograph as the same calibration principle is used here. The main difference here is that each pyrometer channel combined quantum efficiency previously illustrated in figure 76 is taken into account when calculating the calibration light intensity P_{CAL}. The spectral radiance emitted by the tungsten strip filament $R_s(\lambda)$ (that is, the power emitted per unit area, per unit solid angle and per unit wavelength interval) is given by:

$$R_s(\lambda)=\frac{2\cdot c^2\cdot h\cdot\varepsilon(\lambda,T)}{\pi\cdot\lambda^5}\cdot\left(e^{\frac{hc}{\lambda kT}}-1\right)^{-1}=\frac{C_1\cdot\varepsilon(\lambda,T)}{\pi\cdot\lambda^5}\cdot\left(e^{\frac{C_2}{\lambda T}}-1\right)^{-1} \qquad \textbf{(89)}$$

Where $C_1 = 3.74177 \text{ x}10^{-16}$ W.m^2 and $C_2 = 0.014388$ m.K are respectively the first and second radiation constants, and $\varepsilon(\lambda,T)$ is the emissivity of Tungsten as a function of wavelength and temperature. The calibrated lamp has a known brightness temperature T_B which is the temperature at which a perfect blackbody would emit the same amount of radiation at 650 nm from which the true filament temperature T_S can be obtained considering the exponential term >>1 in equation 89 given the temperatures and wavelengths used here:

$$T_s=\left(\frac{1}{T_B}+\frac{\lambda}{C_2}\cdot\ln\left(\varepsilon(\lambda,T_S)\right)\right)^{-1} \qquad \textbf{(90)}$$

With the known emissivity of Tungsten as a function of temperature and wavelength, the filament light intensity (radiance) as a function of wavelength can be computed and each input photomultiplier light intensity P_{CAL} be expressed as:

$$P_{CAL}=A_{strip}\cdot 4\pi\cdot\int_{\lambda 1}^{\lambda 2}R_s(\lambda)\cdot\tau_f(\lambda)\cdot d\lambda \qquad \textbf{(91)}$$

Where A_{strip} is the measurement volume V_m circular surface emitting area sampled on the strip tungsten strip filament, that is $A_{strip}=\pi\cdot r_{Vm}^2=3.801\text{x}10^{-6}$ m^2.λ_1 and λ_2 are the start and end of the considered wavelength range (typically 400-800 nm). The system assumes that the area is emitting uniformly over 4π steradians. $\tau_f(\lambda)$ is the pyrometer channel overall quantum efficiency considered. Then the gain calibration factors are measured for a wide range of gain control voltage V_G and at least two different lamp brightness temperatures, therefore defining the pyrometer gain calibration. At each gain V_G set, photomultipliers are considered as linear with the gain G_{CAL} defined as:

$$G_{CAL}=\frac{I_m}{P_{CAL}} \qquad \textbf{(92)}$$

With I_m the current level measured in microamperes during calibration. Gain curves are typically exponential curves and therefore an exponential fit is performed on the gain calibration results curve, as displayed on figure 82.

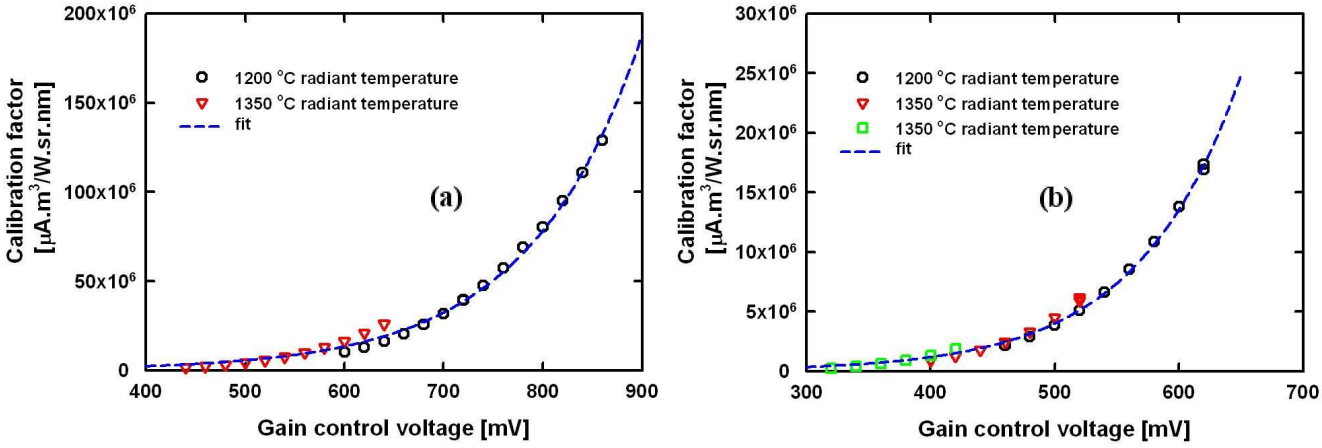

Figure 82: Gain calibration results of the photomultipliers in terms of calibration factor vs gain control voltage V_G.
(a) 700 nm channel (PMT_2)
(b) 500 nm channel (PMT_1)

Exponential fit results are given below, with C_{G1} and C_{G2} respectively the gain calibration function of respectively PMT_1 and PMT_2.

$$C_{G1}=3.37168\cdot10^{4}\cdot\exp\left(9.793586\cdot10^{-3}\cdot V_G\right) \qquad \textbf{(93)}$$

$$C_{G2}=6.37968\cdot10^{3}\cdot\exp\left(1.300921\cdot10^{-2}\cdot V_G\right) \qquad \textbf{(94)}$$

Taking into account deviations, non-linearities and I_m measurement uncertainties, absolute light intensity uncertainties obtained are estimated in the range 5-8%, with relative uncertainties rising when the light level is decreased.

Now that the optical and electronics designs of the dual wavelength pyrometer have been detailed, together with the calibration of the photomultiplier tubes, the system is ready to be programmed and, once programmed, to be deployed as a measurement instrument.

IV.3.2.4. Pyrometer software interface.

The dual wavelength pyrometer is automated using a purpose-made software written under Labview®. The software operations are dictated by the electronics design. In practice (see figure 80), each photomultiplier tube module control voltage V_G is controlled via an applied voltage V_{DAQ}. The relation between V_{DAQ} and V_G being characterized and calibrated (see appendix E), the software includes a full automation for the gain (or consigne) voltage V_G to be applied to each photomultiplier according to the user requirements. Also, the total current gain used (G_1 x G_2) is declared by the software user. Once the gain of the photomultipliers are set, a few seconds are waited by the software in order for the photosensors to stabilise before measurements are taken. All measurements performed are triggered on the Q- switch TTL signal from the Quanta Ray laser unit.

The following parameters can be configured on the first tabulated page of the software (see figure 83):

- oscilloscope vertical sensitivity [V/div] for each photomultiplier and the power meter readout. Note that PMT_1 is denoted in the software as "blue channel", PMT_2 becomes " red channel" and the power meter "photodiode".
- oscilloscope timebase [seconds/div]
- current amplifications for the red and blue channels

Note that the number of oscilloscope captures and the consigne voltages V_G, and pretrigger value can be updated at any time while the program is running for ease of measurement setup by the user. The software also features a live display of the state of the DAC's used to generate V_{DAQ} as errors may be generated on a random basis. A filtering and discrimation function is also available for live measurement display, including a threshold level above which filtering is started whereas the filter itself is a simple moving average of which the peak width is modulable. Measurements are buffered on an onboard memory, which can be reset using the "validate oscilloscope…" button. A save would save all measured currents, signal intensities and temperatures measured. A simple stop button stops all measurements and reset all devices (USB, onboard memory buffer and oscilloscope). Details are available on figure 83 below.

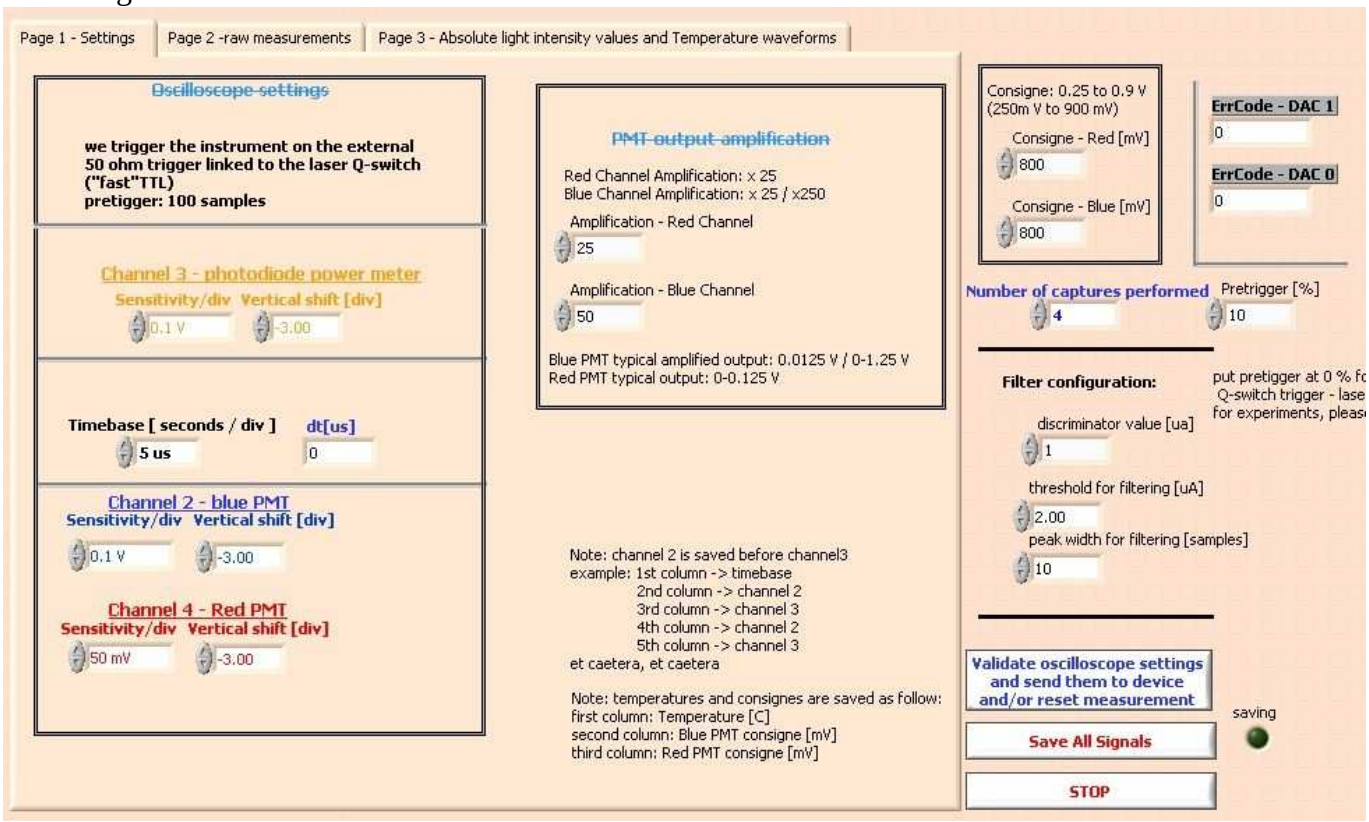

Figure 83: software Settings tabulated page

Once the measurements are started, a live acquisition and display of LII signals takes place on the "raw measurements" page (see figure 84), and displays simple photomultiplier currents.

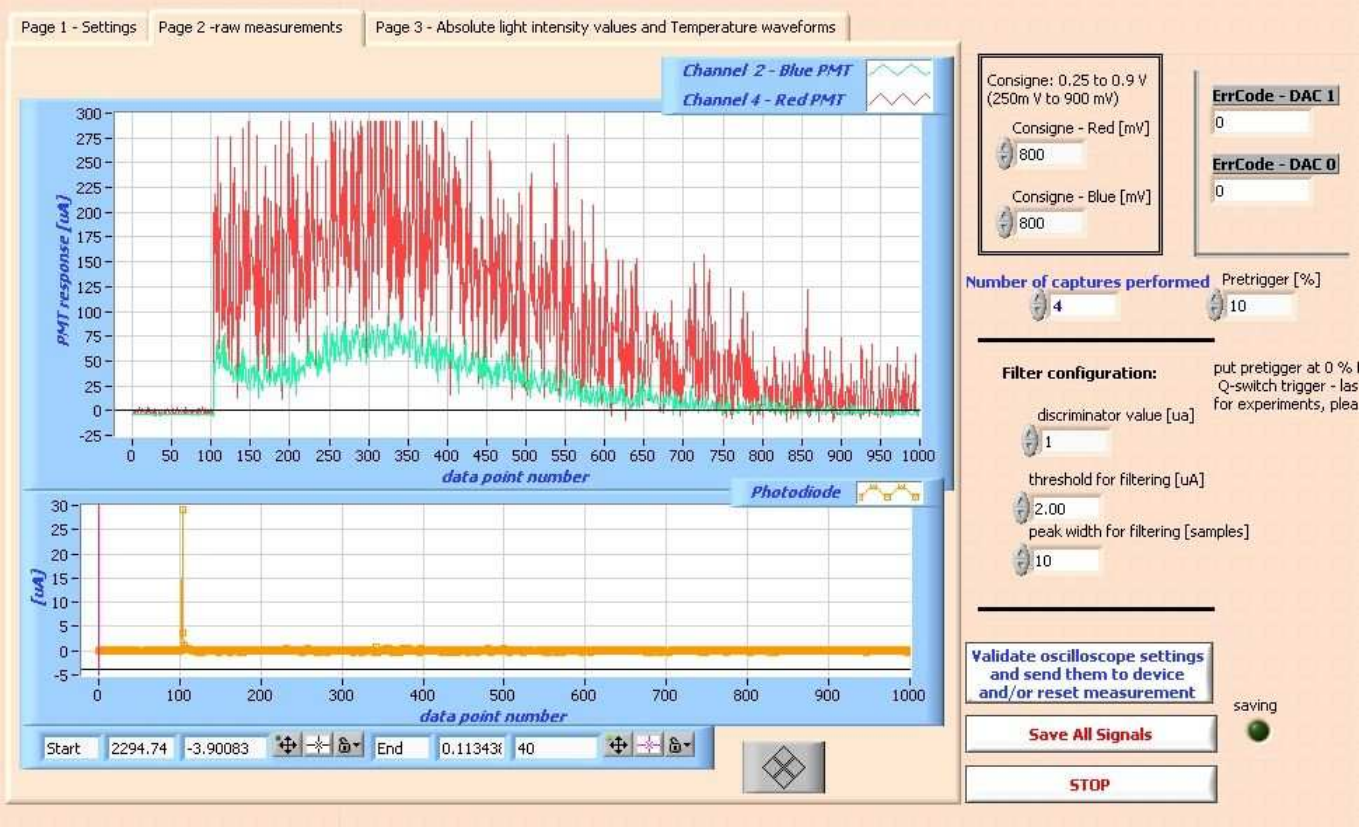

Figure 84: "raw measurements" tabulated page.

Then, using the discriminator value, threshold start for filtering and the specified filtering peak width, signals are automatically filtered, base current substracted and processed in order to obtain an accurate view of the light intensity measured and corresponding temperatures as determined by the pyrometric method (see figure 85).
As a summary, the software was an adequate data acquisition system capable of controlling and automating the pyrometric system measurement while storing all selected measurements taken. The software also included a live processing feature in order to provide the user with a qualitative view of the measurement being taken.

Overall, the dual wavelength pyrometer is a complete detection system on its own. In terms of the work involved in setting such a measurement system, both complete electronics and optical designs were necessary. Implementation and assembly itself required multiple calibrations and checks while providing a software interface proved a complex operation, both in terms of automation and data processing. In more technical terms, the dual wavelength pyrometer has a time resolution of 6 nanoseconds and can record and process LII under vacuum signals. However, the dual wavelength represents only part of the detection system involved for the Laser-Induced Incandescence under vacuum investigation, as the pyrometer was associated with an absolute light intensity calibrated Intensified CCD camera, which measurement method, calibration and image processing methods are the subject of the following section.

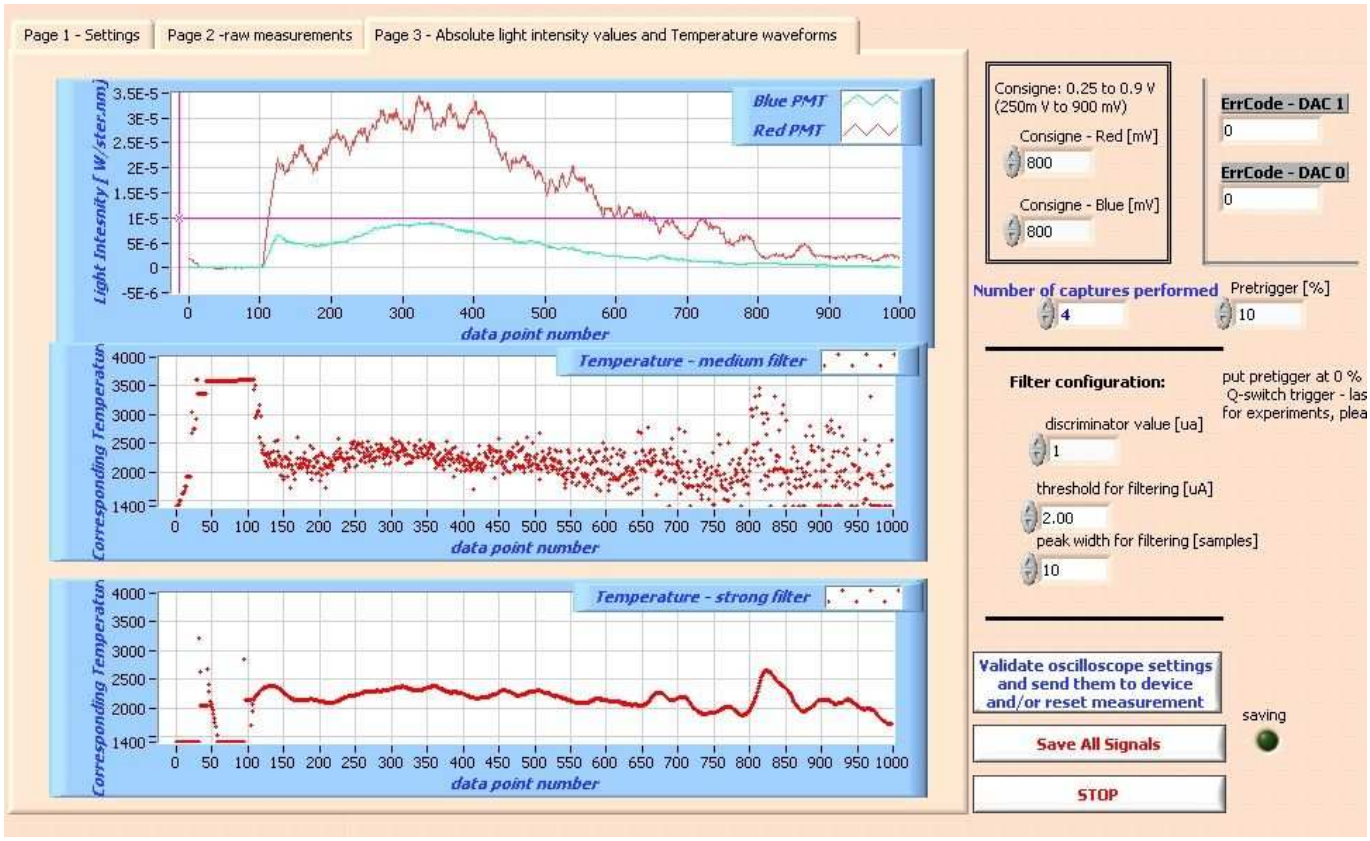

Figure 85: "Absolute light intensity values and Temperature waveforms" software tabulated page. Note that temperature values displayed here are erroneous as PMT_2 light intensity measurements were later corrected using the latest calibration factors from equations 93 and 94.

IV.3.3. The absolute light intensity calibrated Intensified CCD (ICCD) Camera .

The Intensified CCD camera fulfilled three distinct roles throughout the LII under vacuum investigation:

- The camera provided absolute light intensity measurements, after a radiance calibration had been applied to the camera readout. This way the detectivity gain achiever by the LII under vacuum technique could be proved.
- The camera was also used to image carbon agglomerates and characterize them in terms of size, intensity, and physical phenomena occurring.
- And finally, the camera was used to perform Particulate Image Velocimetry (PIV) on eventual agglomerates ejecta.

IV.3.3.1. The two- dimensional absolute light intensity measurement coupled to temperature sensing principle.

The first use of the camera was to provide two- dimensional absolute light intensity measurements coupled to the pyrometer temperature measurement. Indeed, if a two dimensional absolute light intensity measurement is performed simultaneously to the soot temperature measurement, the 2D map for local soot volume fractions can be obtained. And extension of this principle is the measurement of primary particle per agglomerate or aggregate, provided that optically agglomerates are isolated and sufficient (time integrated) light levels are obtained. The instantaneous signal emitted by an ensemble of n of primary particle of diameter d_p over a wavelength region $\Delta\lambda = \lambda_2 - \lambda_1$ is expressed in equation 95 (Michelsen, 2003), assuming the measurement plane emits as a Lambertian surface over 4π steradian:

$$S_{agg} = n \cdot 4\pi^2 d_p^2 \cdot \int_{\lambda 1}^{\lambda 2} \varepsilon_\lambda \cdot \frac{2 \cdot \pi \cdot h \cdot c^2}{\lambda^5 \left[\exp\left(hc/\lambda \cdot k \cdot T\right) - 1\right]} d\lambda \qquad \textbf{(95)}$$

When the signal is processed using a gated system , that is performing a time-integrated measurement, temperature variations as a function of time have to be taken into account and the particle temperature T becomes a function of time T(t). The LII signal S_{gate} emitted over a period of time $\Delta t = t_2 - t_1$ and sensed by a device of quantum efficiency Σ(λ) and light collection efficiency Ω then becomes:

$$S_{gate} = n \cdot \Omega \cdot 4\pi^2 d_p^2 \int_{t1}^{t2} \int_{\lambda 1}^{\lambda 2} \varepsilon_\lambda \cdot \frac{2 \cdot \pi \cdot h \cdot c^2}{\lambda^5 \left[\exp\left(hc/\lambda \cdot k \cdot T(t)\right) - 1\right]} \cdot \Sigma(\lambda) d\lambda dt \qquad \textbf{(96)}$$

Therefore, if one can measure S_{gate} using a photometrically calibrated apparatus, the possibility arises for determining the number of primary particulates n within an aggregate by measuring its produced signal. However three conditions have to be respected: firstly S_{gate} has to be isolated and measurable; secondly the particulate temperature history has to be measured independently; thirdly the primary particulate diameter has to be either assumed or measured. In this case the primary particulate diameter is specified as 15 nm and this value has been used throughout the experimental data processing. In parallel, the particulate temperature history is measured by the pyrometer. Therefore, if the particulate number within an ensemble

of primary particulates can be measured, then obviously and more generally the ICCD system permits the measurement of particulate matter concentrations on a larger scale. The section that follows will be dedicated to determine the ICCD camera system quantum efficiency in order to later perform a radiance calibration.

IV.3.3.2. ICCD camera optics spectral transmissivity calibration

The Intensified camera is equipped with, from the measurement volume to the intensifier: a 700 nm short-pass filter, a 500 nm long-pass filter, a Nikon f/2.8 macroscopic lens and an 82 mm extension tube. Although approximate transmissivity data was available for both optical filters, no details were available for the macroscopic lens transmissivity. Also, the position of the lens, that is 13 cm from the measurement volume V_m meant that optical filters were not used in the typical assumed approximation that all incoming rays are incident perpendicular to the filter surface. Therefore a spectrometric calibration was necessary in order to calibrate the ICCD receiving optics quantum efficiency. In order to perform this calibration, the filters, lens and extension tube were set to image the measurement volume V_m and then carefully removed from the ICCD to be calibrated in their final set position. Front optics calibration was performed by using the tungsten strip filament lamp as a reference. The filament being placed at the imaging distance of the lens assembly, the filament image was then relayed onto the spectrometric measurement system imaging surface by the ICCD receivers optics. Therefore, by comparing the original lamp spectrum and the spectrum measured with the ICCD optics relaying the same lamp spectrum , the transmissity of the receiving optics could be determined, as illustrated in figure 86:

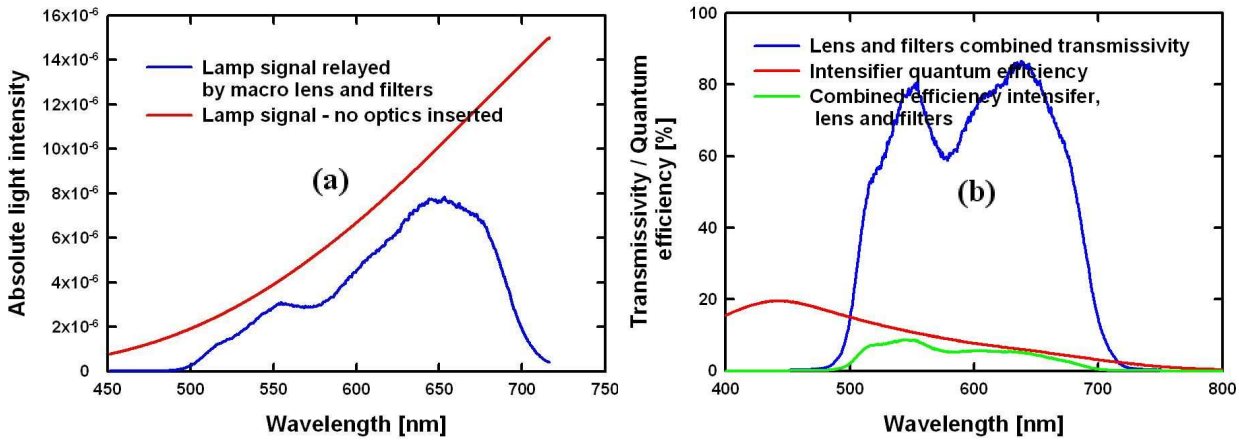

Figure 86: ICCD system spectral efficiency calibration.
(a) absolute light intensity measurements: original lamp signal (red) measured using the spectrometric system described in section V.2.1. and lamp signal relayed by the assembled filters, macro lens and extension tubes (blue).
(b) 2D system combined quantum efficiency determination. The blue curve represent the results obtained in (a). Intensifier quantum efficiency data (red) was provided by the manufacturer

The optics transmissivity data was then combined with the intensifier quantum efficiency data provided by the manufacturer and the total ICCD quantum efficiency

determined adequately. As a summary, the Intensified CCD camera is equipped with what can be called a high efficiency 200 nm bandpass filter centred at 600 nm combined to an f/2.8 (~13 % light collection efficiency) macro lens and an intensifier featuring between 5-10 % quantum efficiency for the wavelength range of interest. This system, once spectrally calibrated, was then ready to be calibrated in terms of absolute light intensities.

IV.3.3.3. ICCD camera absolute light intensity calibration

In order to perform an absolute light intensity calibration on the Intensified system, images of the strip filament lamp calibrator at controlled brightness temperatures were taken with the intensified CCD camera. The procedure and monitoring of the lamp are the same as described in section IV.2.1.2 for the spectrograph absolute light calibration. The ICCD camera was always run at the maximal intensifier micro-channel plate voltage (900V) in order to use the highest system sensitivity setting available. All calibration images were at first background substracted taking a filament image at high temperature with a set gate setting and then the same filament image at room temperature was substracted from the calibration image. Since all measurements and calibrations are performed in a dark room and are shielded from any reflections (computer screens, laser flash lamps, etc…), it was found that background substraction could be performed by substracting the value 66 (RMS 1.2) to each pixel readout value as no background image else than what appeared to be the camera frame grabber ADC offset was discernable. In order to define precisely the calibration (or sensing) surface per pixel, an ICCD spatial calibration was performed using reflections of different laser beam profiles on test paper that had been precisely measured during beam profiling and concluded to a spatial resolution of 22±0.1 μm per pixel. The Intensified system was not flatfielded, as the spatial detector was assumed to present a uniform spatial sensitivity within the central sensing region of V_m and the calibration filament presented limited spatial uniformity (see figure 88 for details). Indeed, the filament radiance uniformity presented a temperature-dependency, with a tendency to provide increased illumination uniformity with increasing brightness temperature. Therefore a square central area of 0.7 mm side (1024 pixels) was used for calibration, with an average pixel value varying within less than 5% across the calibration surface above 1500 °C brightness temperature. Gate durations and filament temperatures were limited in order to provide readout values of less than 1000 counts per microsecond, which is the manufacturer's specified sensitivity linearity limit of the intensifier. The absolute light intensity calibration method itself is described in sections IV.2.1.2. (Spectrograph absolute light calibration) and IV.3.2.3 (Photomultiplier tubes calibration), with the sole difference that the average ICCD counts value was counted per pixel and was then ratioed with the incoming light intensity onto each pixel imaging surface (22 μm side squarre). Three lamp brightness temperatures were used: 1613.4 ˚C,1656.8˚C and 1726.4˚C. The calibration results are contained in figure 88.

The measurement principles have been explained for measuring calibrated 2-D soot volume fractions profile by combining an absolute light calibration applied to an intensified CCD camera and the temperature readouts of the dual wavelength pyrometer. The ICCD camera is now calibrated and absolute light intensity measurements can be taken. The second function of the ICCD camera is also to

characterize incandescent carbon agglomerates in terms of size, intensities emitted and physical phenomena occurring. This will be the subject of the following section.

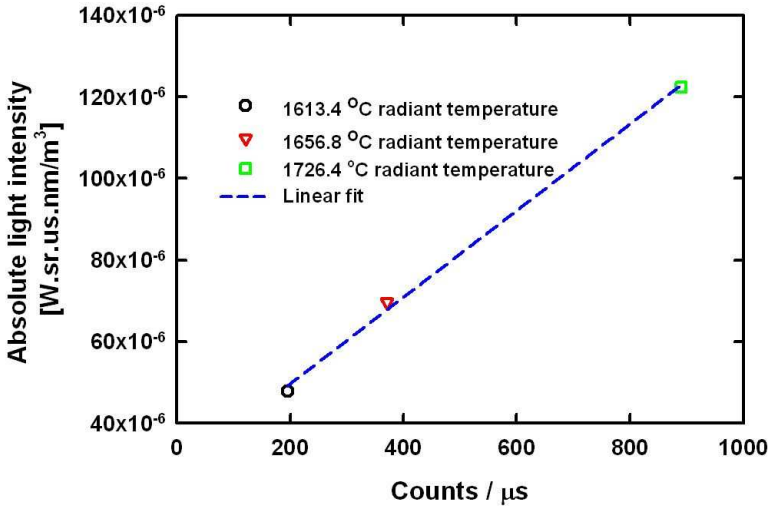

Figure 87: average pixel calibration factor calculated for the Intensified CCD camera system.

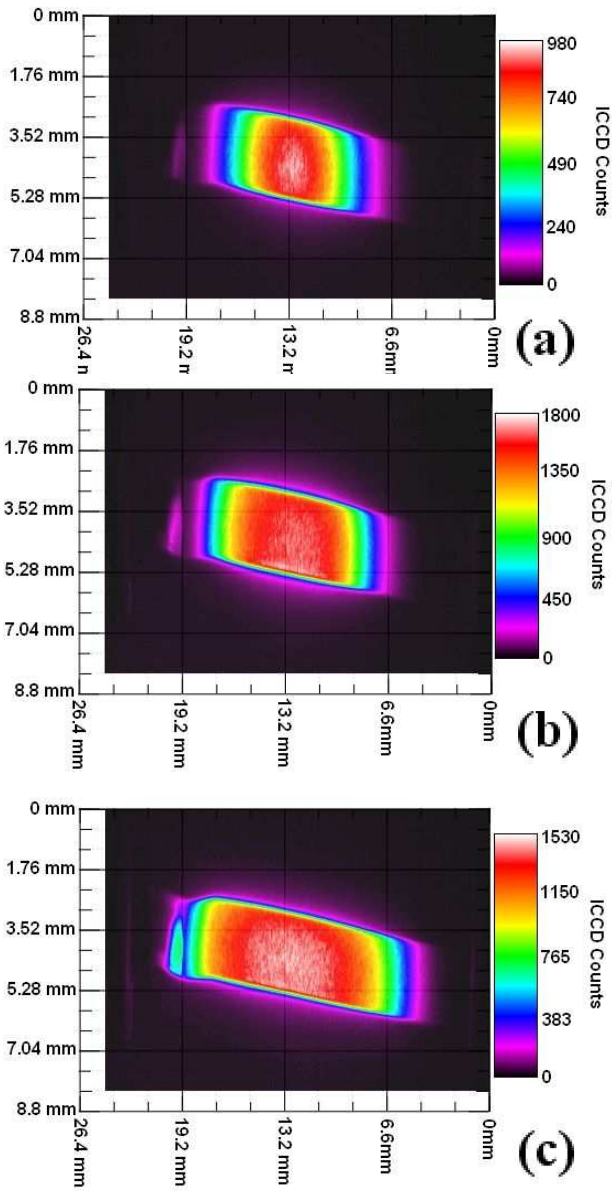

Figure 88: Calibration strip filament uniformity and brightness temperature. All measurements units are in ICCD counts.

(a) 995 °C filament brightness temperature imaged with a 50µs intensifier gate duration

(b) 1297 °C filament brightness temperature imaged with a 10µs intensifier gate duration

(c) 2011 °C filament brightness temperature imaged with a 100 ns intensifier gate duration.

IV.3.4. The Intensified CCD camera : a mean for imaging carbon agglomerates and perform characterizations.

As described earlier, the sample bottle contained a carbon black powder containing both large visible agglomerates and smaller non-visible agglomerated carbon nanoparticulates maintained under high vacuum. Bearing in mind this detail, images of incandescent agglomerates were taken using the Intensified CCD camera system. Images were then processed using Machine Vision algorithms available within the Labview® packages. Some algorithms were modified in order to compensate for measurements not included initially within the software package. A typical machine vision process is illustrated by figure 89. The typical measurements obtained were: the Feret diameter (that is, the longest between the two ends of a particulate), particulate centre position, circularity factors, number of ICCD counts per agglomerate, maximal count value, etc.

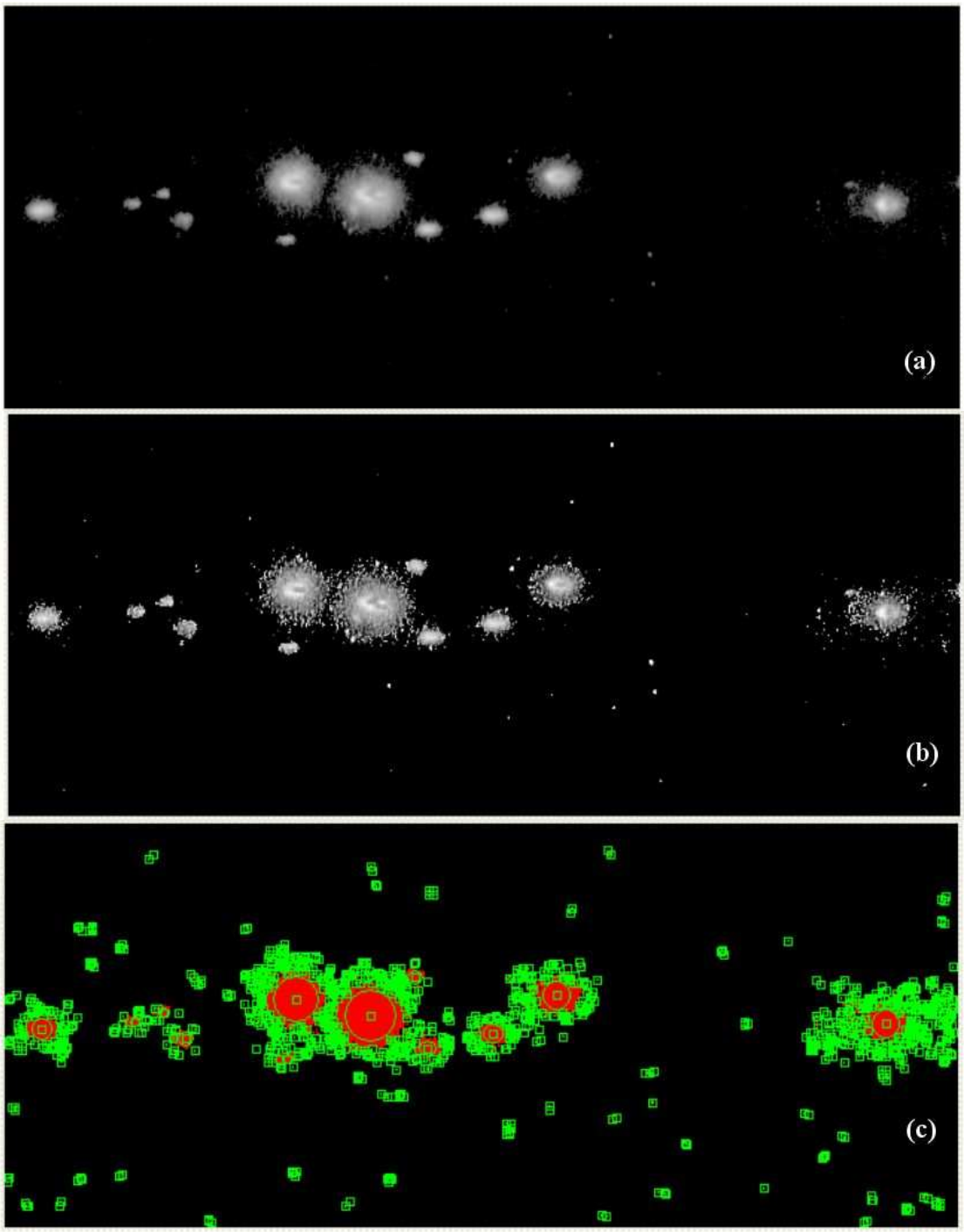

Figure 89 : Image analysis principle using imaging software algorithms.
(a) original measurement image (black and white)
(b) convolution filtering: highlighting details and separating particulates
(c) agglomerates separation and individual morphological analysis

IV.3.5. ICCD and PIV measurements: adaptation of the Particulate Image Velocimetry (PIV) method to ejecta velocity measurements.

As this will be unveiled in chapter V, carbon agglomerates exhibited an explosive behaviour: one large agglomerate would disaggregate into many hundreds (typically 500-2000) smaller aggregates (ejecta) over a 50 μs time scale. Since the phenomenon is faster than typical double-framed camera capacities, ejecta velocities and exit angle where measured using an analogue to single-frame double-exposed PIV. Effectively two intensifier exposures at different delays after laser irradiation are stored onto one single CCD frame that is then readout. The resulting image is a superposition of the original agglomerate with the later ejecta. As the transfer function of an intensifier is a pseudo-voigt function, each particulate centre is actually marked by a sharp intensity two-dimensional peak. By adapting a peak finding algorithm, each peak imaged was then discriminated for shouldering (that is, two peaks interleaved producing an imaginary third one), its intensity recorded as well as its position. The velocity and exit angle of the ejecta from the original agglomerate is then calculated by manually declaring the centre of explosion. The process is visually described in figure 90.

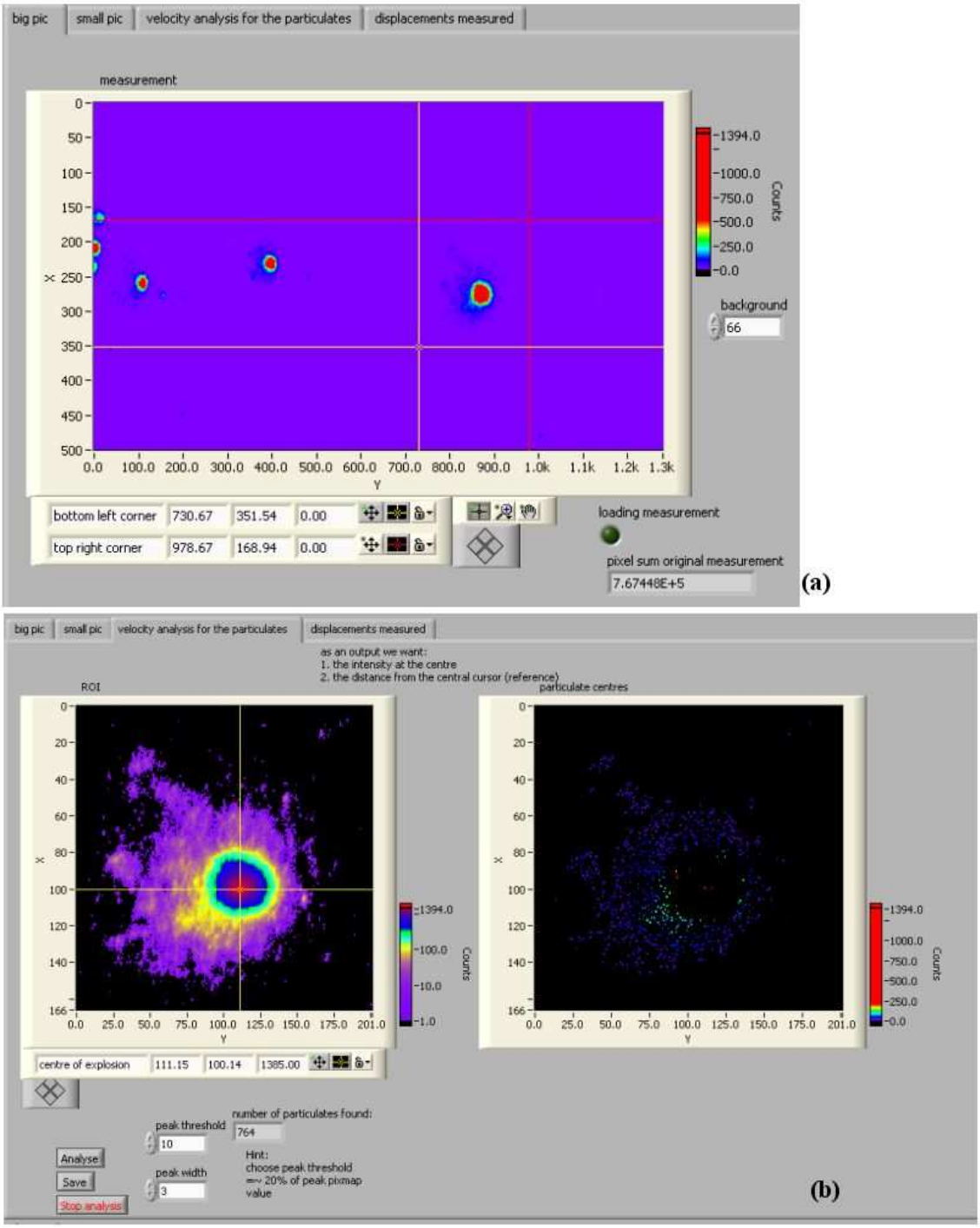

Figure 90: Ejecta velocity measurements.

(a) Isolating an explosion : selection of a Region Of Interest (ROI) using red and yellow cursors

(b) Two –dimensional peak detection. The centre of explosions is manually marked by a cursor.

The conclusions to this subchapter describing the LII under vacuum investigation system are the following:

(1) A near-uniform laser spatial profile of reasonable quality guarantees spatial temperature uniformity within the measurement volume during laser-induced incandescence
(2) Associated with the excitation laser beam are two complex and combined detection instruments: a dual wavelength transient pyrometer and a calibrated ICCD camera
(3) The dual wavelength transient pyrometer had to be purpose-built for this investigation to take place. All design details are given and the system is fully automated. The resulting system is capable of 6 ns time resolution, possess gains high enough for measuring practical LII signals and is calibrated in terms of absolute light intensity to within 5 to 8%.
(4) With the pyrometer performing what are effectively time resolved LII measurements under vacuum, LII under vacuum temperature instantaneous temperature decays can be measured, as well as instantaneous soot volume fractions.
(5) The combination of the pyrometer and a calibrated ICCD camera permits absolute light calibrated 2D LII measurements: with the soot instantaneous temperature measured by the pyrometer, the spatial intensity map measured by the ICCD can be interpreted in terms of local 2D soot volume fraction measurements.
(6) The ICCD camera is also used to measure the characteristics of carbon agglomerates and eventually perform double exposed single frame PIV with a specific computational method.

Following the rather successful investigation of LII under vacuum led at Cranfield University, the sample roller bottles were taken to NRC, Canada. Not only this approach highlighted a desire to validate the results obtained, but also to perform measurements with higher resolution and reach a better understanding of the thermodynamics surrounding LII under vacuum. Therefore the NRC measurement systems are the subject of the following section.

IV.4. Details of the NRC measurement systems

Overall, the results obtained with the pyrometer coupled to the ICCD system proved consistent and reliable. However, they were limited by the detection limits to a fluence range of 0.15 to 0.24 J/cm^2 as the system could not be optimised to measure low concentrations of particulate matter (<1ppb) within a reasonable timeframe and temperature measurement uncertainties were probably in the order range of 50 to 100 K. Therefore the same sample bottles as the ones which endured the measurements taken at Cranfield together with the roller bottle apparatus were sent to the National Research Council (NRC) with the present author as part of a six week measurement campaign which started October 2005. This test campaign aimed at performing high accuracy LII under vacuum measurements at low to medium fluence (up to 0.15 J/cm^2) with state-of-the-art dual wavelengths pyrometric systems. I am very grateful to the Combustion Technology research team at the Institute of Chemical Process and Environmental Technology, NRC, Canada for their invitation and all their advice and help during these experimentations, in particular to Gregory J. Smallwood and Dave R. Snelling for their experience and initiative in letting me use their laboratory as well as Bob Sawchuck, Daniel Gareau, Daniel Clavel for their technical help in implementing the systems and providing means of signal analysis together with Fengshan Liu, Kevin Thomson and Kyle Daun for their sympathy and most precious guidance.

All laser-induced incandescence measurements were performed using the optical layout described in figure 91, which is an adapted version of the dual-laser pulse experimentation test stand that was in use at NRC.

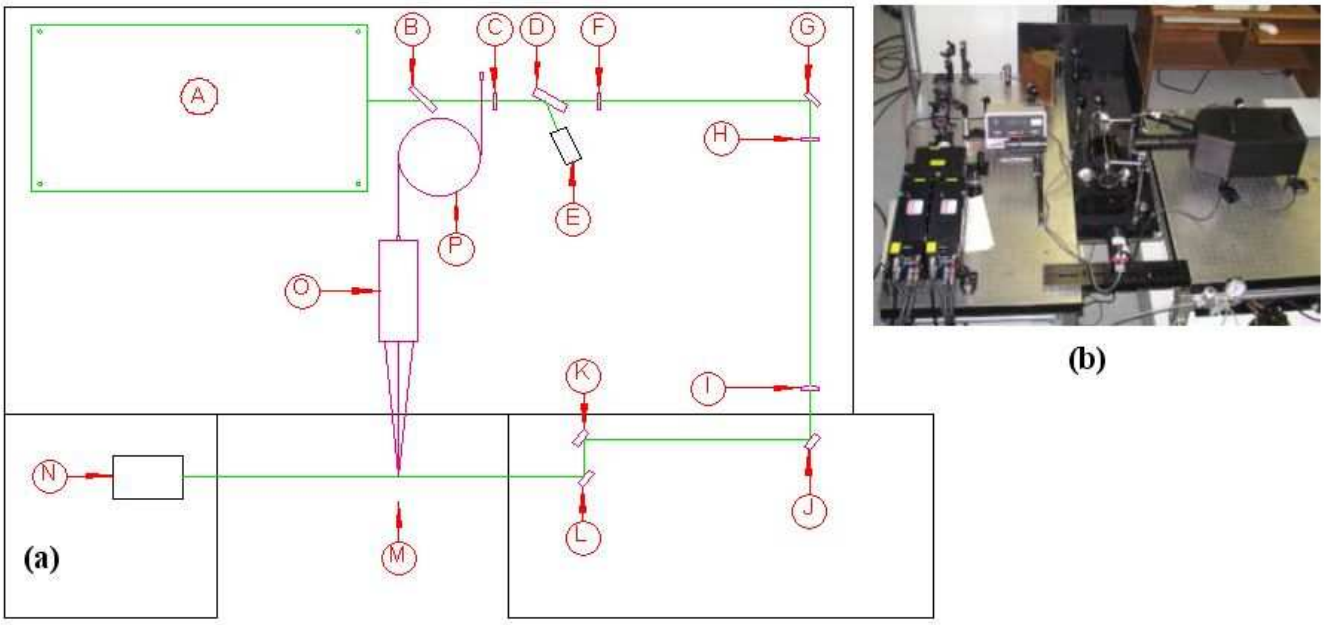

Figure 91: Experimental NRC measurements layout Bob Sawchuck (2005). See text for labels and explanations.
(a) Standard LII system configuration
(b) Top view including both "standard" and "high sensitivity" LII measurement systems, with the high sensitivity sitting on the right hand side of the sample bottle and the collection lens of the "standard" on the left hand side of the sample bottle.

The different parts constituting the measurement system are enumerated below:

(A) A Big Sky CFR200 pulsed Nd-YAG dual head laser is used as the LII excitation source. Being initially part of a dual pulse LII system, this laser presented a defective spatial laser profile on the second pulse. Therefore only single laser pulse LII signals were performed.

(B) A 532nm mirror (New Focus #5124) was tilted down and therefore not reflecting the laser beam during LII measurements. This mirror was inserted into the laser beam path for reflecting the laser beam onto a laser beam spatial profiling system when needed.

(C) A ½ waveplate (CVI QWPM-532-10-2) placed on a rotating mount is then used to adjust the polarization angle of the laser beam.

(D) The thin film plate polarizer (CVI TFP-532-PW-2025) is then used as a laser energy adjustement, as its transmission varies as a function of incoming laser beam polarization. Reflection from the polarizers are sent into a beam dump and only the transmitted part of the laser beam is later used. Maximum transmissivity is achieved for a vertically polarized waveplane and the polarizer transmits uniquely the vertically polarized component of the laser beam.

(E) Beam trap

(F) A second ½ waveplate (CVI QWPM-532-10-2) is then used to tilt the polarization plane of the laser beam from vertical to horizontal. Although this has no application here, this polarization plane change is intended to ease scattering measurements and allow them to be performed at the same height than that of the laser beam.

(G)(J)(K)(L) Are 532 nm mirror (New Focus #5105) are used as a mean of laser beam delivery and spatial position adjustments.

(H) is a precision engineered gold plated rectangular aperture (National aperture slit,1.5mm wide by 2.5 mm tall) through which the laser beam is centred. The image of the laser beam passing through this aperture is then relayed by a 250mm focal length spherical lens (I) (Thorlabs #LA-1461 BK7 25 mm diameter)onto the measurement volume (M). The laser energy passing through the measurement volume is consecutively measured by an absorptive power meter (N) (Scientech model 38-0101).

(O) The LII signal produced within the measurement volume is then conditioned by an LII signal collection lens assembly, which is indeed very similar to the collection and light conditioning system assembled at Cranfield (see section V.3.1.1.1 and figure 82) in the fact that the assembly comprises a front collection lens and a Gaussian beam reducing telescope. The main difference between the NRC and Cranfield pyrometric instrument system is that the output light from the Gaussian telescope is sent through a fiber optic delivery system allowing the photomultipliers to sit away from the measurement stand within a

(P)

demultiplexing box comprising dichroic mirrors and eventual attenuation filters, with the LII signal traveling through an optical fiber (Ceramoptec, 1mm core diameter, 5m length).

The laser output light beam was frequency-doubled from 1064nm to 532nm and operated with a 10Hz pulse repetition rate. The energy delivered to the measurement volume was controlled by means of operating at a constant near-maximum flash-lamp power variably attenuated using the combination of the ½ waveplate (C) and thin film thin polarizer (D) as a variable attenuator. This energy attenuation system was used rather than flash-lamp power changes in order to maintain a constant laser spatial energy profile. The laser temporal energy profile was measured using a high speed silicon photodetector (Thorlabs DET210 silicon PIM photodiode, 1ns rise time) in combination with a digital storage oscilloscope (Lecroy model 7100). The photodiode was effectively measuring the laser temporal energy profile using the scattered signal from an optical flat with a time resolution of 100ps. Results are given in figure 92.

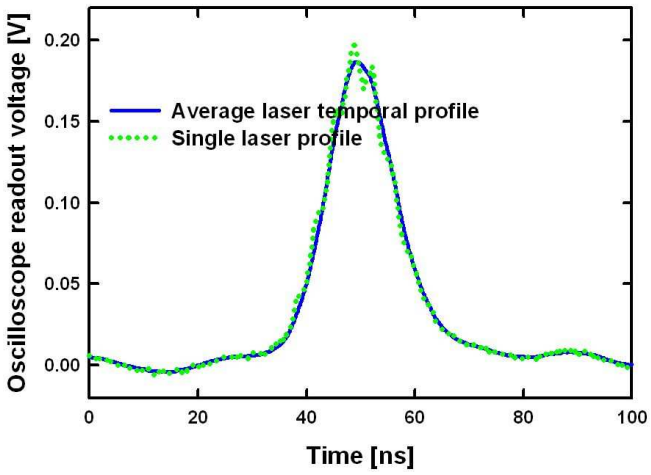

Figure 92: 532 nm (big sky dual head CFR200) laser pulse temporal profile as measured with an oscilloscope. Note that the single profile measurement are typical of multimodal spectral intensity variations. The average was computed internally using a 100 multipulse averaging routine. When approximated to a Gaussian, this laser temporal profile was later fed to the current LII model as having a full-width at half maximum measured at 14.7ns.

The aperture (H) was imaged magnified by a factor 2:1 onto the measurement volume, forming a near-uniform rectangular laser irradiation profile characterized by energy profile non-uniformities totalizing less than 5% over the measurement volume. Eventually the laser energy required to perform medium laser fluence measurements (above 0.100 J/cm2) damaged slightly the gold-plated aperture but amounted to non-significant energy profile non-uniformities and negligible surface increase. The signal collection assembly (O) was mounted at a 90 degrees angle from the laser beam propagation axis and delivers signal to a demultiplexer box similar in design to the pyrometric system assembled at Cranfield. The main difference is the fiber optic delivery system, allowing the detectors to sit in a demultiplexer box two meters away from the measurement stand. The demultiplexer box is configured for LII signals at 444.918 nm on a first channel (blue channel) using a Hamamatsu H5783

Photomultiplier Tube Module (serial number 833-477) and LII signals at 782.756 nm on a second channel (red channel) using a Hamamatsu GaAs PMT. A third channel is configured for the measurement of 532nm Rayleigh scattering from the carbonaceous particulate matter. Typically, since signals were in the ppb concentration range, no attenuation was used in front of all detectors. This demultiplexer system is later referred to in the text as a standard sensitivity LII system.
Signal collection efficiencies (front detector filters transmissivity) are given in figure 93 for the standard LII signal analysis systems.

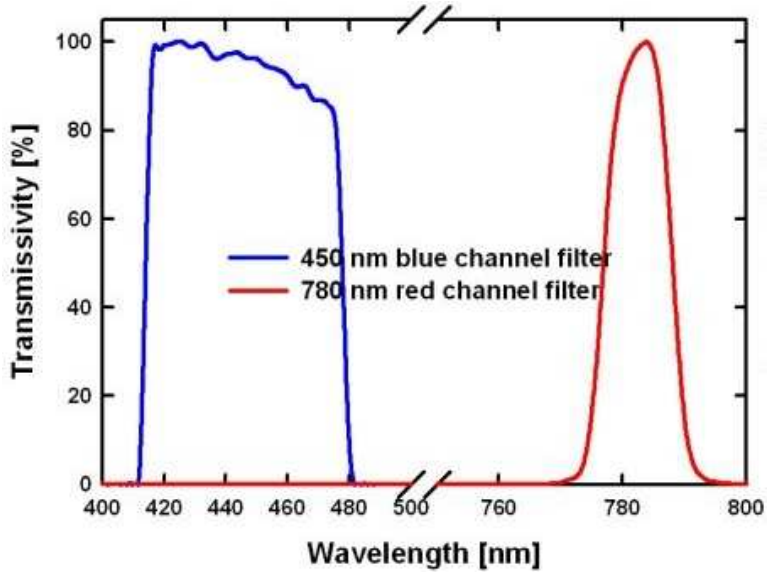

Figure 93: Transmissivity of the standard sensitivity system.

Time resolved laser-induced incandescence measurements were recorded using a digital storage oscilloscope (Lecroy Wavepro 7100, Serial Number 1161) with a time resolution ranging from 1ns to 10ps in order to later filter-out digitally the photomultiplier shot-noise using a high rejection bandpass filter resampling Kaiser-Bessel filter set for variable resampling time resolution. Typical measurements were resampled at 1ns for the first microsecond of LII signals, followed by 10ns for the next 4 microseconds and concluding at 100ns time resolution at all later measurements. Oscilloscope acquisition triggers were fed from the laser head Q-Switch output pulse. A picture of the measurement system is available in figure 94.
Therefore LII signals were retrieved in terms of output voltages produced by the photomultipliers output current through the oscilloscope 50Ω front impedance. Both photomultiplier tubes gains were controlled externally, either using a control voltage supply in terms of a reference DC voltage supply stepped down using a potentiometer arrangement in the case for photomultiplier tube modules, or using a high voltage power supply for stand alone photomultipliers.
All photomultipliers were calibrated using an irradiance standard following the procedure described by Snelling et al. (2001) at a set gain. All gain curves relative to the set calibration gain were characterized and available as data sets, thanks to Dan Clavel (2005). Therefore a calibration factor could be calculated for each photomultiplier gain. Then, with the calibration factor know for each photomultiplier and the voltage output measured by the oscilloscope, soot temperature could be determined as well as the soot volume fraction. In terms of soot temperature calculation, the soot particles were assumed to obey the Rayleigh regime and they were also assumed to possess a constant E(m) value for both detection central wavelengths.

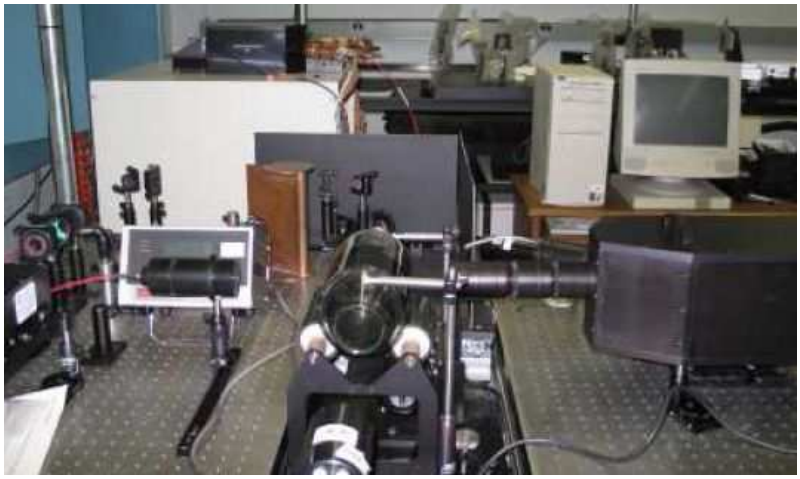

Figure 94: Measurement system picture. In the centre, the roller bottle sits on an adapted roller apparatus providing more agitation than the one used at Cranfield (in this case > 200 rpm are provided). Also, the roller apparatus is fixed on a sliding arm in order to "track" carbon nanoparticles "packets" providing therefore more consistent and repeatable carbon particles concentrations. On the left of the roller bottle sits the fibre-optic coupled collection system used for the standard LII system. On the right sits the high sensitivity LII system

IV.5. Chapter IV conclusions.

Although a molecular beam sampling system equipped with an aerodynamic lens would be an ideal mean to sample airborne particles into a medium vacuum circa 10^{-2} mbar, the available resources were not available. Instead, a sealed roller bottle containing a few grams of carbon black powder (a form of heavily agglomerated soot) held below 10^{-3} mbar was chosen as a suitable sample to perform LII under vacuum. Rotation of the bottle by means of a roller bottle apparatus insured the obtention of a "free fall" of particles into later measurements volumes.

A spectrographic measurement system was assembled in order to perform a physical check: if incandescence spectra were present under vacuum, last longer than 50 microseconds and are consistent with a radiative temperature decay, then LII under vacuum had been obtained. However, the low sensitivity of the system limited the measurements to be performed uniquely at high laser fluences. Also, the laser beam had limited spatial uniformity and the expected temperature measurements were expected to reflect this fact.

Following the eventual success of the measurements obtained with the spectrographic system, a more complex experimental setup was assembled. Instantaneous light intensity and soot temperature measurements were coupled to 2D imaging. As well, the laser spatial fluence uniformity was greatly increased with the use of a more uniform laser profile and relay imaging of the laser beam crossing an aperture onto the measurement volume. The dual wavelength pyrometer was designed and implemented as part of the present thesis. All optical and electronics design are given in IV.3.2.1(Optical design) and IV.3.2.2 (Electronic design of the pyrometer.). The

instrument itself is a state of the art time resolved LII detector system, and required optical modelling together with an elaborate electronic design. This lead to the obtention of a fully automated instrument. Even though the instrument was limited by a low sensitivity signal acquisition system (Gould 4074A Digital Storage Oscilloscope), LII measurements for both medium and high laser fluences were expected to be resolved.
In parallel, A novel 2D soot volume fraction measurement technique was applied. By measuring simultaneously the effective soot temperature and imaging the emitted signals in terms of absolute light intensities, 2D soot volume fraction measurements are obtained. Temperature measurements were provided by a dual wavelength pyrometer while 2D intensity measurements were performed with a calibrated Intensified CCD camera. Besides, the Intensifier CCD camera was also used to size agglomerates and perform Particle Image Velocimetry (PIV).
Therefore the system assembled was quite complex, and could perform general measurements of all aspects of the physics occurring under vacuum, in terms of temperature measurements, soot volume fraction measurements, agglomerate behaviour and characteristics.

A third experimental system was also employed at NRC, Canada. The system consisted in a high resolution dual wavelength pyrometer. This system permitted high resolution time-resolved LII under vacuum measurements at both medium and low fluences and completed the previous investigations with both low fluence and absorption measurements capability.
The details of the measurements performed with these three measurements systems are elaborated in chapter V, which follows.

Chapter V – LII under vacuum measurements

All the laser-induced incandescence under vacuum measurements presented throughout this chapter have been performed on the same medium, that is carbon black powder agitated by a roller system inside a roller bottle under high vacuum (below 10^{-3} mbar). Even though a continuous sampling method would have been preferred, the sample used for the results obtained qualifies as soot and is, through agitation, similar in its properties, agglomeration state and grain sizes to soot obtained from pool fires, heavy duty and early diesel engines, and obviously carbon black.

Initial spectrographic measurements were performed at circa 0.3 J/cm^2. Spectra were recorded to confirm the obtention of blackbody continuums which would then confirm the obtention of incandescence signals. Also, signals lifetime and extrapolated temperatures were checked against modelling of radiative temperature decays.

Further investigations included the use of a dual wavelength pyrometer coupled to imaging using a light intensity calibrated system. The laser fluence was varied between 0.1 to 0.28 J/cm^2. The various aspects of the signals obtained that were then studied were:

(1) the shapes of the broadband time-resolved LII signals
(2) the effective temperature measured , their uncertainties and their link to modelled results
(3) the eventuality of thermally excited emission from C_2 during the first 170 ns.
(4) the soot volume fraction behaviour
(5) the characterization of agglomerates explosions and their dynamics
(6) the performance of the 2D absolute light intensity calibrated system in terms of aggregate sizing and sensitivity.

Finer measurements were later performed at the National Research Council (Ottawa, Canada) in order to provide high accuracy low and medium fluence (0.04 to 0.16 J/cm^2) time-resolved LII under vacuum measurements. This investigation was led to both confirm and validate the results obtained at Cranfield University, but also complete the study of LII under vacuum by providing low fluence and highly resolved measurements. This particular study was centred on the following aspects:

(1) establishing repeatability of LII under vacuum signals and measured temperatures on a pulse to pulse basis
(2) performing multipulse averaged time-resolved LII under vacuum measurements
(3) comparing modelled absorption, sublimation and radiative absorption rates with the model
(4) highlighting specific temporal and thermal behaviours.

V.1. LII under vacuum feasibility study.

The spectrographic system (see figure 95) was assembled and dedicated to measure what was potentially laser induced incandescence under vacuum signals. The system was run at a high fluence level in order to maximise the signal intensity from the measurement bottle inside the roller bottle and compensate for the low sensitivity of the spectral imaging system. Therefore the expected peak LII temperature was to be measured circa 4200 Kelvin for an refractive index function E(m) of 0.4 and this illustrated in figure 34 (chapter III). The requirements for the signals obtained by laser irradiation under vacuum of carbon black particles to be associated with laser-induced incandescence were that:

(1) the signals produced by the particles are continuum spectra typical of blackbody radiation from soot
(2) if a peak particle temperature was measured, the peak particle temperature would be in the region of 4200 K
(3) signals would last more than 50 microseconds.
(4) In the case of a signal lasting more than 50 microseconds, a temperature decay could be measured at associated with laser-induced incandescence under vacuum.

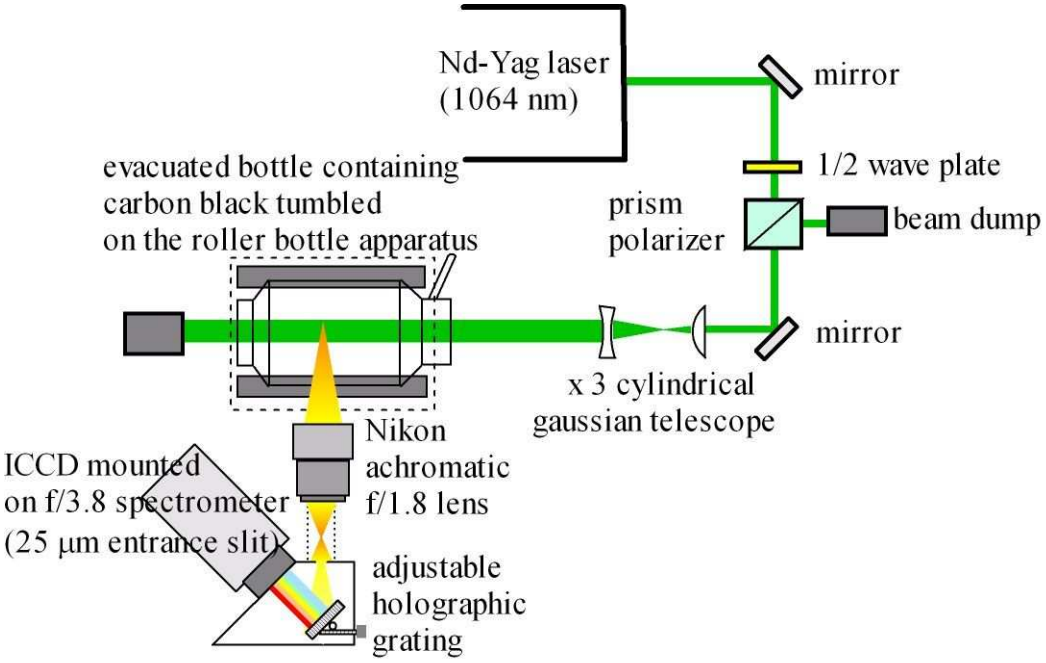

Figure 95: Spectrographic LII under vacuum measurement system layout. A detailed description of the system is provided in section IV.2.(details of the spectrographic system used to validate the presence of LII under vacuum).

With the spectrographic system synchronized on the laser pulse, spectral measurements were taken approximately 10 nanoseconds after the laser pulse irradiated the measurement volume, followed by measurements at 5, 10, 15, 20, 25, 30, 35, 40, 50 and 60μs after the laser pulse. The spectra obtained are illustrated in figure 96. At first sight, all the spectra measured could be associated with spectral continuums and eventually blackbody. Also, if the spectra were to be associated with a temperature decay, their intensity would diminish with time and temperature. This

trend is clearly visible in figure 96. As well, even though the spectrum measured 10 nanoseconds after laser irradiation is nearly spectrally flat (as the spectrum of a body above 4000K would be), the other spectra follow a clear tendency to shift toward the red part of the spectra. This, associated with the decay in intensity with time, also would be very consistent with a temperature decay with time. Overall, the spectra measured were consistent with blackbody radiation of particle temperature decay with time.

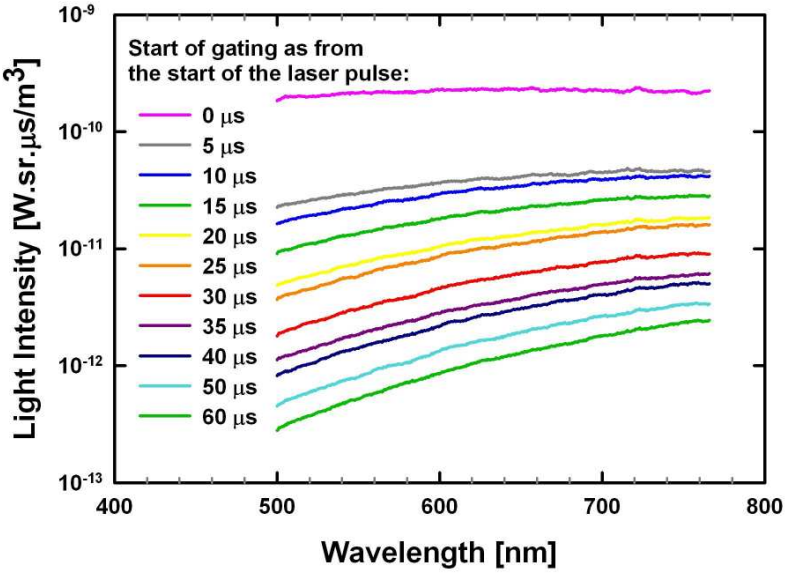

Figure 96: Spectral measurements obtained with the spectrographic system.

In order to determine the associated soot temperature measured in figure 96, a pyrometric ratio approach was used (with the perspective of using a 2-color real-time pyrometric system for later experiments). Measurement values comprised within the regions 500.2-520.4nm and 700.3 - 720.0 nm were respectively averaged to provide a central 510nm and 710 nm average intensity value. Hence the noise contribution the spectra measured was reduced and the ratio of the observed signals at 710 and 510 nm could be expressed as (Beyer & Greenhalgh, 2006):

$$\frac{I(\lambda_1,T)}{I(\lambda_2,T)}=\frac{\lambda_2^5\left(e^{\frac{hc}{k\lambda_2 T}}-1\right)}{\lambda_1^5\left(e^{\frac{hc}{k\lambda_1 T}}-1\right)}\frac{\varepsilon_{\lambda 1}}{\varepsilon_{\lambda 2}} \qquad \textbf{(97)}$$

with λ_1 = 710 nm, λ_2 = 510 nm and T the actual particulate matter temperature. Reordering equation 97 leads to the following expression for T (assuming a constant emissivity ε for a particle emitting in the Rayleigh regime):

$$T=\frac{hc}{k}\cdot\frac{1/\lambda_1-1/\lambda_2}{\ln\left(I_2\lambda_2^5/I_1\lambda_1^5\right)} \qquad \textbf{(98)}$$

and equation 98 develops into:

$$T = \frac{h\,c}{k}\cdot\frac{1/\lambda_1 - 1/\lambda_2}{\ln\left[E(m_1)/E(m_2)\right] + \ln\left(I_2\lambda_2^6/I_1\lambda_1^6\right)} \qquad \textbf{(99)}$$

Equations 98 and 99 are valid only for a particle in the Rayleigh limit where the emissivity, ε_λ can be expressed as:

$$\varepsilon_\lambda = \frac{4\pi d_p E(m)}{\lambda} \qquad \textbf{(100)}$$

The constants h, k and c are respectively the Planck constant, the Boltzmann constant and the velocity of light. Note that if E(m) is invariant between the two wavelengths, the ratio of emissivities at λ_1 and λ_2 reduces to unity in equation 97. This is assumed here. Two different temperatures can be calculated using equations 97 to 99:

(1) either a constant emissivity value over the spectral range is assumed and a colour temperature is obtained. This would imply that emission from large carbon black particles predominate and that the sample optically behaves as bulk material;

(2) or a constant refractive index function E(m), a more realistic "soot" temperature can be deducted, provided the particles present satisfy the Rayleigh criterion ($\pi d_p < \lambda_{em}$, with λ_{em} the dominant blackbody emission wavelength in the case of a temperature decay).

The calculated temperatures are given in table 5 .

Time from LII peak temperature [µs]	**Gating duration [µs]**	**Pyrometric ratio [ ]**	**Colour temperature [K]**	**Soot temperature [K]**
0	**0.1**	1.0982	4803	4189
0	**1**	1.4158	4228	3755
5	**1**	1.8375	3775	3401
10	**1**	2.1628	3542	3214
15	**1**	2.5474	3338	3049
20	**1**	2.9850	3164	2905
25	**1**	3.3259	3056	2816
30	**1**	3.7372	2948	2726
35	**1**	3.9803	2893	2679
40	**1**	4.3732	2816	2614
50	**1**	5.0177	2710	2525
60	**1**	5.5096	2640	2468

Table 5: Temperature measurement results using a 2-color ratio at 510nm and 710 nm and considering both "soot" and colour temperatures.

The measured colour (or blackbody) temperatures were found 500 Kelvin higher than expected. In terms of soot temperatures, the recorded peak temperature of 4189 K could be associated with LII absorption for an E(m) value of 0.4 and a laser fluence of 0.3 J/cm^2. Each of the spectrum obtained was compared to the spectrum corresponding to both temperatures measured by pyrometry. These are contained in figures 97 and 98.

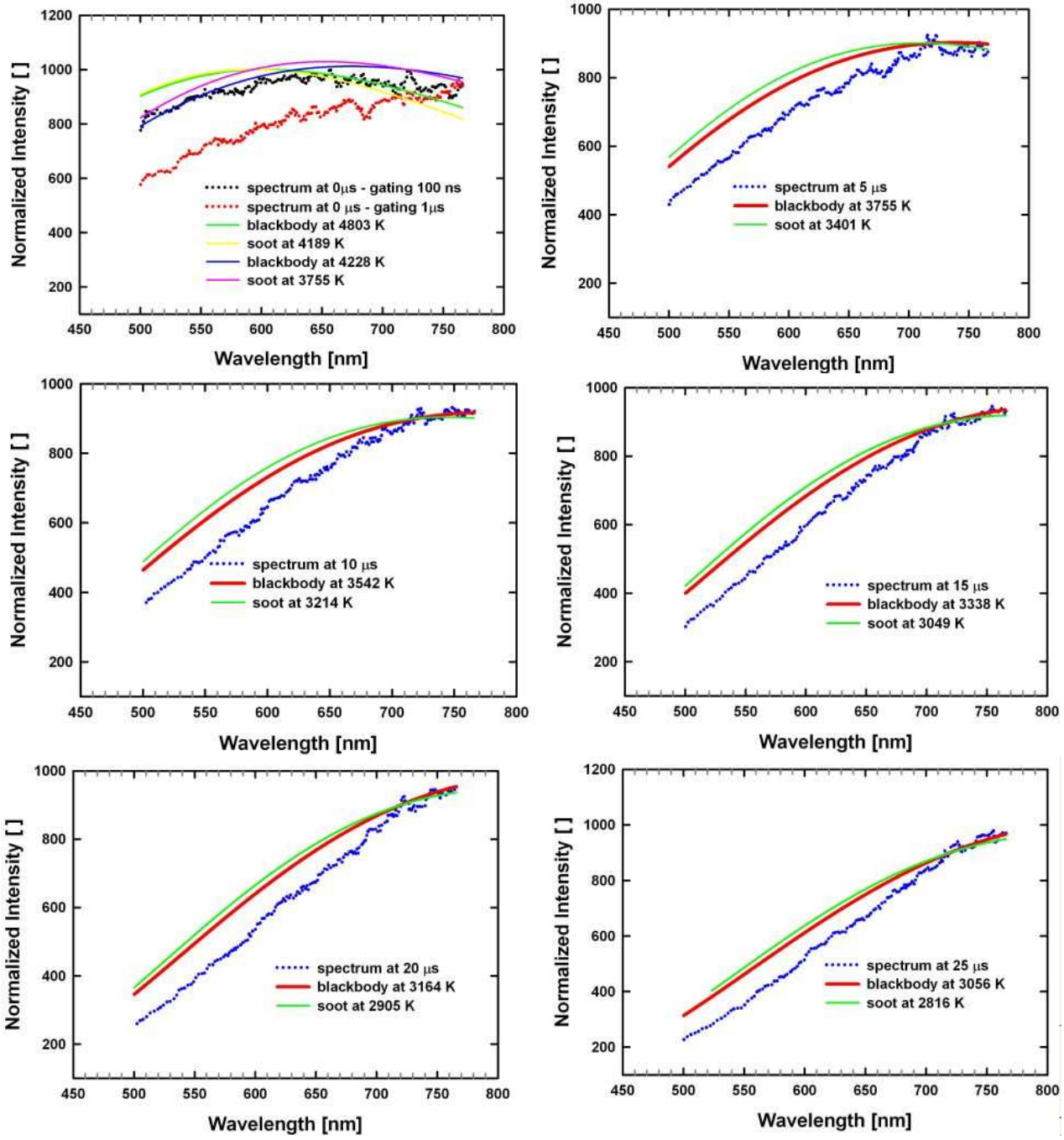

Figure 97: First 25 µs spectra compared with the blackbody and soot temperature spectra deducted during calculations.

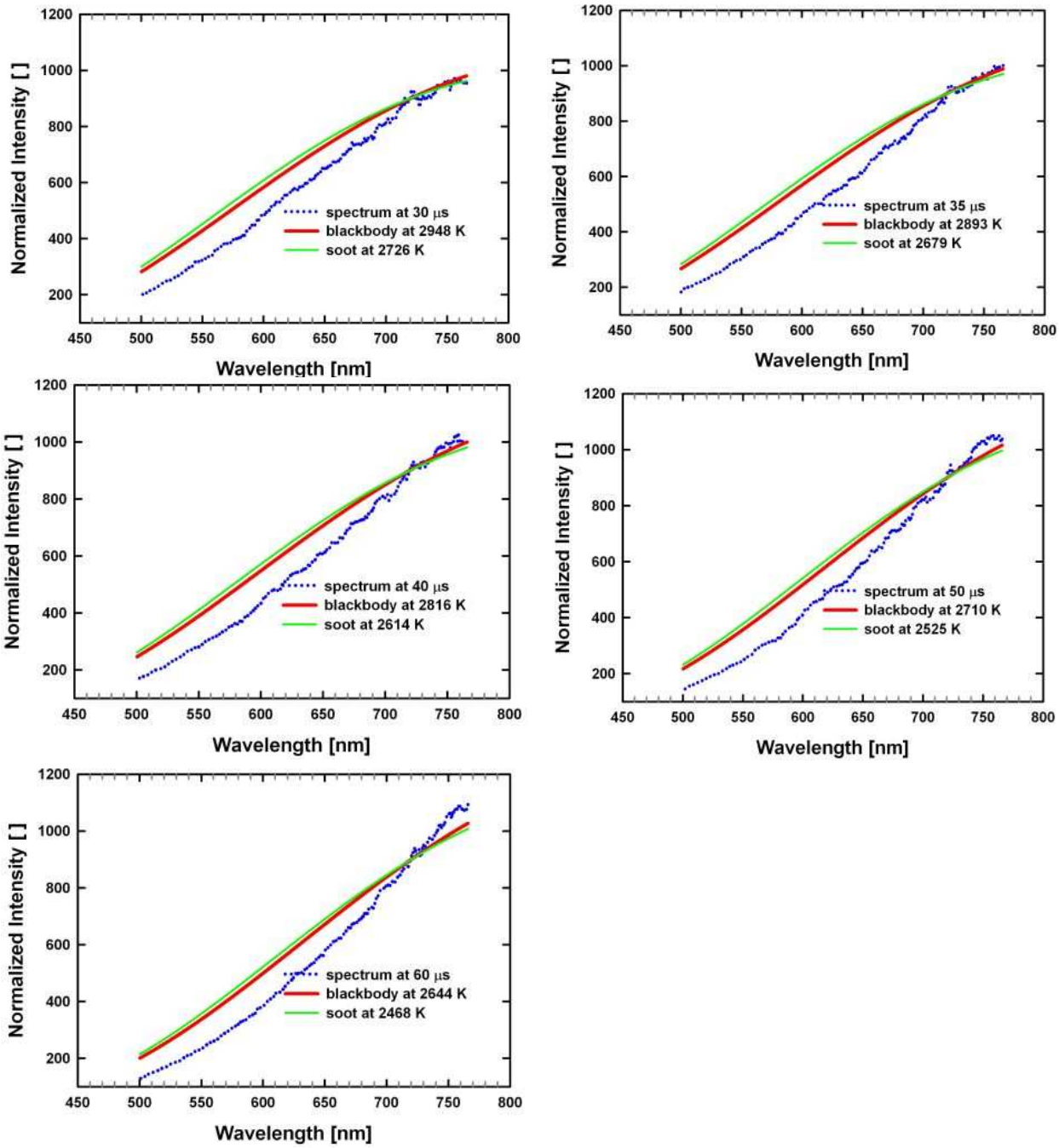

Figure 98: Spectra obtained between 30 to 60 µs after the LII peak temperature compared with the blackbody and soot temperature spectra deducted during calculations.

Except for the peak temperature for 4228 K in the top left section of figure 97, no exact match was found between the measured spectra and the spectra corresponding to the pyrometric ratios measured. There are two explanations for this:

(1) the laser spatial profile being not perfectly uniform, the emitted spectra are red shifted by a large proportion of the particles within the measurement emitting at lower temperatures than the dominant signals.

(2) the gating time (one microsecond) actually integrates the particle temperature decay and temperature changes between 6 and 70 Kelvin are occurring between the start and end of the intensifier exposure.

Clearly, these two explanations apply here, and the spectra measured can be believed to be red-shifted due partly to temperature variations during the spectrograph exposure and temperature non-uniformities due to a laser spatial fluence lack of uniformity.

A few points summarize the characteristics of the signals measured:

(1) at high fluence (0.3 J/cm^2) and with a spectrographic system of limited sensitivity, 60 microseconds of laser-induced light signals were recorded from the soot under vacuum within the roller bottle

(2) continuous spectra characteristic of an incandescence temperature decays (decrease in light intensity associated with red shifting) have been measured.

(3) the temperatures associated with these spectra, when considered in terms of soot temperature, appear realistic for LII under vacuum. In particular the peak soot temperature of 4200 K measured a few nanoseconds after the laser pulse matches an expected 4200K for E(m) = 0.4 at a laser fluence of 0.3 J/cm^2.

(4) temperatures were measured by pyrometric ratio between 710 and 510 nm. Discrepancies between the expected spectra and the measured ones are due to red shifting, which is associated with temperature decay during the measurement itself (6 to 70K temperature difference between the beginning and end of the intensifier gating) and temperature non-uniformities caused by the laser spatial fluence profile imperfections.

Therefore the measured spectra were consistent with laser-induced incandescence under vacuum and were characteristic of a long-lived (at least 60 microseconds) temperature decay from a peak temperature of approximately 4200K. Overall, the "soot temperature" approach rather than the colour temperature gives realistic temperature measurements. Indeed, colour temperatures are 200 to 600K higher than expected. Within chapter III.2.3. (Sublimation Under Vacuum), it is established that the sublimation heat loss rate becomes negligible after approximately 10 microseconds during LII under vacuum for a laser fluence of 0.3 J/cm^2 .Hence the LII under vacuum temperature decay as from 10 microseconds and onwards is dominated by the radiative heat transfer. Using the soot temperature at 10 microseconds after laser irradiation as a starting point, seven radiative cooling decays were generated, with E(m) values ranging between 0.2 and 0.4 . The measured cooling decay and the modelled temperature curves are illustrated in figure 99.

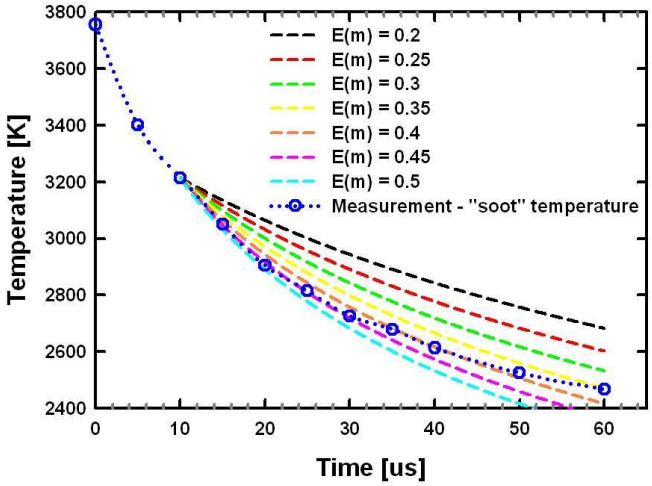

Figure 99 : Measured temperature decay using the "soot" temperature approach and theoretical comparative curves.

Hence it can be established that the temperature decay measured by the spectrographic system can be attributed to laser-induced incandescence under vacuum. Indeed, a radiative temperature decay can be associated to the measurement obtained and a value of E(m) comprised between 0.35 and 0.45 can be measured for this sample with a laser fluence of 0.3 J/cm^2.

The conclusion of this first experimental investigation was that laser-induced incandescence under vacuum signals can be obtained upon laser irradiation. The spectral characteristics of the signals obtained at 0.3 J/cm^2 are typical of LII and correspond to both predicted peak temperatures and modelled radiative temperature decays. This justified the assembly of a more complex measurement system capable of both tire-resolved LII measurements and imaging for both medium and high laser fluences. The results obtained with the measurement system described in IV.3. (The LII under vacuum investigation system: a dual wavelength pyrometer coupled to a calibrated Intensified CCD camera) are the subject of the following section.

V.2. LII under vacuum investigation at medium and high laser fluences.

The LII under vacuum investigation was performed at Cranfield University. In order to alleviate instrumentation needs, it was chosen to perform both medium and high fluence measurements at Cranfield and to later perform low fluence LII under vacuum at NRC, Canada. The measurement system used throughout this section is composed of a dual wavelength pyrometer system coupled to a calibrated ICCD camera. Spatial fluence uniformity is provided by relay imaging a rectangular aperture onto the measurement volume. This is illustrated in figure 100 below and all experimental details and measurement methods are described in section IV.3.

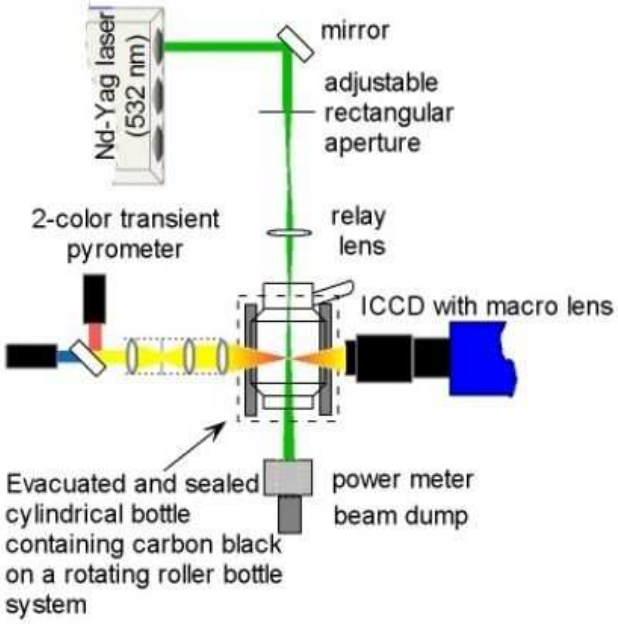

Figure 100 : The LII under vacuum investigation system, featuring a uniformly laser irradiated sample volume, an absolute light intensity calibrated ICCD and a 2-color transient pyrometer. The measured sampled is suspended carbon black held under vacuum below 10^{-3} mbar.

In order to identify the shape and relative signal intensities, the first time-resolved LII measurements were performed using a simple uncalibrated photomultiplier tube to measure unfiltered broadband LII signals.

V.2.1. Broadband LII under vacuum signals

Initial measurements were performed using a lens imaging the probe volume onto a photomultiplier tube to collect broadband LII under vacuum signals. The obtained PMT signals were then captured by a digital storage oscilloscope interfaced to a computer. The laser fluence for these measurements was 0.2 J/cm^2. Figure 101 below shows two typical single shot LII signals median-filtered with a time constant of 50ns for clarity plus an ensemble average (unfiltered) of 500 LII pulses. As expected, the obtained LII signals were longer than 50 microseconds. The signals were also very variable in both shape and intensity from shot-to-shot; a large majority of them showing an increase in LII signals a few microseconds after the laser pulse. The average LII signal did not show any increase of signal and this is due a very variable position of the second intensity peak, which averaged to a negligible amount over 500 pulses.

The strong variability of the signals and the apparently anomalous delayed increases in LII signal levels could be due to:

(1) a morphology change in particles leading to more matter being "seen" by the photo detector

(2) an overall increase in particles temperature.

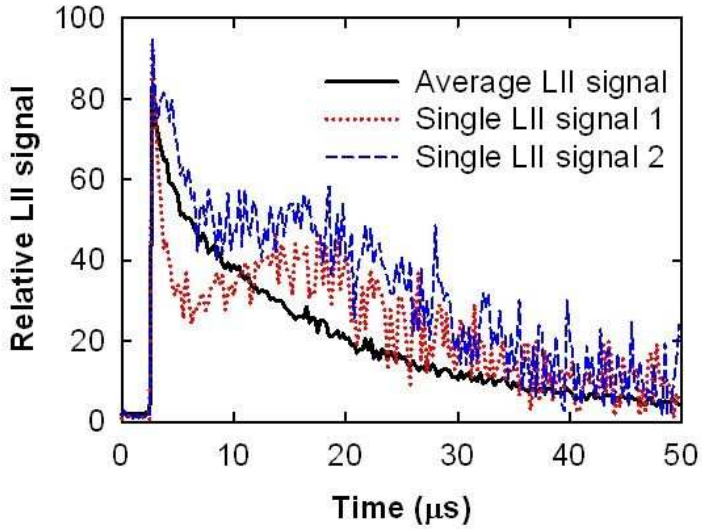

Figure 101: Typical broadband LII under vacuum signals. Single LII signals 1 and 2 are filtered with a time constant of 50ns for clarity and the average LII signal was obtained by averaging 500 LII pulses.

V.2.2. Temperature measurements and comparison with theory

The dual wavelength pyrometer records time resolved LII signal intensities at 500 and 700 nm. Therefore the instantaneous soot temperature can be calculated using the same approach as described in section V.I(LII under vacuum feasibility study) and equations 97 to 100. The colour (or blackbody) particle temperature can be expressed as (assuming constant emissivity between 500 and 700 nm):

$$T=\frac{hc}{k}\cdot\frac{1/\lambda_1-1/\lambda_2}{\ln\left(I_2\lambda_2^5/I_1\lambda_1^5\right)} \qquad \textbf{(101)}$$

and the "soot" particle temperature expresses as (assuming Rayleigh emission):

$$T = \frac{hc}{k}\cdot\frac{1/\lambda_1 - 1/\lambda_2}{\ln\left[E(m_1)/E(m_2)\right] + \ln\left(I_2\lambda_2^6/I_1\lambda_1^6\right)} \qquad \textbf{(102)}$$

With the indices 1 and 2 referring to each photodetector sensed light intensity and centre wavelength of the pyrometer.

Even though the "soot" temperature approach was proved more reasonable than the colour temperature in section V.I., it is important as this stage of the discussion to elucidate whether large soot agglomerates emit as separate large entities or rather as an ensemble of nanoparticles. The roller bottle contains a carbon black powder, which is composed in great part of large visible agglomerates of soot. Because the sample is rotated and tumbled into the measurement volume, possibly the largest signal contributors will be agglomerates of soot nanoparticles larger than 100 microns. Optically, a spherical entity ;which has a circumference smaller than the wavelength of light emitted or absorbed; obeys the Rayleigh scattering theory. Clearly this would be the case for the carbon black primary particles contained in this sample of carbon black: the primary soot particle is specified by the manufacturer to have a median diameter of 15 nm. However, because agglomeration is not negligible here, a large entity; such as an agglomerate of diameter much larger than the wavelength of light emitted or absorbed; could obey the Mie scattering theory and therefore absorb and emit light in the same manner as bulk graphite. In the eventuality of Rayleigh emission and absorption, the "soot" temperature approach (equation 102) would become applicable. Reciprocally, Mie emission and absorption would favour the "colour" temperature approach (equation 101).

In order to solve this dilemma, 500 single shot LII signals were collected at each laser fluence. These could then be processed using one of the two approaches:

(1) Averages were formed from 300 individual single pulse LII signals. Due to the low concentration of particulate matter (less than 100 ppb on average), which lead to weak signals, it was noticed that the first 200ns of the signal were partially corrupted by either the Q-switch noise or a possible C2 emission. Therefore the first 500 ns of the LII signals were discarded.

(2) On a single shot basis. Due to very large variations in soot volume fractions from shot to shot, each single LII measurement had to be filtered according to the intensity level. This was aimed at eliminating signals which exceeded the sensible dynamic range of the detectors. Weak signals from photomultiplier tubes presented levels of shot noise in the range of 30% to 50%. Therefore the signals were digitally filtered through a second order bandpass Bessel filter

and then median filtered. This resulted in minimal signal level distortions (<5%) and a decreased time resolution to of order 500ns, which in this vacuum case is still short compared to the overall decay. Again the first 500 ns were rejected for the reasons given directly above.

In parallel, three sets of 200 ICCD images were taken at 500 ns after the later pulse with a gate duration of one microsecond for each of the three laser fluences (0.18 J/cm^2, 0.24 J/cm^2 and 0.28 J/cm^2) used during experimentation. The images obtained were then processed to estimate the average agglomerate diameters and their individual contribution to the overall averaged LII signals. The results obtained are illustrated in figure 102:

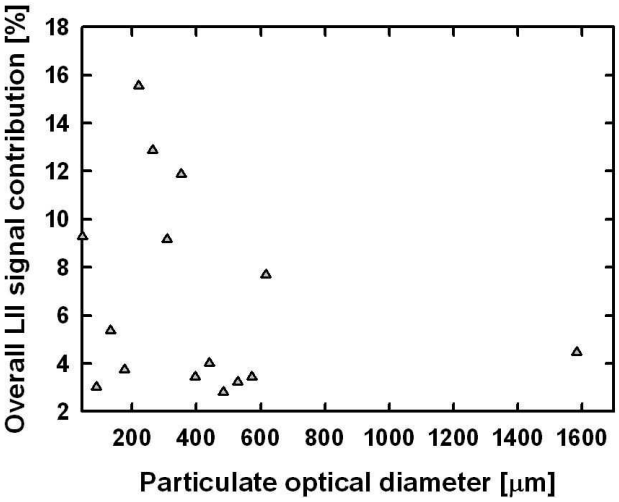

Figure 102: Overall LII signal intensity contributions as a function of agglomerate diameter at 500 ns after the laser pulse, obtained by image processing 200 ICCD images at a fluence of 0.18 J/cm^2. Similar results were obtained at 0.24 and 0.28 J/cm^2 with a large majority of signal contributors of optical diameter > 132 μm.

The main signal contributors are from carbon black clusters of diameters below 132μm (12.3%); agglomerates with diameters ranging from 132 to 400 μm diameter (62%) and particles larger than 400 μm (25.7 %). Hence the main signal contribution is from carbon black agglomerates larger than 132 μm diameter and this contributes to 87.7% of the measured LII signals intensities. The ICCD system was also used to investigate later times with gate delays set to 10, 20, 30 and 40 μs after the laser pulse. It was found that particles of diameter larger 100 μm were the dominant signal contributors for the first 20 microseconds, after which structural changes occur.

The resulting absorption efficiency K_{abs} was then computed for the laser fluences of interest. And the corresponding LII peak temperatures were computed. An example is given in figure 103 for a laser fluence of 0.24 J/cm^2.

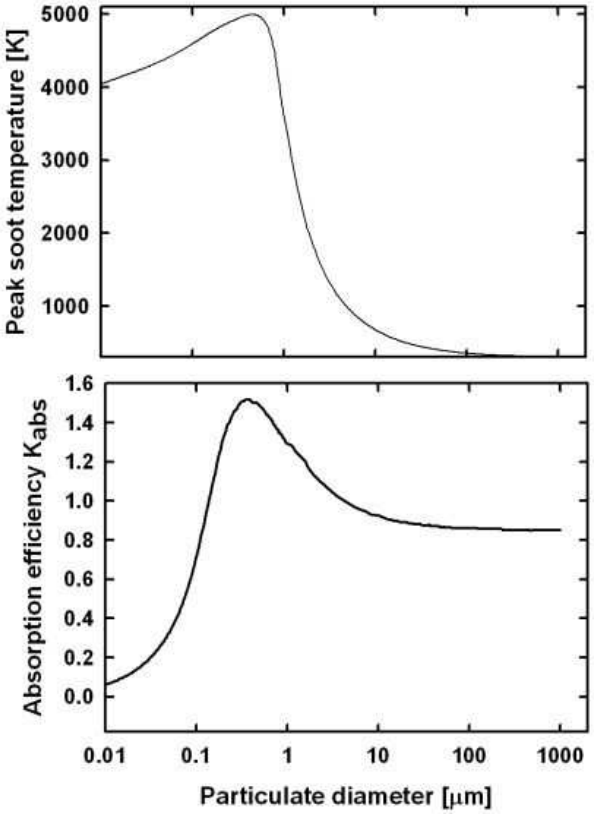

Figure 103: Absorption efficiency for a refractive index m = 1.57 – 0.56i at 532 nm and the corresponding modelled LII peak temperatures for a fluence of 0.24 J/cm^2 as a function of carbon particle diameter using Mie theory.

The following conclusion was reached: if carbon black agglomerates of diameters in majority larger than 100 microns were to behave as individual Mie absorbers, this would lead to peak LII temperatures below 500K upon laser excitation in the present experimental conditions. Very clearly this was not the case and the average temperature decays presented in figure 104 show measured peak temperatures above 3200K.

The average pyrometric ratios obtained as a function of time were processed using the two distinct approaches, either the Mie approach (Bohren and Hoffman, 1998) or the Rayleigh limit. Not surprisingly, Mie theory applied to large particles fails to predict the temperature decays. The large particles present in this study either only weakly contribute to the average, because they are statistically extremely small in number, and/or Mie does not apply even in these extreme cases. The application of the Rayleigh theory produces an acceptable fit for an E(m) between 0.4 and 0.6. This large range of value for E(m) is likely to be due to temperature errors ranging from 120K to nearly 150K from 3000K to 2400K. However this result may well be due to the low peak temperatures predicted for large particles of 500K which would lead to vanishingly low signals. Thus the observed results may simply reflect the dominance of hot particles which will be the small ones in or near the Rayleigh limit. In reality particles will not behave precisely in the Mie limit as they exceed the Rayleigh criterion due to their chain-like and fractal structure. Clearly further work is required to study the optical properties of aggregates and agglomerates in this transition regime and the impact of detailed morphology on LII. Overall and throughout this study, the

laser-induced incandescent carbon black can be considered acceptably as dominated by Rayleigh absorption and emission. This translates into the conclusion that agglomerates of carbon of diameters up to a few hundred microns can be assumed to behave as ensembles of agglomerated Rayleigh emitters and scatterers.

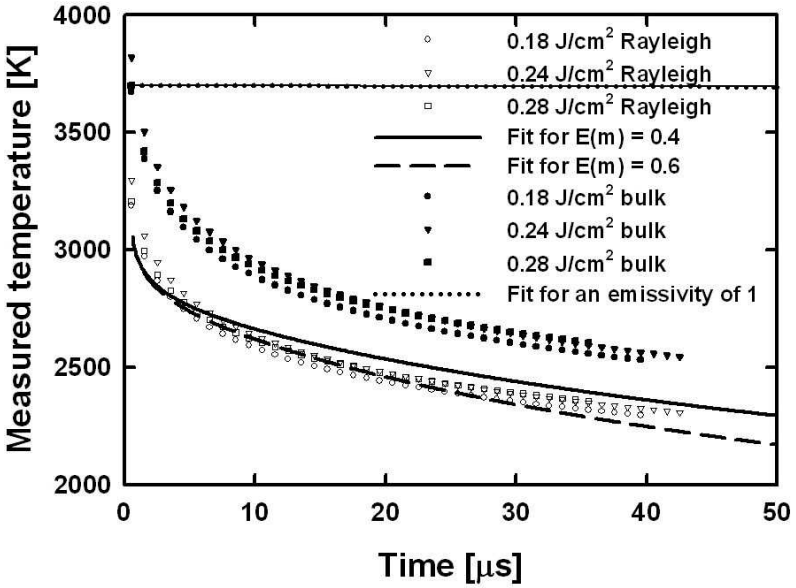

Figure 104: Measurements obtained and fit with theoretical temperature decays. The pyrometric ratios obtained at fluences of 0.18, 0.24 and 0.28 J/cm^2 were processed using two different methods: particulate temperatures were first calculated assuming that particles emit in the Rayleigh regime and subsequent fit to data for E(m)=0.4 and 0.6 were performed. The second (Mie) approach was also put into practice and is labelled "bulk", but both corresponding temperature decays and fit for an emissivity value were not consistent.

V.2.2.1 Temperature measurements uncertainties

Temperature errors were estimated using a simple approach reported by De Iuliis et al. (2005). Considering the error in measuring the LII signals and applying the error propagation theory, the error ΔR on the pyrometric ratio R (500/700nm) is:

$$\Delta R/R=\sqrt{\left(\Delta S_1/S_1\right)^2+\left(\Delta S_2/S_2\right)^2} \qquad \textbf{(103)}$$

Where $\Delta S_{1,2}$ is the error in the LII measurements $S_{1,2}$ at 500 and 700 nm respectively. By considering the expression for soot temperature, T_s (see equations (103) and (104)), it is possible to obtain:

$$\Delta T_s/T_s=T_s/\left(C_2\cdot\left(1/\lambda_1-1/\lambda_2\right)\right)\cdot\Delta R/R \qquad \textbf{(104)}$$

here C_2 is the Planck radiation constant equal to $h.c/k$, h is Planck's constant, c the velocity of light in a vacuum, k Boltzmann's constant and $\lambda_{1,2}$ refers to the wavelengths chosen. The uncertainties calculated for a temperature of 3,000K was 120K for averaged LII measurements with $\Delta S_1 / S_1$ = 0.047, $\Delta S_2 / S_2$ = 0.098 and 260K for a typical single shot data with $\Delta S_1 / S_1$ = 0.137 and $\Delta S_2 / S_2$ = 0.192. In

general, average temperature measurements and single shot data agreed within <300K.
In general, temperature uncertainties of 50K and less are common for time-resolved LII detector systems. The present detection system is limited by the acquisition and preamplification noise, as well as the dynamics of the LII signals under vacuum. Indeed, large variations in signal levels were complicated by additional signal pick-ups that were associated with suspected C_2 emissions, which are the subject of the following section.

V.2.3. A suspected C_2 thermally induced emission

Intense sublimation is triggered for fluences above 0.1 J/cm2 and when incandescent soot nanoparticles reach temperatures higher than 3000K. At these temperatures, intense sublimation levels will last in the order of 2 microseconds after laser irradiation. The sublimative stage was imaged using the ICCD for these two microsecond and an typical image is presented in figure 105-a for a laser fluence of 0.24 J/cm^2.

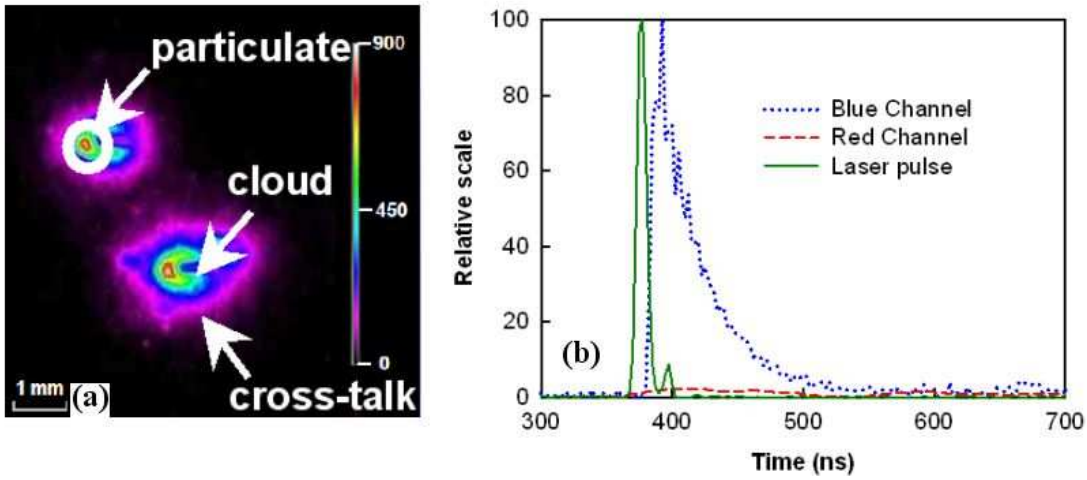

Figure 105: First 2µs LII signals.
(a) ICCD measurement of the incandescent particulates for a gate duration of 2µs and a delay of 500 ns after laser irradiation. The scale is in ICCD counts whereas laser beam propagation is from the left to the right.
(b) Initial signals presented characteristic 170 ns long emission peak for low carbon concentrations (circa 1 ppt). LII signal level is more reliably measured by the red channel (PMT_2) whereas the blue channel (PMT_1) presents the emission peak. Note that when soot temperature is close to 4000K, blue and red channel should be of similar signal level. The laser pulse as measured by the power meter is traced in green.

Images obtained during these two microseconds for a fluence of 0.24 J/cm^2 clearly showed a bright C shape light emission emitting nearly half the particulate signal level surrounding the particle and following the laser propagation direction, suggesting an effect similar to photonic wind. This particular feature suggested the presence of a cloud of thermally excited C_2 being taken away by the laser beam. For low LII signal levels detected by the pyrometric instrument at high fluence levels,

unusual high spikes lasting on average 170 ns were noticed (figure 105-b), suggesting that extreme material sublimation rates can be associated with small clusters (of optical size less than 100 microns). The frequency at which these pulses were measured also increased with increasing fluence levels.
Hence, if gaseous C_2 emission is present, one can formulate the hypothesis that the gaseous thermal excitation signal level is much higher than the LII signal produced by small clusters smaller than 100 microns and becomes predominant (figure 105-b).

Also, the 500 nm bandpass (25nm FWHM) interference filter used on the pyrometer has potential to transmit two lines of the Swan band (C_2) emission spectrum, respectively at 512.94nm (medium) and 516.52 nm (strong)**.** This is illustrated in figure 106-a. Unfortunately, measurements performed with the spectrographic system did not lead to the discrimination of C_2 Swan band emissions (figure 106-b) due to the limited signal- to- noise resolution of the measurement system and hence no other conclusion than a strong suspicion of thermally excited gaseous C_2 emission could be reached.

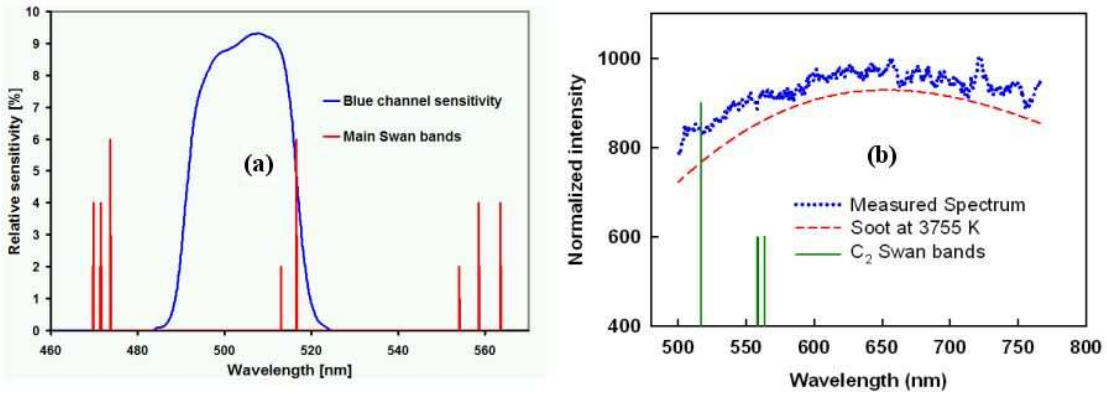

Figure 106: C_2 Swan bands spectral investigation
(a) 500 nm filter used in front of PMT_1 transmissivity versus wavelength and location of the main Swan bands. Clearly two Swan bands are eventually transmitted by the filter.
(b) Spectrum measured in conditions similar to the present experiment for a laser fluence of 0.3 J/cm^2 with a 100ns gate duration and just after laser irradiation. Effectively emission lines are not discernable due to a low signal-to-noise ratio.

In addition to the suspicious signal spikes detected on the 500 nm channel of the pyrometer, the uncalibrated photomultiplier tube measurements also showed some anomalous signal spike during LII under vacuum. These will be the subject to be discussed in the following section.

V.2.4. Anomalous incandescence behaviour and agglomerate dynamics.

The initial LII under vacuum measurement in the subchapter V.2. were performed with a broadband uncalibrated and unfiltered photomultiplier tube. A reminder of the general LII signal pulse shapes obtained is available in figure 107 below.

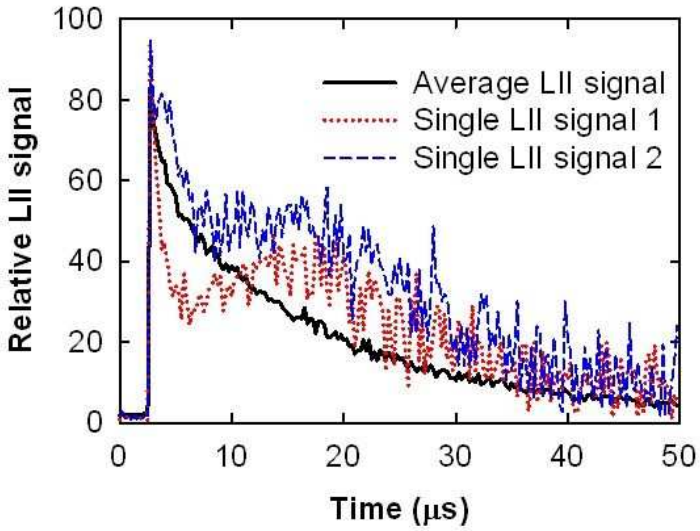

Figure 107: Typical broadband LII under vacuum signals. Single LII signals 1 and 2 are filtered with a time constant of 50ns for clarity and the average LII signal was obtained by averaging 500 LII pulses.

This initial investigation concluded to an apparent incandescence signal increase after the intensity peak of LII due to either a subsequent temperature increase or a soot volume fraction increase within the measurement volume. The typical delay between the initial LII peak and the "secondary" peak could be measured to stand between 10 and 20 microseconds for medium laser fluences. This delay would eventually reduce in some cases to between 2 and 5 microseconds for 0.24 J/cm^2 and larger fluences. A large number of single pulse LII measurements recorded by the pyrometer and featuring a "double intensity peak" were isolated and analyzed at three laser fluences (0.15, 0.24 and 0.28 J/cm^2). An example of the obtained signals is available in figure 108 for a fluence of 0.24 J/cm^2.The corresponding average temperature history is given on the right hand side of figure 108. This figure illustrates the typical behaviour associated with the "secondary peak" for LII: after 12 µs, the LII signal increases whereas the pyrometric ratio of the two photomultiplier signals remains approximately constant and the soot temperature decays slowly with time. This is consistent with a significant increase in the detected soot volume fraction. In general, this phenomenon was systematically similar for numerous measurements albeit that the timing of the secondary rise varied between 1 and 15µs. The ratio of the secondary soot volume fraction peak to the initially measured soot volume fraction was measured for 500 single-shot measurements performed at 3 fluences and is reported in figure 109. Even though this ratio varies a lot between single-pulsed LII recordings, a trend could be identified and an increased SVF with fluence was noticeable. It is also important to note that after 30µs, even though the measured temperature remained nearly constant, an apparent drop in soot volume fraction was remarkable. A possible explanation for the increase in soot volume fraction would be that for a soot primary

particle embedded in the core of an aggregate or agglomerate it would be heated initially through conduction but its radiation would then be trapped by the surrounding cluster of nanoparticles to which it belongs. A later disaggregation of the cluster would then reveal such a particle to the photodetectors. One would further note that in the situation of agglomerate explosions, after 30µs the particles would have likely travelled to the limits of the pyrometric system measurement volume aperture and this may account for the fall in signal. Also, an observation of fluence sensitivity has been previously made by Smallwood and Stagg (2006) in ambient LII measurements of soot or carbon black. The conditions of the two observations differ significantly and it may be that they are not related. Clearly though these anomalous phenomena warrant a more detailed investigation and this is covered in the next section.

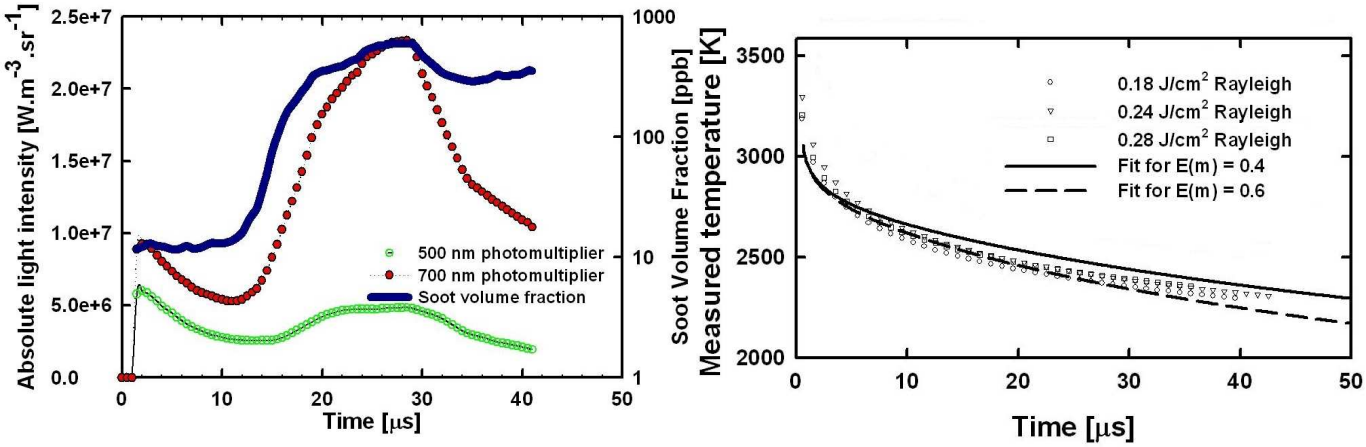

Figure 108: Example of the anomalous behavior of the incandescence signal for a fluence of 0.28 J/cm^2 for a single shot LII signal after noise filtering, left. The average measured temperatures are given on the left.

.

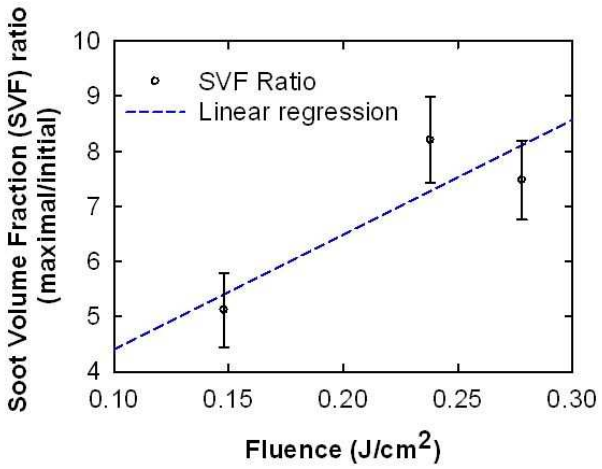

Figure 109: Average ratios and standard deviations of initial and peak soot volume fraction measured for the three laser fluences we measured.

V.2.5.Agglomerates explosions.

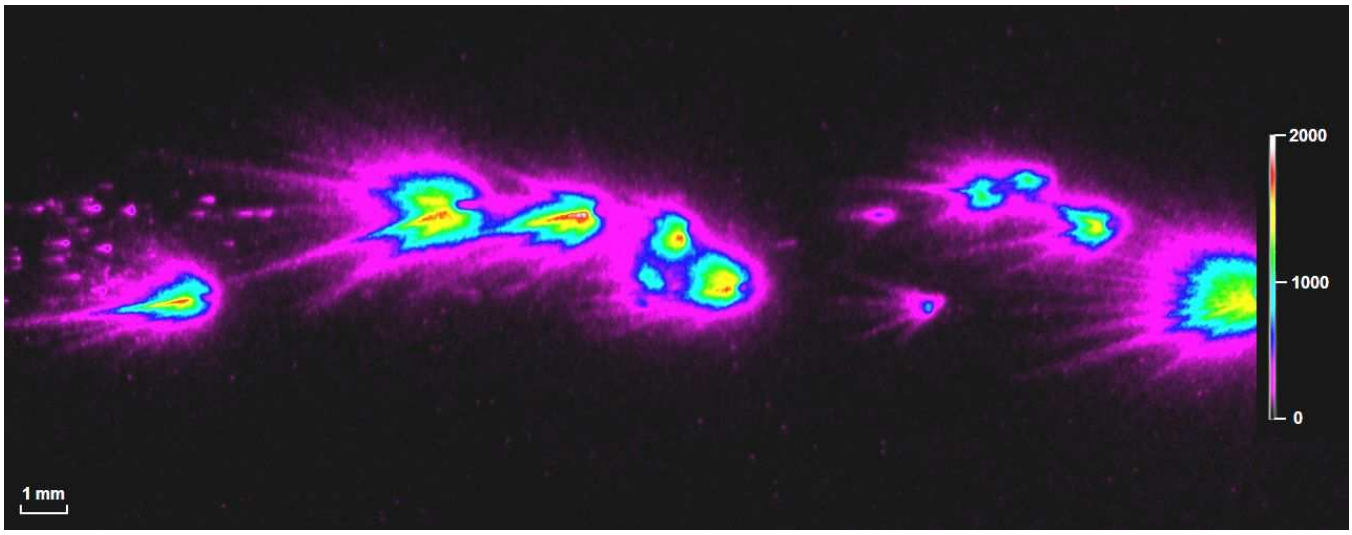

Figure 110: Time-integrated (from the start of the laser pulse for a gate duration of 50µs) ICCD measurement taken at 0.24 J/cm^2 laser fluence and revealing miniature "starbursts".

A large number of time-sequenced measurements were made from separate laser pulses using the ICCD with the intensifier gate timing and width set to illustrate the various phases of particles behaviour. The most striking feature of these images is that what were initially large carbon black particles behave as miniature starbursts and explode following laser irradiation at both medium and high fluences (see figure 110 above). A sequencing of the micro explosions is given in figure 112. After five microseconds, the fragmented clusters expand to fill a significant volume. In order to quantify this effect a large number of time-integrating images (100 per ICCD gating and laser fluence) were recorded with the gate opening and shutting timing set to 0-1, 0-2, 0-3, 0-4, 0-5, 0-10, 0-20 and 0-50 microseconds where 0 refers to the end of the laser pulse. Using this data the average Feret diameters (defined as the average longest distance between two points for an exploding particle) was calculated and is shown for three laser fluences in figure 111. It was found that after 30 µsec, explosions were on average larger than 2.2 mm, thus some of the area covered by the exploding cluster would now fall outside the probe volume of our pyrometer and hence diminution in apparent soot concentration would occur. A second important point is that although the temperatures measured for the particles were nearly independent of laser fluence (see figure 104), the total light emitted was observed to decrease as the applied fluence reduced from 0.28 to 0.18 J/cm^2 .

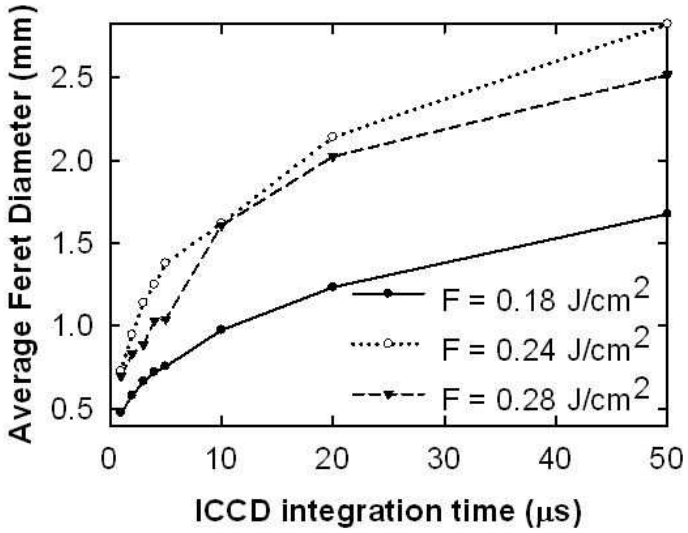

Figure 111: Average Feret diameter (see text) as a function of time for an agglomerate explosion. Each point represents an average of approximately 300 measurements.

The behaviour of agglomerates (loosely grouped aggregates) and large aggregates (tightly bound chains of primary particles) could not be dissociated and in the subsequent discussion both are referred to as clusters for simplicity. The results clearly correlate with the anomalous incandescence behaviour discussed in V.2.4 . The explanation for this behaviour appears to be that, following thermal excitation by the laser, clusters undergo at least one micro explosion. The probability of explosion seems to increase with fluence and therefore may well be initiated by sublimation or associated processes. Ideally this should be validated at lower fluences as well to determine if this is a threshold effect, this is obviously an important area for a future study. It is believed that the increase in signal, which is not accompanied by any observed increase in temperature, is due to the fragmentation of the large clustered particles. It is normally assumed in LII that the primary particles are optically thin and that they are evenly illuminated and thermally excited and that the emitted radiation is not in any way shielded. For large clusters this may well not be true. Thus they will be preferentially heated on the side facing the laser beam. And, even for cluster of several dozens of microns, heat conduction occurs on a sub-nanosecond time scale. It is highly probable, that by rapid internal conduction within a large tightly structured cluster, that a number of primary particles heat up which would otherwise be shielded from the laser beam. Fragmentation of these clusters will then reveal effectively unseen hot primary particles to the detector resulting in an increase in signal, though not temperature. The later point is clearly supported by figures 110 and 111. As the agglomerate explosion expands beyond the viewing area of the detector the signal then falls consistent with figure 108. Clearly higher fluences will both provide more energy to be conducted within the cluster prior to fragmentation and this will further increase the vigour.

In parallel, particulate matter soot volume fraction measurements deducted from LII signals in ambient air do also show sensitivity to fluence whereas those measured in flames do not. Conditions at 1 bar are such that bath gas conductive cooling and the increased bath gas pressure should reduce this phenomenon both in reducing the

excitation and by forming a barrier to limit the explosions. However it is very probable that soot in ambient air will likely have undergone more aggregation and agglomeration than that in or near its formation region in a hot flame.

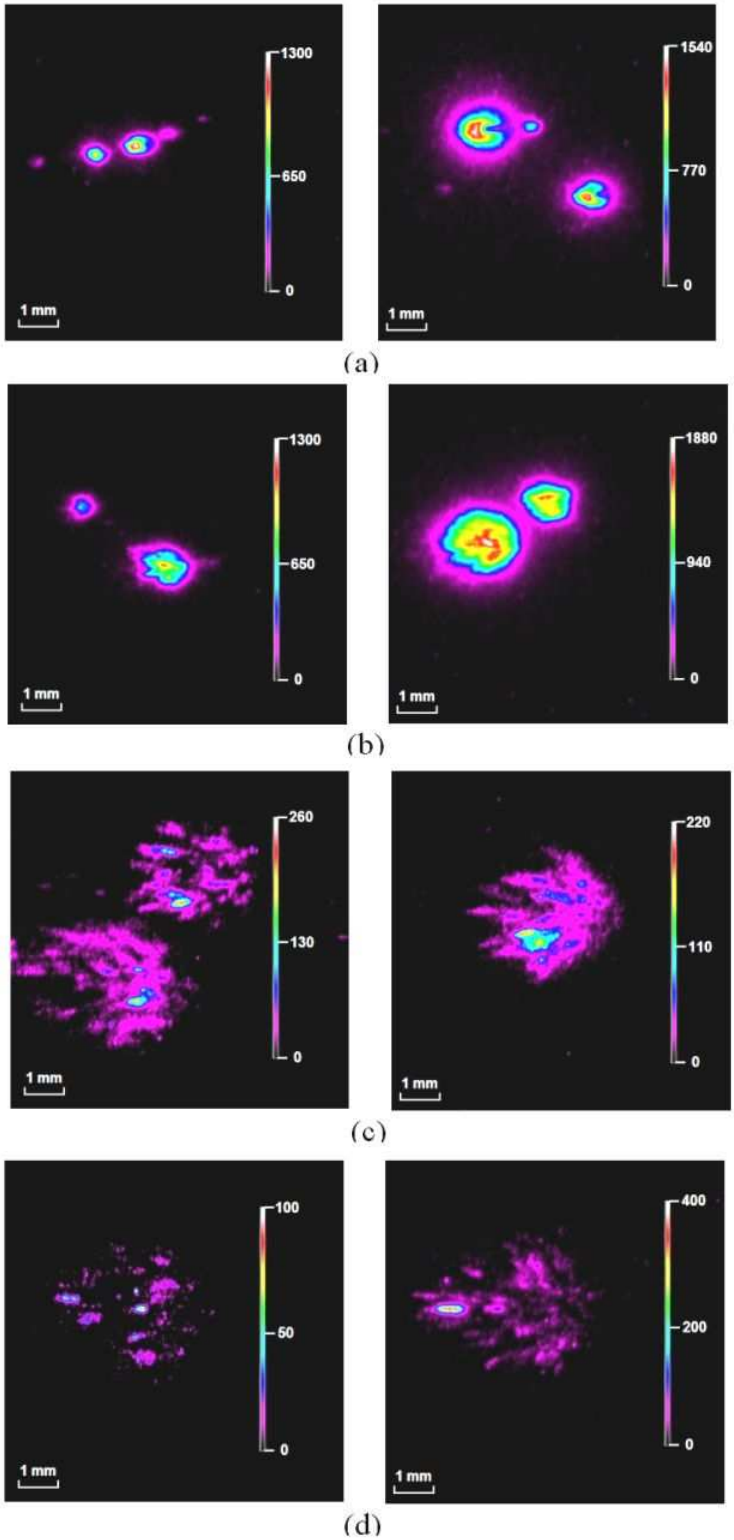

Figure 112: Images of incandescence from particles irradiated with a fluence of 0.18J/cm^2 (left) and a fluence of 0.24J/cm^2 (right) with the intensifier gate timing open and shut at: (a) 0-5 µsec after laser pulse, (b) 5-10 µsec after laser pulse, (c) 20-25 µsec after laser pulse, (d) 25-30 µsec after laser pulse. All color scales in ICCD counts.

V.2.6 Agglomerate/ aggregate particles dynamics.

Following excitation hot incandescent carbon black clusters could be observed for at least 50 microseconds following laser excitation. This offered the possibility to investigate the dynamical behaviour of the particles by utilizing an analogy of Particle Image Velocimetry (PIV)**.** Although double exposing the intensifier was possible over a microsecond timescale, double framing the CCD array was not. Therefore double-exposed PIV on a single CCD frame was performed: the first exposure being set at 2μsec after the start of the laser pulse and the second set either at 8 or 14μsec for a constant gate duration of 1μsec. Measurements were all conducted using a laser fluence of 0.24 J/cm^2. The images obtained were therefore composed of the main initial carbon cluster as witnessed by the 2μsec exposure, superposed with typically 200-300 ejecta at 8μs and well over 2000 ejecta at 14μs from the second exposure. This is illustrated in figure 113:

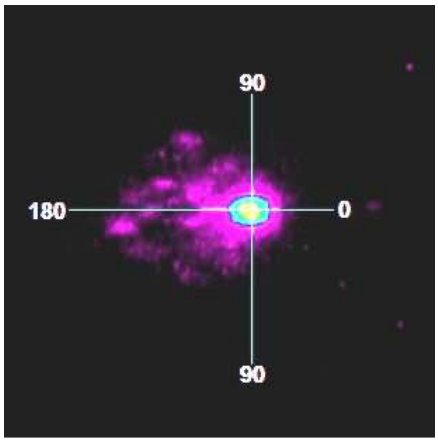

Figure 113: An example of a single frame, double exposure PIV image. Laser propagates left to right and the first exposure is at 2 μsec and second at 14 μsec both with a gate width of 1μs. The very bright spot is the initial particle from the first exposure and the scattered ejecta are from the second.

Each carbon cluster was located on the image using its central location for large clusters of size of order 60μm or larger, while smaller ejecta were located using the peak of a cross-talk which is typically a pseudo-Voigt 2 dimensional profile. Each initial carbon cluster was then classified depending on its optical diameter into 4 size classes:

(1) class 1 includes clusters/particles of diameter greater than 1200μm and up to 2400μm
(2) class 2 includes diameters between 750 and 1200μm
(3) class 3 diameters between 88 to 750μm
(4) class 4 includes all particles less than 88μm diameter.

Since explosions were assumed to be broadly spherical in shape , and our depth of imaging field is larger than 4 mm, our measurements are a 2D compressed observation of this spherical event. Computed velocities were thus classified as either

in-plane for ejecta having the maximal measured velocity or out of plane for reduced velocities. Based on a sample of 400 images the results are shown in figure 114:

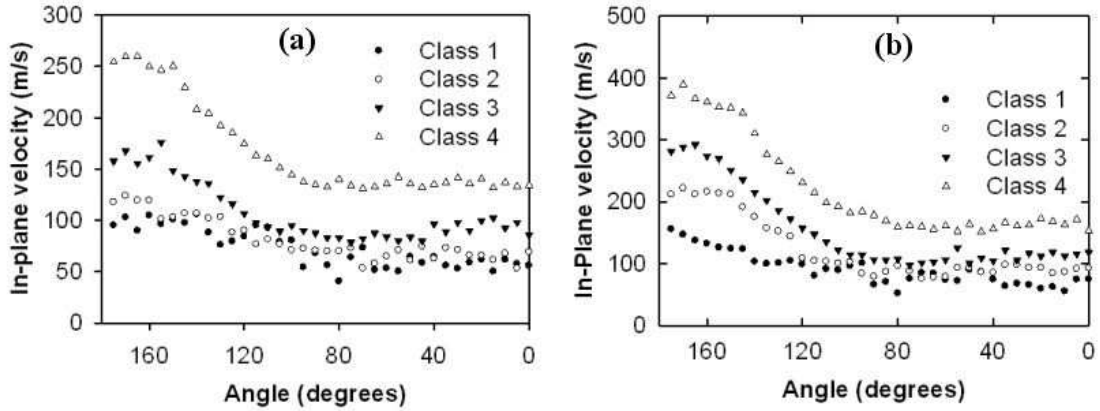

Figure 114: Velocities of in plane ejecta (see text for definition):
(a) 2-8 μsec image pairs
(b) 2-14 μsec image pairs.
See text for classes of particles.

The relative distribution of the number of ejecta, as a function of the polar angle, was found to be dominated by those travelling in the direction opposed to the propagation of the laser beam, see figure 115:

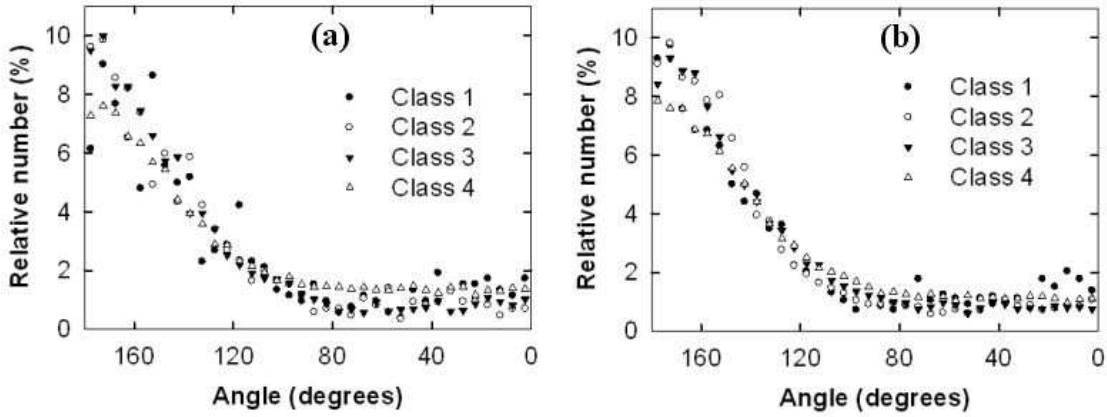

Figure 115: Relative ejecta number as a percentage.
(a) 2-8μsec image pairs and
(b) 2-14μsec image pairs.
See text for classes of particles.

The peak intensity value, relative to the initial peak intensity of the initial cluster, showed slightly larger ejecta to be present mainly toward 180 degrees. Large carbon clusters also tended to eject larger clusters towards the laser (see figure 116-b). If these clusters are not optically thin then the area facing the laser will suffer the greatest thermal shock during the initial laser pulse before heat is redistributed through the particle by primary particle to primary particle thermal conduction throughout the cluster. Hence the most thermally disturbed part of the cluster should produce the greatest amount and velocity for the ejecta, as observed.

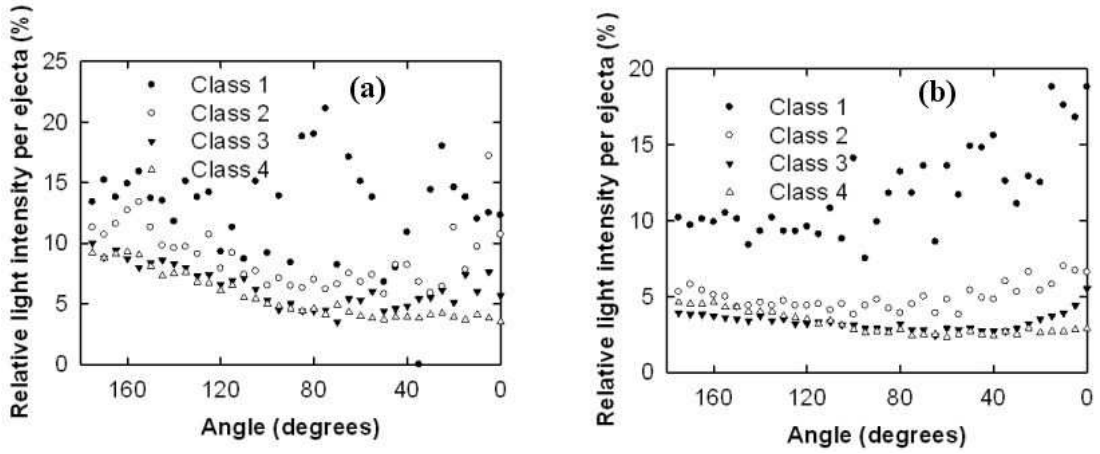

Figure 116: Relative size of ejecta based on intensity (see text):
(a) 2-8μsec image pairs
(b) 2-14μsec image pairs.
See text for classes of particles.

A comparison of the results obtained for the 8 and 14μsec separated image pairs leads to a number of important observations:

(1) the vast majority of ejecta travel in the direction opposed to the laser beam direction and, statistically, do not change direction because the number distributions are similar.
(2) the larger carbon clusters tend to remain at a 0 angle and this is most evident for larger initial clusters.
(3) the relative sizes of ejecta near 180˚ statistically diminish by a factor of approximately 2 between measurements at 8μs and 14μs.
(4) the velocities of the ejecta markedly increase between the 8μs and 14μs separated image pairs with at least some correlation to the initial cluster size.

Together all these observations suggest that there is a strong likelihood that chain explosions of the carbon clusters following the initial fragmentation were occuring. This would be consistent with ejecta accelerations and size diminution. The initial cluster location has an interesting feature: although clusters are central to the explosions, they were not observed to change positions. Therefore agglomerate explosions could proceed from the outside of the cluster into its centre but from the centre of the cluster towards its periphery.

An outstanding issue in this analysis remains the initial mechanism which induces the fragmentation and provides the impetus for the ejecta. The annealing of primary soot particles by fluences in the range 0.15 to 0.3 J/cm^2 has been observed and reported by Vander Wal et al (1999 1&3). The evidence for the morphology change in Vander Wal et al(1999 1&3) is not entirely clear with some data suggesting ~20% volume shrinkage and some indicating swelling. In conventional atmospheric pressure LII rapid cooling would likely quench the annealing effect. Obviously any significant morphology changes would sterically challenge the aggregate. In addition, in our modelling work it is clear that for vacuum conditions sublimation is also ever present. Either or both postulates are potential drivers for the fragmentation.

V.2.7. Measurements performed on isolated aggregates.

The ICCD system was photometrically calibrated and simultaneous pyrometric temperature measurements were obtained. Therefore, provided that ejecta or particles can be isolated within an image, their individual light intensity emission can be determined and therefore the number of primary particle per ejecta (or aggregate) can be estimated. 200 ICCD measurements were performed at a laser fluence of $0.24 J/cm^2$ after a 30µsec delay (see figure 117). The measured soot temperature was approximately constant at 2,550K for a 5µsec ICCD gating time.

Assuming a manufacturer specified 15 nm median primary particle diameter for carbon black powder used during these measurements, equation 96 can be applied to retrace the LII absolute signal intensity to the number of primary particle per isolated aggregate:

$$S_{gate} = n \cdot \Omega \cdot 4\pi^2 d_p^2 \int_{t1}^{t2} \int_{\lambda 1}^{\lambda 2} \varepsilon_\lambda \cdot \frac{2 \cdot \pi \cdot h \cdot c^2}{\lambda^5 \left[\exp\left(hc / \lambda \cdot k \cdot T(t) \right) - 1 \right]} \cdot \Sigma(\lambda) d\lambda dt \qquad \textbf{(96)}$$

Where S_{gate} is the integrated light intensity measured per aggregate, n is the number of primary particles per aggregate, T(t) is the actual measured temperature by the pyrometer. $\Sigma(\lambda)$ is the ICCD efficiency function, which was determined in section IV.3.3.2 (ICCD camera optics spectral transmissivity calibration) and is illustrated in figure 86-b. The number of primary particles per aggregate can therefore be calculated from the measured signal per aggregate S_{gate}:

$$n = \frac{S_{gate}}{\Omega \cdot 4\pi^2 d_p^2 \int_{t1}^{t2} \int_{\lambda 1}^{\lambda 2} \varepsilon_\lambda \cdot \frac{2 \cdot \pi \cdot h \cdot c^2}{\lambda^5 \left[\exp\left(hc / \lambda \cdot k \cdot T(t) \right) - 1 \right]} \cdot \Sigma(\lambda) d\lambda dt} \qquad \textbf{(105)}$$

The results obtained are contained in figure 118. The smallest particle detectable was equivalent to 6 or 7 primary 15 nm particles, while presuming to be in a small aggregate. This limit corresponds to a signal to noise ratio of approximately 5. The criteria for distinguishing an ensembled group of primary particles were:

(1) for a single illuminated and isolated pixel an intensity value > 5 times the camera noise;
(2) that a group of illuminated pixels required a minimal average separation of 5 pixels between itself and other non-touching areas to be recognised as an individual cluster.

It should be noted that these clusters of primary particles have been exposed to intense sublimation and prolonged annealing and are not monodisperse in size; therefore the results given in figure 118 need to be considered with care and simply illustrate the potential of this approach to soot/carbon black measurement. Even though these results have to be considered with great care, they demonstrate the potential of laser induced incandescence under vacuum in terms of detectivity. It is indeed not conceivable for "standard" LII to perform such a low concentration measurement and resolve on the scale of aggregate and soot primary particles emission intensities. For LII under vacuum, this has been made possible thanks to greatly lengthened signals and an associated gain in detectivity of more than 300.

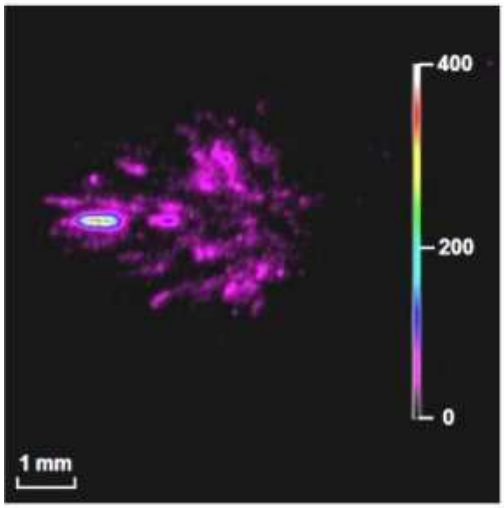

Figure 117: Image of an exploded cluster for a gating of 25-30µsec after laser excitation. The color scales is in ICCD counts.

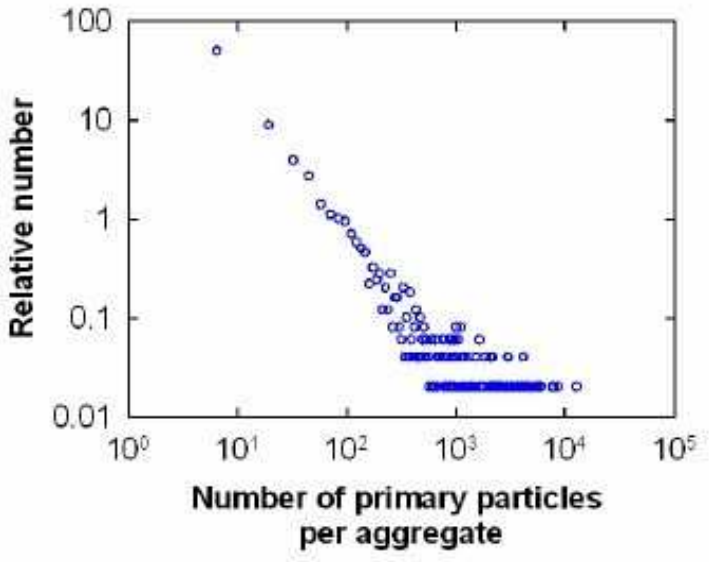

Figure 118: Plot of the relative number (%) of particles versus the number of primary particles measured per isolated aggregate based on 15 nm diameter primary particles.

V.2.8. Conclusions to this LII under vacuum investigation.

Even though a more thermophysical approach was expected at first, the first systematic investigation of large carbonaceous clusters during LII was performed . Carbon nanoparticles isolated in free space in a high vacuum (below 10^{-3} mbar) endured Laser-Induced Incandescence and produced long-lived light pulses as expected. Series of experiments was performed. The latter have consisted of a pyrometric study of the particles following from laser thermal excitation and a number of imaging experiments to determine the dynamical behaviour of the particles. Based on results and analysis, the following main points can be concluded:

(1) That carbon black clusters, even of size larger than 200 μm, irradiated by a laser pulse have an optical absorption and radiative behaviour in a vacuum which is similar to isolated single primary soot particles.
(2) That in a vacuum, because the cooling of the particles is rapidly dominated by radiation, it is possible to estimate E(m) for the carbon nanoparticles directly from pyrometry of the particles. The results for high and medium fluences are consistent with an E(m) value comprised between 0.4 and 0.6, with an accuracy is limited by temperature uncertainties in the order range of 100K.
(3) Sublimation is a major contributor to agglomerate dynamics and was suspected to result into non negligible levels of C_2 thermally excited emission for the initial 170 ns.
(4) After a delay of about 2 to 5 μsec large clusters of carbon nanoparticles fragment. This fragmentation process leads to high velocities up to 400 m/s for the ejecta and there is experimental evidence which supports this fragmentation process occurring over an extended period of microseconds as a chain of events. The origin of this fragmentation is not clear and two phenomena postulates for inducing fragmentations: annealing and sublimation. Both sublimation and annealing are linked and associated to brutal morphological changes for primary particles.
(5) LII signals tend to dramatically increase after a delay of about 5 μs though this is not matched by any measurable change in temperature. It was also found that LII signals increase with increasing fluence.
(6) It is postulated that for large clusters that the particles are not optically thin and that they are heated preferentially of the side facing the laser. This leads to a situation following fragmentation that more hot primary particles are revealed to the detector than could be observed when the cluster was tightly bound, hence increasing the signal and the effective soot volume fraction measured.

The initial motivation for this investigation was to establish the tire-resolved temperature decays for LII under vacuum and compare them with modeled E(m) values. The second motivation was to apply a novel 2D calibrated LII measurement method in order to assess the gain in sensitivity associated with greatly lengthen LII signals for a time-integrating measurement device. In this instance an intensified CCD camera. Even though these two objectives were achieved, the very nature of the sample measured deepened our understanding of the physics occurring during LII.

Indeed, main signal contributors were carbon black agglomerates in the order range 100 to 200 microns diameter. Throughout this study, these were established to :

(1) emit and absorb light similarly to their constituent nanoparticles

(2) disaggregate and "explode" when incandescent during LII.

The dynamics of these agglomerate behaviours were dependent of fluence and could prove also dependent of cluster size. Indeed, a general trend was observed: the highest the laser fluence, the shortest and the most vigorous the agglomerate explosions and the sooner they would occur.

The soot volume fraction observations can be defined as optical shielding: incandescent soot nanoparticles radiation is shielded from the photodetectors by adjoining particles within the same agglomerate or aggregate. Clearly this was the case for the first microseconds of LII for agglomerates.

There is a greater probability that smaller agglomerates dissociate on a time scale of less than one microsecond and therefore the same trend would be observable for atmospheric LII. Because imaging is not foreseeable on timescales of less than one microsecond for individual agglomerates, this would translate into an increase in measured soot volume fraction with laser fluence. As well as a diminution of optical shielding, a reduction in heat shielding, whereupon the effective heat conduction rate of soot nanoparticles is reduced and therefore the measured primary soot particle diameter becomes overestimated by a large factor, would become observable. Indeed, the vast majority of modern particulate matter emissions are in the PM_{10} class range (particulate matter particles smaller than 10 microns) and the rapid morphological changes that are at the origin of agglomerate dissociation under vacuum can be expected to occur in standard conditions.

V.3. Laser –Induced Incandescence Under vacuum at NRC ,Ottawa (Canada): a high accuracy investigation into low and medium fluences.

As discussed previously in chapter IV, although results obtained at Cranfield proved consistent and reliable, they were limited to a fluence range of 0.15 – 0.24 J/cm^2 as the system could not be optimised to measure low concentrations of particulate matter (<1ppb) and temperature uncertainties were higher than 50K. Therefore measurements were performed at the National Research Council (NRC) on the carbon black sample roller bottles. High accuracy LII under vacuum measurements were performed at low to medium laser fluence (up to 0.15 J/cm^2) with a state-of-the-art dual wavelengths pyrometric system which is described in details in section IV.4 (Details of the NRC measurement system).

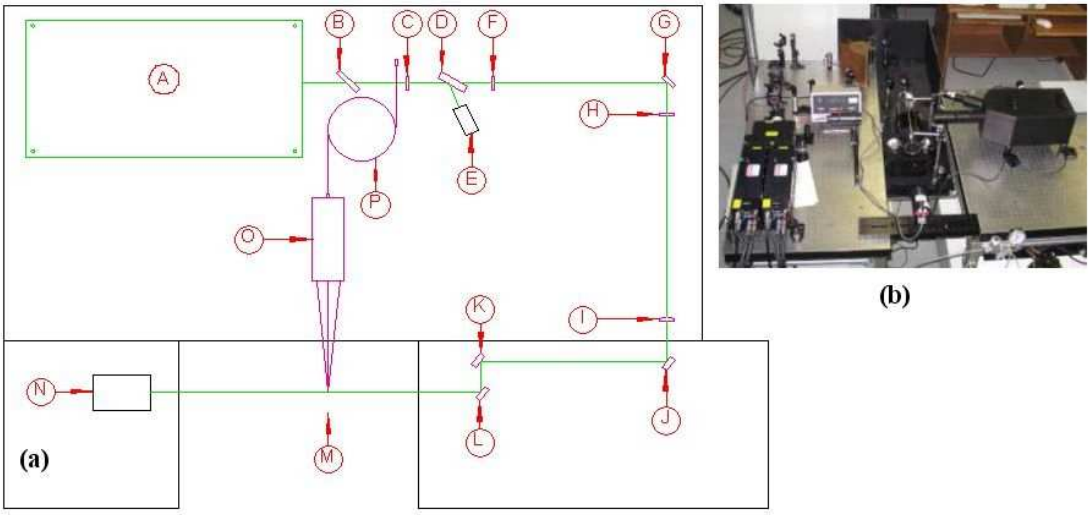

Figure 119: NRC dual wavelength pyrometer measurement system (details available in section IV.4)

The objectives of the investigation were to:

(1) establish the validity and consistency of the LII signals obtained in terms of temperature repeatability. Given the resolution of precedent measurement system at Cranfield (300K shot to shot), it was not clear whether the temperature history between LII signals would be repeatable and to what extent.

(2) Provided LII under vacuum temperature histories are repeatable between single LII measurements, perform high accuracy multipulse LII under vacuum measurements for the fluence range between 0.05 to 0.15 J/cm^2.

(3) Compare the temperature curves obtained with modelling of laser absorption, sublimation and radiation

V.3.1. Laser-Induced Incandescence under vacuum - temperature measurements repeatability

Before performing high- resolution temperature measurements using a multipulse-averaging technique, laser-induced incandescence signals under vacuum had to be characterized as to whether they are repeatable in terms of temperature curves on a single LII pulse basis. As the Cranfield system achieved a single-pulse resolution circa 300K on average at medium to high laser fluence (0.15 to 0.24 J/cm2), it was not clear whether LII under vacuum signals would prove repeatable in terms of temperature measurements at lower fluences (0.04 to 0.15 J/cm2) and to which extent.
For this experiment the LII system described in IV.4 (Details of the NRC measurement system) was used to record 150 to 200 single-pulse measurements at various laser fluences ranging between 0.07 J/cm^2 and 0.153 J/cm^2.
Each Laser-Induced Incandescence signal was separately recorded using an oscilloscope time resolution of 400ps and later filtered and resampled. Additional filtering was also considered at low fluences in order to obtain comparable temperature data.
For experimental measurements, 0µs denotes the start of the laser pulse. A remarkable trend was that, although temperature profiles are modelled to be similar with fluence as from 10µs after the laser pulse and onward, signal levels were rising with increasing laser fluences, from the minimal signal detection level to extremely consistent signals, therefore increasing the Signal-to-Noise Ratio (SNR) of the measurements obtained with increasing fluences. This increase in signal levels was consistent with an increase in measured soot volume fractions, as displayed in figure 122. A general observation is that the noise levels increased with decreasing temperatures, with large noise levels below soot temperatures of 2200K.
Signal filtering was adapted to the evolution of the noise level, with initially a 1ns resampling and filtering rate for the first nanosecond of signal, followed by a higher noise rejection with 10ns filter and resampler time constant and finally the highest noise rejection with 100ns filter and resampler time constant for signals below 2500K.

The averaged LII signals obtained are available in figure 120 for both blue and red channels as a function of time and fluence, while the average temperature curves and soot volume fraction measured are illustrated on figure 121-a and 122, respectively.
An excellent temperature repeatability was found within the error range of single-shot measurement exploitation. This illustrated in figure 121-b. Also, no deviations in terms of temperature repeatability were measurable and temperature repeatability was therefore estimated to be better than 50 K for a fluence of 0.153 J/cm^2.

In terms of soot volume fraction, although maintaining exactly the same carbonaceous particulate matter concentration within the measurement volume was difficult, variations between experiments in terms of soot volume fractions would be in the order range of 50 to 100% and these would be eventually lowered to less than 50% with multipulse averaging. However, the averaged measured soot volume fractions (SVF) presented in figure 122 shows an increase in the measured soot volume fraction of nearly 100 times with fluences increasing from 0.07 to 0.153 J/cm^2.

An excellent repeatability in terms of temperature measurements was observed. Therefore performing multipulse averaged LII measurement was possible. Multipulse

averaged LII exploitation lowers greatly the measurement noise level and therefore increases the resolution and accuracy of the temperature measurements obtained during LII under vacuum.

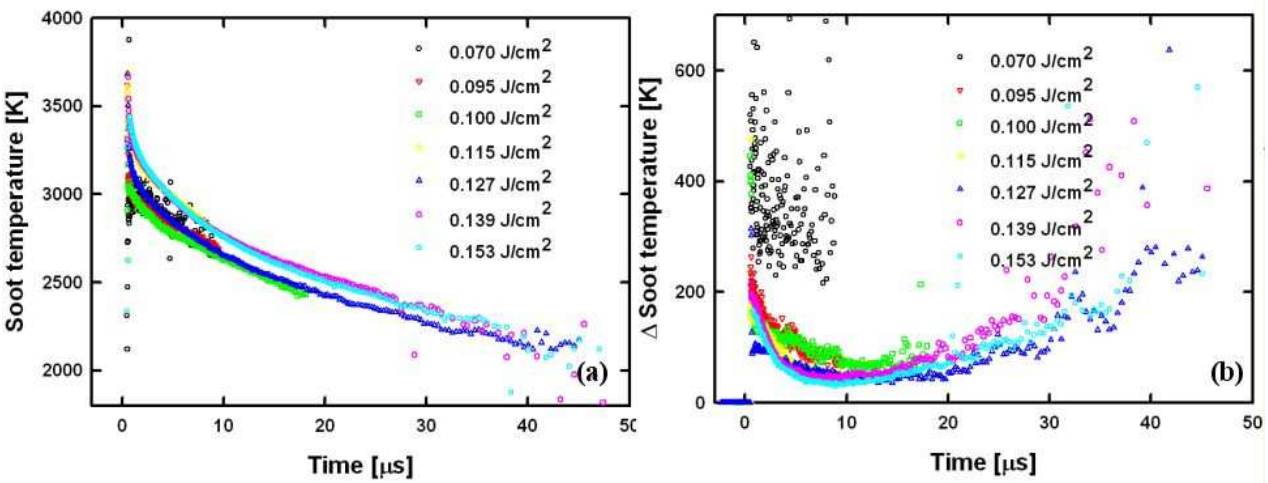

Figure 120 : Average LII absolute light intensities as a function of time measured for a fluence ranging from 0.070 to 0.153 J/cm^2 for both demultiplexer channels:
(a) blue channel
(b) red channel

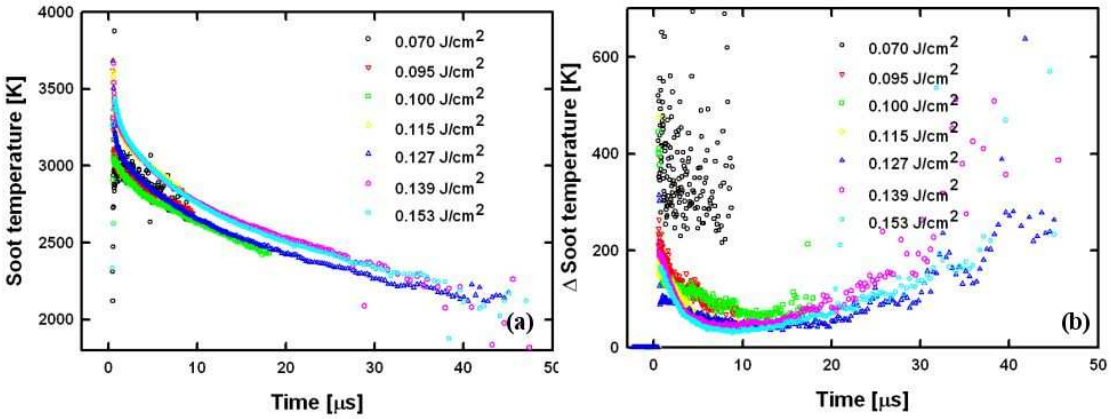

Figure 121: Average of temperatures measured on a single-shot basis (a) and temperature reproducibility (b), illustrated as a standard variation for typically 150-200 single-shot LII measurements.

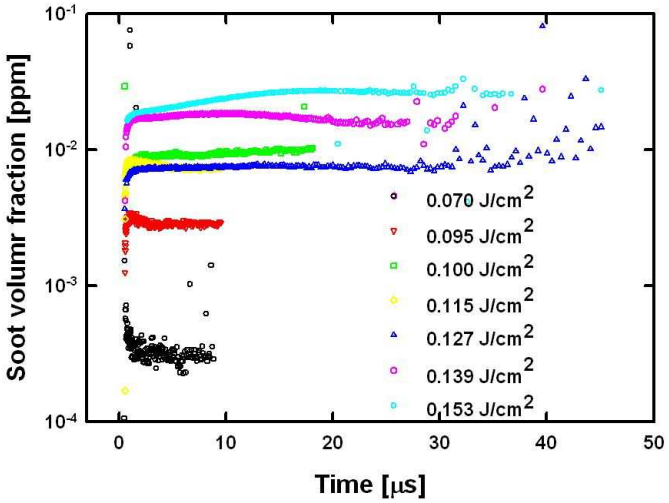

Figure 122 : Average soot volume fractions measured at difference fluences. Note the noticeable variation of a factor of 67 to 100 difference in soot volume variation with fluence between the lowest fluence achievable for this experiment (0.070 J/cm^2) and the highest one (0.153 J/cm^2) whereas the effective carbon concentration was approximately constant.

V.3.2 Multipulse averaged LII under vacuum measurements.

Multipulse LII under vacuum measurements were performed so that a comparison between modelled and practical LII signals and temperatures could be made. 6000 multipulse averages were measured for each laser fluence..
A novelty here consisted in performing laser beam absorption measurements as well as temperature decay measurements. This followed an investigation into the Q-switch noise behaviour of the system, as typically absorption measurements during LII measurements were corrupted by a high level of noise due to the laser Q-switching and therefore producing a high level of RF noise being apparent on both detectors channel. Although reducing Q-switch noise using a physical mean remains an attractive option, this is hardly achievable even when using additional Faraday cages and shielded cables. A more straightforward observation concluded that:

(1) the Q-switch noise is repeatable when multiply averaged
(2) the jitter between the oscilloscope trigger and the Q-switch noise recording on the oscilloscope channels scales to nearly 20 ps.

These two parameters allowed for Q-switch noise substractions when taking LII measurements: the Q-switch noise itself was measured using the same oscilloscope recording setting as would be used for recording LII signals, and later substracted during initial data processing once the LII signals were recorded. Therefore for each measurement 6000 pulse averages were recorded with the laser firing but no light signal collected by the optical demultiplexer. This allowed for a reduction of a factor of approximately 30 in terms of Q-switch noise. The signals were then processed and filtered (see section V.3.1 for filtering details).

The overall temperature resolution reached well below 5K in some cases. Overall temperature uncertainties were difficult to estimate and are indeed within the range 10-20 K provided the E(m) assumption of a constant value over the visible range remains applicable in the present case. The results obtained for low fluence

measurements - from 0.046 to 0.081 J/cm^2 - are presented in figures 123 and 124. Two horizontal scales (0-1µs and 1µs-90µs) are available for clarity, as at first LII signal decays are fast (due to sublimation) during the first microsecond, to become slower and radiative-dominated later on. Note that the presence of Q-switch noise on the red channel is a residue of the Q-switch substraction combined to a relatively high noise pick-up from the red channel photomultiplier tube when compared to the blue channel. This can be explained by the fact that red-sensing devices and measurements effected toward 800 nm are generally more prone to shot noise and therefore noise pick-up (in this case a multi-alkali red-enhanced photocathode was used). Similar behaviour was observed on the Cranfield LII system. Clearly an absorption study could not be performed for the low fluences as signals were corrupted by the remnants of the Q-switch noise. A few interesting trends to note were that:

- Initial sublimative temperature decays are present as rapidly decaying soot temperatures become apparent during the first microsecond.
- All temperature measured between the 10-20µs time interval agreed within 50K and comforted the belief that the emitting primary particle size distribution is nearly uniform in terms of temperatures, as modelled earlier .
- The soot volume fractions measured increased by factor of approximately 20 between 0.046 J/cm^2 and 0.081 J/cm^2 and indeed increase with fluence, providing a measurable increase in absolute intensity light signal levels. However, since the actual soot volume fraction is not known and varied by an estimated 50-100%, no particular study of SVF increase with fluence was envisaged.
- Similarly to the insight provided by the experiments led at Cranfield University, a neat increase in SVF with time was clearly noticeable for the first 25µs of LII signals, followed by either a drop in SVF or a carbonaceous particulate matter concentration remaining approximately constant. This again confirms the hypothesis that agglomerate explosions are occurring and that consequent excited particulate matter overall filling volume exceeds the measurement volume after ~ 25µs.

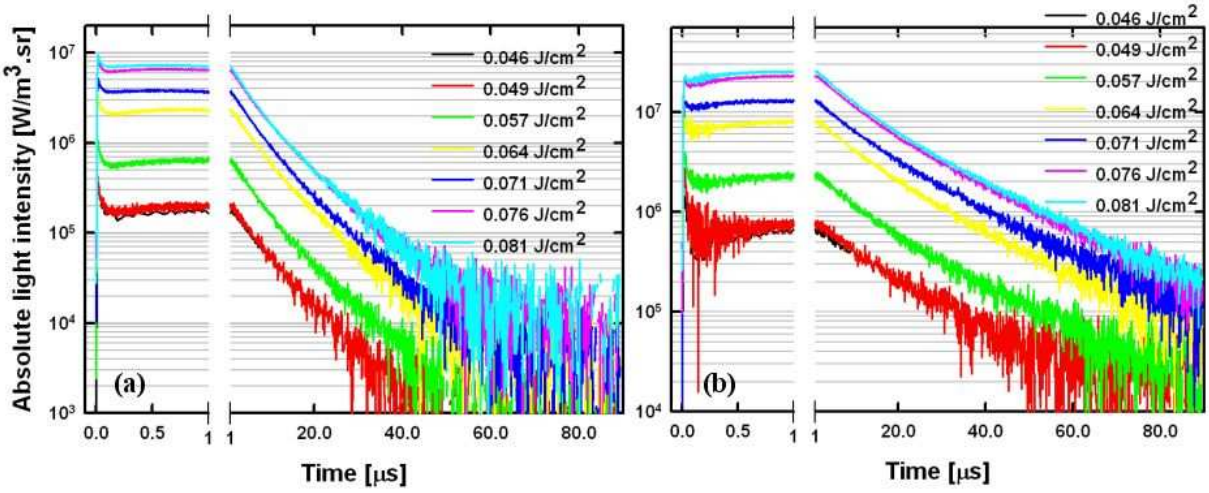

Figure 123: Absolute light intensities as a function of time measured for laser excitation fluences ranging between 0.046 J/cm^2 (minimal fluence achievable) and 0.081 J/cm^2: (a) blue channel (b) red channel

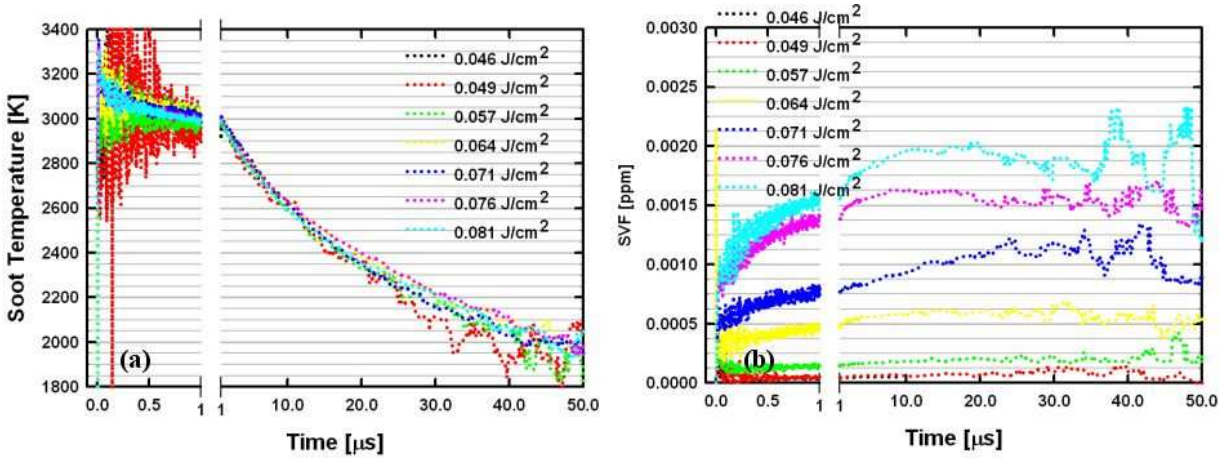

Figure 124: Soot temperature and Soot Volume fraction (SVF) as functions of time for laser excitation fluences ranging between 0.046 J/cm^2 (minimal fluence achievable) and 0.081 J/cm^2 (medium fluence) and computed using absolute light intensity data displayed on figure 129: (a) Soot temperature (b) Soot volume fraction.

Since the measured signal levels and consequently the soot volume fraction are increased with further increasing fluence, excellent results were obtain for laser irradiation fluences comprised between 0.086 and 0.145 J/cm^2. Results are presented as absolute light intensity channel exploitation (figure 125) or temperature measurements (figure 126). Also, the soot volume fraction temporal profiles display sharp increases associated with agglomerates dissociations. Clearly, this is a constant phenomenon as from laser fluences as low as 0.046 J/cm^2.

Therefore a situation were significant sublimation was not obtained and the soot volume fraction measurements performed showed obvious signs of agglomerates dissociation: initial sharp rises followed by large increases in the measured soot volume fraction with time are clearly observable on figure 124-b. The sole physical phenomenon that can be attributed to this behaviour is annealing of primary soot particles. Annealing consists of graphitic reorientations and rearrangements (interstitial migrations) for primary soot particles resulting into both expulsion of carbonaceous matter from the centre of primary particles and an overall morphological rearrangement into fullerenic structures. These two phenomena clearly result into large scale expulsions of carbonaceous matter from primary soot particles within the agglomerates combined with brutal morphological changes overcoming the Van der Waals attraction forces between aggregates within agglomerates. These obviously result into agglomerate dissociations at low fluences were sublimation does not provide significant contribution. For higher fluences though, intense sublimation associated with annealing explains further decreases in light shielding from agglomeration and more vigorous agglomerate dissociations.

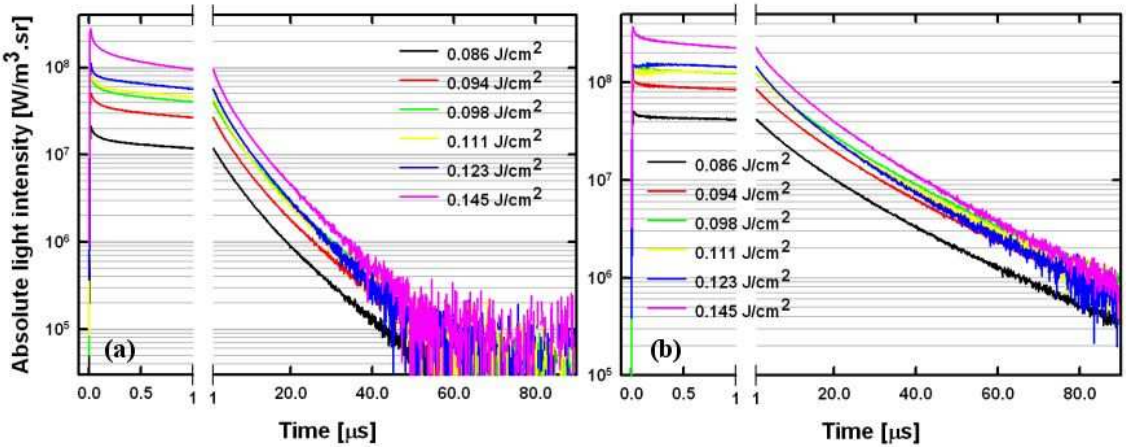

Figure 125: absolute light intensities measured for laser excitation fluences ranging between 0.086 J/cm^2 (medium fluence) and 0.145 J/cm^2 (high fluence).
(a) Blue demultiplexer channel
(b) Red demultiplexer channel

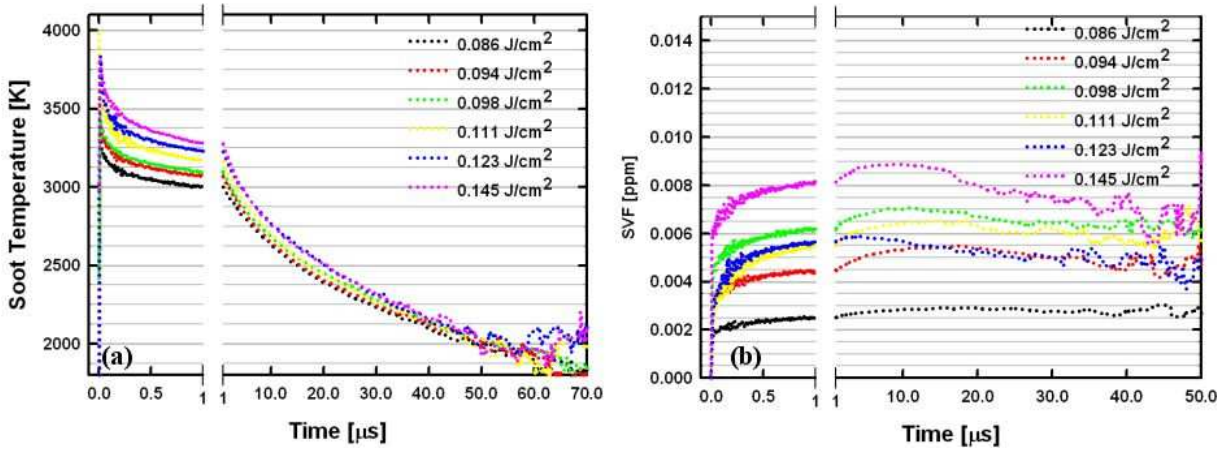

Figure 126: Soot temperature and Soot Volume fraction (SVF) for laser excitation fluences ranging between 0.086 J/cm^2 (minimal fluence achievable) and 0.145 J/cm^2 (medium fluence) and computed using absolute light intensity data displayed on figure 125.
(a) Soot temperature
(b) Soot volume fraction (SVF)

In parallel, observations for agglomerates at atmospheric pressures were also obtained from a source of "cold carbon". The measurements obtained on Vartan Grigorian's "cold carbon" generator together with a description of the apparatus are available in appendix G. The apparatus provided extremely an extremely repeatable and stable particulate matter concentration, with LII measurements differing by 6.7% on a pulse-to pulse basis. The device generated spherical agglomerates, which were measured by Transmission Electron Microscopy (see appendix G for details) , with a median diameter of 236 nm for a median primary soot particle diameter of 18nm. Measurements were performed with the NRC measurement system using the multipulse averaging technique at fluences ranging between 0.067 J/cm^2 and 0.150 J/cm^2 in the centre of the exhaust plume at atmospheric pressure and a gas

temperature of circa 90 °C. The results obtained are illustrated in figures 127, 128 and 129. As it was expected following the work published by Smallwood and Stagg (2006), it was found that the average soot volume fraction measured was rising with increasing laser irradiation fluences, as shown on figure 129-b. Therefore an extrapolation of the phenomena observed for large agglomerates enduring dissociations during LII over 2 to 15 µs under vacuum can be made for much smaller and more common agglomerates in the hundreds of nanometres diameter scale. A very obvious 32% reduction in the primary particle diameter measured by LII with fluence was noticeable together as well as an increase in soot volume fraction by a factor of 3 between 0.067 J/cm^2 and 0.150 J/cm^2. On one hand, such large reductions in terms of primary particles diameters cannot be attributed to sublimation at medium fluences and a reduction of the primary particle diameter of 32% is more likely for a laser fluence of circa 1J/cm^2. On the other hand, provided the structural entities of which the measurement was performed remained identical, a decrease rather than an increase in terms of measured soot volume fractions would be expected. Hence agglomerate dissociations on a nanosecond timescale provides a plausible explanation for the observed rise in soot volume fraction with fluence. These dissociations would result into a net diminution in optical shielding within agglomerates with increasing fluence. And this would furthermore be associated with a net diminution of thermal shielding during heat conduction for individual nanoparticles within the agglomerates and hence provide an excellent explanation for the reduction in the measured primary particle diameter associated increasing fluence. However it remains clear that the primary particle diameter measured for a fluence of 0.15 J/cm^2, that is 28 nm, remains far from the actual median soot primary particle measured at 18 nm. Hence agglomerate dissociations were not complete on the 200 to 400 ns timescale the atmospheric measurements were performed and eventually higher fluences would be required to obtain realistic size measurements for primary particles enclosed within agglomerates with laser-induced incandescence.

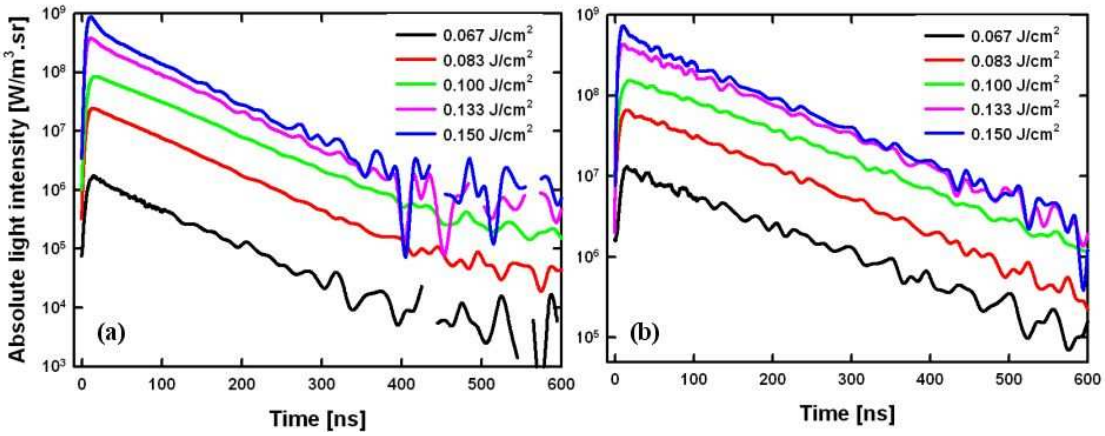

Figure 127: LII signal absolute light intensity signals recorded from 35mm above the cold carbon generator drier outlet for five different laser fluences, ranging from 0.067 to 0.150 J/cm^2:
(a) Blue channel measurements
(b) Red channel measurements.

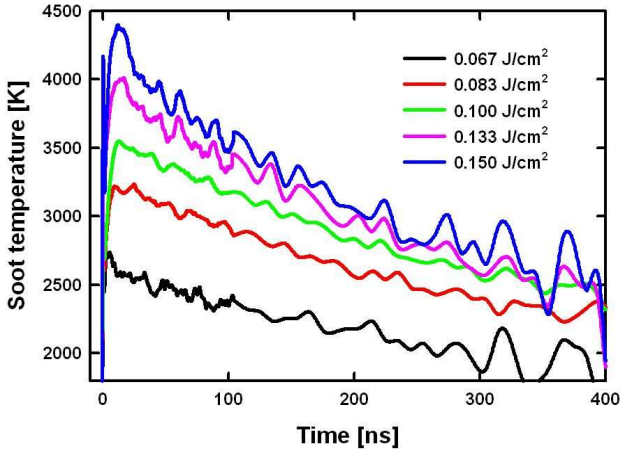

Figure 128: Laser-Induced incandescence temperature as a function of time curves obtained from the exploitation of the results presented in figure 127.

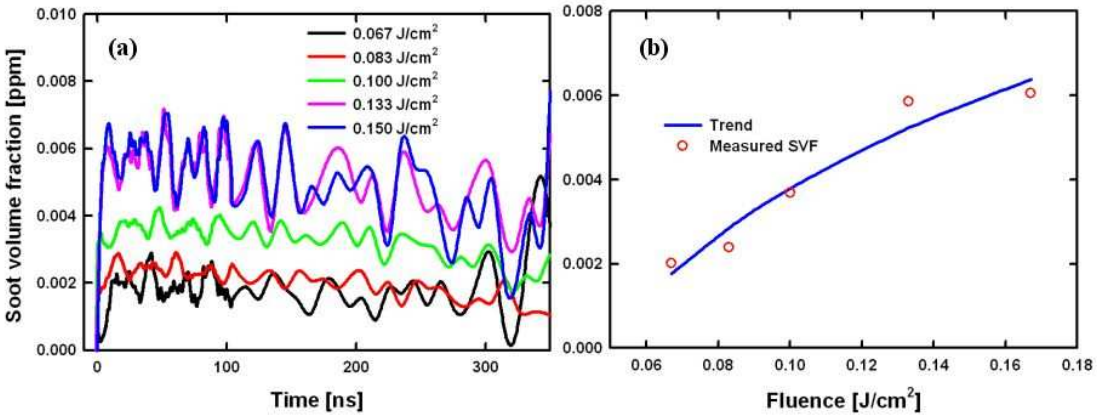

Figure 129: Instantaneous (a) and time-averaged (b) soot volume fraction as a function of time and fluence.

V.3.3. Laser absorption studies.

An initial E(m) determination by laser absorption means was performed throughout the laser fluences range, extending Snelling et al.(2004) assumption that LII peak temperatures are independent of primary particle size at low fluence into the medium fluence range (>0.081 J/cm^2) by taking into account that:

(1) no conduction is present, and therefore primary particle size dependence of the peak LII temperature is diminished ;
(2) primary particle size is assumed monodisperse at 15 nm diameter ;
(3) sublimation modelling is assumed to agree with practical measurements during the particle heat-up phase of LII.

Therefore the laser temporal profile (approximated as a Gaussian with 14.7ns FWHM) was fed into the laser-induced incandescence model for the fluence range 0.064 to 0.145 J/cm^2 and the peak modelled temperature matched with the measured peak LII temperature by means of varying the modelled E(m) value for absorption at 532nm. The obtained results are given in table 6. An average E(m) value of 0.47±0.05 was found, which is indeed 16% higher than the values measured by Snelling et al. (2004) for flame soot aggregates. Given the overall level of agglomeration within the carbon black clusters, high values for E(m) were expected.

Laser Fluence [J/cm^2]	**Measured soot peak temperature [K]**	**Estimated corresponding E(m) value**
0.064	~ 3150	0.52
0.071	~ 3200	0.48
0.081	~ 3250	0.43
0.094	3410	0.40
0.111	3726	0.45
0.123	3833	0.54
0.145	3819	0.44

Table 6: E(m) modelled values for the peak temperatures measured from 0.064 J/cm^2 to 0.145 J/cm^2. LII soot peak temperatures for fluences of 0.064, 0.071 and 0.081 J/cm^2 are approximated within 50K as the noise level did not permit an accurate peak temperature determination.

In addition, the model overestimates the initial temperature decay rates (see figure 130), which were assumed to occur because of sublimation heat losses. Clearly annealing is to be considered and graphite crystallisation rates are exothermic and should therefore diminish heat loss rates for the first ~500 ns (Michelsen, 2003). The results obtained were rather unexpected as the traditional C_2-C_3 sublimation modelling was supposed to underestimate initial sublimative temperature decay rates by a factor of nearly 60% (Michelsen, 2003). For studies beyond the scope of this present work, incorporating Hope Michelsen's sublimative heat loss rates into the LII model has great potential to result into a direct measurement of the annealing heat loss rates. A later correction for the electron transit times of the photomultipliers tubes was applied using a scattered 532 nm signal from an optical surface sensed by all three photomultiplier tubes of the NRC LII system at various gain settings. The LII measurements could then be aligned with the average scattered laser pulse measured

for each multipulse average and the delay between the peak of the laser pulse and the LII peak soot temperature occurring measured, see figure 131. Results are compared with theoretical modelled temporal locations and were remarkable in terms that at low fluence, when absorption is considered as the dominant heat transfer mechanism, the peak soot temperature occurred up to 31 ns (at 0.04 J/cm^2) prior to its theoretical temporal location, meaning that eventually for fluences bellow 0.09 J/cm^2 laser absorption is not the sole thermodynamic effect contributing to soot particles heat-up. Again, annealing emerges as a possible explanation for earlier than expected soot peak temperatures, which would mean as well that E(m) is largely overestimated at low fluences. However , it is not clear whether E(m) is overestimated as the results displayed in table 6 are consistent over the whole fluence range with an average value of E(m) = 0.47. As well, for fluences greater than 0.09 J/cm^2, peak soot temperature locations agree with theoretical locations and therefore provide a support for future investigations.

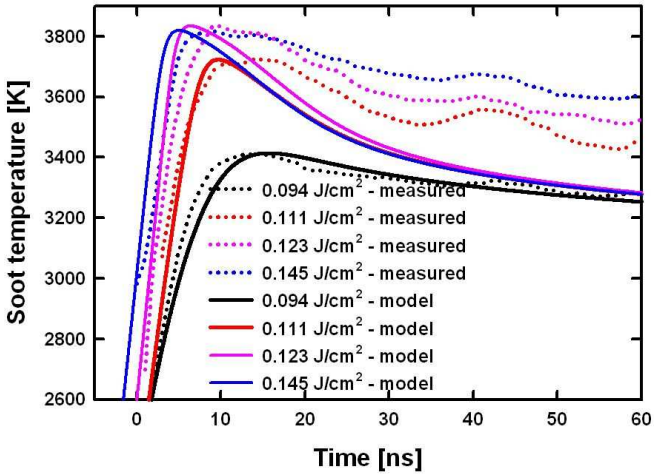

Figure 130: absorption modelling and LII temperature rise time – for measured E(m) values (See table 7)– note that model and measurements agree within 2 ns for the rise time, which is near the photomultiplier tubes response times (1-1.5ns).

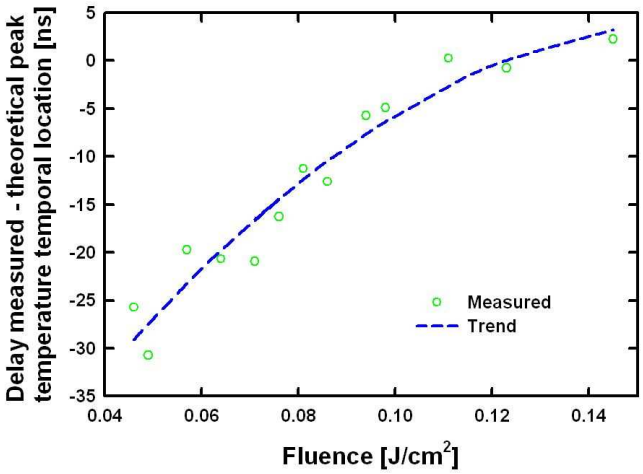

Figure 131: Comparison between the measured temporal soot peak temperature locations and the modelled ones .

V.3.5. Sublimation temperature decays

Theoretical modelling in chapter III lead to the conclusion that sublimation is the dominant heat loss terms during the first 10µs of LII temperature decays under vacuum, while gradually becoming negligible when compared to radiative heat loss rates as from circa 10µs after the occurrence of the peak LII soot temperature.
Hence LII peak soot temperature were fed into the model and the measured temperature decays compared with modelled temperature decays for all the laser irradiation fluences utilized during this experimentation , and the results are illustrated by the figure 132:

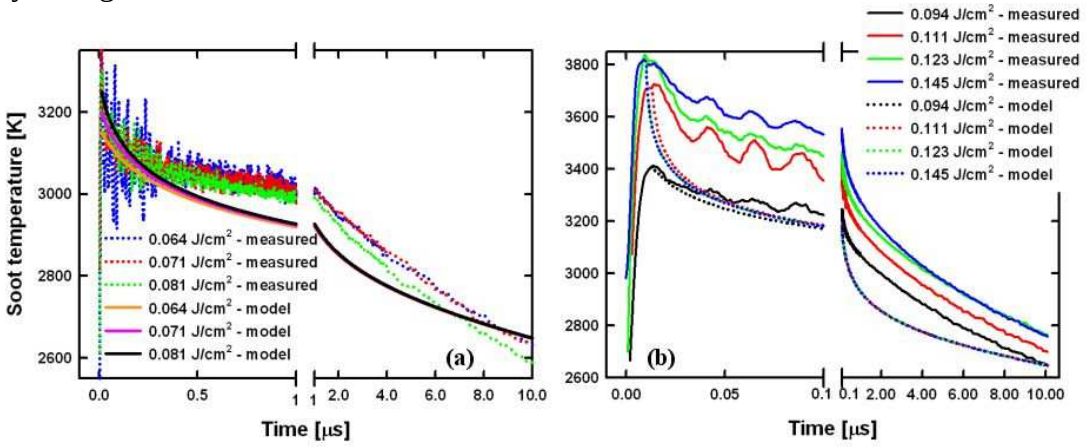

Figure 132: comparison between modelled and measured sublimative temperature decays, present during the first 10µs of LII temperature decay for all the laser irradiation fluences measurements were taken at. Clearly sublimation rates are overestimated by the model for all fluences:
(a) Fluences ranging from 0.064 J/cm^2 to 0.081 J/cm^2
(b) Fluences > 0.094 J/cm^2.

An obvious observation is that in all cases sublimation heat loss rates are overestimated by the model, from the first microsecond to the end of the remaining 9 microseconds. At low fluences, the modelled temperature becomes equal and then higher than the actual measured temperature circa 7µs : this can be assumed to be the start of the radiative temperature decay and therefore should not be taken into consideration. The following can be postulated:

(1) Carbon sublimation is modelled for a single soot primary particle and is based on the fact that carbon sublimation occurs by expulsions of mainly C_2 and C_3 carbon chains away from the particle inner and outer volume, with expulsion jets (vapour) velocities measured for graphite surface as achieving the velocity of sound. Clearly this assumption can be questioned, as we are facing here the case of strongly agglomerated soot agglomerates and it can be assumed that the conditions for sublimation velocities to reach their modelled rates are not met, resulting in lowered velocities and therefore lower sublimation rates.
(2) Annealing again could be considered to play a role. Annealing however has been so far estimated to take place over less than 500 ns (Michelsen, 2003). Establishing the time scale on which partial or complete annealing as well as the structural entities obtained has great potential for further researchs.

(3) Eventually associated with the first point is that the effective surface of the primary particles that is allowed to sublimate is lowered, due to particles being entangled and therefore thermally shielding each other from sublimating.

Clearly, I believe that all three possibilities are occurring here, and this mainly because all fluences are concerned. Using the results available it was not possible to investigate further and separate agglomeration and heat shielding factors from annealing. In order to separate these two factors, LII under vacuum would have to be performed on non-clusterous particulate matter and this would represent an extension of the present work.

V.3.6. Radiative temperature decays.

It has been demonstrated previously that radiative heat losses are the largely dominant heat term as from 10µs after laser irradiation. Therefore the measured temperature curves were fit with modelled radiative curves of matching E(m) value, as described in figure 133:

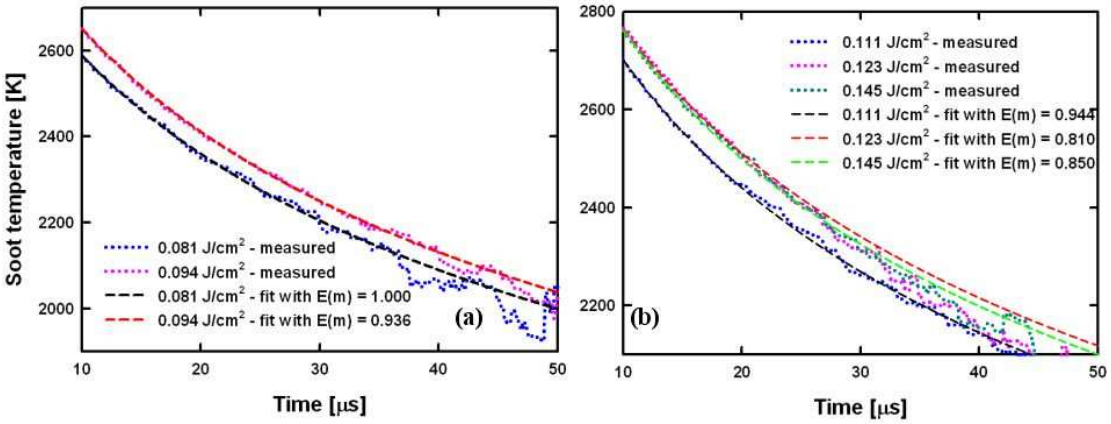

Figure 133: comparison 10 us and after – radiative temperature decay
(a) for fluences from 0.081 J/cm2 to 0.094 Jcm2
(b) for fluences of 0.111 J/cm2 and above

Curve fits were applied with excellent correlation coefficients obtained between 0.4 to 1%, so clearly the shape of temperature variations versus time is typical of radiative temperature decays. However, corresponding E(m) values are found to be ranging from E(m) = 0.810 to 1, and this is a factor two difference between these measurements and the ones obtained by absorption (E(m) = 0.47). as well, the measured E(m) value by radiative temperature decay decreased with increasing fluence, from 0.1 to 0.85 for respectively laser fluences of 0.081 to 0.145 J/cm^2.
Clearly, two trends can be identified:

(1) over the first nanoseconds of LII signals, consistent E(m) values were measured by absorption.
(2) the radiative temperature decays measured over tens of microseconds were quenched toward large E(m) values.

It is also recognised that large E(m) values are associated with agglomeration (Mackowski, 2006). Furthermore, the measurements were performed with laser fluences of up to 0.145 J/cm^2 and a 17.5 ns FWHM laser excitation pulse whereas the measurements at Cranfield yielded E(m) measurements comprised between 0.6 and 0.4 for laser fluences ranging between 0.15 and 0.28 J/cm^2 and a 7.5 ns FWHM laser

excitation pulse. The discrepancy between the E(m) measurements obtained at Cranfield can therefore be explained by a large difference in terms of instantaneous laser peak power, with the Cranfield laser system delivering up to 4 times more peak power than the NRC system. Hence a relationship between the agglomeration state during the radiative temperature decay and the initial laser peak power can be established, with particles being more effectively disaggregated at higher laser peak powers. The fact that during the first nanoseconds and for the peak LII temperatures reasonable E(m) values were found would then rely on emission of only the outer layer of the agglomerates radiating and absorbing laser light freely, with the remaining nanoparticles being subject to optical shielding. This would also explain the negligible soot volume fraction measured at the start of LII for measurements such as the ones illustrated by figure 126-b.

V.3.7. An exception

The following LII signals presented in figures 134 and 135 (analysis) were observed during four series of multipulse averaged (3000 LII pulses per average) measurements performed consecutively at a fluence of 0.084 J/cm^2. Even though these signals were extremely reproducible at this time, they could be measured only during one day of test and successive attempts to repeat them were unsuccessful. The peak temperature was measured at 3320 K, corresponding to an estimated E(m) value of 0.42.

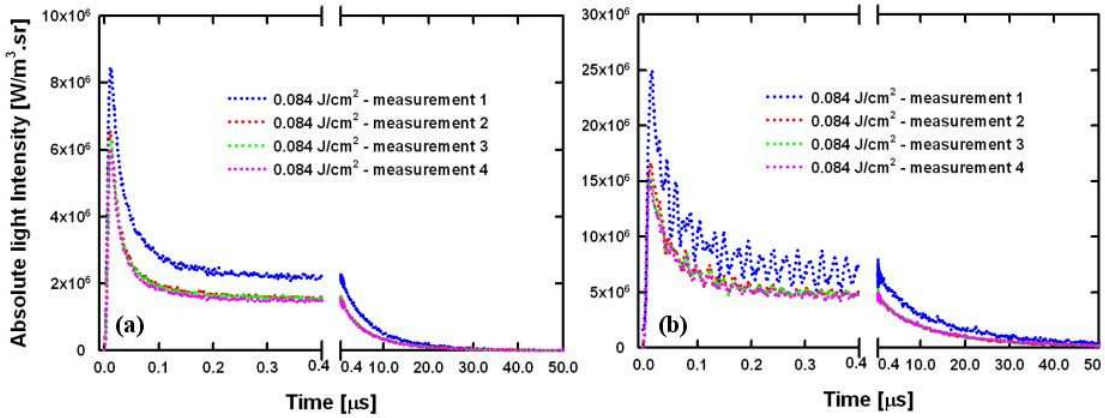

Figure 134: Absolute light intensity measurements performed at 0.084J/cm^2
(a) blue channel
(b) red channel

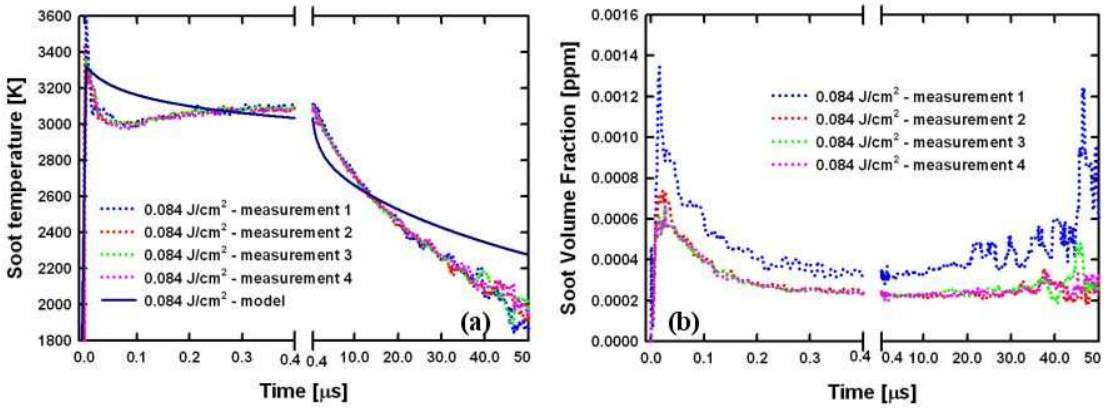

Figure 135: Temperatures and soot volume fractions for a fluence of 0.084J/cm^2
(a) Temperature
(b) Soot volume fraction

Obviously, an apparent heating phase is taking place between 100ns to 1µs, following what could be assimilated to an initial sublimative temperature decay. Reheating occurred from ~ 3000 K at 100 ns to bring the temperature up to 3150K 900 ns later. Furthermore, the initial sublimative peak is correlated to an initial sharp drop in soot volume fraction followed by a steady decrease and then a more typical SVF increase after 5µs. Therefore, a physical phenomena resulted into significant heat gains in terms of internal particle energy occurred from 100ns to 1 µs after the initial appearance of LII signals and overcome sublimation heat loss rates.

In the absence of oxygen, the only known exothermic reaction to laser-induced incandescence is crystallisation (annealing).Therefore conditions existed in which crystallisation could be optimised to the stage of becoming the dominant heat transfer.
The results presented in figure 134 and 135 lead to the following conclusions:

(1) annealing, although it cannot be discriminated against radiation and sublimation yet, is taking place
(2) an optimum configuration existed at 0.084 J/cm^2 and an annealing-dominated temperature profile for circa one microsecond was obtained.
(3) further LII under vacuum investigation could focus on discriminating the crystallisation thermal term and therefore characterize and confirm the physical understanding that has been laid out in the literature (Michelsen, 2004).

Chapter VI – Concluding remarks

At the beginning of this project, the Laser-Induced Incandescence (LII) technique had recently transitioned from requiring an external calibration with a source of particles having a known concentration and size to a novel calibration technique based on an absolute light intensity calibration. Indeed, prior to LII migrating to being an independent measurement technique, measurements were taken utilizing in general the whole incandescence emission spectrum in the visible and deriving soot particle sizes and concentrations from an hypothetical peak temperature and reference measurements performed on particulate matter sources more or less well characterized. The invention of the independent calibration technique by Smallwood, Snelling et al. in 2001 led to the following measurement capability during LII: time-resolved LII would yield both particle temperatures and light intensity measurements and provide a direct link between theoretical modelling and practical situations. This overall enhancement of the technique was based on using 2-color pyrometry to measure particle temperature and calibrating the pyrometric system in terms of absolute light intensity provided direct measurements of particle concentrations. However, the pyrometric technique imposed limitations in terms of measurement volumes configurations and sizes and the technique evolved into extractive sampling from exhaust streams and performing measurements within well-controlled sampling cells. In parallel, the spectral emission measured represented only a fraction of the visible incandescence spectrum emitted during LII as two bandpass filters were used simultaneously to resolve instantaneous particle matter temperatures. Because of these new constrains imposed by this measurement method, LII measurements became limited to resolving only a few parts per billion in terms of particulate matter concentration.

Therefore an increase in sensitivity was clearly the focus and early in the project two directions became evident: either a technical solution was achieved, with the use of faster optics, larger probe volumes and increased collection and transmission efficiencies; or a physical solution could be reached, with a larger number of photons emitted per unit primary soot particle. With these two choices in mind, Professor Greenhalgh and I started a fruitful collaboration with the Combustion Research Group at the National Research Council (NRC, Ottawa, Canada). Our common objective was to achieve each between 100 and 1000 times greater sensitivities for LII and resolve parts per trillion particle matter concentrations. The approach I favoured at Cranfield was to obtain physically more signal per unit primary soot particle, whereas Greg Smallwood and Dave Snelling focussed on revising optical designs and increasing collection and transmission efficiencies, bearing in mind that our combined efforts would eventually lead LII into sub-parts per trillion sensitivities…

From the start of this project, two methods for increasing the emission of photons per primary soot nanoparticles were identified: either higher nanoparticles temperatures or longer signal durations could have been used. Clearly, higher temperatures were attractive, has they would have been associated with larger instantaneous incandescence signals. However, bringing carbon nanoparticle temperatures above 4000 K during LII also implies large sublimative losses and therefore overall decreases in signal. However, this could have been compensated by performing measurements in conditions were sublimation would lead to large concentrations of

thermally excited C_2 vapours being released from the particle carbonaceous structure and produce large emission signal levels. Unfortunately, This route was not chosen as it would not constitute laser-induced incandescence, require extremely high laser fluences and prevent any particle morphology measurement to be performed because of the large volumic losses required to achieve large sublimative rates.

Instead, a more subtle approach was to lengthen LII signals. Typically, LII is associated with sharp light pulses lasting less than a microsecond. Short signal durations are due to the rapid heat conduction from the laser-irradiated soot particle to its surrounding gas. Therefore a decrease conductive heat loss rates was necessary in order to lengthen LII signals. Hence the principle of LII under vacuum was defined: by performing LII under vacuum, light signals could be modelled to last up to 100 microseconds and the associated gain in number of photons emitted per primary soot particle was predicted to be in the order range of 50 to 300 (depending on primary soot particle size). In parallel, because heat conduction away from the unit soot particle is reduced to negligible, the sublimative and the radiative properties of soot nanoparticles could be measured by the technique.

Initially, the Laser-Induced Incandescence model was provided by NRC. It was soon extended to include Hope Michelsen's mathematical interpretation for heat conduction and radiation. Due to the complexity of computing LII over timescales far longer than the initial nanoseconds of laser excitation, the model was also migrated into a finite-difference solver. Extensive modelling was performed and led to the conclusions that 10^{-2} mbar is the upper pressure limit at which conductive heat transfer remain negligible for all particle sizes and LII under vacuum can be obtained. Also, following laser energy absorption, radiation heat transfer would be accompanied by soot sublimation for excitation laser fluences above 0.06 J/cm^2. Therefore two situations could be envisaged: either laser absorption would be followed by a long-lived radiative heat transfer; or laser energy absorption would be followed by sublimation for the first ten microseconds and then radiation. The first case would apply for laser fluences below 0.06 J/cm^2 and would be constituted of two phenomena that are independent of particle size but depend directly on the soot refractive index. The second case (absorption, followed by sublimation and then radiation) reinstates particle size dependence for the first microseconds of LII. In both cases, particle light absorption and emission (radiation) can be directly measured and a direct measurement of the particle refractive index function E(m) is possible during both processes. The novelty of the laser-induced incandescence under vacuum is the capability to measure directly the radiative heat loss rate and therefore E(m) without any particle size dependence. Moreover, the uncertainties associated with performing an E(m) measurement depend directly on the particle temperature uncertainty and E(m) measurements can be resolved within less than 7%, which is remarkable when compared to the widely used extinction measurements method. In addition, sublimation heat loss rates can be directly measured above 0.06 J/cm^2 and annealing, being exothermic, could become detectable for temperatures as low as 2500 Kelvin.

In order to put the theory into practice, a suitable particle-laden aerosol could have been drawned into vacuum by using a molecular beam. Unfortunately, the technical requirements and resources exceeded the scope of the project. Therefore a simpler "roller bottle" system was adopted: purpose-made cylindrical bottles were filled with

a few grams of carbon black powder, then evacuated to below 10^{-3} mbar and sealed. The later rotation of a bottle on a dedicated apparatus ensured the obtention of free-falling particles cascading into the measurement volume within the bottle. A set of bottles containing all similar amounts of carbon black was produced an all LII under vacuum measurements performed throughout this study were made inside these bottles. Carbon black is a soot produced in controlled conditions, in order to produce desired primary soot particle sizes and aggregation factors. However, settling soot as a powder implies large scale agglomerations. Therefore the soot sample used during this project was actually agglomerated particulate matter clusters of sizes up to a millimetre in diameter. Because LII is a phenomenon occurring on the primary particle scale and not the whole agglomerate, the validity of applying LII to carbon black was not questioned. In addition, successful LII particulate matter measurements have been performed on heavy duty diesel engines, which also produce large visible soot particles.

The first LII under vacuum measurements performed consisted of measuring spectral emission from the vacuum sample after laser irradiation at 0.3 J/cm^2.Effectively, the light signals obtained lasted more than 60 microseconds and presented the spectral characteristics of LII< that are high temperature continuum (blackbody) spectra throughout the visible range. Although spectra were red-shifted due to temperature non-uniformities, a pyrometric exploitation yielded a measured temperature decay from 4190K to 2470K over 60 microseconds. This temperature decay could be associated with a temperature decay for its last 50 microseconds, with a measured E(m) value comprised within 0.35 and 0.45. Therefore long-lived signals were obtained from carbon black particles; spectrally they could be assimilated to blackbody (incandescence) spectra; and the measured temperature decay matched with expected LII under vacuum temperature decays, proving the reality of the LII under vacuum concept.

Following this initial success, a more complex measurement system was assembled at Cranfield. It comprised a dual-wavelength pyrometer designed and calibrated according to the NRC absolute light calibration technique and an Intensified CCD camera. The novelty of the system was that the ICCD system was calibrated in terms of absolute light intensity while the pyrometer recorded instantaneous temperature profile. The combination of both measurements yielded pointwise temperature temporal profiles and soot volume fractions and time-integrated two-dimensional soot volume fractions measurements. In addition, the use of an ICCD camera to provide time-integrated absolute light intensity LII measurements was very ambitious in terms that obtaining instrument readouts on average 300 times more sensitive (due to the integration of the number of photons per primary soot particle over 5 to 50 microseconds onto the CCD pixels) had potential to resolve aggregate morphology in terms of number of primary particles per soot particle. Besides, the ICCD camera could also be used to size agglomerates and perform Particle Image Velocimetry (PIV). In practice, due to sensitivity limitations of the pyrometric system, measurements were performed for medium and high laser fluence (0.1 to 0.24 J/cm^2).

To our greatest surprise, the measurements obtained for LII under vacuum of agglomerated carbon black particles permitted an extensive study of the effects of agglomeration for Laser-Induced Incandescence at medium and high laser fluences.
The study lead to the conclusions that:

- Carbon black clusters, even of diameter larger than 200 microns, when irradiated by a laser pulse, have an optical absorption and radiative behaviour in a vacuum that is similar to isolated primary soot particles and tend to obey Rayleigh absorption and radiation.
- Soot agglomerates disaggregate during and after laser irradiation and fragmentation becomes evident after a delay of between 2 to 5 microseconds after laser irradiation. Ejecta velocities were measured by PIV to reach up to 400 m/s away from the original agglomerate and agglomerate dissociations appeared to be the result of chains of dissociations.
- Overall, carbon black agglomerates were dissociated into aggregates within 20 to 30 microseconds and it can be established that the time required to completely dissociate an agglomerate depends on its size prior to LII taking place.

In parallel, LII measurements highlighted that:

- The first microsecond of LII signals recorded by the pyrometer was affected by what was potentially identified as high levels of thermally excited C_2 vapour emissions.
- After 2 to 5 microseconds, that is when carbon clusters dissociate, large LII signal intensity rises were recorded. Particle temperatures were not modified during these intense secondary LII peaks. However soot volume fraction levels would rise by more than 5 times the initially recorded soot volume fractions during agglomerate dissociations. This could be explained by the notion of optical shielding. Indeed, before agglomerate dissociation, blackbody emission originating from nanoparticles within the agglomerate is extinct by adjoining particles and therefore would not reach the detector. Agglomerate dissociations would then reveal a large number of previously optically shielded particles and explain the secondary LII intensity peaks .
- Radiative heat transfer measurements yielded approximate E(m) values comprised between 0.4 and 0.6.

In addition, time-integrated ICCD measurements resolved signal levels as low as the equivalent incandescent 6-7 primary particles aggregates for dissociated particles at 2550K and signals integrated over 5 microseconds. This sensitivity clearly is the highest recorded to date for LII and proves the exceptionally high gain in photons emitted per primary soot particle for LII under vacuum measurements.

Further measurements were effected in collaboration with the Combustion Research Group at NRC. There, a high resolution dual wavelength pyrometer associated with extremely uniform laser spatial fluence profiles could provide precise temperature profiles and soot volume fraction measurements for LII under vacuum. The objectives of the research effort performed at NRC were to:

- establish the repeatability of the temperature profiles measured at Cranfield and perform highly resolved multipulse averaged LII under vacuum measurements.
- perform low fluence LII under vacuum measurements
- compare the temperature and temporal profiles of LII under vacuum at various fluences with our current model.

Temperature profiles repeatability proved excellent on a shot-to-shot basis and therefore allowed us to perform multipulse averaged LII under vacuum measurements. The first observations arising from multipulse measurements was an

increase in the measured soot volume fraction by nearly a factor of 1000 with the laser fluence increased from 0.046 to 0.153 J/cm^2. This trend was also accompanied by secondary soot volume fraction peaks located typically a few microseconds after laser irradiation. The overall soot volume fraction trend with fluence could be associated with a large drop in optical shielding within agglomerates occurring as from the start of LII and implied agglomerate dissociations occurring during the laser absorption phase and the first 100 ns of signals. Also, the fact that agglomerate dissociations occurred at fluences below 0.06 J/cm^2 (whereby sublimation is negligible) highlighted not only the role of sublimation, but also annealing as a cause for agglomerate dissociations. Because annealing consists of crystalline rearrangements within primary particles, brutal morphological changes and carbon clusters expulsions could overcome the Van der Waals forces that agglomerate carbon black nanoparticles together and hence induce large scale dissociations. For higher fluences though, intense sublimation explain further decreases in optical shielding and more vigorous agglomerate dissociations. Parallel measurements performed on a stable source of spherical carbon black agglomerates (236 nm median diameter) at atmospheric pressure also provided the same trend in signal intensity with fluence, furthermore coupled to large reductions in thermal shielding between soot primary particles for heat conduction. Therefore soot agglomerates dissociations is at the heart of the measured LII signal intensities increases with increasing laser fluences and evidences of net diminutions in optical shielding within agglomerates can be found under both vacuum and atmospheric conditions, whereby dissociations also induce net diminutions in thermal shielding between primary soot particles.

Comparisons between modelled results and those obtained experimentally were performed on three aspects of LII under vacuum:

- laser energy absorption and peak particle temperatures
- sublimation heat loss rates
- E(m) measurements during the radiative heat transfer

At low fluences for LII under vacuum, laser absorption occurred on a faster rate than expected, meaning that a secondary phenomenon was increasing particles heat gain rates. Again annealing, being exothermic, emerged as a plausible explanation. For laser fluences above 0.06 J/cm^2, an average E(m) value of 0.47 was measured.

In terms of sublimation heat losses rates, it appeared in all cases studied that the actual sublimation heat loss rates appeared to be systematically overestimated by the model. This was surprising, as the inverse was expected: indeed the sublimation model is based uniquely on C_3 sublimation and should have underestimated the actual sublimative heat loss rate by circa 40%. Agglomeration can provide an explanation for this: thermal shielding between agglomerated particles would restrict carbon vapour flux and creates pressures zones, effectively reducing sublimation heat loss rates. In parallel, annealing could also concurrence sublimation and compensate for heat losses by exothermic crystallisation of particulate matter.

Whereas E(m) measurements during laser absorption yielded an acceptable value of E(m) = 0.47, the radiative temperature decay were measured to produce E(m) values comprised between 0.8 and 1. This also contrasted with the E(m) measurements performed at Cranfield (E(m) = 0.4 – 0.6). The sole explanation for such a divergence was that the laser used for the measurements performed at Cranfield delivered four times the instantaneous power the NRC laser would for the same fluence level. Therefore the carbon black clusters could have not been fully dissociated and presented a higher effective E(m) value during the radiative heat transfer phase.

An interesting exception was also noticed at 0.084 J/cm^2, where significant heat gains literally reheated the sample particles during the first microsecond of LII under vacuum. According to the current knowledge of LII, the only explanation for this was that eventually optimum conditions were reached to induce to such an extent that the sublimation heat losses were overcome.

Outcomes of the research

Laser-Induced incandescence has been established through this study as a measurement method that can deliver exceptionally high sensitivity, with the potential to resolve individual aggregates morphology. Therefore the overall aim of the project, which was to extend the sensitivity of LII to sub-parts per trillion concentrations of particulate matter, was largely fulfilled.

In addition, dedicated modelling and theoretical interpretations provide a basis for the LII under vacuum method and an upper pressure limit of 10^{-2} mbar was calculated for the measurement method to be applicable. Moreover, the measurement method allows for a direct measurement of the refractive index function E(m) to be performed during the radiative heat transfer temperature decay characteristic of the last 50 to 90 microseconds of LII signals under vacuum. Eventually this E(m) measurement method could outperform the current extinction measurement method and provide uncertainties below 7%.

Agglomerate dissociations during LII were observed for the first time and optical and thermal shielding within agglomerates were established. Clusterous particulate matter dissociations could be proved to originate from both annealing and sublimation and occur both under vacuum and at atmospheric pressure. They are also the cause of LII signal increase with laser fluence that can be observed for agglomerated particulate matter measurements.

However, throughout this study agglomerate dissociations dynamics did not allow for a complete distinction to be made between the physics of LII under vacuum and agglomerate dynamics. This was largely due to the sample on which measurements were performed and presents the largest limitation of this study. The measurements performed at NRC attempted to measure absorption, sublimation and radiation heat loss rates directly from LII under vacuum signals. The outcomes established that: annealing was present and quenched sublimation heat loss rates and laser absorption as well as initiating agglomerate dissociations; agglomeration did affect radiative E(m) measurements and large values (0.8 to 1) of E(m) were obtained as a consequence; and conditions where optimum annealing rates could be observed could be met.

Recommendations for further work

Future work on laser-induced incandescence under vacuum should be performed on non-agglomerated particulate matter. Temperature measurements during LII under vacuum would then possibly yield : radiative heat transfer measurements (including resolving precisely E(m) without having to deal with optical shielding and its associated quenches in terms of optical absorption and emission), direct measurements of sublimation heat loss rates and annealing rates.
Obtaining precise measurements of these thermo-physical parameters would therefore deepen the understanding of the physics of LII and provide a basis for modelling corrections. Ideally the sample measured should also be characterised independently using transmission electron microscopy and its morphology precisely controlled prior to LII measurements being performed. Hence clear relations between particles morphology and their physical properties could be determined.
These imply that static systems such as a sealed roller bottle or the use of settled particulate matter powder should not be pursued in order to perform LII under vacuum measurements. Therefore molecular beam sampling is the sampling method which should be favoured in order to provide controlled flows of particulate matter under vacuum. In particular, aerodynamic lens systems present great interest as they provide high particle transmissivity and focussing within LII measurement volumes that are limited in size (from 2 to 16 mm diameter).
In addition, the exceptional sensitivity of LII under vacuum for time-integrating photodetectors permits the resolution of particle morphology in terms of number of particles per aggregate. An extension of the technique would be to use this sensitivity for the measurements of refractory nanoparticles in general, but also atmospheric concentrations of particulate matter and air pollution monitoring.
And finally, because the technique eventually requires reduced laser powers and less sophisticated measurement systems than for atmospheric LII, instrument developments could benefit from the overall potential simplification of the measurement technique and commercialization could be envisaged.

References

A

AIAA 2003, (American Institute of Aeronautics and Astronautics). Laser - Induced Incandescence (LII) page. [http://www.aiaa.org/tc/amt/techniques/lii.html]. Accessed 24/08/2003.

Artium instrument, Sandia National Laboratories. Accessed august 2004. [http://www.ca.sandia.gov/pmc/LII/Commercialization/schematic.html].

Boman Axelsson, Peter O. Witze. 2001. Qualitative Laser-Induced Incandescence Measurements of Particulate Emissions During Transient Operation of a TDI Diesel Engine. SAE Technical Paper Series 2001-01-3574.
Notes: Presented at the Fall Fuels and Lubricants Meeting and Exhibition, San Antonio, Texas, September 24-27, 2001

B

M. Balthasar and M. Frenklach. 2005.Proc. Comb. Inst. 30, 1467-1475.

D.J. Bryce .1996. Development and application of planar laser techniques for iso-thermal flow and soot diagnostics, Msc ed., . Kings Norton Library: Cranfield University.

Vivien Beyer and D.A. Greenhalgh, Laser Induced Incandescence under high vacuum conditions. 2006. Applied Physics B 83: 455-467.

Craig F. Bohren and Donald R. Huffman.1998.Absorption and Scattering of light by small particles, Chichester, ed. Wiley

C

M.Y. Choi, G. W. Mulholland A. Hamins and T. Kahiwagi. 1995. Comparisons of the Soot Volume Fraction Using Gravimetric and Light Extinction Techniques. Combustion and Flame 102: 161-9.

Mun Young Choi, and Kirk A. Jensen. 1998. Calibration and Correction of Laser-Induced Incandescence for Soot Volume Fraction Measurements. Combustion and Flame 112: 485-91.

Cabot Carbon. Technical information request answered april 2005.

Cabot carbon - CAB-O-JET 200 coating explanations – plus.pdf . 2006 manual edition.

David J. Creasey, Peter A. Halford-Maw Dwayne E. Heard Michael J. Pilling and Benjamin J. Whitaker. 1997-1. Implementation and Initial Deployment of a Field Instrument for Measurement of OH and HO_2 in the Troposphere by Laser-Induced Fluorescence . J. Chem. Soc., Faraday Trans. 93(16): 2907-13.

David J. Creasey, Dwayne E. Heard Michael J. Pilling Benjamin J. Whitaker Martin Berzins Roger Fairlie. 1997-2. Visualisation of a Supersonic Free-Jet Expansion Using Laser-Induced Fluorescence Spectroscopy: Application to the measurement of Rate Constants at Ultralow Temperatures. Applied Physics B 65: 375-91.

D

W.H. Dalzell and A.F. Sarofim; Optical Constants of Soot and Their Application to Heat-Flux Calculations; Journal of Heat Transfer, February 1969, Transactions of the ASME, pp.100-104

Dan Clavel. November 2005. Explicative emails and data sets comprising calibration factors and LII systems parameters.

S. De Iuliis, F. Cignoli and G.Zizak.2005. Appl. Opt. 44, 7414-7423.

Dr. Lee Doherty (Cranfield University), 2003. Communication.

R.W. Dreyfus, Roger Kelly and D. E. Walkup. 1987. Laser-Induced Fluorescence Study of Laser Sputtering of Graphite. Nuclear Instruments and Methods in Physics Research B23: 557-61.

W.H. Dalzell and A.F. Sarofim. February 1969. Optical Constants of Soot and Their Application to Heat-Flux Calculations. Journal of Heat Transfer, Transactions of the ASME: 100-4.

R. A. Dobbins, R.J. Santoro and H.G. Semerjian, Analysis of Light Scattering From Soot Using Optical Cross Sections for Aggregates, Twenty-Third Symposium (International) on Combustion / The Combustion Institute, 1990 / pp. 1525-1532

E

Alan C Eckbreth. November 1977. Effects of Laser-Modulated Particulate Incandescence on Raman Scattering Diagnostics. Journal of Applied Physics 23, no.13: 4473-9.

F

A.V. Filippov, M. W. Markus and P. Roth. 1999. In-Situ Characterization of Ultrafine Particles by Laser-Induced Incandescence: Sizing and Particle Structure Determination. Journal of Aerosol Science 30, no. 1: 71-87.

A. V. Filippov, M. Zurita and D. E. Rosner.2000.J. Colloid Interface Sci. 229, 261-273

Laurence E. Fried and W. Michael Howard. 1 April 2000. Explicit Gibbs Free Energy Equation of State Applied to the Carbon Phase Diagram. Physical Review B 61, no. 13: 8734-43.

Courtesy of Fisher Scientific catalogue 2004, p.243

Fengshan Liu, personnal communication, November 2005.

G

Karl A. Gingerich, Heidi C. Finkbeiner and Richard W. Schmude Jr. 1994. Enthalpies of Formation of Small Linear Carbon Clusters. Journal of the American Chemistry Society 116: 3884-8.

Robert M. Green and Peter O. Witze. 2000. Laser-Induced Incandescence and Elastic-Scattering Measurements of Particulate-Matter Volume Fraction Changes during Passage Through a Dilution Tunnel. Proceedings of the 10th International Symposium on Applications of Laser Techniques to Fluid Mechanics.

Greg Smallwood, communication, 20 July 2004

Vartan Grigorian. 2001. An Investigation into the Characterisation of the Laser Induced Incandescence Method for the Measurement of Soot in Practical Systems, PhD ed., Kings Norton Library: Cranfield University.

Vartan Grigorian. November 2005. Email (electronic attachement)

H

D. L. Hofeldt. 1993. Real-Time Soot Concentration Measurement Technique for Engine Exhaust Streams. , SAE Paper 930079.

Hoyt C. Hottel and Adel F. Sarofim. 1967. Radiative transfer. New-York: McGraw-Hill.

Hamamatsu courtesies:
[http://www.hpk.co.jp/Eng/products/ETD/pdf/PMT_construction.pdpage1]

[http://sales.hamamatsu.com/assets/pdf/catsandguides/PMT_modules.pdf p.17]
[http://sales.hamamatsu.com/assets/pdf/catsandguides/PMT_modules.pdf p.17]
[http://sales.hamamatsu.com/assets/pdf/catsandguides/PMT_modules.pdf]
accessed July 2006

J

Murray Johnston. Sampling and analysis of individual particles by aerosol mass spectrometry. Journal of Mass Spectrometry, 35, pp.585-595, year 2000.

K

Kermit C. Smyth and Christopher R. Shaddix, The Elusive History of m = 1.57 - i 0.56 for the Refractive Index of Soot, Combustion and Flame 107, pp. 314 –320
E.H. Kennard. 1938. Kinetic theory of gases: with and introduction to statistical mechanics, London, ed McGraw-Hill.

U.O. Koylu, G. M. Faeth T. L. Farias and M. G. Carvalho. 1995. Fractal and Projected Structure Properties of Soot Aggregates. Combustion and Flame 100: 621-33.

U.O. Koylu.1997-1. Quantitative Analysis of In Situ Optical Diagnostics for Inferring Particle/Aggregate Parameters in Flames: Implications for Soot Surface Growth and Total Emissivity.. Combustion and Flame 109: 488-500.

U.O. Koylu and G.M. Faeth. 1996. Spectral Extinction Coefficients of Soot Aggregates From Turbulent Diffusion Flames. Journal of Heat Transfer, Transactions of the ASME 118: 415.

U.O. Koylu and G.M. Faeth. 1992. Structure of Overfire Soot in Buoyant Turbulent Diffusion Flames at Long Residence Times. Combustion and Flame 89: 140-56.

U.O. Koylu, C. S. McEnally D. E. Rosner and L. D. Pfefferle. 1997-2. Simultaneous Measurements of Soot Volume Fraction and Particle Size / Microstructure in Flames Using a Thermophoretic Sampling Technique. Combustion and Flame 110: 494-507.

Douglas J. Krajnovich. 8 January 1995. Laser Sputtering of Highly Oriented Pyrolytic Graphite at 248 nm. J. Chem. Phys. 102 (2): 726-43.

L

F.Liu, K.J. Daun, D.R. Snelling, G.J. Smallwood. 2006. Heat conduction from a spherical nano-particle: status of modeling heat conduction in laser-induced incandescence. Applied Physics B 83:355-382.

S.C. Lee and C.L.Tien; Optical Constants of Soot in Hydrocarbon Flames, Eighteenth Symposium (International) on Combustion, The Combustion Institute, 1981, pp. 1159-1166.

H. R. Leider, O. H. Krikorian and D. A. Young. 1973. Thermodynamic Properties of Carbon up to the Critical Point. Carbon 11: 555-63.

Robert Dean Larrabee. 1957. The spectral emissivity and optical properties of Tungsten. Research Laboratory of electronics, Massachussets Institute of technology, Cambridge, Massachusetts.

N

NIST Technical Note 1297, 1994 edition: Guidelines for evaluating and Expressing the Uncertainty of NIST Measurement Results; Barry N. Taylor and Chris E. Kuyatt, sept. 2004

M

Mackowski, D. W., A simplified model to predict the effects of aggregation on the absorption properties of soot particles, J. Quantitative Spectroscopy and Radiative Transfer, Vol. 100, pp. 237-249, 2006.

Gregory R. Markowski.1987. Improving Twomey's Algorithm for Inversion of Aerosol Measurement Data. Aerosol Science and Technology 7: 127-141.

Samantha A. Murphy, Kelly A. Berube Frederick D. Pooley and Roy J. Richards. 1998. The Response of Lung Epithelium to Well Characterized Fine Particles. Life Sciences 62, no. 19: 1789-99.

Lynn A. Melton. July 1984. Soot Diagnostics Based on Laser Heating. Applied Optics 23, no. 13: 2201-8.

B.J. McCoy and C. Y. Cha. 1974. Transport Phenomena in the Rarefied Gas Transition Regime. Chemical Engineering Science 29: 555-63.

B. Mewes and J. M. Seitzman. 20 January 1997. Soot Volume Fraction and Particle Size Measurements with Laser Induced Incandescence. Applied Optics 36, no. 3: 709-17.

Hope A. Michelsen. 2003. Understanding and predicting the temporal response of laser-induced incandescence from carbonaceous particles. Journal of chemical physics, volume 118, number 15.

Hope A. Michelsen. 2006. Laser-induced incandescence of flame-generated soot on a picosecond time scale. Applied Physics B 83: 443-448.

B. Michel, Th. Henning C. Jager U. Kreibig. 1999. Optical Extinction by Spherical Carbonaceous Particles. Carbon 37: 391-400.

Microphysical description of LII. accessed 31/01/2006. http://www.ca.sandia.gov/pmc/LII/theoretical.model/index.html

K.R. McManus, M. G. Allen and W. T. Rawlins. 1997. Quantitative Detection and Imaging of Soot Particles by Laser Induced Incandescence . 35th Aerospace Sciences Meeting & Exhibit.

K.R. McManus, J. H. Franck M. G. Allen and W. T. Rawlins. 1998. Characterization of Laser-Heated Soot Particles Using Optical Pyrometry. 36th Aerospace Sciences Meeting & Exhibit.

O

M.N. Ozisik. 1993. Heat Conduction. New York: John Wiley and Sons.

P

Particulate Matter Collaboratory .2006-1. LII description page. [http://www.ca.sandia.gov/pmc/LII/index.html]. Accessed 17/07/2006.

Particulate matter collaboratory. Overview. [http://www.ca.sandia.gov/pmc/LII/Applications/overview.html]. Accessed 24 August 2003.

Arpad B. Palotas, Lenore C. Rainey Adel F. Sarofim John B. Vander Sande and Paolo Ciambelli. 1996. Effect of Oxidation on the Microstructure of Carbon Blacks. Energy & Fuels 10: 254-9.

R

Ricardo Quarterly Review, 2002. Legislators becoming more particular - about particles. 12-3.

E. A. Rohlfing. 1988. Journal of Chemical Physics 89, 6103.

P. Roth and A.V. Filippov. 1996. In Situ Ultrafine Particle Sizing by a Combination of Pulsed Laser Heatup and Particle Thermal Emission. Journal of Aerosol Science 27, no. 1: 95-104 .

S

Sandia National Laboratories. GDI - SI Engine. Accessed 2006 [http://www.ca.sandia.gov/pmc/LII/Applications/diesel_engine.html].

Bob Sawchuck. November 2005. Email containing the experimental systems schematics and principles

Christopher R. Shaddix and Kermit C. Smyth. 1996. Laser-Induced Incandescence Measurements of Soot Production in Steady and Flickering Methane, Propane, and Ethylene Diffusion Flames. Combustion and Flame 107: 418-52.

David R., Snelling, Gregory J. Smallwood, I. G. Campbell J. E. Medlock and OmerL. Gulder. 1997. Development and Application of Laser Induced Incandescence (LII) as a Diagnostic for Soot Particulate Measurements. AGARD 90th Symposium of the Propulsion and Energetic Panel on Advanced Non-Intrusive Instrumentation for Propulsion Engines.

David R. Snelling, Gregory J. Smallwood Robert A. Sawchuk W. Stuart Neill Daniel Gareau Wallace L. Chippior Fengshan Liu Omer L. Gulder and William D. Bachalo. 1999. Particulate Matter Measurements in a Diesel Engine Exhaust by Laser-Induced Incandescence and the Standard Gravimetric Procedure. SAE Technical Paper Series 1999-01-3653. Presented at Fall Fuels and Lubricants Meeting and Exhibition, Toronto, Ontario, Canada, October 24-28, 1999.

David R. Snelling, Gregory J. Smallwood Robert A. Sawchuk W. Stuart Neill Daniel Gareau Daniel J. Clavel Wallace L. Chippior Fengshan Liu Omer L. Gulder and William D. Bachalo. 2000-1. In-Situ Real-Time Characterization of Particulate Emissions from a Diesel Engine Exhaust by Laser-Induced Incandescence. SAE Technical Paper Series 2000-01-1994. Presented at International Spring Fuels and Lubricants Meeting and Exposition, Paris, France, June 19-22, 2000

David R. Snelling, Gregory J. Smallwood Omer Gulder William D. Bachalo and Subramanian Sankar . 2000-2. Soot Volume Fraction Characterization Using the Laser-Induced Incandescence Detection Method. The 10th International Symposium on Applications of Laser Techniques to Fluid Mechanics.

David R. Snelling, Gregory J. Smallwood Robert A. Sawchuk W. Stuart Neill Daniel Gareau Daniel J. Clavel Wallace L. Chippior Fengshan Liu Omer L. Gulder and William D. Bachalo. 2000-3. In-Situ Real-Time Characterization of Particulate Emissions from a Diesel Engine Exhaust by Laser-Induced Incandescence. SAE Technical Paper Series 2000-01-1994. Presented at International Spring Fuels and Lubricants Meeting and Exposition, Paris, France, June 19-22, 2000

David R. Snelling, Fengshan Liu, Gregory J. Smallwood, Omer L. Gulder. 2004. Determination of the soot absorption function and thermal accommodation coefficient using low-fluence LII in a laminar coflow ethylene diffusion flame. Combustion and flame 136, pp. 180-190.

David R. Snelling, F. Liu G. J. Smallwood and O. L. Gulder. 2000-1. Evaluation of the Nanoscale Heat and Mass Transfer Model of LII: Prediction of the Excitation Intensity. Proceedings of NHTC 2000, 34th National Heat Transfer Conference .

David R. Snelling, Gregory J Smallwood Omer L. Gulder Fengshan Liu and William D. Bachalo. 2001. A Calibration-Independent Technique of Measuring Soot by Laser Induced Incandescence Using Absolute Light Intensity.

David R. Snelling, Gregory J. Smallwood Omer L. Gulder, inventor. 30 January 2001-2. Methods and Apparatus for Applying Laser Induced Incandescence for the Determination of Particulate Measurements. US Patent No. 6,181,419 B1.

David R. Snelling, Gregory J. Smallwood, Omer L. Gulder. 28 November 2000-5. Absolute Intensity Measurements in Laser Induced Incandescence. US Patent No. 6,154,277.

Stephan Schraml, Stefan Dankers Katharina Bader Stefan Will and Alfred Leipertz. 2000. Soot Temperature Measurements and Implications for Time-Resolved Laser-Induced Incandescence (TIRE-LII). Combustion and Flame 120: 439-50.

S. Schraml, S. Will A. Leipertz T. Zens and N. D Alfonso. 2002. Performance Characteristics of TIRE-LII Soot Diagnostics in Exhaust Gases of Diesel Engines. SAE Technical Paper Series 2000-01-2002.

J. H. Seinfeld and S.N. Pandis. 1998. Atmospheric Chemistry and Physics from Air Pollution to Climate Change. New York: John Wiley and Sons.

C. Schulz, B.F. Kock, M. Hofmann, H. A. Michelsen, S. Will, B. Bougie, R. Suntz, G. Smallwood. 2006. Laser-induced incandescence: recent trends and current questions. Applied physics B 83 : 333-354.

Gregory J. Smallwood, David R. Snelling F. Liu Omer L. Gulder. August 2001-1. Clouds over Soot Evaporation: Errors in Modelling Laser-Induced Incandescence of Soot. Transactions of the ASME (American Society of Mechanical Engineering) 123: 814-8.

Gregory J. Smallwood, 2003. Communication

G. Smallwood and B. J. Stagg, unpublished experimental data (2006).

Gregory J. Smallwood, David R. Snelling Omer L. Gulder Dan Clavel Daniel Gareau Robert A. Sawchuk and William D. Bachalo. 2001-2. Quantitative Laser-Induced Incandescence Measurements of Particulate Matter from the Exhaust of a Direct Injection Spark Ignition Automobile. International Energy Agency XXIII Task Leaders Meeting on Energy Conservation and Emissions Reduction in Combustion.

Gregory J. Smallwood, David R. Snelling Omer L. Gulder Dan Clavel Daniel Gareau Robert A. Sawchuk and Lisa Graham. 2001-3. Transient Particulate Matter Measurements from the Exhaust of a Direct Injection Spark Ignition Automobile. SAE Technical Paper Series 2001-01-3581.
Note: Presented at Fall Fuels and Lubricants Meeting and Exhibition, San Antonio, Texas, September 24-27, 2001

Gregory J. Smallwood, David R. Snelling W. Stuart Neill Fengshan Liu William D. Bachalo and Omer L. Gulder. 2001-4. Laser-Induced Incandescence Measurements of Particulate Matter Emissions in the Exhaust of a Diesel Engine. The Fifth International Symposium on Diagnostics and Modelling of Combustion in Internal Combustion Engines.
Notes: . Last accessed on 24 August 2003

G. Smallwood and B. J. Stagg, unpublished experimental data (2006).

Robert J. Santoro and Christopher R. Shaddix. 2000. Laser-Induced Incandescence. Applied Combustion Diagnostics. Katherina Kohse-Hoinghaus and Jay B. Jeffries ed., 252-86.

T

Nigel P. Tait . 1994. Development of planar laser diagnostics techniques for fuel and soot imaging in combustion applications, PhD ed., . Kings Norton Library: Cranfield University.

K.A. Thomson, D.R. Snelling, G.J. Smallwood, F.Liu. 2006. Laser induced incandescence measurements of soot volume fraction and effective particle size in a laminar co-annular non-premixed methane/air flame at pressures between 0.5-4.0 Mpa. Applied Physics B 83:469-475.

S. Twomey.1975. Comparison of Constrained Linear Inversion and an Iterative Nonlinear Algorithm Applied to the Indirect Estimation of Particle Size Distributions. Journal of Computational Physics 18: 188-200.

V

B.M. Vagliego, F. Beretta, and A. D'Alessio, In Situ Evaluation of the Soot Refractive Index in the UV-Visible from the Measurement of the Scattering and Extinction Coefficients in Rich Flames, Combustion and Flames 79, pp. 259-271 (1990)

Randall L. Vander Wal, Mun Young Choi and Kyeong-ook Lee. 1995. The Effects of Rapid Heating of Soot: Implications When Using Laser-Induced Incandescence for Soot Diagnostics. Combustion and Flame 102: 200-4.

Randall L. Vander Wal. Laser-Induced Incandescence: Detection Issues. November

1996-1. Applied Optics 35, no. 33: 6548-59.

Randall L. Vander Wal, Z. Zhou and Mun Young Choi. 1996-2. Laser-Induced Incandescence Calibration via Gravimetric Sampling. Combustion and Flame 105: 462-70.

R.L. Vander Wal, Ticich and A.B. Stephens.1998. Applied Physics B 67:115.

Randall L. Vander Wal and Jensen, Kirk. March 1998. Laser-Induced Incandescence: Excitation Intensity. Applied Optics 37, no. 9: 1607-16.

Randall L. Vander Wal, Thomas M. Ticich and A. Brock Stephens. 1999-1. Can Soot Primary Particle Size be Determined Using Laser-Induced Incandescence? Combustion and Flame 116: 291-6.

Randall L. Vander Wal and Thomas M. Ticich. 20 March 1999-2. Cavity Ringdown and Laser-Induced Incandescence Measurements of Soot. Applied Optics 38, no. 9: 1444-51.

Randall L. Vander Wal and Mun Y. Choi. 1999-3. Pulsed Laser Heating of Soot: Morphological Changes. Carbon 37: 231-9.

Martin von Allmen. 1987. Laser Beam Interactions with Materials, Physical Principles and Applications. Springer-Verlag, Berlin.

S

B.J. Stagg and T.T. Charalampopoulos, Refractive Indices of Pyrolytic Graphite, Amorphous Carbon, and Flame Soot in the Temperature Range 25º to 600ºC, Combustion and Flame 94, pp. 381-396 (1993)

W

Richard T. Wainner, 1999. " An analytical and quantitative analysis of the laser-induced incandescence of soot",PhD thesis, Georgia Institue of Technology.

Peter P. Wegener. 1974. Gas Dynamics, A series of Monographs, Molecular Beams and Low Density Gas Dynamics. New York: Marcel Dekker Inc.

Stefan Will, Stephan Schraml Katharina Bader and Alfred Leipertz. 20 August 1998. Performance Characteristics of Soot Primary Particle Size Measurements by Time-Resolved Laser-Incandescence. Applied Optics 37, no. 24.

Eric Wienstein. Sphere Radiative Cooling. 24 August 2003-1. [http://scienceworld.wolfram.com/physics/SphereRadiativeCooling.html].

Eric Wienstein. Blackbody Radiation. 24 August 2003-2. [http://scienceworld.wolfram.com/physics/].

Peter O. Witze. 2001. Diagnostics for the Measurement of Particulate Matter Emissions from Reciprocating Engines. Proceedings of The Fifth International Symposium on Diagnostics and Modelling of Combustion in Internal Combustion Engines COMODIA 2001.

Peter O. Witze, Simone Hochgreb David Kayes Hope A. Michelsen and Christopher R. Shaddix. 20 May 2001-2. Time-Resolved Laser-Induced Incandescence and Laser Elastic-Scattering Measurements in Propane Diffusion Flame. Applied Optics 40, no. 15: 2443-52.

J.S. Wu, S. S. Krishnan G. M. Faeth.1979. Refractive Indices at Visible Wavelengths of Soot Buoyant Turbulent Diffusion Flames. Journal of Heat Transfer, Transactions of the ASME 119: 230-7.

C.H. Wu, U. Mszanowski J. M. L. Martin. 1998. The Impact of Larger Clusters Formation C_5, C_6, C_7, C_8, C_9, and C_{10} on the Rates of Carbon Sublimation at Elevated Temperatures. Journal of Nuclear Materials 258-263: 782-6.

R.W.Weeks and W.W. Duley. October 1974. Aerosol-particle sizes from light emission during excitation by TEA CO_2. Journal of Applied Physics 45, no. 10: 4661-2.

X

F. Xu, A. M. El-Leathy C. H. Kim G. M. Faeth. 2003. Soot Surface Oxidation in Hydrocarbon/Air Diffusion Flames at Atmospheric Pressure . Combustion and Flame 132: 43-57.

Xuefeng Zhang, Kenneth Smith et al. 2002-1. A numerical Characterization of Particle Beam Collimation by an Aerodynamic Lens-Nozzle System: Part I. An individual Lens or Nozzle. Aerosol Science and Technology 36, Pp. 617 631 (2002) .

Xuefeng Zhang and Kenneth A. Smith et al. 2002-2.Numerical Characterization of Particle Beam Collimation: Part II integrated Aerodynamic Lens-Nozzle system.

Appendix A - Soot optical properties

A.1. Data Available in the Literature

Many complex refractive indices for soot, $m = n - i.k$, are proposed in the literature, depending on the wavelength of light and the origin of the soot:

Origin of soot	**Authors**	**Wavelength *[nm]***	**Real part n**	**Imaginary part, k**	**E(m) *[ ]***
Compressed pellets of soot from acetylene flame	Dalzell and Sarofim (1969)	435.8	1.56	0.46	0.217
		450.0	1.56	0.48	0.226
		550.0	1.56	0.46	0.217
		650.0	1.57	0.44	0.206
		806.5	1.57	0.46	0.215
Compressed pellets of soot from propane flame	Dalzell and Sarofim (1969)	435.8	1.57	0.46	0.215
		450.0	1.56	0.5	0.235
		550.0	1.57	0.53	0.246
		650.0	1.56	0.52	0.244
		806.5	1.57	0.49	0.228
Polystyrene and Plexiglas flame soot	Lee and Tien (1981)	UV and Visible	1.9	0.55	0.193
Ethene flame soot	Dobbins et al. (1990)	UV and Visible	2.1	0.55	0.163
Commonly used	Smyth and Shaddix	UV and Visible	1.57	0.56	0.260
Pyrolytic Graphite	Greenaway et al.(1969)	UV and Visible	2.73	1.4	0.2
Pyrolytic Graphite at 300 K	Stagg and Charalampopoulos (1993)	400.0	2.377	1.656	0.274
		433.0	2.529	1.528	0.240
		467.0	2.637	1.422	0.216
		500.0	2.641	1.386	0.213
		533.0	2.648	1.383	0.211
		567.0	2.649	1.395	0.212
		600.0	2.656	1.394	0.211
		633.0	2.684	1.399	0.207
		667.0	2.717	1.433	0.204
		700.0	2.767	1.438	0.197
Pyrolytic Graphite at 475 K	Stagg and Charalampopoulos (1993)	400.0	2.404	1.652	0.269
		433.0	2.544	1.508	0.237
		467.0	2.656	1.429	0.213
		500.0	2.658	1.388	0.210
		533.0	2.674	1.377	0.207
		567.0	2.675	1.382	0.207
		600.0	2.674	1.394	0.208
		633.0	2.699	1.401	0.205
		667.0	2.741	1.431	0.201
		700.0	2.788	1.444	0.195

Origin of soot	**Authors**	**Wavelength** ***[nm]***	**Real part n**	**Imaginary part, k**	**E(m)** ***[ ]***
Pyrolytic graphite at 675 K	Stagg and Charalampopoulos (1993)	400.0	2.416	1.654	0.267
		433.0	2.562	1.515	0.234
		467.0	2.675	1.407	0.209
		500.0	2.681	1.376	0.206
		533.0	2.691	1.362	0.203
		567.0	2.695	1.365	0.203
		600.0	2.695	1.379	0.204
		633.0	2.710	1.391	0.202
		667.0	2.731	1.428	0.202
		700.0	2.761	1.462	0.200
Pyrolytic graphite at 875 K	Stagg and Charalampopoulos (1993)	400.0	2.423	1.651	0.235
		433.0	2.555	1.525	0.236
		467.0	2.675	1.407	0.209
		500.0	2.681	1.366	0.205
		533.0	2.687	1.363	0.204
		567.0	2.695	1.363	0.203
		600.0	2.691	1.385	0.205
		633.0	2.710	0.392	0.202
		667.0	2.733	1.418	0.201
		700.0	2.776	1.439	0.196
Amorphous carbon at 300 K	Stagg and Charalampopoulos (1993)	400.0	2.175	1.206	0.284
		433.0	2.258	1.102	0.251
		467.0	2.323	1.025	0.227
		500.0	2.321	0.991	0.222
		533.0	2.331	0.981	0.219
		567.0	2.337	0.977	0.217
		600.0	2.343	0.982	0.217
		633.0	2.356	0.986	0.215
		667.0	2.371	1.019	0.217
		700.0	2.434	1.005	0.205
Amorphous carbon at 475 K	Stagg and Charalampopoulos (1993)	400.0	2.176	1.216	0.285
		433.0	2.272	1.099	0.248
		467.0	2.330	1.019	0.225
		500.0	2.333	1.987	0.283
		533.0	2.343	1.978	0.282
		567.0	2.247	1.969	0.300
		600.0	2.353	1.975	0.280
		633.0	2.361	1.974	0.278
		667.0	2.362	1.031	0.221
		700.0	2.436	1.009	0.205

Origin of soot	**Authors**	**Wavelength *[nm]***	**Real part n**	**Imaginary part, k**	**E(m) *[ ]***
Amorphous carbon at 675 K	Stagg and Charalampopoulos (1993)	400.0	2.196	1.209	0.280
		433.0	2.279	1.098	0.247
		467.0	2.339	1.021	0.223
		500.0	2.335	0.989	0.219
		533.0	2.345	0.965	0.213
		567.0	2.348	0.696	0.214
		600.0	2.353	0.974	0.213
		633.0	2.357	0.982	0.214
		667.0	2.374	1.022	0.217
		700.0	2.425	1.010	0.207
Amorphous carbon at 875 K	Stagg and Charalampopoulos (1993)	400.0	2.204	1.215	0.279
		433.0	2.293	1.103	0.244
		467.0	2.348	1.023	0.222
		500.0	2.347	0.989	0.217
		533.0	2.356	0.970	0.212
		567.0	2.359	0.963	0.211
		600.0	2.355	0.978	0.214
		633.0	2.367	0.978	0.212
		667.0	2.384	1.006	0.213
		700.0	2.442	1.004	0.203
Propane soot pellet at 300 K	Stagg and Charalampopoulos (1993)	400.0	1.396	0.403	0.216
		433.0	1.434	0.376	0.196
		467.0	1.462	0.360	0.184
		500.0	1.484	0.347	0.174
		533.0	1.496	0.352	0.175
		567.0	1.536	0.374	0.180
		600.0	1.522	0.355	0.173
		633.0	1.527	0.376	0.182
		667.0	1.544	0.357	0.171
		700.0	1.550	0.367	0.175
Propane soot pellet at 575 K	Stagg and Charalampopoulos (1993)	400.0	1.392	0.404	0.218
		433.0	1.431	0.374	0.196
		467.0	1.464	0.354	0.181
		500.0	1.482	0.345	0.174
		533.0	1.494	0.348	0.173
		567.0	1.537	0.370	0.178
		600.0	1.521	0.352	0.172
		633.0	1.529	0.365	0.177
		667.0	1.541	0.361	0.173
		700.0	1.548	0.366	0.175

Origin of soot	**Authors**	**Wavelength *[nm]***	**Real part n**	**Imaginary part, k**	**E(m) *[ ]***
Propane soot pellet at 875 K	Stagg and Charalampopoulos (1993)	400.0	1.399	0.409	0.219
		433.0	1.439	0.380	0.198
		467.0	1.472	0.360	0.182
		500.0	1.491	0.352	0.176
		533.0	1.502	0.354	0.175
		567.0	1.544	0.377	0.181
		600.0	1.530	0.358	0.173
		633.0	1.535	0.379	0.183
		667.0	1.548	0.369	0.176
		700.0	1.560	0.368	0.174
Acetylene flame soot	Koylu and Faeth (1996)	UV and Visible	1.54	0.48	0.229
Graphite	Vaglieco et al.(1990)	UV and Visible	1.90	0.55	0.193
Overfire soot	Wu et al	351.0	1.36	0.35	0.193
		405.0	1.45	0.40	0.206
		488.0	1.58	0.48	0.222
		514.5	1.58	0.51	0.235
		632.8	1.71	0.53	0.219

A. 2. Evaluation of the emissivity of soot primary particles

The emissivity for a single carbonaceous can be done using the Mie Scattering theory following expressions:

$$E(m) = -\mathrm{Im}\left(\frac{m^2-1}{m^2+2}\right)$$

$$E(m) = \frac{6 \cdot n \cdot k}{\left(n^2 - k^2 + 2\right)^2 + 4 \cdot n^2 \cdot k^2}$$

$$\varepsilon_\lambda = \frac{8 \cdot \pi \cdot a \cdot E(m)}{\lambda}$$

Where E(m) [ ] is the refractive index function, *a [cm]* the radius of the particle, λ *[cm]* the light wavelength and ε_λ *[ ]* the emissivity (equal to absorptivity, according to Kirchoff's law) of the particle.

Using these expressions, the emissivity of soot particles can be evaluated as a function of wavelength over the visible spectrum:

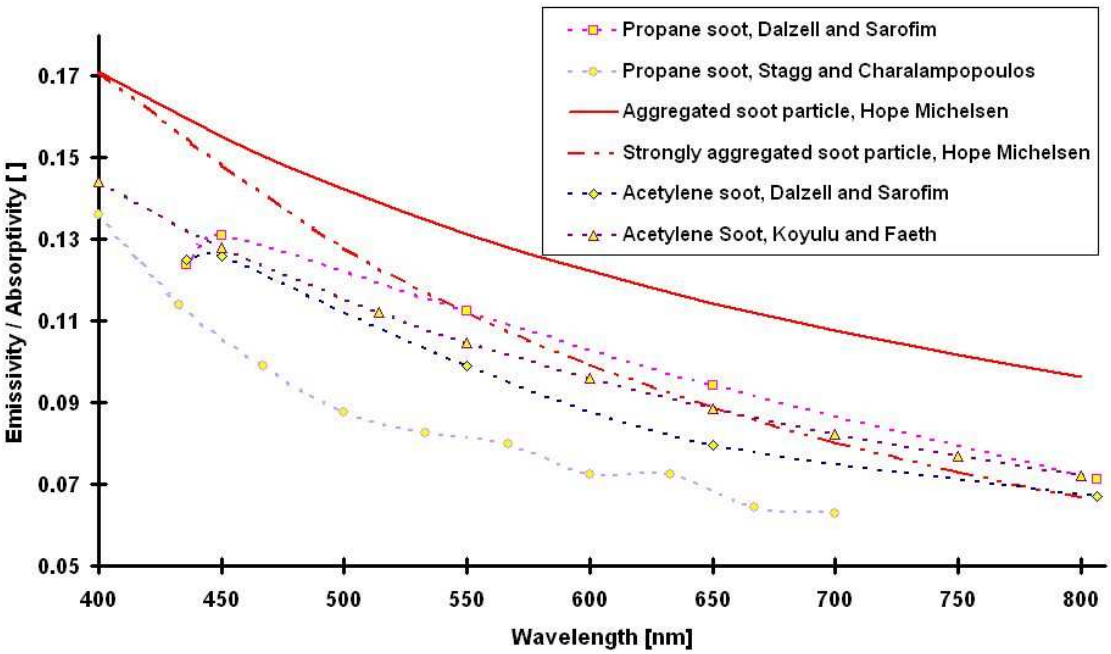

Figure 136: Emissivity as a function of wavelength for a 20 nm propane or acetylene soot particle.

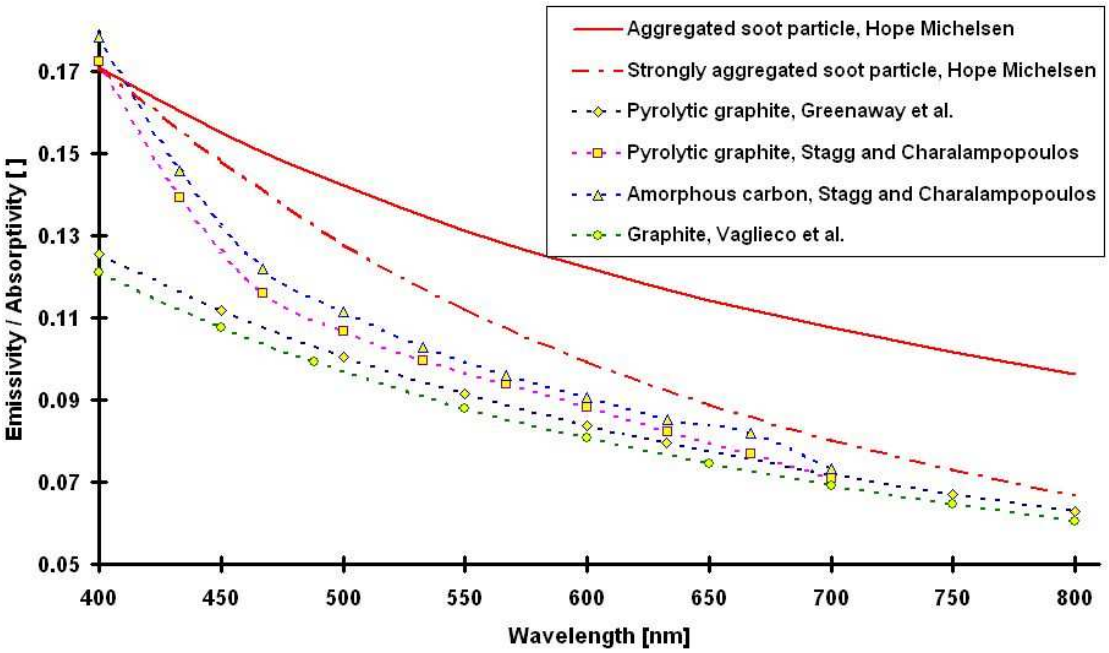

Figure 137: Emissivity as a function of wavelength for a 20 nm carbonaceous particle.

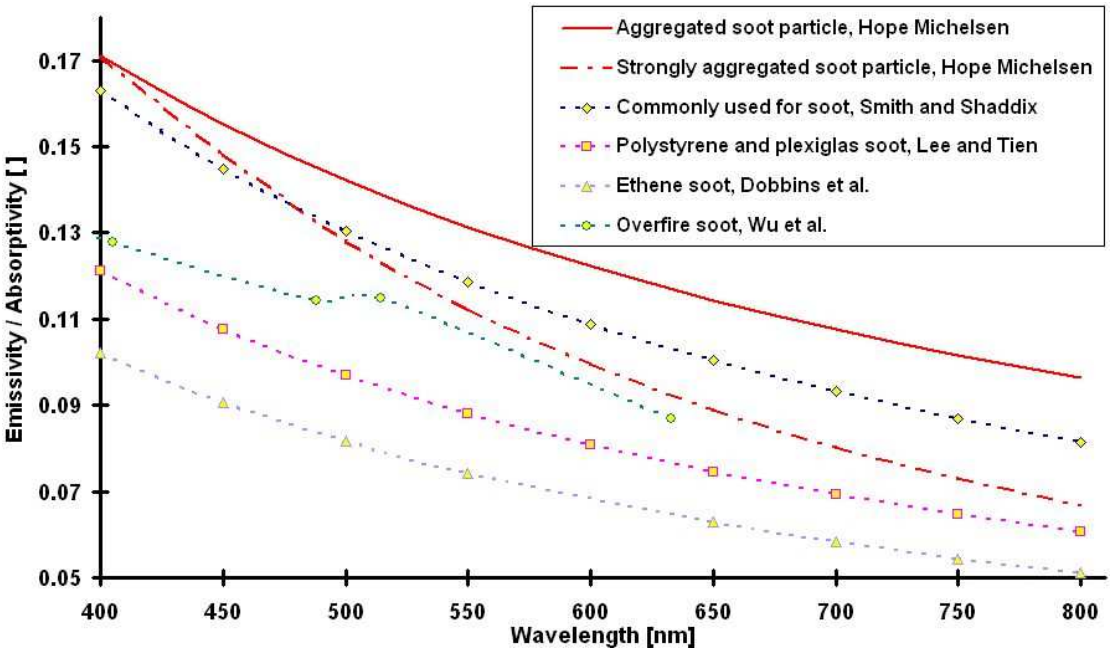

Figure 138: Emissivity as function of wavelength for other types of soot.

The data is compared to Hope Michelsen's (2003) proposed expression for the emissivity of soot as a reference for all kinds of soot:

$$\varepsilon_\lambda = \frac{4 \cdot \beta \cdot a}{3 \cdot \lambda^\xi}$$

Where β [ ] and ξ [ ] are fractal parameters and are given for aggregated soot particles and more strongly aggregated ones:

Soot physical state	**β**	**ξ**
Aggregated soot particles	28.72	0.83
Strongly aggregated soot particles	0.101	1.39

As it can be observed on figures 136 to 38, good agreement between proposed values within each type of soot could eventually be found in the wavelength range 550 - 800 nm. However, as the data found in the literature demonstrate it, the practical evaluation of emissivity for a soot particle can vary by up to 50%. The use of two colour pyrometry might therefore mask the effect of the wavelength dependence over the soot optical properties by the use of the ratio of lights emitted, therefore reducing the problem of the soot emissivity to the problem of the variation of emissivity between two wavelengths.

Appendix B: A "classical" LII implementation: engine exhaust particulate matter emissions test campaign at Millbrook Proving Ground.

During two weeks in April 2004 the Artium LII 200® instrument has been made available to us by the National Research Council (NRC) Particulate Matter Collaboratory and the Artium firm. The main purpose of this loan was an in-situ evaluation of the instrument at Millbrook Proving Ground.The instrument is a commercial Laser-Induced Incandescence apparatus, featuring the self-calibration technique patented by the NRC (Smallwood et al., 2001).

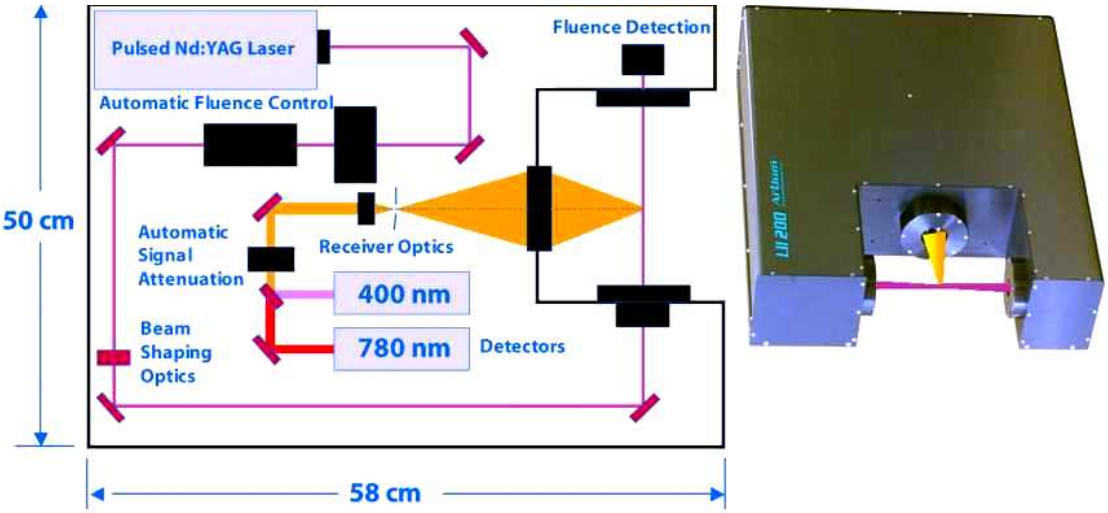

Figure 139: Schematic of the compact LII system included in the Artium instrument (left) and picture of the instrument (right) (Artium instrument, 2004)

Soot sampling is performed at constant flow (5l/min), from a vehicular exhaust to a LII sampling cell where the aerosol is then fired with an Nd-YAG pulsed laser beam. The result is a 200 to 300 ns light pulse due to blackbody radiation from the heated soot particles (currently the maximum temperature achieved is the order of 3500 to 4000 K for fluences approaching 0.1 J/cm^2). The LII light pulse is collected at two different wavelengths (see figure 140) and analyzed using calibrated photomultipliers and a transient digitizer (in this case 100 million samples per second). The soot particulate temperature decay is then computed using the two-colour pyrometry theory. Since the cooling decay is a function of the soot primary particulate diameter the soot particles are sized using their heat conduction properties. Once the particulate size is calculated the number of particulates emitting light inside the measurement volume can be computed. This results in a soot volume fraction measurement (currently in parts per billion, i.e. one ppb = 1.9 μg.m^{-3} of particulate matter).
In this case a small 40 mJ Nd-YAG laser firing at 20 pulses per second is used. Therefore each measurement is a quasi-instantaneous measurement of the soot particles concentration and size of the primary particle.

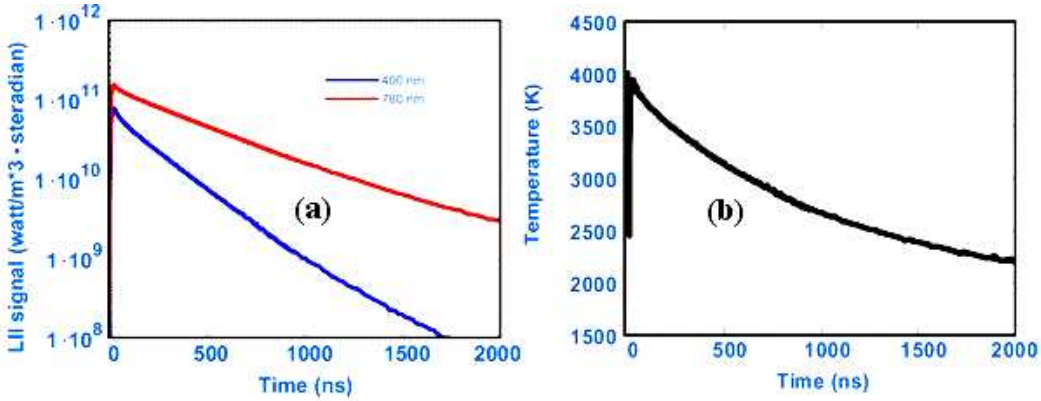

Figure 140: Using the intensity ratio of light at two wavelengths the particulate temperature can be computed.

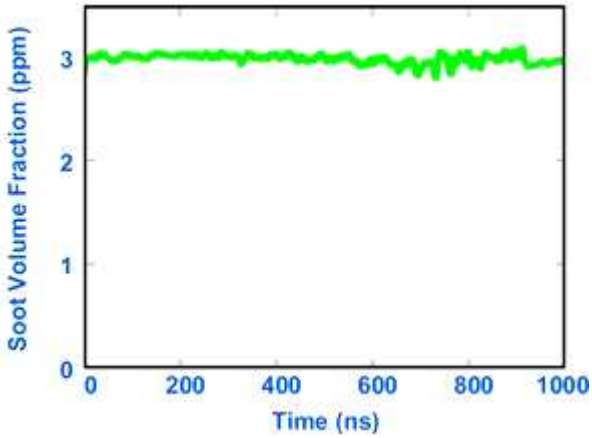

Figure 141: The amount of light collected can be directly related to a soot volume fraction assuming the computed particle size.

Installation of the instrument was performed by Gregory J. Smallwood (National Research Council, Ottawa, Canada).Measurements were performed by Dr. Glenn Sherwood, Millbrook Proving Ground Technical team and I. I was mainly in charge of data processing. The aim of the instrument has being brought to UK was for an evaluation of the LII instrument by Millbrook Proving Ground and Qualitative measurement of two EGR maps for Eminox™, a company specialized in reducing pollutant emissions, on a London Bus.

B.1. Evaluation of the LII Technique: test configuration for the Vauxhall Frontera™.

The LII evaluation for Millbrook Proving Ground took place on a 2.2L Dti Vauxhall Frontera (Turbo-diesel engine asserted with a Common Rail injection system, manual gearbox, registration number MBK 94). The test configuration is given in figure 142 below:

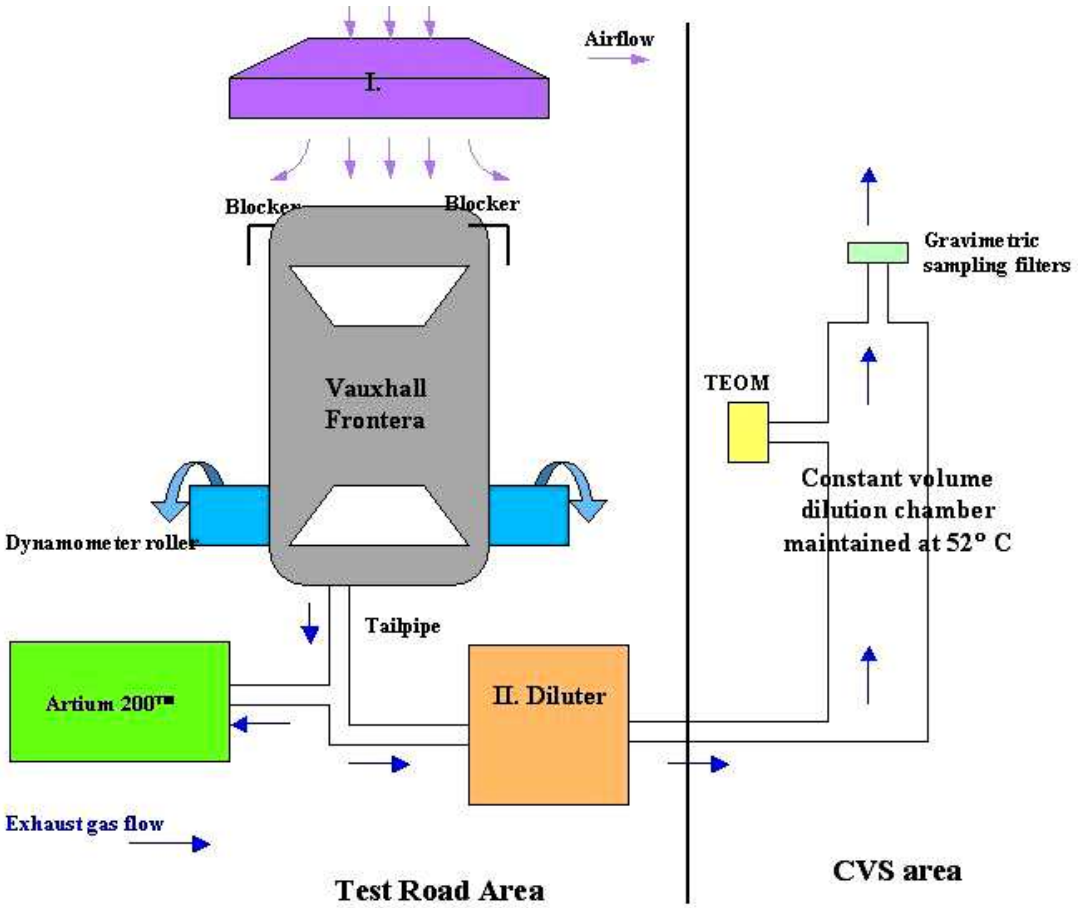

Figure 142: The Millbrook proving ground emission test area configured for the Vauxhall Frontera®.

The test road area is separated from the CVS (Constant Volume Sampling) area because of the high level of vibrations and noise occurring during testing. Usually and ELPI (electrical low pressure impactor) is also available but for this day it was not made available. The fan imitates the airflow against the car while driving. Since the year 2000 standard emission test procedures exclude the warm-up part of the tests, which lasts 40s to allow the engine to reach normal operating temperature. However testing on a cold engine introduces repeatability errors (the warm-up emissions vary greatly from test to test). Therefore the car was let to warm up before each drive cycle. The same procedure was used on the London bus later on. One Euro 4 cycle and two MLBT (Millbrook London Transport Bus Drive) cycles were performed.
The tailpipe gases were either directly sampled to the LII instrument or diluted to the Constant Volume Sampling (CVS) chamber. In this case the CVS chamber is equipped with a TEOM (tapered element oscillating microbalance) and gravimetric filters. The air sampled in the chamber is kept at 52°C to avoid water and

hydrocarbons condensation that could lead to measurement errors. Part of the exhaust gases are passed through the gravimetric filters that retain then the particulate matter emitted. These filters are weighted before and after the test and the mass of particulate matter deposited is deducted from these mass measurements.

The TEOM (Tapered Element Oscillating Microbalance) is made of a piezoelectric oscillating element that detects the passage of aerosol particles according to their specific masses. Particles passing before the tapered element provoke a change in oscillating frequency that can be related to a particulate matter mass concentration in the sampled volume. This way of proceeding is called the constant volume sampling procedure.

The car being a rear wheel drive in these conditions, the rear wheels are placed on rollers linked to a dynamometer.

The car is then being driven accordingly to two test cycles:

(i) The euro 4 cycle (see figure 143), defined by the procedure 98/69 EC for diesel emission tests. Every part of a drive cycle imitates real road conditions. This test in particular comprises of four times the same urban cycle (current European urban speeds) and one motorway (or extra-urban) cycle.

(ii) The Millbrook London Transport Bus Drive (MLTB) cycle (see figure 144), which was generated using real time data collected from a London Bus travelling on Route 159 from Streatham to Baker Street via Whitehall and Oxford Street.

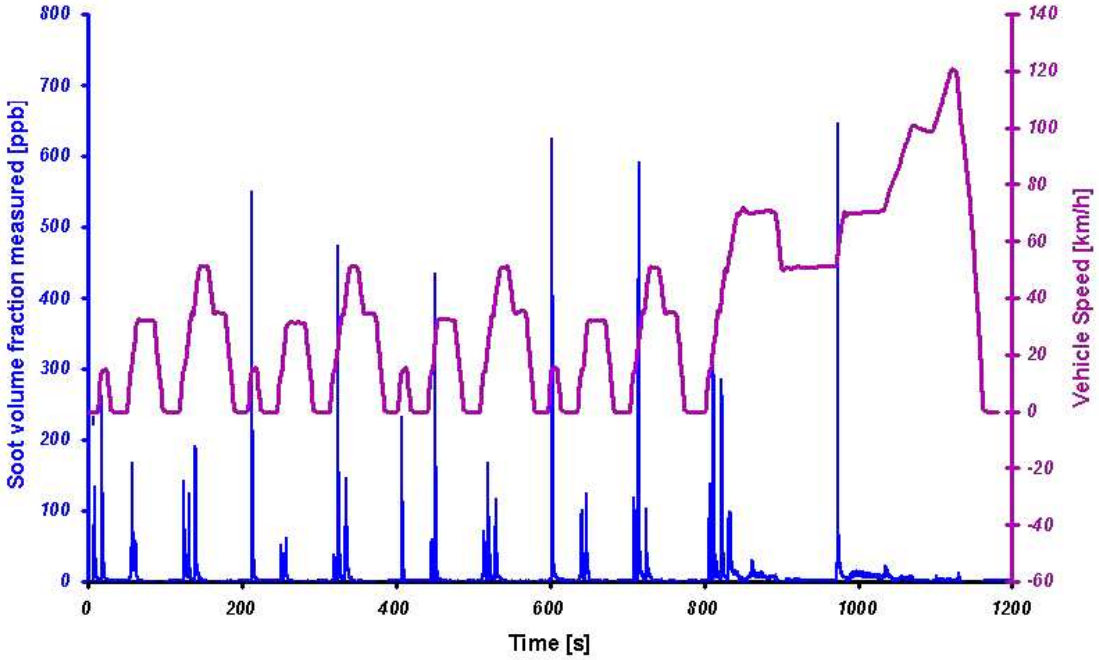

Figure 143: Euro 4 cycle for the Vauxhall Frontera™. The speed of the vehicle is marked in purple and the soot volume fraction measured by the Artium™ instrument is shown in blue. One can easily recognise the 5 parts of the cycle – 4 urban cycles and one motorway.

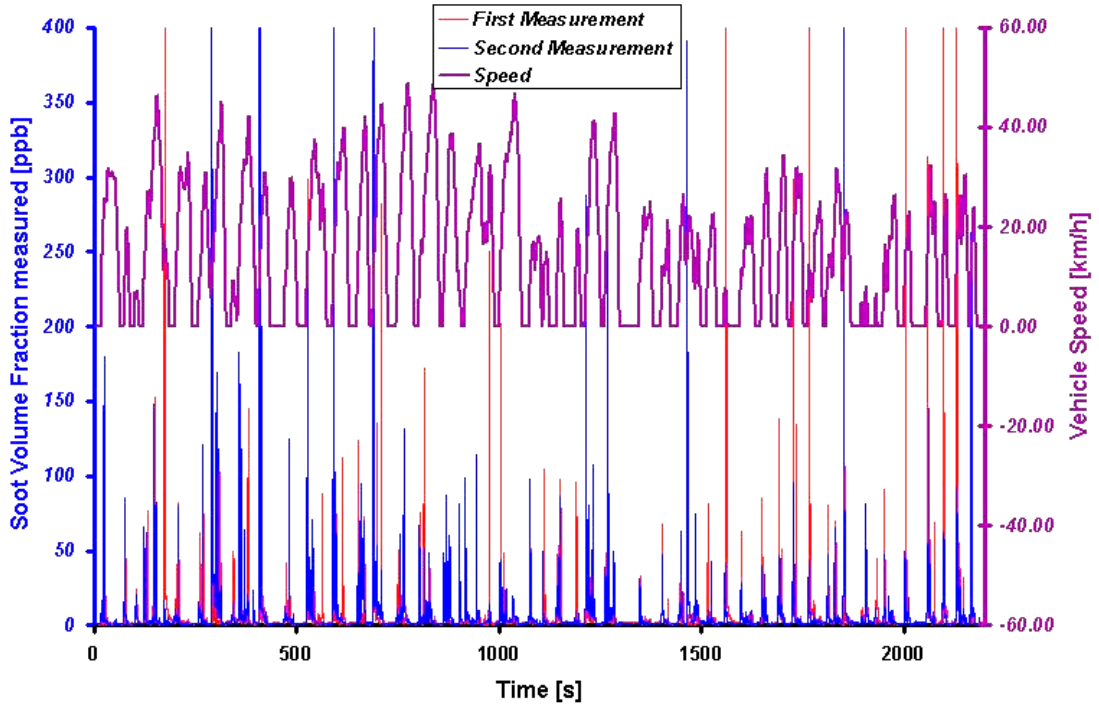

Figure 144: MLBT cycle for the Vauxhall Frontera™. The speed of the vehicle is marked in purple and the soot volume fraction measured by the Artium™ instrument is shown in blue.

The LII200® Artium instrument uses the following sampling layout:

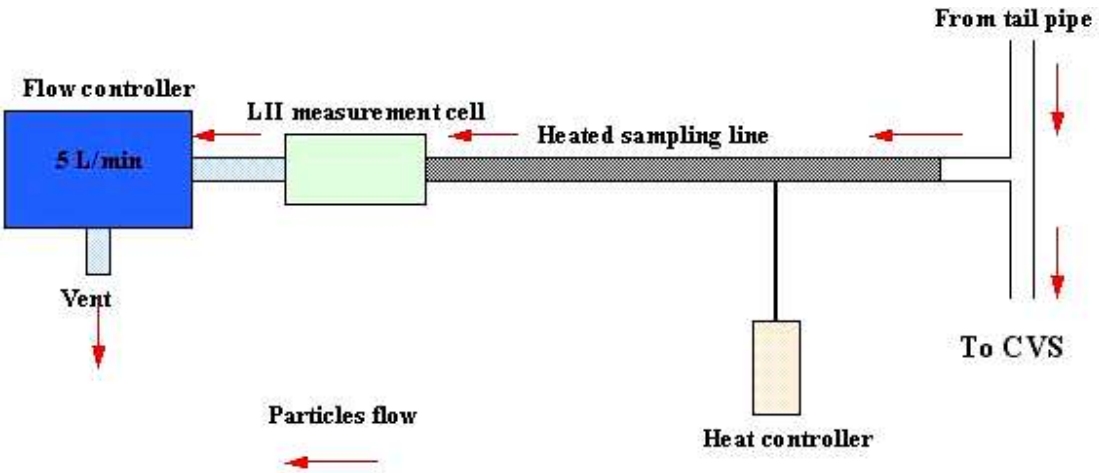

Figure 145: Sampling procedure for the Artium instrument.

The sampling line is maintained at 60° C to avoid any kind of condensation that could arise in the sampling cell since condensation creates liquid droplets that would produce a strong scattering signal and decrease the quality of the signal. The exhaust gases are continuously sampled at 5L/min to the LII measurement cell where the measurement is taken.

B.2. Evaluation of the LII Technique: results for the Vauxhall Frontera™ and comparisons LII - Tapered Element Oscillating Microbalance (TEOM) and gravimetric sampling

The calculation of the mass of particulate matter emitted by the vehicle can be computed the following way: one ppb (part per billion) of particulate matter concentration represents 1.9 µg.m^3 of particulate matter measured in the LII measurement cell. To retrace it to the mass of particulate matter emitted by the vehicle, one can use the following equation:

$$V_{mg} = 10^{-3} \times 1.9 \times V_{ppb} \times \frac{F_{exhaust}}{F_{sampling}} \quad \textbf{(106)}$$

Where $F_{exhaust}$ *[l/min]* is the flow rate produced by the engine at the tailpipe, $F_{sampling}$ *[l/min]* is the sampling flow rate and V_{ppb} *[ppb]* is the concentration measured by the instrument. V_{mg} *[mg]* is the mass of particulate matter produced by the vehicle. Note that the same calculation is applied on the CVS side for the TEOM apparatus.

During the evaluation it appeared clearly that the LII instrument was measuring significantly less particulate matter than the gravimetric technique and the TEOM. This is believed to be due either to a wrong exhaust flow measurement on the tailpipe side or a lack of dynamic range from the photo-multipliers (saturation occurring at peak particulate matter concentration). However the LII measurements were proportional to the TEOM reading and therefore a proportionality factor C_f *[ ]*was calculated against the gravimetric results to give us a corrected reading $V_{corrected}$ *[ppb]*:

$$V_{corrected} = C_f \times V_{ppb} \quad \textbf{(107)}$$

Measurement	Correction Factor
Euro 4 cycle	33.54
London cycle - 1	32.87
London cycle - 2	34.68

Final result: $C_f = 33.7 \pm 0.9$

Table 9: calculated correction factors for LII against gravimetric sampling.

This permitted a direct comparison between the TEOM readouts and the LII ones:

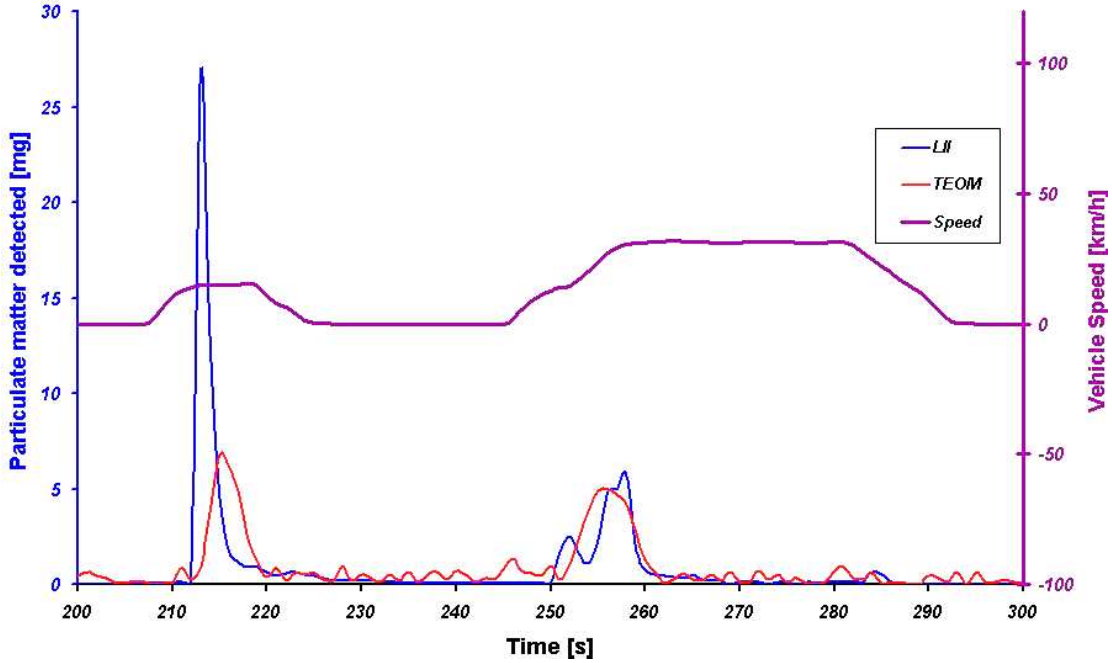

Figure 146: LII corrected response (instantaneous measurement 20 time / sec) and TEOM (Tapered Element Oscillating microbalance) response (Nominal integration time: 1 s) for the Urban part of the euro 4 cycle.

The particulate matter peak at 212 seconds illustrate perfectly the difference between the LII and the TEOM time response: whereas the LII performs a series of 20 instantaneous measurements per second the TEOM has a limited time response (>1 s) that limits its reading to only part of the emitted particulate matter during transients and presents a longer time resolution than the LII instrument.
As seen on the figure above and figures 147 and 148, it is obvious that most of the particulate matter is being produced during transients Again sharp temporal location of the particulate matter peak production is highlighted by LII. Note that the TEOM reading presents a lower signal to noise ratio. This might be due to the fact that LII measures only the carbonaceous part of the particulate matter and that the TEOM measures the entire particulate matter. However the TEOM is extremely sensitive to any kind of humidity or condensation and at 52 ˚C hydrocarbon or SO_2 condensation is still possible, leading in perturbations and noise on the readings.

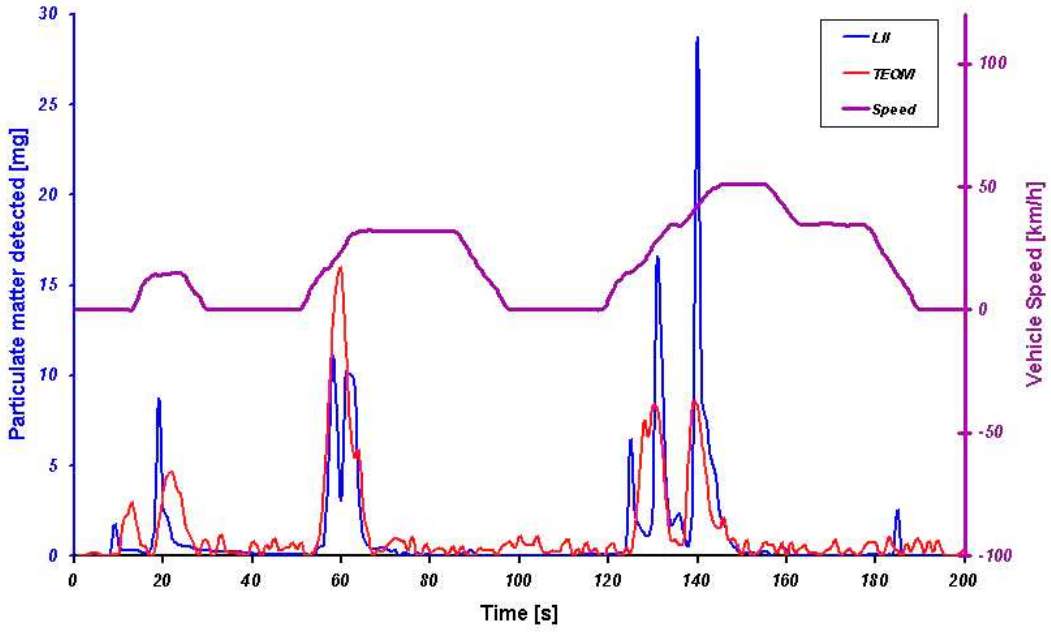

Figure 147: Corrected TOEM and LII signals during part of the Euro 4 urban cycle.

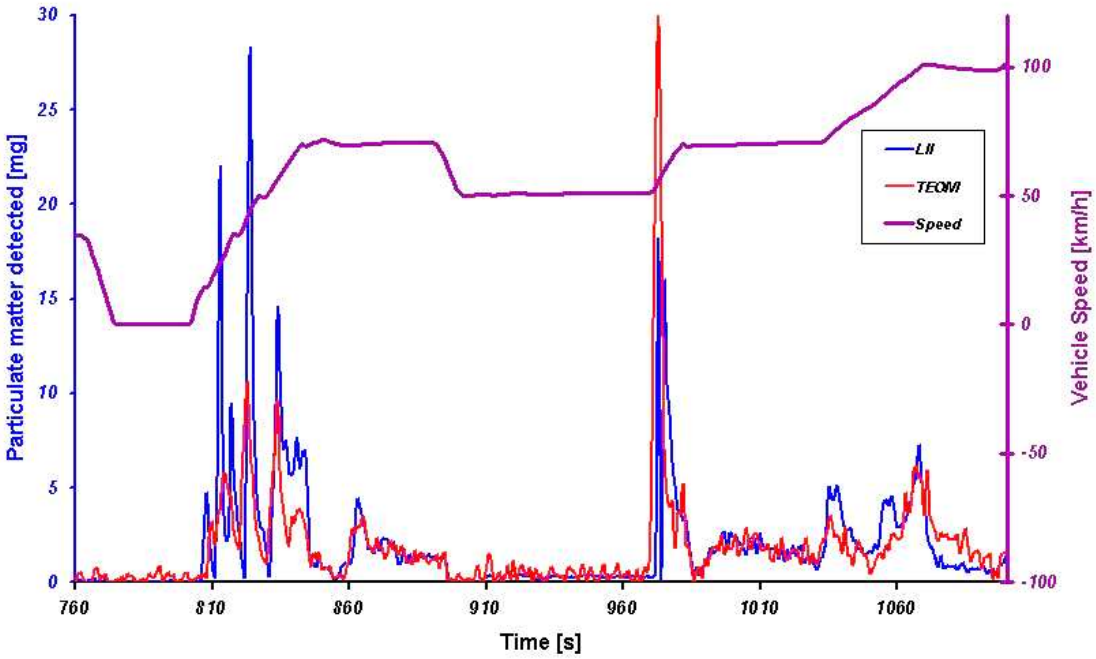

Figure 148: Extra urban part of the Euro 4 – cycle.

The two London cycles tests permitted to demonstrate clearly that the LII instrument was particularly suited for urban driving conditions measurements (see figures 146,147&148). Where the TEOM performed approximately and exposed a low resolution the LII instrument allowed the testers for high temporal resolution and quantitative determination.

B.3. Application of the LII Technique for characterization of EGR maps: London bus test configuration.

The second task for us at Millbrook Proving ground was to evaluate the efficiency of two distinct EGR engine control maps for Eminox™. Currently this firm runs an emission reduction program with London Transports to reduce the emissions produced by their buses. To reduce emissions from such diesel engines, two techniques are combined: the EGR (exhaust gas recirculation into the engine) technique and the implementation of a particulate trap filter on the exhaust line. The EGR main role is to reduce NO_x emissions and the particulate trap filter filters out of the exhaust the particulate matter produced by the engine through particulate matter oxidation processes. In this case the bus tested was a Dennis Dart™ powered by a Cummins™ B130 diesel engine coupled to an automatic gearbox.
The test configuration was similar (see figure 150) to the one used for the preceding vehicle (See section III.2. for details).

Figure 149: Test Road Area during the London bus tests.

Again, realistic road conditions were reproduced and warm-up time was allowed to increase the repeatability of the experiments .Only the Millbrook London Transport Bus Drive (MLTB) cycle was used. During these tests an Electrical Low Pressure Impactor (ELPI) was available. Such an instrument uses electrostatic charging to separates particulates according to their size and directs them into thirteen sizing stages (one size range per stage) were they are counted. Therefore the reading of this instrument is an average particulate number counted per size range.

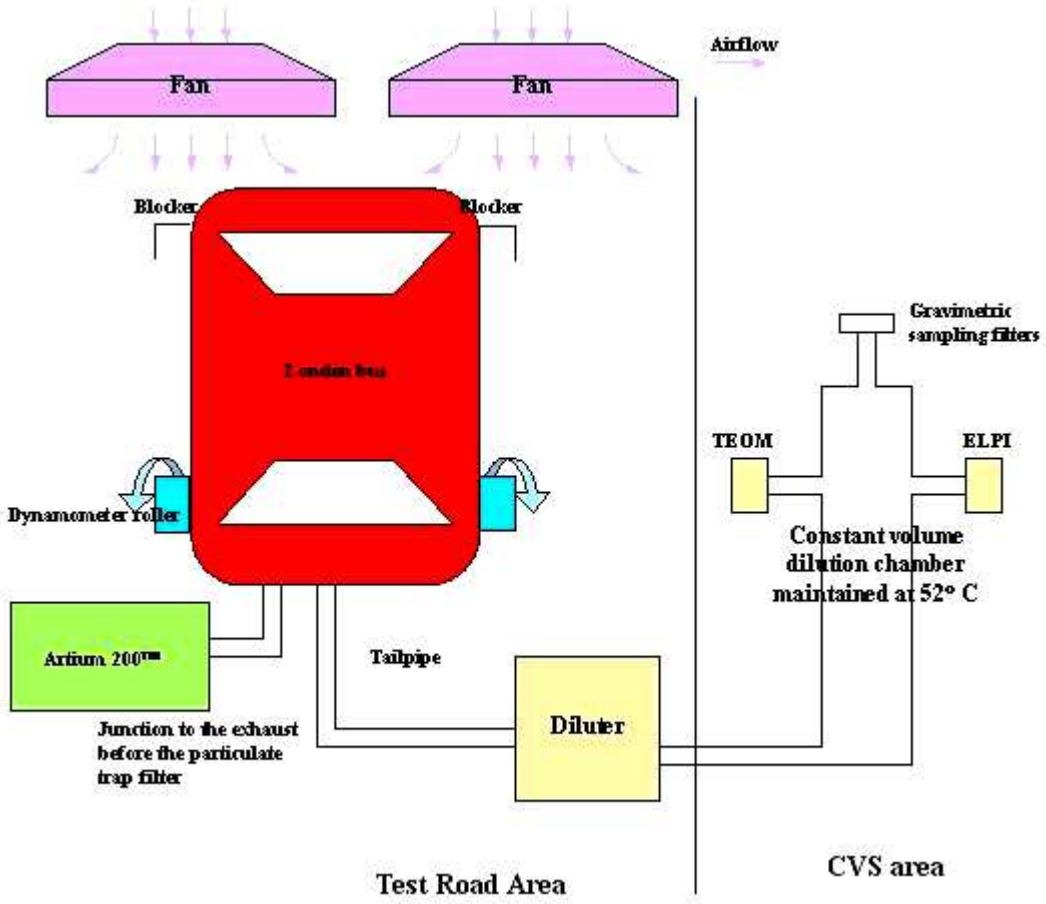

Figure 150: Test configuration for the London bus.

B.4. Application of the LII Technique: comparison of LII against an Electrical Low Pressure Impactor (ELPI).

The LII instrument counts as well the particulate number according to their sizes since for each measurement it calculates the primary particulate size or diameter *D [m]* and the soot volume fraction V_{ppb} *[ppb]*. The number of particulates detected during one measurement can be evaluated using the following expression:

$$N_{particulates} = \frac{V_{ppb}}{\frac{\pi D^2}{3} \times \rho_s} \quad \textbf{(108)}$$

$N_{particulates}$ is expressed in particulates per cubic meter, and ρ_s is the soot density *(1900 $\mu g.m^3$)*. Using this opportunity two tests were performed by bridging the LII instrument sampling location to the bus tailpipe to perform a comparison between ELPI and LII. Results are presented in figure 151. On can observe that the LII technique has a high size resolution whereas the ELPI shows more of a trend in agglomerate size distributions. As well, the LII technique measures the primary particulate size whereas the ELPI doesn't and measures rather the aggregate or agglomerate size. This explains why the size distribution is constant on the LII side for both tests whereas the ELPI shifts toward more heavily agglomerated soot particles.

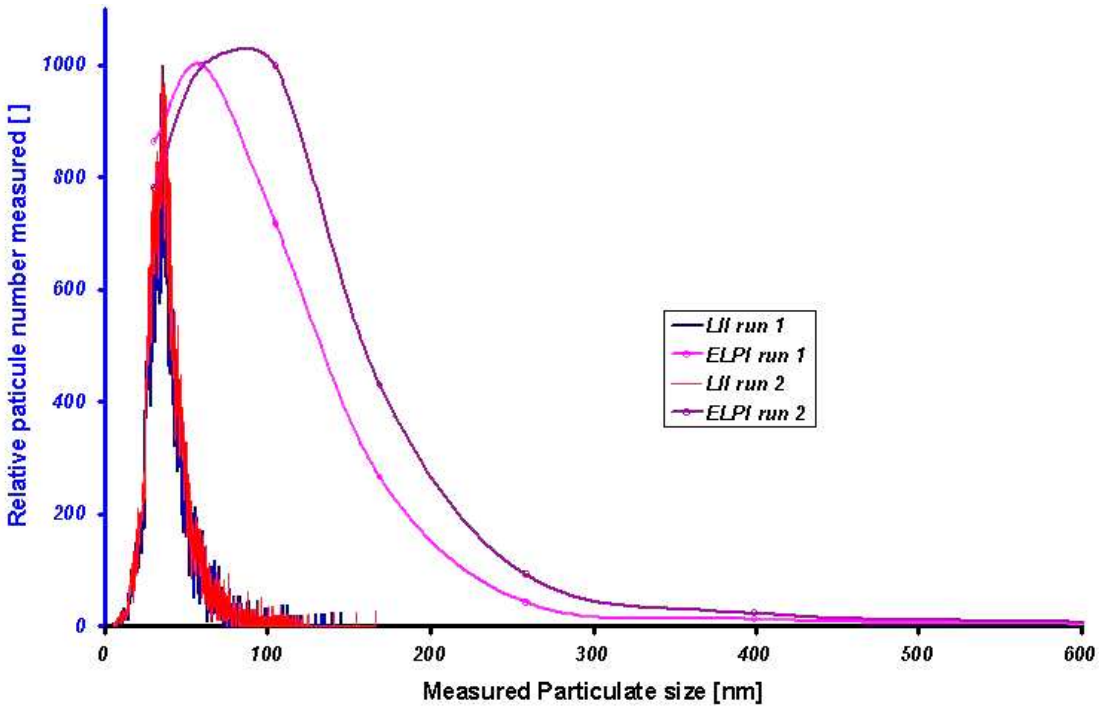

Figure 151: comparison between the ELPI readings and LII measurements.

B.5. Application of the LII Technique: evaluation of two EGR maps efficiencies.

Exhaust Gas Recirculation systems (EGR) are computer- controlled in such a way that the exhaust gases can be recirculated into the engine and regulated using a valve system for different engine running conditions. Therefore the EGR map determines the operation of the EGR valve. The reason why LII was required is that the TEOM apparatus cannot perform any measurement in raw exhaust gases (i.e. before the silencer or the particulate trap filter) since the apparatus cannot withstand condensation and hydrocarbon traces. Whereas LII, as a non-intrusive technique, can be deployed in any kind of environment. Since neither the exhaust flow measurement was available in the portion of the exhaust before the particulate trap filter nor in the tailpipe the LII data was kept in terms of volumic concentrations. Each EGR map was tested twice, and the results for each map were averaged. The repeatability of this method was then estimated to be in the order of 5 %.

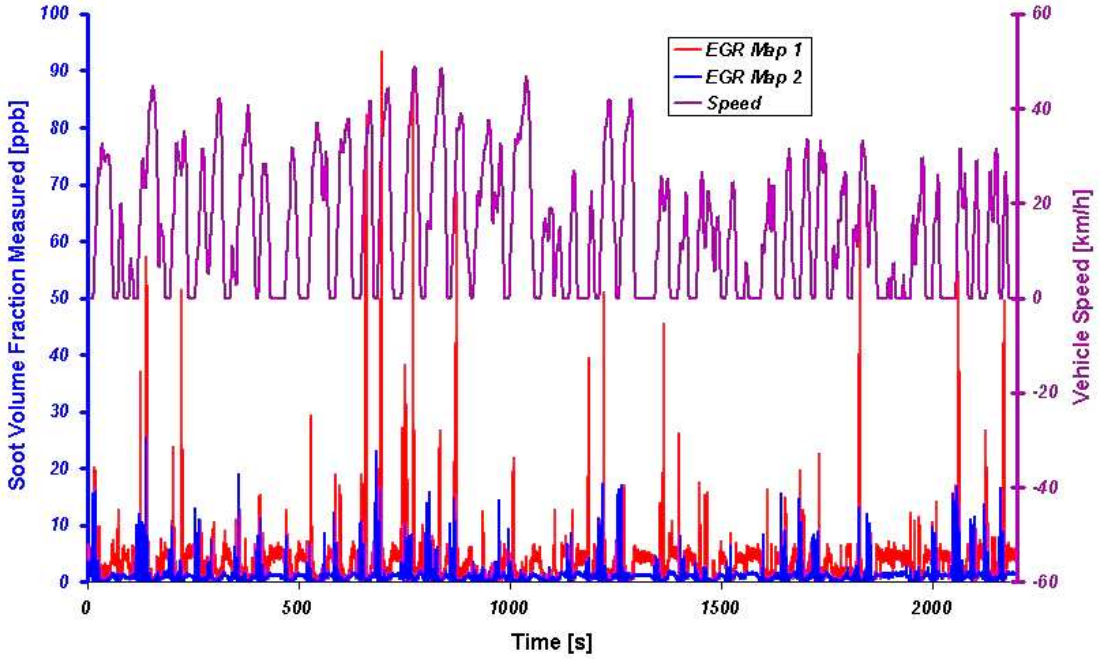

Figure 152: Results obtained using LII before the particulate trap filter for 2 EGR maps.

The results are qualitative and clearly show that the second EGR map presents lower peak concentrations and emission baseline.

Appendix C – First LII under vacuum experiment

Chapter III led to the conclusion that 10^{-2} mbar is a prerequisite for measuring LII under vacuum signals and obtain radiative temperature decays. The aim of this section is to highlight the experimental attempts and considerations that have been put into practice to achieve the requested pressure of 10^{-2} mbar and lower. In order to provide an initial understanding of the technical difficulties associated with sampling soot nanoparticles under vacuum, an attempt to measure laser-induced incandescence signals at low pressure was performed. The following experimental setup was assembled:

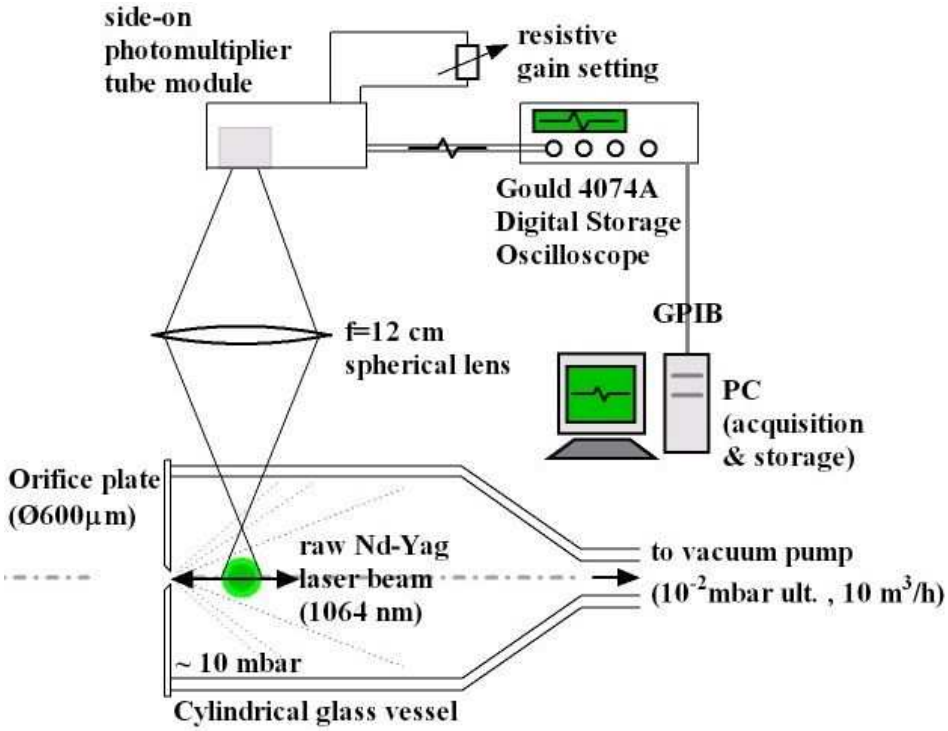

Figure 153: Low pressure LII sensing using an orifice backed by a high-capacity vacuum pump. Incandescence signals were measured using a simple collection lens and an unspecified side-on photomultiplier tube module in the throat of the gaseous expansion after obtention using a raw laser beam at 1064 nm. All measurements were stored on computer after being measured using the oscilloscope.

The system comprised of a simple glass tube with 600µm orifice on one side and a Quickfit® glass adaptor on the other side. The glass adaptor was then used to link the sampling system to a large capacity (10 m^3/hour) scroll pump (ultimate pressure of 10^{-2} mbar) in order to maintain a vacuum within the glass cylinder. The glass vessel pressure was estimated circa 10 mbar. Laser-induced incandescence signals were then created using a 1064nm Nd-YAG pulsed laser (pulse duration of 7.5 ns). Incandescence signals were then collected through the cylinder borosilicate walls and imaged onto a side-on Photomultiplier Tube (PMT) module photocathode using a spherical 12 cm focal length lens. Signals were recorded on a digital storage oscilloscope, processed and stored via an IEEE 488 (GPIB) serial communication. Eventually a 30 % rise in the recorded LII signal area, which is proportional to the integrated number of photons emitted within the sample volume was estimated.

This experiment led to the following conclusions:

- with a primary particle size know to be comprised between 25 and 40 nm, LII under vacuum would necessitate a gas surrounding pressure of less than one mbar. Clearly this is not achieved in this conditions
- because one of the highest capacity roughing pump available is used here, the pressure conditions needed for LII are not achievable with a simple evacuation system and therefore a complex two stages vacuum system is required to achieve the conditions necessary to LII under vacuum.

Appendix D – Roller bottle & quickfit® adaptor drawings

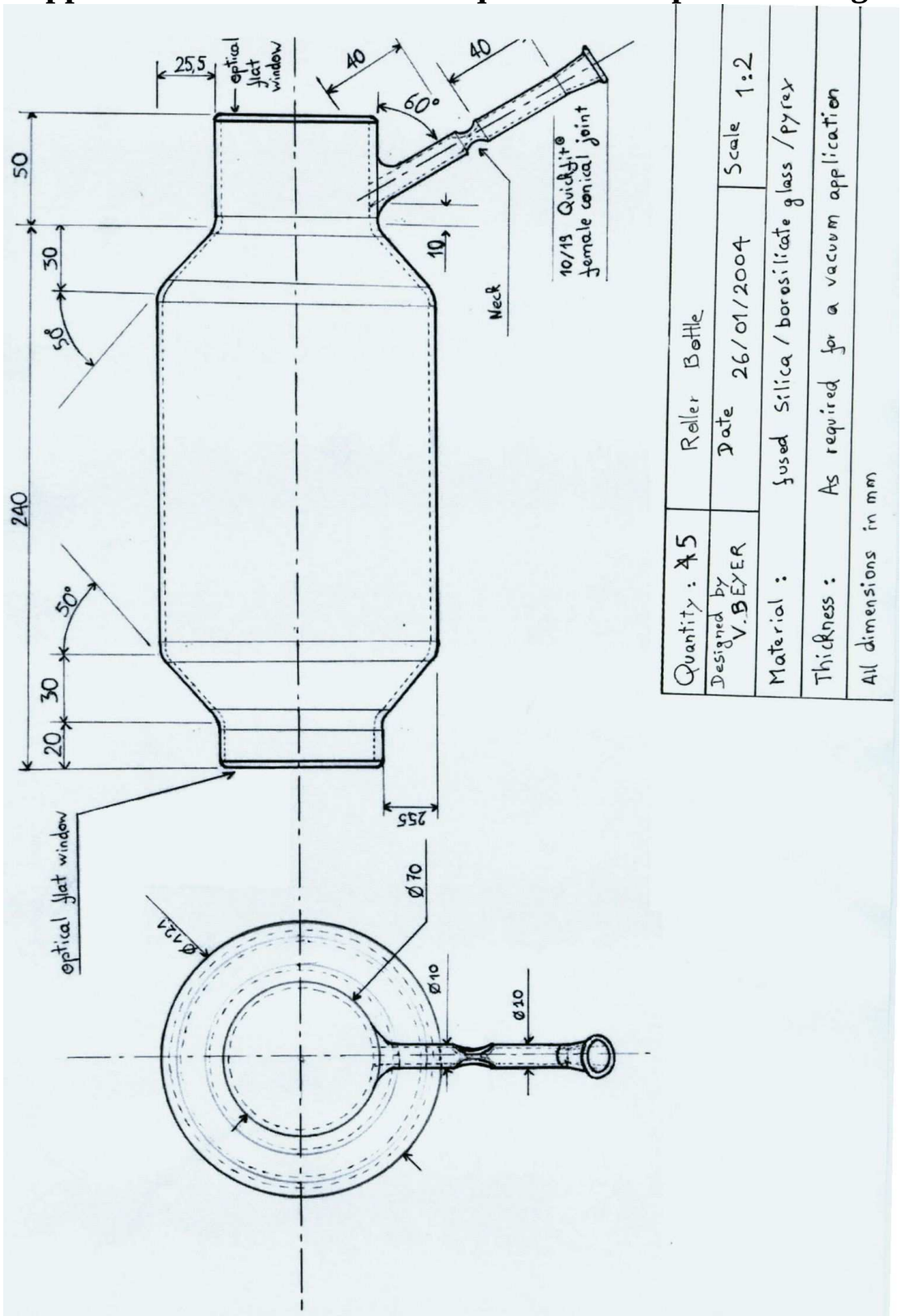

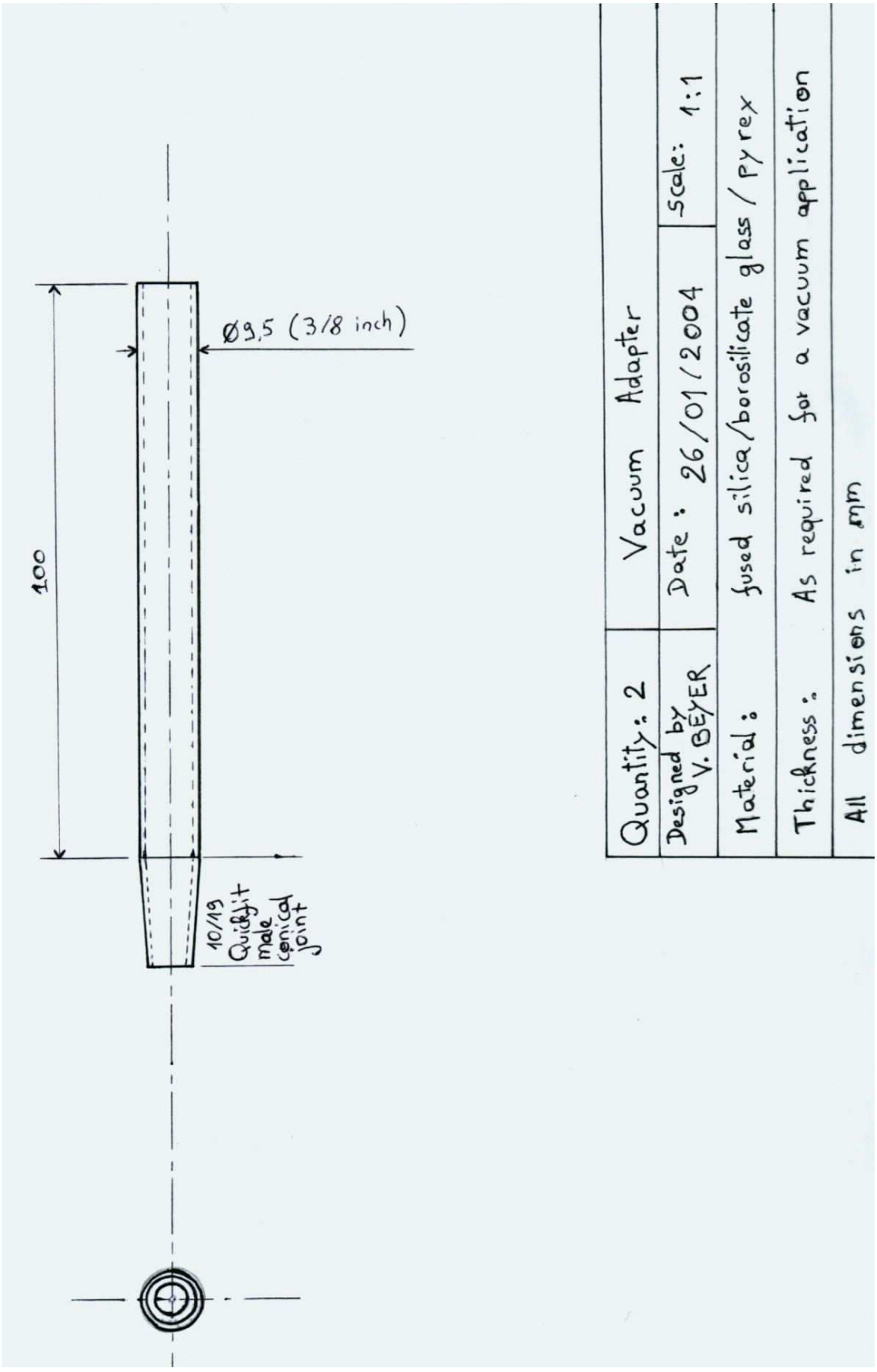
Ø9,5 (3/8 inch)
100
10/19 Quickfit male conical joint
Quantity: 2
Vacuum Adapter
Designed by V. BEYER
Date : 26/01/2004
Scale: 1:1
Material : fused silica/borosilicate glass / Pyrex
Thickness : As required for a vacuum application
All dimensions in mm

Appendix E – Pyrometer assembly and electronics investigation and calibrations

E.1. Pyrometer assembly and optical alignment.

A view of the instrument ready to take measurement is available on figure 154 below:

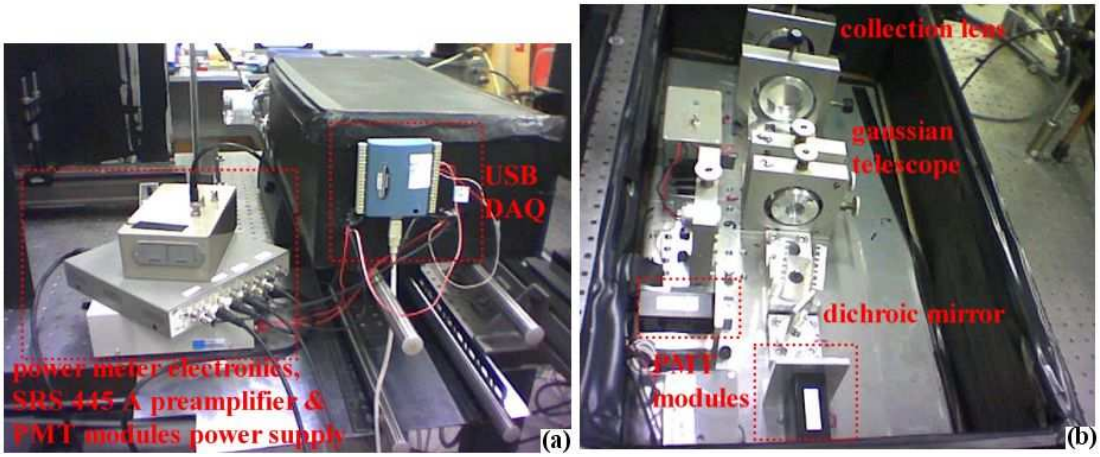

Figure 154: Details of the transient 2-color pyrometer once manufactured and assembled: (a) back view (b) top view. See text on the images for details.

As one can foresee, optical mounts are XY adjustable and the optical part of the system required a precise optical alignment. This was performed using the included laser diode L_a (see figure 155). Alignment was performed using the reflections of the laser beam from a prism to provide a visible trace of the detection axis and was performed in the following order (details are given in figure 155 below):

- With the dichroic mirror M_d removed, the laser beam was aligned and attenuated at the centre of PMT_1 and the measurement volume location marked on a fixed piece of white paper target acting as a reference. Note that the dichroic mirror was not inserted on the optical path before aligning PMT_2.
- The front collection lens L_1 was then inserted and aligned, followed by the front lens of the Gaussian telescope (L_1), the limiting aperture a_3 and the Gaussian telescope back lens L_2. Note that the apertures a_2 and a_4 are included on the lens optical mounts and were adjusted so as to be self-centring.
- The dichroic mirror M_d was finally inserted and the alignment laser beam centred on PMT_2 front filter If_2.

Both photomultiplier tube modules mounts are apertured according to the required dimensions for a_5 and assembled in a self-centring way, as well as the visible interference filters If_2 and If_1, which mounts on top of a_5.

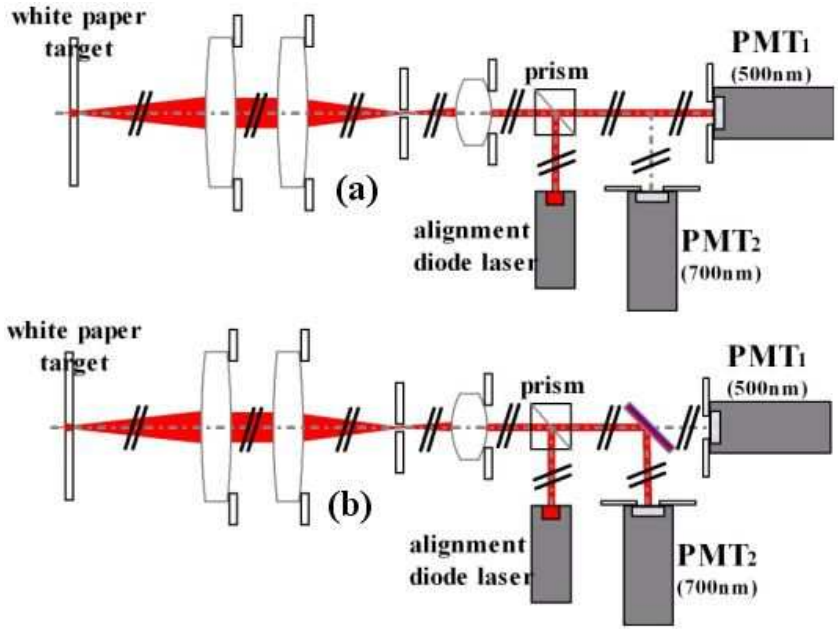

Figure 155: Alignment schematic (not to scale) of the optical elements (top view):
(a) alignment based on the detection axis and PTM_1
(b) alignment of PMT_2.

Before calibrating the device, an attempt to characterize the preamplifier channels was performed and the precision voltage divider had to be calibrated.

E.2. Pyrometer: preamplifier gain investigation

The use of amplifiers typically increases signal noises and additional gain errors. Foreseeing consequent difficulties, it was decided to check the SRS 445 channels.
The following electrical setup was used (see figure 156):

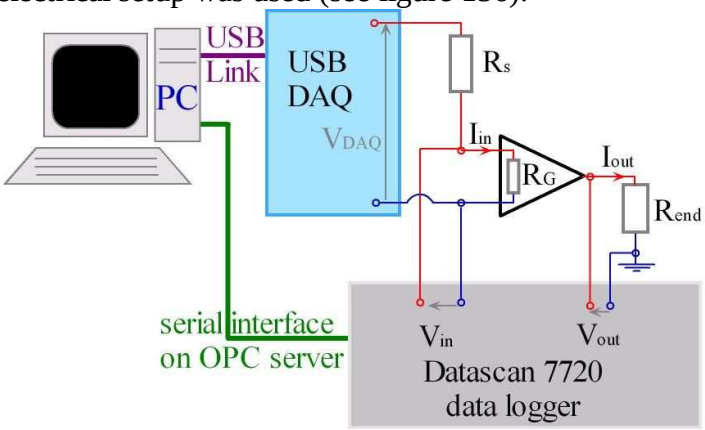

Figure 156: Electrical circuit used for the SRS 445 preamplifier gain characterization.

The setup used had the main characteristic of being entirely automated and computer - controlled. Similarly to the gain control voltage V_G, a DAC from the USB acquisition board is used to produce the voltage V_{DAQ} and therefore induce a current I_{in} through the preamplifier impedance R_G (50Ω typical). A precision 10 KΩ shunt resistor R_s is used in order to reduce I_{in} current from a 0- 15 mA range to a more adapted 0- 400 µA, therefore matching experimental conditions. Preamplifier gain is then measured

as the ratio of input and output voltages, respectively V_{in} and V_{out}, with V_{out} being measured across a precision 50 (0.01%)Ω resistor identical to the oscilloscope front impedance. Measurements were taken using a high accuracy computer-controlled datalogger and were automated using Labview® and an accuracy of less than 0.01 µA were achieved with a noise level in the same order range. An example of a preamplifier gain measurement is given in figure 157.

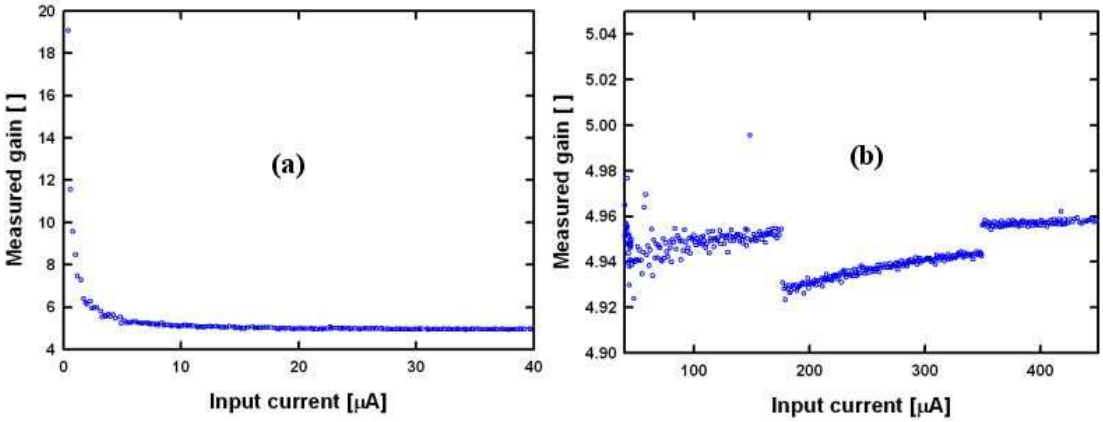

Figure 157: Gain versus input current I_{in} measurement taken on channel 1 of the SRS 445 A preamplifier:
(a) Input current range 0-40 µA
(b) Input current range 40-400 µA.

As described on figure 157 (a) above, gain linearity is an issue below 10 µA, as gains nearing 20 are achieved by the device, illustrating a poor discrimination capacity from the current amplifier. Figure 157 (b) shows a very characteristic gain change between 180 and 360 µA. This is typical of a preamplifier output base voltage fluctuation with time (here approximately 5 mins testing time), in this case bearing consequences such as a 2% error in gain whereas the preamplification system guaranties gain linearity to 1% . Fortunately, LII measurements are pulsed measurements, were a light pulse is discriminated against its immediate base voltage.
The conclusions of the preamplifier tests were that:

- the preamplifier can be used solely for light pulses measurements, were base current levels are continuously corrected for
- all four preamplifier channels presented poor discrimation capabilities below 10µA and therefore any measurement taken with an overall current level below circa 15µA should be discarded.

Next to be characterized are the two precision resistor divider bridges used to set the gain control voltage V_G of each photomultiplier tube module separately.

E.3. Pyrometer: gain voltage control V_G calibration

Gain control voltage calibrations were performed measuring V_G between the points T_1 and T_2 (see figure 156) using the high accuracy datascan 7720 datalogger and comparing it to the software - set V_{DAQ} voltage while the PMT module was kept blanked while turned on to reproduce measurement conditions. Care was taken not to saturate or damage photocathodes during testing. Four calibrations were performed in order to determine PMT_1 and PMT_2 bridges dividing factors and obtain an overall repeatability estimate. Detailed test Results are presented on figure 158 whereas dividing factors are indicated within table 6.As the set voltage V_{DAQ} was varied from 0.6 to 4 V, respective gain control voltages V_G were measured and a linear fit to data performed, with the slope of the linear fit being equal to the dividing factor.

Calibration Number	PMT_1 dividing factor	PMT_2 dividing factor
1	0.330923268	0.330770039
2	0.330923336	0.330795821
3	0.330922375	0.330795239
4	0.330923272	0.330795429
Mean dividing factor	**0.3309231**	**0.330789**
Uncertainty	**0.00000023**	**0.0000067**

Table 10: precision resistor divider bridges dividing factors overall calibration results.

Deviations from an ideal linear fit were also averaged and estimated for both photosensors PMT_1 and PMT_2 , as illustrated in figure 158 (b) and (c). The nominal resolution capacity of the acquisition board coupled to the voltage dividers was estimated circa 320µV. As demonstrated on figure 158, both circuits were extremely repeatable, with a repeatability value < 10µV constant over V_G voltage range, and such a performance would be expected from precision resistors stability. However systematic errors appeared and made up for the total error. PMT_1 errors are within expected limits, that is errors oscillating around 320µV without exceeding 400µV whereas PMT_2 errors start at 1.6 mV for V_G = 200 mV to decrease to 300µV for V_G=600mV and increase again to remain below 1 mV for V_G comprised between 600 to 900 mV. These systematic deviations from a linear behaviour are typical from a Digital to Analogue Converter, as non-linearities are common feature. Fortunately 1 mV error on V_G remained acceptable and no use of PMT_2 is foreseen for control voltages below 600 mV.

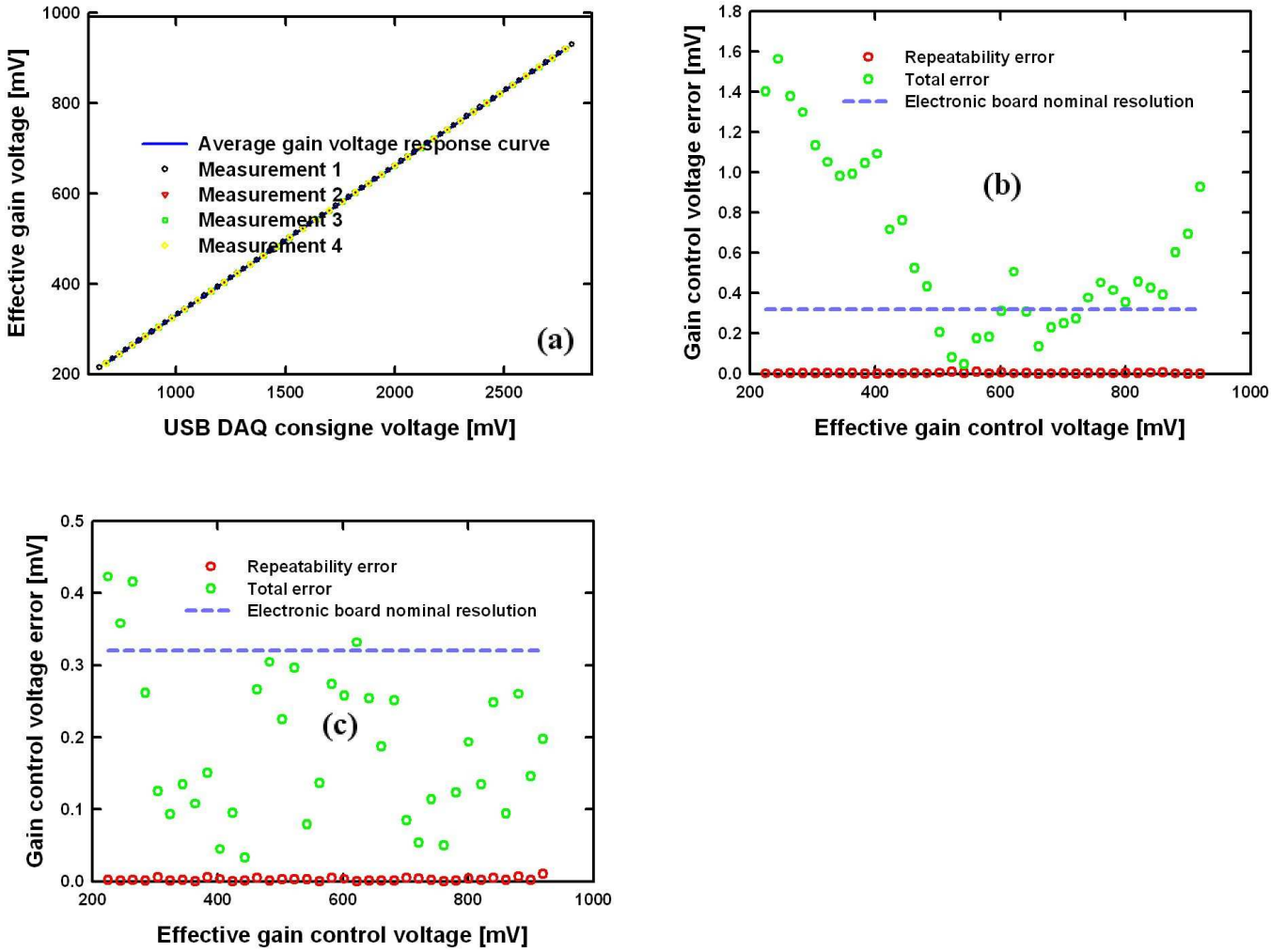

Figure 158: gain control voltage V_G calibration

(a) calibration curve for PMT_1: effective gain voltage V_G vs USB DAQ consigne voltage V_{DAQ}

(b) plot of average deviations (error) from the calibration curve vs effective gain control voltage for PMT_2

(c) plot of average deviations (error) from the calibration curve vs effective gain control voltage for PMT_1

Appendix F - Multipulse averaged LII under vacuum measurements: data analysis intercomparisons.

LII oscilloscope raw signal voltage measurements taken at three different fluences (0.078, 0.093 and 0.100 J/cm^2) were chosen as reference data in order to perform a comparison of the signal analysis approaches between the present doctorant and NRC well-experienced LII signal analyst, Dan Clavel. Analysis results in terms of absolute light intensity (figure 159), Soot temperature and soot volume fraction (figure 160 a&b). Excellent agreement was found, with less than 1% deviations in terms of absolute light intensities. Temperature agreement was within 5K, and discrepancies in soot volume fractions were found to be mainly due to different time-averaging parameters, resampling and filtering time constants, as were in general all discrepancies.

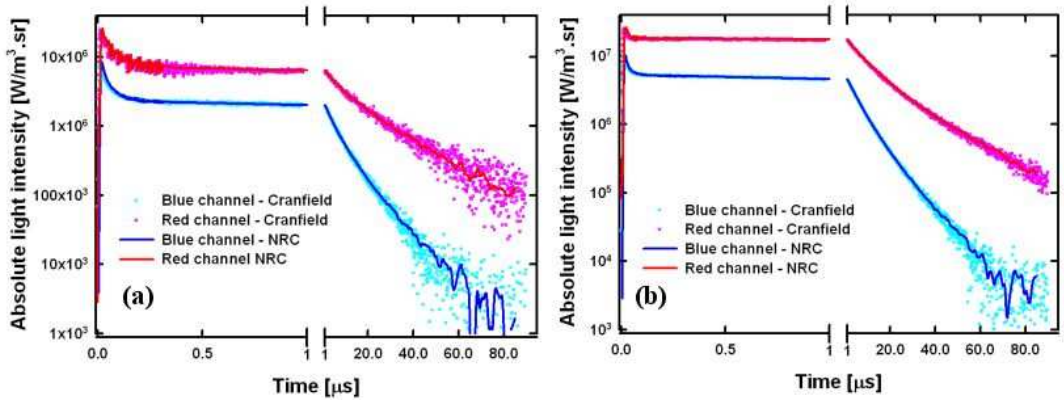

Figure 159: Absolute light intensity signal analysis comparison between Cranfield and NRC:
(a) for a fluence of 0.078 J/cm^2
(b) for a fluence of 0.093 J/cm^2.

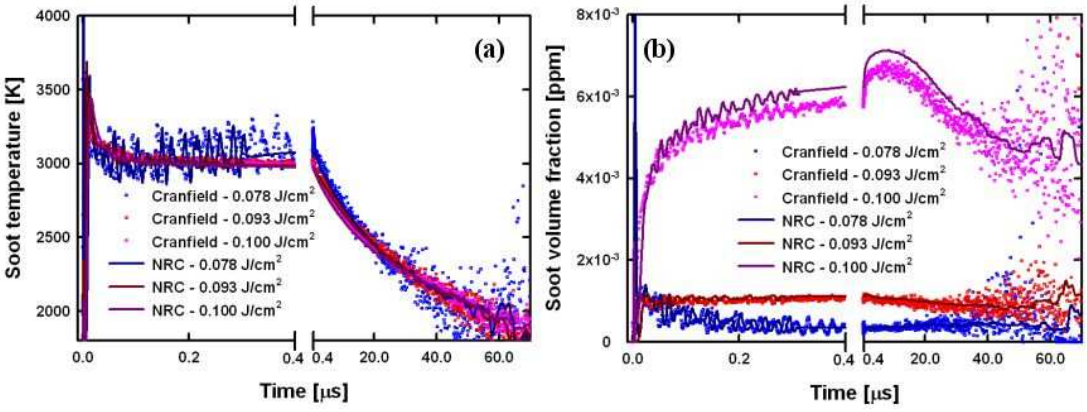

Figure 160: Temperature (a) and soot volume fraction (b) signal analysis comparison between Cranfield and NRC.

Appendix G - Development of a cold carbon (soot) aerosol generator as a way of characterising soot agglomeration effects.

Laser-Induced Incandescence measurements were first developed as a flame combustion process monitoring technique and successfully performed as a non-touching in-flame measurement technique, with excellent results correlations obtained against reference thermophoretic measurements, validating the laser-based technique as one of the most efficient and reliable means to assess local flame soot concentration. However, atmospheric and exhaust measurements are of increasing interest for the scientific community, legislators and automotive manufacturers. Short time residence, soot nucleation and oxidation are typical of flame conditions. Therefore flames intrinsically produce soot primary particles and aggregates, whereas out-of-flame soot agglomerates due to electrostatic Van der Waals attraction forces. Agglomeration in terms of number of aggregate per agglomerate varies with time and therefore depends on: (i) initial structure of soot aggregates and eventual charges (ii) airborne residence time, with typically agglomerates becoming larger with time. Consequently, in order to provide a thermodynamic insight and determine the detection behaviour of soot agglomerates, a source for providing well-characterized reference airborne carbon agglomerates is required in order to characterize laser-induced incandescence measurement issues when performing out-of-flame measurements. Even though airborne particulate matter measurements are common, such as carbon black production measurements and tailpipe emission measurements, they indeed prove erratic in terms of both absolute soot volume fraction measurements – differences of a factor 30 were measured at Millbrook between the reference gravimetric filter measurements and the Artium LII 200® measurements-and primary particulate diameter measurements – with primary particulate diameters often overestimated by LII measurements when compared to Transmission Electron Microscope (TEM) imaging as a reference.

Vartan Grigorian's (2001) cold carbon generator was used as an aerosol generator. The design principle of the device is first explained. This device is based on the atomization of an aqueous suspension of carbon black which is passed through a dual stage impactor and consequently dried using an evaporator. Initial LII measurements were performed using an Artium LII200 instrument to establish the repeatability of the aerosol particulate matter concentration obtained. These measurements were then followed by transmission electron microscopy measurements of the obtained agglomerates in order to characterize their morphological properties. Further study include LII signals repeatability and behaviour with fluence.

G.1. The cold carbon generator: design principle

During the course of his doctoral studies, Vartan Grigorian (2001)designed and implemented a soot aerosol generator. An attempt to characterize this soot generator had been made by Vartan Grigorian but the results appeared as inconsistent as the instrumentation he used later appeared to be faulty . The aim of this instrument is to produce a soot aerosol as close to monodisperse as possible in terms of particulate size distribution (Vartan Grigorian, 2001). The device is depicted in figure 161. The apparatus is cylindrical in shape. Full design explanations and drawings are available within Vartan Grigorian Ph.D. thesis (2001) and at Cranfield University School of Engineering drawing office.
The soot generator comprises of five stages:
(i) The atomiser is a pressure atomizer or nebuliser, originally designed the same way as a typical medical nebuliser. Such a device uses the a flow of compressed air (applied to the atomizer pressure inlet) to create a carbon ink flow by suction into a cylindrical reduction and break up the liquid stream into a spray of droplets. This configuration avoids the need of pressurizing the carbon black solution. At the output of the atomiser is obtained a polydisperse aerosol droplet spray of which the mean droplet diameter is dictated by the actual diameter of the reduction.

(ii) The inertial impactor works by passing an aerosol through a nozzle and directing the output jet against a flat plate. The impaction plate deflects the flow to form an abrupt 90-degree bend in the streamlines. In this case the nozzle is formed by the space between the reservoir edge and a baffle plate. The impaction plane is then formed by the vertical plane (internal wall of the generator). The instrument is arranged in such a way that large carbon black droplets acquire sufficient inertia to make them adhere to the generator wall and fall into a drip channel bringing them back to the bottom of the reservoir and therefore only the small and medium- sized droplets of the aerosol are allowed to traverse the first impaction stage.

(iv)A second impaction stage is formed by a virtual impactor stage: the flow (and therefore the droplets contained within the flow) are accelerated through a conical nozzle and cross a small region (in this case 2 mm) at the centre of the impactor before being collected by another nozzle and directed to the evaporator stage. The design of such impactor is based on the principle that evacuating the centre of the impactor using a small capacity vacuum pump attached to the virtual impactor pressure inlets and equipped with a control valve should take away any particle of small inertia (i.e. small particle since inertia is proportional to mass). Technically during experimentation it became obvious that evacuating the virtual impactor was not an easy thing to realize, since it do become feasible to achieve a flow that would not drag the entire aerosol content away (see figure 161).

(v) The last stage is an evaporator to permit the transition from size-selected carbon black droplets to solid carbon black particulates. As well, the evaporator is kept at temperatures above 80 degrees Celsius to completely eliminate the presence of water droplets from the aerosol, which would be a subsequent scattering media for any kind of optical measurement.

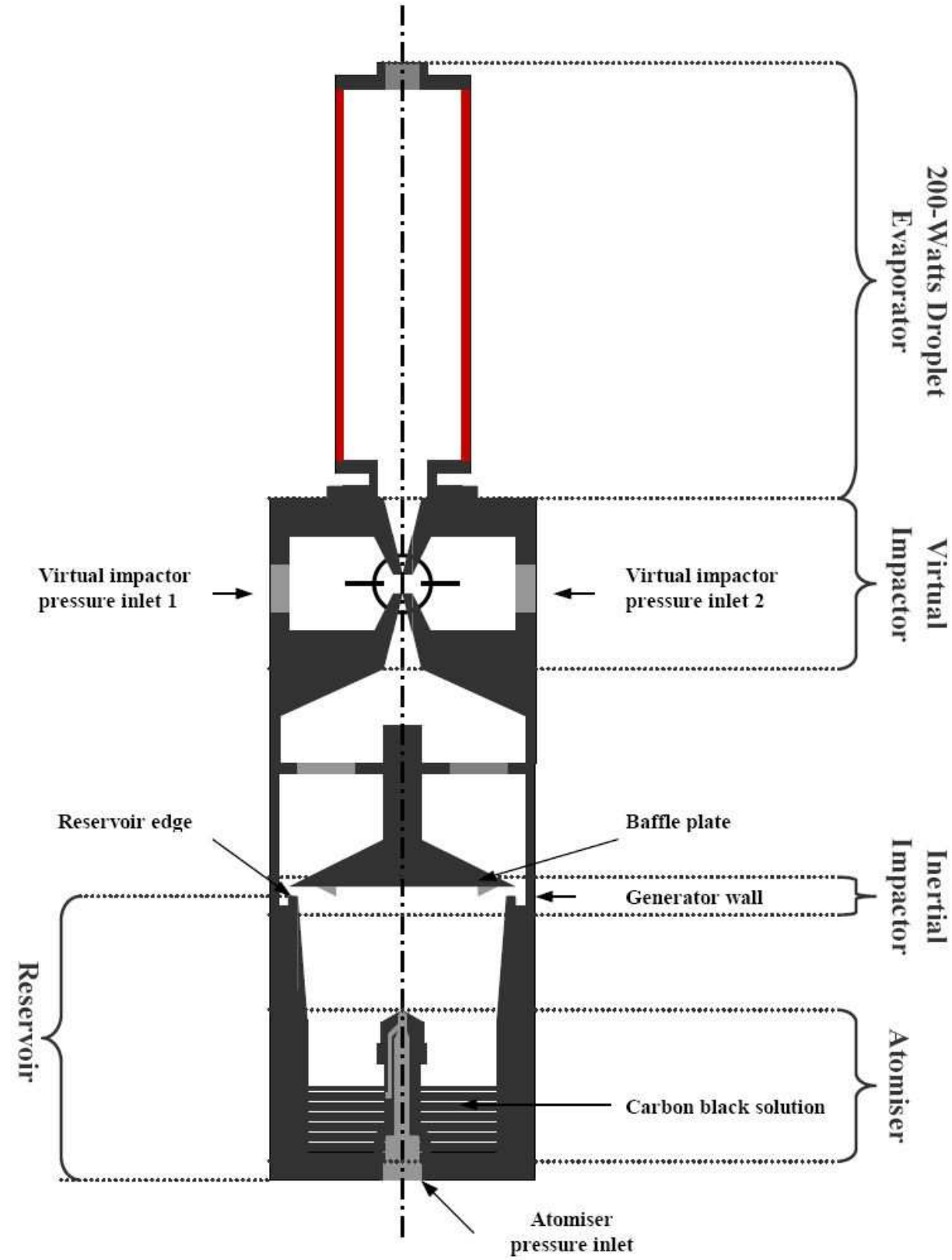

Figure 161: Cold carbon aerosol generator working schematic – inside view.

G.2. The cold carbon generator: ink properties and droplet evaporation principle

Carbon black is used for making ink dispersion. However, creating an homogeneous ink dispersion and avoiding the formation of clots are not straight forward as carbon black does not naturally disperse in solvents. Although dispersions can be obtained by means of ultrasonic agitation of carbon black powders within a mixed water-ethanol solvent, such dispersion remains homogeneous for only a limited time period (24-48 hours only) and does not permit long-term repeatability and stability as well as introducing additional errors in terms of sample ink preparation. Therefore a more complex carbon black dispersion was envisaged (Vartan Grigorian, 2001) in the form of a chemically-treated carbon black ink dispersion that is stable and homogeneous with time. In this case samples of Cabot Carbon Cab-O-Jet 200® ink-jet printer ink solution were used as a commercially available ready to use aqueous solution. The actual pigments contained in this type of ink are non-spherical carbon aggregates (composed of partially fused, reasonably spherical primary particles) having endured a sulfonation process which in practice consists in bonding SO_3^- ions to the soot aggregate external surface (Vartan Grigorian, 2001). Using this principle, carbon aggregates become indeed charged and repulse each others (see figure 162), avoiding agglomeration by overcoming Van der Waals attraction forces within an aqueous solution and are eventually bound to become polar and therefore soluble in water, behaving in a similar way as ions within an aqueous solution rather than initially a solid suspension. Such a carbonaceous dilution is typically obtained in water as a solvent an bears a 2 years lifetime in terms of dispersion homogeneity.

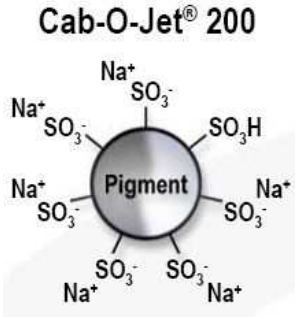

Figure 162 : Cabot Carbon Cab-O-Jet 200 ® ionic configuration schematic – the pigment represented here is indeed a carbon aggregate.(Cabot Carbon, 2006)

Once the carbon dispersion ink becomes atomised into a spray a and the size selection process is performed within the cold carbon generator, a "monodisperse" droplet size spray is then passed trough a drier at temperatures circa 80˚C with a residence time sufficient to proceed to complete water evaporation. As water evaporates away from the initial ink droplet, surface tension and electrostatic forces pull and hold aggregates together, forming a spheroidal agglomerate (see figure 163). Therefore the agglomerate size obtained is a function of the initial ink carbon aggregates concentration and of the droplet size itself. The cold carbon generator then becomes a mean of producing carbon agglomerates in a controlled manner, which comparatively is hardly feasible from flame fumes and representative of airborne soot, as soot formed from combustion has a natural tendency to agglomerate as a function of its airborne residence time.

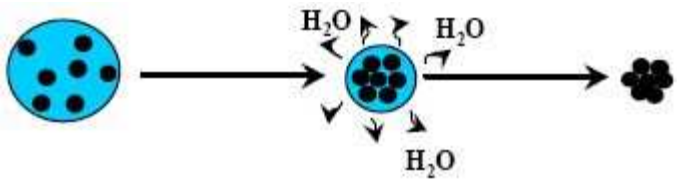

Figure 163: Illustration of soot generator aerosol particle (agglomerate) formation from heated ink droplet. Each dot represents a carbon aggregate (Wainner, 1999).

G.3. Initial measurements performed with the Artium LII 200® instrument.

The Artium LII 200® instrument, once the Millbrook test campaign (see Appendix B for details of the instrument)was duly completed, was made available by National Research Council (Canada) and the opportunity arose to perform absolute light calibrated measurements on the cold carbon generator. Details about the instrument in particular are available in chapter VI. The initial measurements performed with the cold carbon generator were indeed aimed at obtaining a repeatable and traceable calibration aerosol in term of soot volume fraction and primary particulate size. All initial measurements (63 tests) were completed within two days as the National Research Council instrument loan was nearing its end. All measurements were performed by sampling a negligible amount of air from the output aerosol 35 mm upstream of the drier outlet into the LII 200® extractive sampling cell. The atomiser and virtual impactor inlet pressures were monitored using basic dial pressure gauges. Each measurement lasted between 1 and 5 minutes, corresponding to between 600 to 3000 single pulse LII signals acquisitions, for a 10 Hz measurement rate corresponding to the LII 200® internal Nd-YAG laser repetition rate. Carbon black solutions were made by diluting 10 times samples of Cab-O-Jet 200® in distilled water, bringing the initial 20% ink pigment concentration to a diluted 2% pigment (mass) concentration. The first measurements performed consisted in testing the feasibility of evacuating the virtual impactor stage and measuring the output aerosol, as illustrated in figure 164. Virtual impactor testing was carried with a small capacity rotary vacuum pump (10 L/min) linked to a valve providing an evacuating flow from the virtual impactor stage. However, although the evacuation flow was reduced finely using the valve, it soon became obvious that a more elaborated mean of evacuating the virtual impactor stage was required as the whole aerosol content was being drawn into the vacuum pump, which was confirmed by an instrument readout below detection limit (~1ppb). Hence actuating the virtual impactor using a “negative” flow was discarded for the remaining of the test campaign and the next measurements were performed with a valve blocking the virtual impactor compressed air inlets, see figure 165.

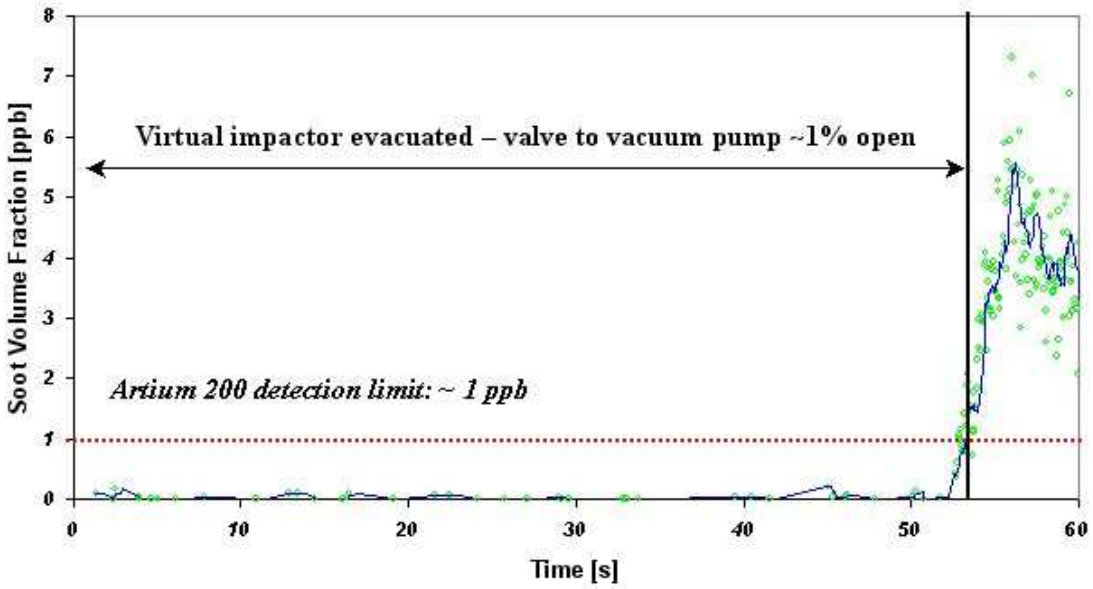

Figure 164: Virtual impactor stage evacuation testing. The blue line is a moving average and the green circles are measurements. The nebuliser was actuated by an inlet pressure of 69 KPa. After 55s the vacuum pump valve was closed and the impactor compressed air inlets blocked.

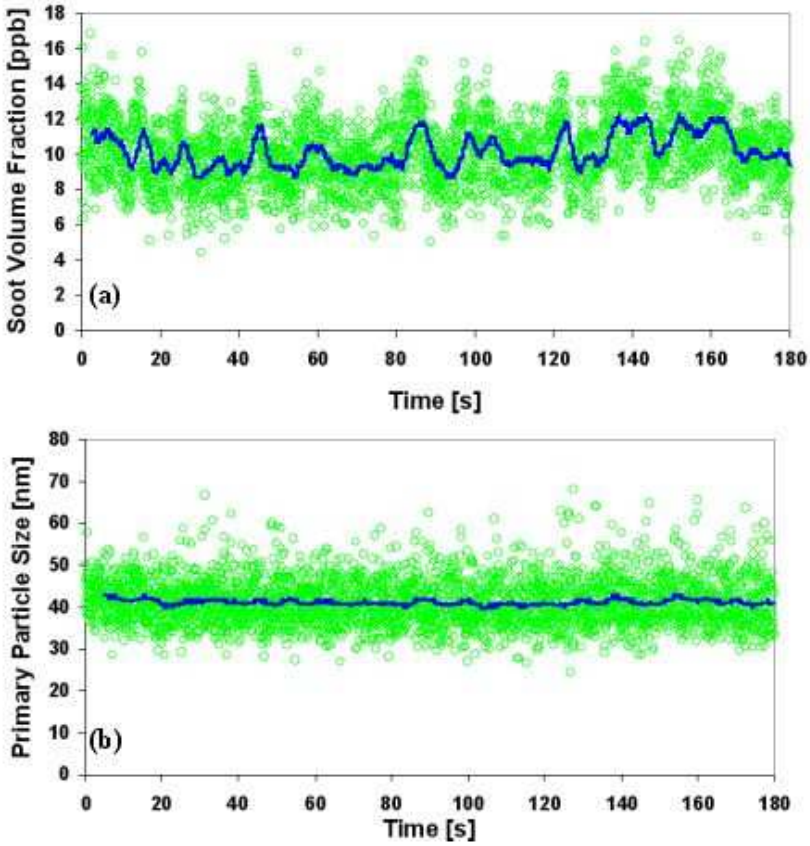

Figure 165: Artium LII200® Soot Volume Fraction (SVF) measurement (a) and primary particle determination (b) for a blocked virtual impactor and atomiser inlet pressure at 69 KPa. The blue line is a moving average whereas green circles represent pointwise measurements. SVF and primary particle measurements are performed on the same dataset (i.e. are simultaneous).

Whereas the soot primary particulate size was measured as nearly constant on an average basis, the soot volume fraction kept on varying. After many trials, it became obvious that any air motion above the generator drier outlet was disturbing the exhaust plume from the generator and hence soot volume fraction measurements. It was then obvious that some mean of stabilizing the cold carbon generator exhaust plume was necessary. A simple solution was found in the form of an application of positive radial flow through the virtual impactor pressure inlets, as described in figure 165:

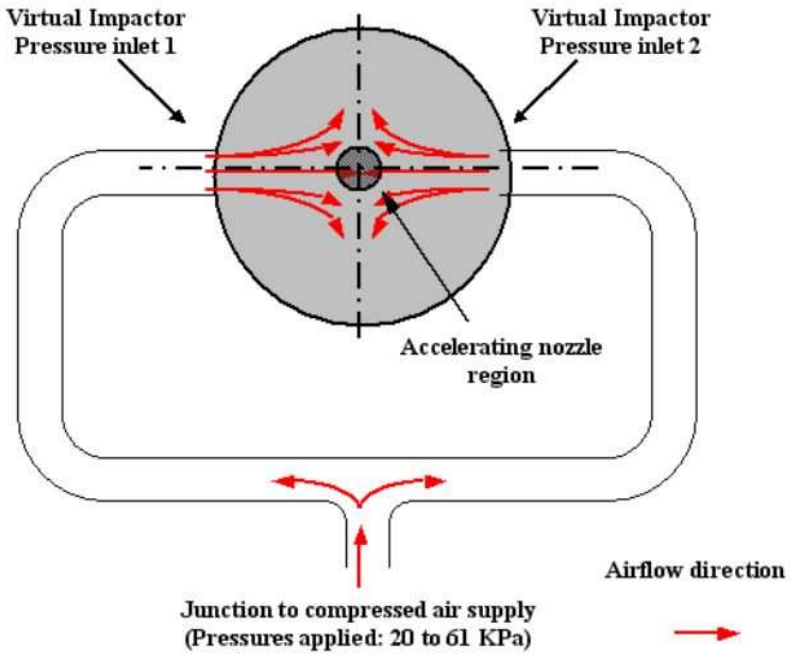

Figure 165: Top view of the virtual impactor in the radial blowing configuration. Since all the flows inside the apparatus are monitored in terms of upstream pressure for each pressure inlet, applying the same positive pressure on both pressure inlets of the virtual impactor has an immediate effect of creating a zone of counterflow at the nozzle location, thus increasing the air flow out to the drier . Since the pressure on the atomiser side has always been maintained above 68 KPa, the air flow direction was maintained from the bottom – atomizer - to the top – drier output.

On one hand, the obvious result of this configuration was that the droplet-carrying aerosol endures a systematic dilution; therefore locally measured aerosol mass concentrations observed were indeed lowered. On the other hand, the increase in airflow stabilized the air flow at the drier output and provided soot volume fraction measurements insensitive to air movements. A typical measurement using this configuration is depicted in figure 166. Given that this configuration provided outstanding stability in term of measured soot volume fraction, it was therefore decided to characterize the cold carbon generator in terms of SVF and particle size (diameter) measurement repeatability and reproducibility. Sixty-three measurements were effected during two days (35 measurements the first day and 28 the next one) with new carbon black diluted ink solutions (4 sample solutions at 2 % concentration in pigment mass per day) and complete dismantling, cleaning and remounting of the instrument on the evening of the first day. Loading of a new diluted ink solution was

done after fully washing the instrument and leaving the cold carbon to dry with the maximum flow of compressed air on and the evaporator at 90 degrees. The aim was to achieve measurements on 3 identical solutions of carbon black at 2% mass concentration per day over two days in order to evaluate both reproducibility and repeatability of the aerosol obtained. Results are presented in table 11.

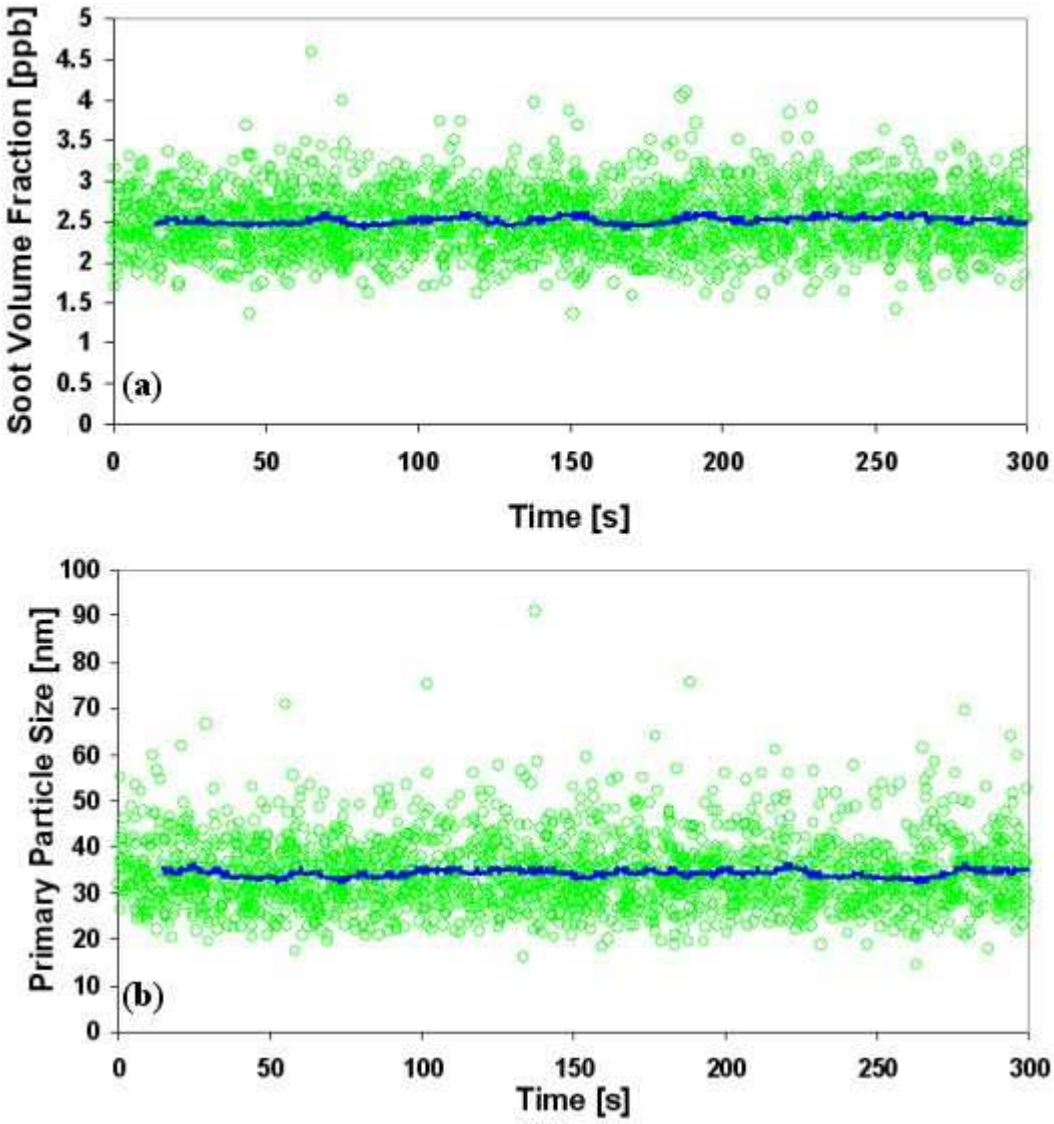

Figure 166: Soot volume fraction (a) and primary particle size (b) recorded by the LII 200® instrument during test 21. The blue line is a moving average whereas green circles represent pointwise measurements. SVF and primary particle measurements are performed on the same dataset (i.e. are simultaneous). Note that the overall SVF stability is greatly enhanced, from a preceding ± 3 ppb (see figure 148) to an actual ± 0.4 ppb. Atomiser pressure inlet was maintained at 69 KPa and virtual impactor applied pressure was 40.5 KPa.

Primary particulate size measurements:

Setting	*Number Of Measurements*	*Average [nm]*	*Reproducibility [nm]*	*Repeatability [nm]*	*Uncertainty on this setting [nm]*
Atomiser inlet at 69 KPa, virtual impactor inlets at 20 KPa	**8**	**35.24**	**6.87**	**2.28**	**6.92**
Atomiser inlet at 69 KPa, virtual impactor inlets at 40.5 KPa	**8**	**30.15**	**7.60**	**1.56**	**7.62**
Atomiser inlet at 69 KPa, virtual impactor inlets at 61 KPa	**8**	**27.39**	**7.75**	**1.68**	**7.77**

Soot volume fraction measurements :

Setting	*Number Of Measurements*	*Average [ppb]*	*Reproducibility [ppb]*	*Repeatability [ppb]*	*Uncertainty on this setting [ppb]*
Atomiser inlet at 69 KPa, virtual impactor inlets at 20 KPa	**8**	**5.05**	**0.75**	**0.45**	**0.77**
Atomiser inlet at 69 KPa, virtual impactor inlets at 40.5 KPa	**8**	**2.57**	**0.46**	**0.31**	**0.47**
Atomiser inlet at 69 KPa, virtual impactor inlets at 61 KPa	**8**	**1.49**	**0.36**	**0.10**	**0.36**

Table 11: Measurement results summary with positive pressure applied on the pressure inlet ports of the virtual impactor.

As one can observe from these results, the primary particulate size measured by the LII200 ® instrument decreases from 35 to 27nm with increasing virtual impactor flow (virtual impactor inlet port pressure increasing from 20 to 61 KPa). It has recently become established in the domain (Liu et al., 2006) that aggregation and agglomeration contribute to virtually "shield" primary particles from colliding with ambient gas molecules, as simply the presence of nearby particles within agglomerates and multiple fusing of primary particles together simply reduce the average available surface of primary particles colliding with air molecules. As well, thermal shielding for primary soot particles increases with both agglomerate and aggregate size. Therefore primary particle size determination using the assumption of single nanoparticulates colliding freely with air molecules does not hold true anymore and any attempt performed using this assumption will result in slower than expected conductive temperature decay and hence an overestimation of the "real" primary soot particle diameter. Clearly this shielding effect was present, as the cold carbon generator is producing solely carbon nanoparticles agglomerates. Therefore any

reduction in averaged particle diameter resulting from an increase in virtual impactor transverse air stream pressure would signify that a droplet size selection process is operated, resulting in a lowered median droplet size and as a consequence a reduced average agglomerate size.

Soot volume fraction measurement obtained are encouraging in terms of stability and repeatability, as for example a resulting 15% minimal uncertainty in terms of SVF is obtained for an atomiser inlet pressure of 69KPa and a virtual impactor pressure inlet of 61 KPa, with repeatability data enabling future results intercomparisons in time. As well, primary particulate size measurements proved enthusiastically repeatable.

An alternative use of the cold carbon generator is to use it as a calibration transfer, as a mean of transferring an initial absolute light intensity calibration to an uncalibrated detector. This has particular interest in terms of simplifying calibration procedures for simple broadband detection systems such as intensified CCD cameras and similar detectors…The soot volume fraction range obtained so far allows for calibration from 1.5 to 13 parts per billion (ppb) with an uncertainty as low as 0.36 ppb. In addition, the cold carbon generator calibration transfer does not provide an integrated SVF value such as total particulate mass (as would the gravimetric procedure) but a concentration within a nearly uniform emitting volume, therefore cancelling the need for the user to measure the effective measurement volume of the equipment to be calibrated, which is an another attraction for 2D imaging measurement calibration.

As the measurements performed with the LII200® instruments proved promising, additional work was undertaken at the National Research Council, Canada. This project comprised of two parts: (1) high resolution microscopic agglomerate imaging (2) performing detailed laser-induced incandescence measurements at various laser fluences.

G.4. Cold carbon generator: agglomerates imaging

Vartan Grigorian (2001)did indeed image some on the typical agglomerates produced by the cold carbon generator by collecting on an unspecified surface within the drier output flow and performed Scanning Electron Microscope (SEM) measurements. In terms of qualitative assessment, SEM micrographs are difficult to process as: (1) SEM is a reflective measurement method, meaning that only electron reflections from the outer surface of a gold-sputtered agglomerate are recorded (2) SEM micrographs are therefore limited as they provide only an overall agglomerate size measurement, but do not bring a detailed insight into the primary particles forming the agglomerate as they are confused with the overall agglomerate surface. Typical SEM micrograph were provided (Vartan Grigorian, 2005) and are included in figure 167:

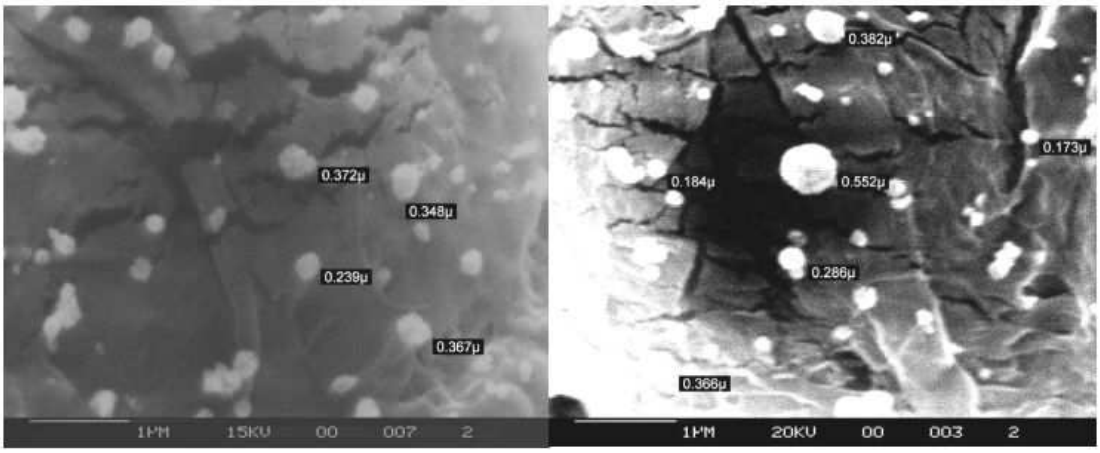

Figure 167 : Typical cold carbon generator agglomerate imaging using the SEM method. The white surfaces are carbon nanoparticles agglomerates produced by the device. Clearly SEM micrographs are suited uniquely to measure agglomerate overall parameters, but do not provide any form of insight on the agglomerate primary particle composition.

It was decided –given the inadequate data that was available – to perform Transmission Electron Microscope (TEM) measurements in order to obtain a better understanding of the agglomerates produced. TEM is more attractive when compared to SEM in terms that: measurements are performed in terms of the transmissivity measurement of an electron beam through the sample to be imaged. Therefore, relative transmissivity measurements are made possible and the underlying structure below the outer surface of the agglomerate becomes apparent. Fortunately TEM measurements where made available at NRC (Canada) with Dr. Kevin Thomson possessing a large experience in terms of soot sampling and TEM imaging. The TEM grid used in this case were made of thin carbon film coated copper grids. The carbonaceous film was used as a sample substrate and present sub-nanometric surface uniformity. The cold carbon generator output plume was sampled at 35 mm above the drier outlet. A reference setting was chosen with the atomiser inlet pressure regulated at 69 KPa and the virtual impactor inlet pressure at 31 KPa was chosen and all measurements performed at NRC, including LII measurements, were performed with these reference inlet pressures. Initial sampling attempts were performed with a thermophoretic retractable arm with the sampling grid inserted at the centre of the plume in the colinear direction to the flow. This way, eventual carbon impaction

would have been avoided and carbon agglomerates would have been sampled using the thermophoretic effect, based on the principle that heated carbon agglomerates (~75˚C) would be attracted by the colder sampling grid and the temperature difference (~50 K) would be sufficient to engender thermophoretic forces large enough to obtain carbon agglomerate adsorbed to the sampling grid surface (carbon film). Successive trials proved unsuccessful and consecutive imaging did not reveal any consistent presence of particulate matter on the sampling grid. Two factors are to be taken into consideration to explain this: (1) thermophoretic sampling is typically performed in flames, meaning the temperature difference sampling grid-sampled medium is in the order range of 700 -1000K ; (2) The preceding point (1) combined with ppb-level (low) soot volume fraction induces that the initial sampling volume agglomerate concentration is extremely low and therefore diminished the chances of success for thermophoretic sampling. Hence it was concluded that unless a nitrogen-cooled cold finger system is used to cool the sampling grid and obtain a ~ 300K temperature difference to initiate thermophoresis, thermophoretic sampling could not be performed. Given the little time available, this option was not implemented and the cold carbon generator plume was consequently sampled with the central drier output flow impacting on the TEM carbonaceous sampling grid surface for 60s and resulting TEM images (2048 by 2048 pixels) are available in figure 168. Imaging revealed the presence of spheroidal carbon agglomerates. TEM micrograph were taken with various degrees of magnification (from 6300:1 to >50 000:1). As illustrated by figure 168, internal agglomerate structure - in particular primary soot particulates - was clearly discernable. The “snowball” shape of the agglomerates is indeed expected and the process leading to their spheroidal formation has been explained earlier. Individual primary soot particulates were discernable throughout the entire volume of agglomerates of optical diameter < 500 nm and became discernable only on the outer circumference of agglomerates of optical diameter > 500nm. Unfortunately, the apparent entanglement within the agglomerate itself did not permit the isolation of the internal aggregation structure. Figure 168 (d) depicts the superposition section of two large spheroidal agglomerates. Since the outer circumference of the agglomerate is visible by relative optical density measurement, it is not suspected that agglomerate coalescence is present, which is an encouraging sign that the cold carbon generator does not produce carbon agglomerate that later coalescence due to Van der Waals force to form larger agglomerates, at least within the residence time of the output drier. Machine vision processing algorithms were applied on discernable agglomerates and primary soot particles and sizing results are presented in figure 169 against the Cabot Carbon Cab-O-Jet manufacturer data. Pigment (aggregate) size measurements were performed by the manufacturer using the dynamic light scattering method: pigments (aggregates) are approximated as spherical and their diameter measured using dynamic light scattering [cite Cabot Carbon] from aggregates dispersed within the solution, using the principle than the Brownian motion of a dispersed particle can be measured as a light scattering vibrational frequency (RF) and the obtained vibrational frequency is proportional to the particulate diameter. In this case a Leeds & Northrup Microtrac® UPA150 particle analyzer was stated as the reference measurement instrument by Cabot Carbon (2006). Therefore the measurements provided are an approximation of aggregates size similar to a particle aerodynamic diameter measurements and are therefore difficult to correlate with more realistic TEM measurement, eventhough they provide an approximate aggregate mean size of the order of 130 nm, with all aggregates stated as <600nm (Cabot Carbon, 2006). Results from the optical TEM measurements were performed on 33 spheroidal

carbon agglomerates. The sphericity of the agglomerates was evaluated through the measurements of their respective Heywood circularity factor, which is the actual optically measured particle perimeter divided by the perimeter of a circle having the same area as the agglomerate itself, with 1 meaning that the agglomerate would be perfectly circular within the measurement plane and eventually forming a perfect sphere by extrapolation. The average circularity factor found was 1.29 ± 0.21, with most dissociations from circularity due to the spherical primary particulate structure forming the outer perimeter of agglomerates and therefore increasing the agglomerate perimeter by a factor > 0.2. The minimal agglomerate Wadell diameter was measured at 66.32nm whereas the maximal diameter reached 1742.94 nm, with a median Wadell diameter of 263.26. These results infirm that: (1) a large range of agglomerate diameters is present, which is certainly due to the fact that the cold carbon generator was operated with the virtual impactor acting as a diluter and therefore decreasing the quality of the size-selection process. Clearly this is a domain with much room for improvement and the present author believes that further research can lead to near-monodisperse agglomerate size distributions; (2) agglomerate sizes can reach manufacturer –stated aggregate sizes, and therefore the possibility exist to produce a controlled amount of well-characterised soot aggregates per agglomerate, which would therefore provide precious data for future agglomeration corrections as well as a qualification and quantification of the thermodynamics effects due to agglomeration, which have not been performed so far. Primary soot particle measurements were performed on 80 isolated structural units, with an average primary particle diameter of 17.96 ± 4.20 nm and a median primary particulate diameter of 18.05nm.

Future improvement suggestions for this aerosol generator comprise:

Modernisation and implementation of automated flow controllers for both atomiser and virtual impactor pressure inlets

(a) Implementation of the second impactor (virtual) stage and obtention of controlled droplet size distribution, together with a complete characterization of the atomiser spray droplet size distribution adjustments and both virtual and inertial impactor performance assessments in terms of droplet size distribution selection.

(b) Carbon ink dispersion improvements in terms of reducing and controlling the surface tension of the carbon aggregate-based ink , which can be effected by mixing the aqueous solution with known quantities of ethanol. Clearly this would result in a neat reduction in terms of atomiser mean droplet size diameter and increase the inertial impactor stage efficiency in order to avoid future LII signal contributions being majored by outstandingly large agglomerates rather than by the median agglomerate size contribution.

(c) As well, repeatable and stabilised soot volume fraction is highly desirable in order to perform studies of measured SVF against laser irradiation fluences and steps have to be performed in order to increase the cold carbon generator output flow stability, either through the installation of a chimney, which would hence provide a longer aerosol residence time medium and therefore incur the risk of agglomerate coalescence; or by increasing the overall flow out of the cold carbon generator with either a larger compressed air supply being fed to the atomiser pressure inlet or incorporating an additional collinear air flow around the nebuliser itself.

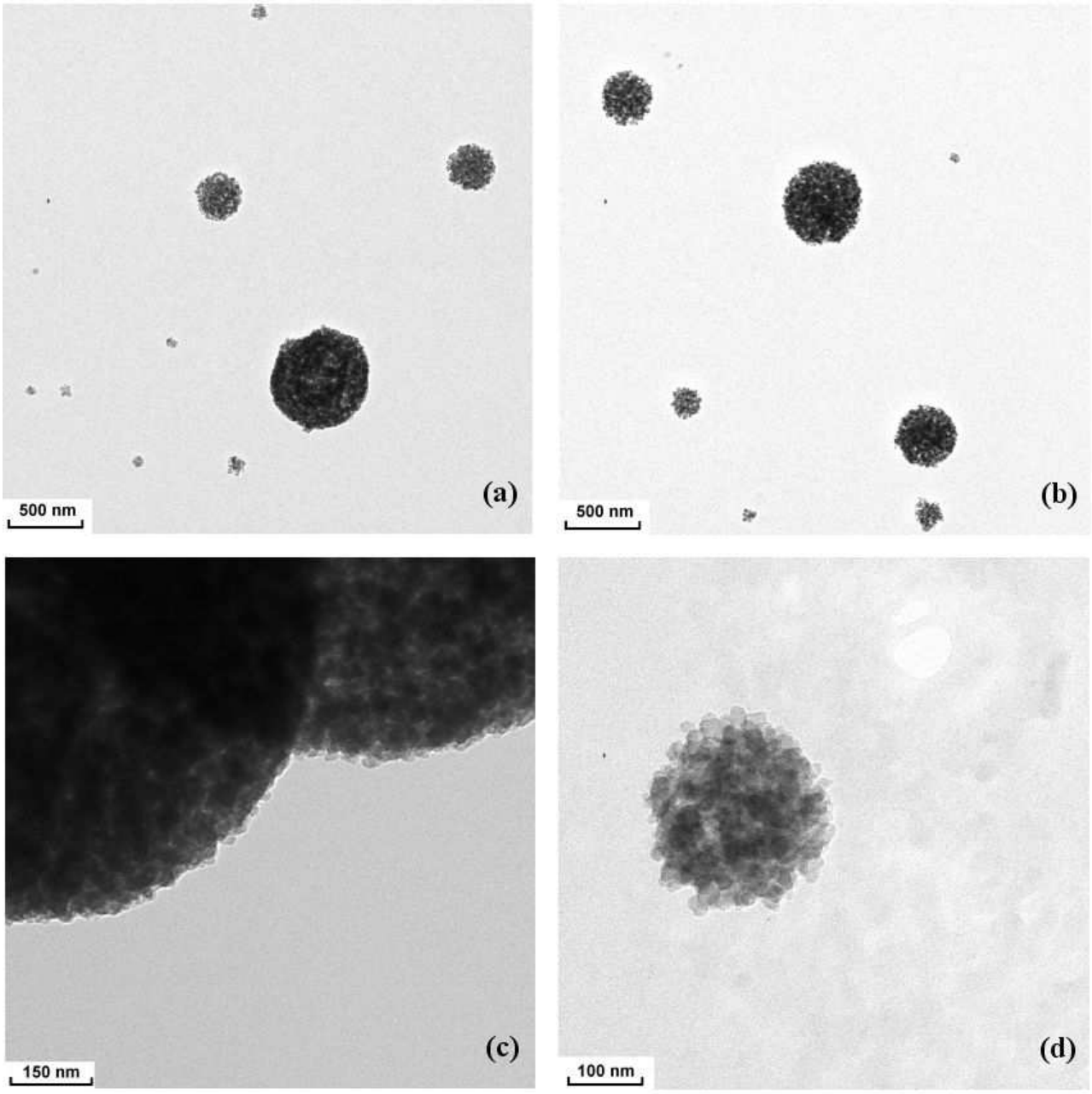

Figure 168: example of high resolution TEM imaging results obtained at NRC. (a) & (b) are 6300:1 magnified images, while (c) has a magnification factor of 24 000:1 and (d) is 33 000:1 magnified. Note that the carbon film substrate in the background presents a smooth uniform negligibly absorbing surface and is hardly discernable.

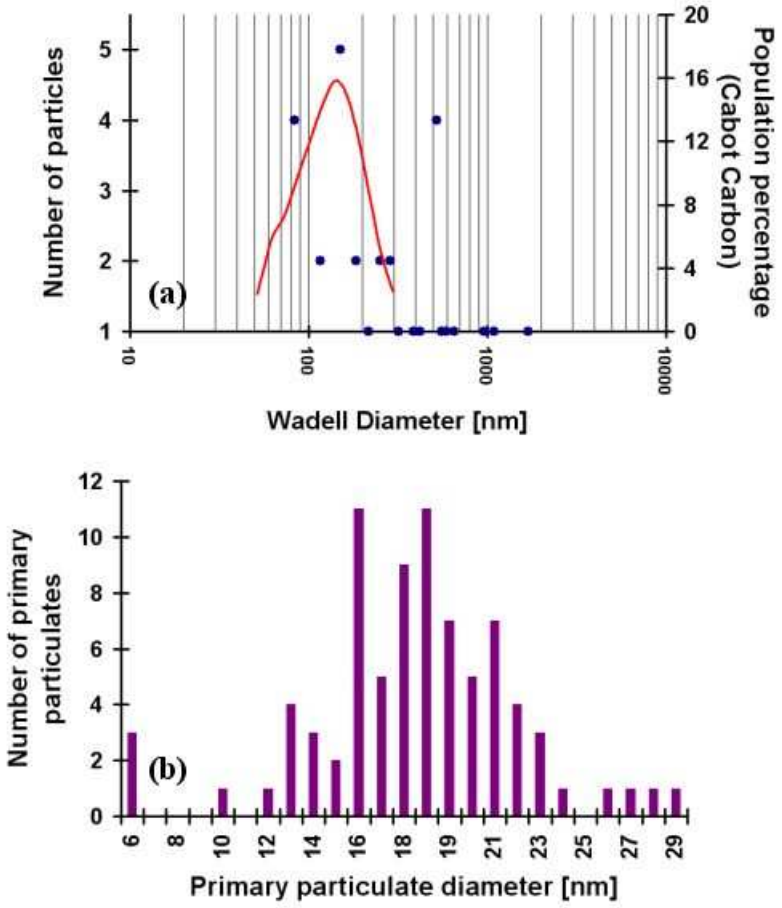

Figure 169: Particle optical size measurement results obtained:

(a) Agglomerate diameter measurements performed on TEM imaging (blue dots) using the Wadell diameter approximation (the actual diameter measured is the diameter of a disk with the same area than the agglomerate) and Cab-O-Jet manufacturer data (red line).

(b) Primary soot particulate diameter histogram measured by the machine vision software operator using a calliper routine.

G.5. Cold carbon generator: Laser-Induced Incandescence applied to atmospheric characterized soot agglomerates.

The work presented in the following section is novel in terms that, to the knowledge of the present author, no similar work has been performed with agglomerates of know size parameters and internal primary soot particle diameters. As well, the outstanding stability and repeatability of the cold carbon generator output plume permits a study of detectable Soot Volume Fraction (SVF) at various fluences and the establishment of a trend between measured SVF and laser irradiation fluences, which indeed matches the observations performed by Smallwood et Stagg (2006).

The laser-induced incandescence instrument used here is the "standard" NRC LII configuration. Figure 170 describes the experimental system implemented here. As stated in the preceding section, the LII measurements presented here where performed in parallel of the LII under vacuum study during the author's placement at NRC (Canada) using similar measurement procedures and data processing methods.

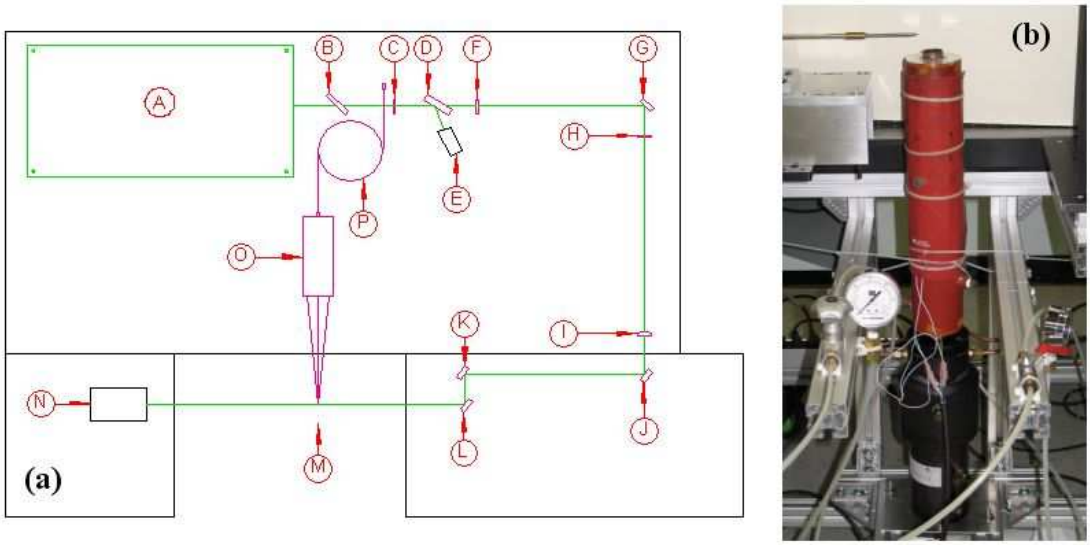

Figure 170: Measurement layout:
(a) Optical stand schematic, see section IV.4. for labels significations.
(b) Image of the carbon generator in place for testing, with the carbon evaporator outlet placed 35mm below the measurement volume M and centred on the measurement volume vertical axis.

The cold carbon generator was operated using a 2% pigment mass concentration of Cab-O-Jet 200® solution diluted in distilled water. The atomiser pressure inlet was operated at the reference 69KPa pressure while the virtual impactor pressure was fed at the reference 31KPa using compressed air. Cold carbon generator plume temperature at the measurement point was measured at approximately 75 ˚C with an an Omega® display unit (model HH23) linked to a K-type thermocouple . Initial measurements were performed in order to assess LII signal stability with 100 single-shot LII signals collected and their light intensity compared and estimated in terms of repeatability for the two LII systems demultiplexer channels (blue and red). Signal repeatability results are depicted in figure 171.

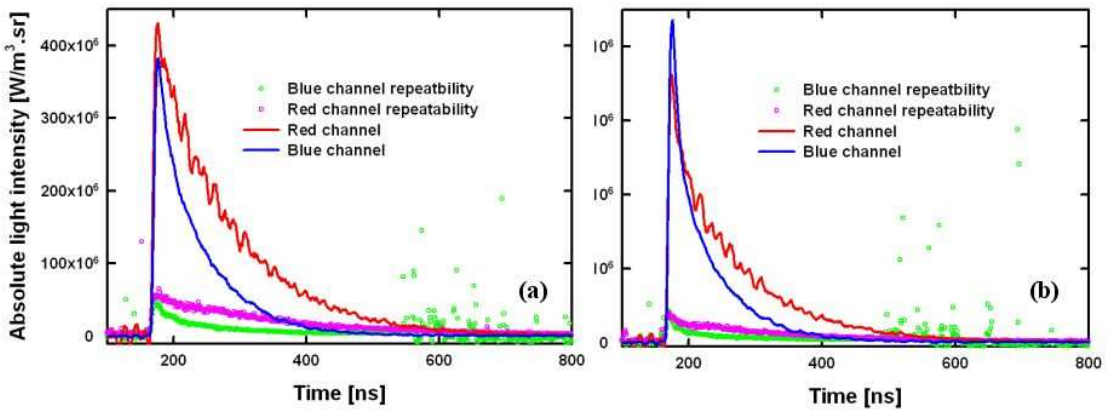

Figure 171 : LII signals repeatability. Measurements were carried by acquiring 100 single-pulse LII signals and measuring the average and standard deviation as a measure of signal repeatability:
(a) for a fluence of 0.133 J/cm^2
(b) for a fluence of 0.167 J/cm^2.

Repeatability measurements were carried at 0.133 and 0.167 Jcm^2 to discriminate for PMT shot noise and background noise level (laser Q-switch noise in particular) as signal levels proved to increase with laser fluence at equivalent soot temperatures. The carbon generator exhaust plume proved extremely repeatable with less than 10% pulse-to-pulse variation (7-8% at 0.167 J/cm2 and 8.5-10% for at 0.133J/cm^2). This confirmed the earlier results obtained with the Artium LII 200® instrument which proved the generator can deliver an extremely repeatable soot volume fraction aerosol measurement on longer time scales (within less than 7%).

The following measurements were performed using the same configuration in terms of atomiser inlet pressure and virtual impactor inlet pressure as well as carbon ink concentration. Measurements were performed for a set of 5 laser irradiation fluences ranging between 0.067 J/cm^2 and 0.150 J/cm^2. 2400 multipulse averages were performed for each laser fluence. LII signal acquisitions were performed with a sampling time resolution of 400ps and later resampled and filtered with 1ns as a filter and resampler time base for the first 100 ns of incandescence signals, followed by a filtering time constant of 10ns for the remaining of the acquired signals. Q-switch noise subtraction was effected on all measurements. Light intensity results are presented in figure 172, followed by temperature computations results (figure 173) and soot volume fractions (figure 174 -a). As it was expected following the work published by Smallwood and Stagg (2006), it was found that the average soot volume fraction measured was rising with increasing laser irradiation fluences, as shown on figure 174-b. As well, an investigation into the absorption regime leading to the determination of E(m) during laser absorption, using the principle that LII peak temperature is independent of primary particle diameters at low laser fluences(Snelling et al, 2004). Therefore the laser temporal profile was fed into the laser-induced incandescence model for fluences of 0.067, 0.081 and 0.100 J/cm^2 and the peak modelled temperature matched with the measured peak LII temperature by means of varying the model E(m) value for absorption at 532nm. The obtained results are given in table 12. An average E(m) value of 0.414 was therefore concluded, which is near the values measured by Snelling et al. (2004) (circa 0.4).

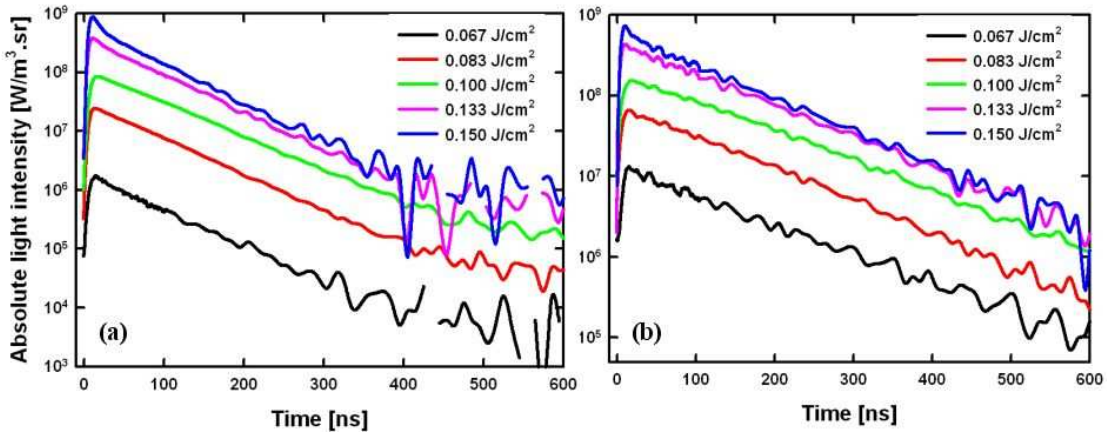

Figure 172: LII signal absolute light intensity signals recorded from 35mm above the cold carbon generator drier outlet for five different laser fluences, ranging from 0.067 to 0.150 J/cm^2:
(a) Blue channel measurements
(b) Red channel measurements.

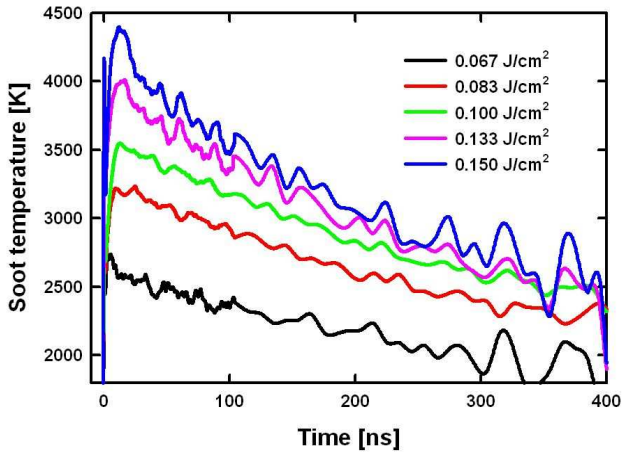

Figure 173: Laser-Induced incandescence temperature as a function of time curves obtained from the exploitation of the results presented in figure 145.

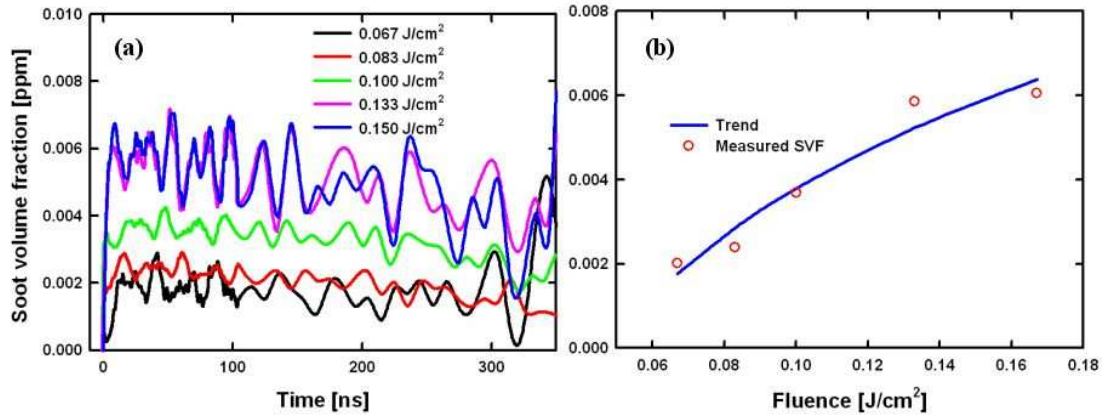

Figure 174: Instantaneous (a) and time-averaged (b) soot volume fraction as a function of time (a) and fluence
(a) instantaneous soot volume fraction
(b) time-averaged soot volume fraction : instantaneous soot volume fractions were averaged over the time interval 20-30 ns were most of them are nearly constant for all fluences.

Laser Fluence [J/cm^2]	Measured soot peak temperature [K]	Estimated corresponding E(m) value
0.067	2737	0.4170
0.083	3217	0.4145
0.100	3547	0.4100

Table 12: E(m) estimates performed for a laser fluence range of 0.067 to 0.1 J/cm^2.

Although the determination of E(m) by absorption means at a given laser excitation wavelength seems attractive, little is known about the actual light absorption behaviour of soot agglomerates, even though application of the physical principle proved successful for E(m) determinations within a flame environment (Snelling et al, 2004), where mostly nucleating soot particles and aggregates are present. Therefore the E(m) measurements presented in table 12 remain hypothetical and assume isolated primary particle laser absorption.

A second type of measurement was made using the conductive temperature cooling decay for all laser fluences from 50 to 300 ns after the start of LII signals. An exponential fit was performed on the observed temperature decay and fed to the model in order to provide a particle diameter measurement. Start fit temperatures were found to be increased with fluence, from 2470K to 3823K and results are presented in table 13 below . The obtained primary particles are found to largely overestimate the actual primary soot particulate diameter, with a factor 2.3 overestimation at 0.067 J/cm^2 with 41 nm measured whereas the actual primary particle diameter was measured by TEM imaging with a median diameter of 18.05nm. However, the primary particle diameter measured using the LII method decreased by a factor 1.3 with the laser fluence increased from 0.067 J/cm^2 to 0.167 J/cm^2 with measured primary particle diameters decreasing from 41 to 28nm.

Laser Fluence [J/cm^2]	Soot temperature at 50ns [K]	Calculated particle diameter [nm]
0.067	2470	41
0.083	3071	36
0.100	3363	36
0.133	3635	30
0.167	3823	28

Table 13: Laser fluence, soot particle temperature at 50 ns (start of experimental fit) and deducted primary particle diameter.

Clearly, overestimated primary soot particle diameters are due to primary particles thermally shielding one from another within tightly agglomerates with relatively less surface available for local gas interactions and heat conduction to the local medium, and therefore cooling temperature decays greatly slowed to provide virtually larger than realistically measured primary particle size measurement using LII. Furthermore, experimentations under vacuum proved that agglomerates, once irradiated by a high power laser pulse - such as the Nd-YAG laser beam produced by the measuring instrument used here – have a tendency to overcome the Van der Waals bonding forces that holds aggregates together within agglomerates and gradually dissociate into smaller entities, reaching the aggregate and primary particle size on a 50µs timescale. This phenomena was generally observed as increasingly more dynamic

with increasing laser fluence and decreasing agglomerate size, meaning that smaller agglomerates enduring increasing laser fluences would dissociate on a shoter timescale. Clearly one can therefore postulate that in the present case, complete agglomerate dissociation cannot occur, as LII signals were present on a microsecond timescale, but that the agglomerate dissociation effect was indeed enhanced with laser fluence and initiation of agglomerate dissociation and eventually agglomerate swelling is present, with agglomerates presenting relatively larger surface areas available for heat conduction to the surrounding gas. This phenomena would explain the results obtained as measured primary particle size decreased with fluence and the hypothetical agglomerate dissociation endure.

Using a different approach and reminding the reader of the principle of sublimation - which typically contribute to LII temperature decays above 2800K - results in mass due in majority to C_2 and C_3 carbon clusters desorption away from soot primary particles. This intrinsic mass loss results in primary particle volume reduction. However, mass losses can only be partially attributed to primary particle diameters reductions as results presented in table 13 represent a mass loss of nearly 32 % from 0.067 J/cm^2 to 0.167 J/cm^2 whereas modelling predicts less than 10% mass loss per primary particle. Hence sublimation cannot be recognised in this case as the sole contribution. Likewise, annealing is starting to draw attention within the combustion domain Hope Michelsen (2003) and is supposed to induce volumic changes such as volumic increases and primary particle structures becoming fused as the originally amorphous carbon anneals and crystallises into graphitic layers, but no conclusions can be drawn on this subject. As a conclusion to this section, the measured change in primary particle diameter with fluence can be attributed to two contributors: (1) agglomerate dissociation, with an increasing dissociation effect with fluence (2) limited sublimation.